29 February 2008 | S10

Science

Quantum Matter

AAAS

Volume 319, Issue 5867

COVER

Like a cauliflower, the quantum critical regime has the same appearance irrespective of viewing distance. Fluctuations prevent a stable phase from developing; instead a patchwork of mixed phases arises. See the special section on quantum matter beginning on page 1201.

Image: Getty Images

DEPARTMENTS

EDITORIAL

SPECIAL SECTION

Quantum Matter

INTRODUCTION

PERSPECTIVES

>> News Focus article p. 1180

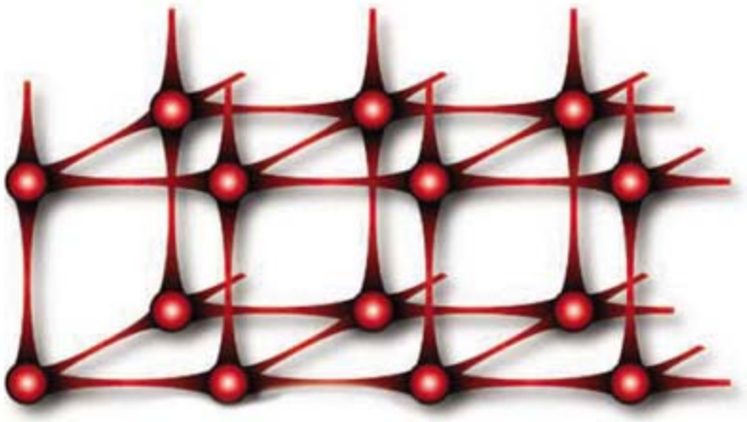

NEWS OF THE WEEK

NEWS FOCUS

CONTENTS continued >>

Science

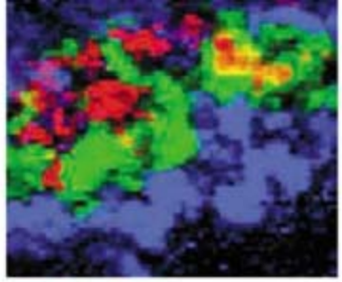

SCIENCE EXPRESS

www.sciencexpress.org

CLIMATE CHANGE

Covariant Glacial-Interglacial Dust Fluxes in the Equatorial Pacific and Antarctica

G. Winckler, R. F. Anderson, M. Q. Fleisher, D. McGee, N. Mahowald

A 500,000-year record shows that more dust, which provides iron and other nutrients, was blown into the equatorial Pacific during glacial periods than during warm periods.

10.1126/science.1150595

GEOCHEMISTRY

Graphite Whiskers in CV3 Meteorites

M. Fries and A. Steele

Graphite whiskers, a naturally occurring allotrope of carbon, have been found in primitive grains in several meteorites and may explain spectral features of supernovae.

10.1126/science.1153578

MEDICINE

TDP-43 Mutations in Familial and Sporadic Amyotrophic Lateral Sclerosis

J. Sreedharan et al.

Mutations in a gene that encodes a protein that aggregates in several neurodegenerative disorders are linked to amyotrophic lateral sclerosis (Lou Gehrig's disease).

10.1126/science.1154584

NEUROSCIENCE

Protein Synthesis and Neurotrophin-Dependent Structural Plasticity of Single Dendritic Spines

J. Tanaka et al.

Pairing of stimuli in hippocampal cells induces secretion of the growth factor BDNF, causing enlargement of individual spines and strengthening of synapses.

10.1126/science.1152864

LETTERS

BOOKS *ET AL.*

EDUCATION FORUM

PERSPECTIVES

1191 & 1244

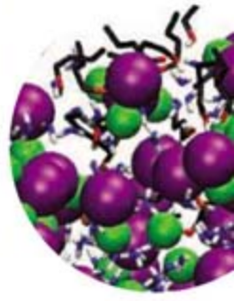

1197

BREVIA

RESEARCH ARTICLE

REPORTS

CONTENTS continued >>

REPORTS *CONTINUED...*

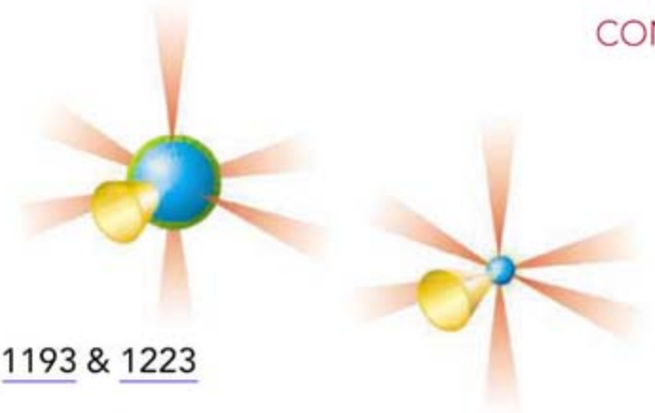

1193 & 1223

AAAS
ADVANCING SCIENCE, SERVING SOCIETY

SCIENCE (ISSN 0036-8075) is published weekly on Friday, except the last week in December, by the American Association for the Advancement of Science, 1200 New York Avenue, NW, Washington, DC 20005. Periodicals Mail postage (publication No. 484460) paid at Washington, DC, and additional mailing offices.

Domestic individual membership and subscription (51 issues): $144 ($74 allocated to subscription). Domestic institutional subscription (51 issues): $770; Foreign postage extra: Mexico, Caribbean (surface mail) $55; other countries (air assist delivery) $85. First class, airmail, student, and emeritus rates on request. Canadian rates with GST available upon request, GST #1254 88122. Publications Mail Agreement Number 1069624. SCIENCE is printed on 30 percent post-consumer recycled paper. **Printed in the U.S.A.**

Change of address: Allow 4 weeks, giving old and new addresses and 8-digit account number. **Postmaster:** Send change of address to AAAS, P.O. Box 96178, Washington, DC 20090–6178. **Single-copy sales:** $10.00 current issue, $15.00 back issue prepaid includes surface postage; bulk rates on request. **Authorization to photocopy** material for internal or personal use under circumstances not falling within the fair use provisions of the Copyright Act is granted by AAAS to libraries and other users registered with the Copyright Clearance Center (CCC) Transactional Reporting Service, provided that $20.00 per article is paid directly to CCC, 222 Rosewood Drive, Danvers, MA 01923. The identification code for *Science* is 0036-8075. *Science* is indexed in the *Reader's Guide to Periodical Literature* and in several specialized indexes.

CONTENTS continued >>

Bigger amygdalas in aggressive teens.

SCIENCE**NOW**

www.sciencenow.org DAILY NEWS COVERAGE

Teen Aggressiveness in the Brain
Tough-to-handle adolescents share bigger amygdala.

New Map for Malaria
Disease prevalence lower than thought.

Giving Earth an Umbrella
Computer models show how releasing clouds of fine particles could cool the planet.

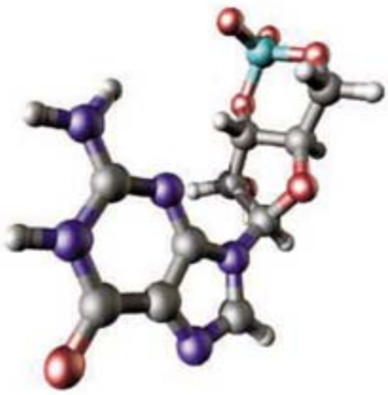

cGMP is a therapeutic target.

SCIENCE **SIGNALING**

www.stke.org THE SIGNAL TRANSDUCTION KNOWLEDGE ENVIRONMENT

MEETING REPORT: cGMP Matters
B. Kemp-Harper and R. Feil
Emerging therapies for treating cardiovascular disorders target the cGMP signaling system.

TEACHING RESOURCE: Using Web-Based Discussion Forums as a Model of the Peer-Review Process and a Tool for Assessment
S. L. Jenkins, R. Iyengar, M. A. Diverse-Pierluissi, A. M. Chan, L. A. Devi, E. A. Sobie, A. T. Ting, D. C. Weinstein
Asynchronous discussion forums have several advantages over in-class journal club discussions.

Jetting to one more faculty interview.

SCIENCE **CAREERS**

www.sciencecareers.org CAREER RESOURCES FOR SCIENTISTS

Research in Translation: Getting Published
S. Carpenter
Careful planning and choosing the right journal are key in publishing translational research.

In Person: Frequent Flyer
A. McNeil
Faculty interviews come with tight scheduling, awkward questions, and jet lag.

Educated Woman, Postdoc Edition, Chapter 13: Fake It Until You Make It?
M. P. DeWhyse
Can Micella regain confidence in her abilities for her interview?

From the Archives: Disasters of the Famous
K. Arney
Prominent scientists' stories of lab errors remind us that everyone makes mistakes.

SCIENCE**PODCAST**

Download the 29 February *Science* Podcast to hear about ice-nucleating bacteria in snow, how bats generate lift at slow speeds, future prospects for Mars research, and more.
www.sciencemag.org/about/podcast.dtl

CREDITS: (SCIENCE NOW) SARAH WHITTLE AND STUDY GROUP; (SCIENCE CAREERS) BRYAN CORREIRA/CREATIVE COMMONS

Separate individual or institutional subscriptions to these products may be required for full-text access.

<< A Blue-Emission Special

The fluorescence of *trans*-stilbene can be used as a probe of its surrounding environment. In solution, it fluoresces only weakly because the excitation energy drives a rapid isomerization to the cis form; in confined environments that inhibit isomerization, fluorescence can be seen more readily. **Debler *et al.*** (p. 1232; see the Perspective by **Armitage and Berget**) have reexamined the intense blue luminescence from a stilbene-antibody complex that was initially described as fluorescence from a complex that formed between the excited state of stilbene and a tryptophan (Trp) residue. The excited-state complex forms via charge transfer to form an anionic stilbene and a cationic Trp. Charge recombination is the source of the intense blue emission.

Asymmetric Explanations

The intense explosions known as "gamma-ray bursts" (GRBs) may be associated with supernova explosions after the death and collapse of a star. Some GRB events could be explained if these explosions are asymmetric, with strong jets emerging from the fireball, and if the jets are in our line of sight. **Maeda *et al.*** (p. 1220, published online 31 January) have looked at the spectra of several such events at times late in the evolution of the emission, when expansion lowers the density of the ejected matter and allows optical photons to escape. This approach permits a glimpse of the far side of the explosion. Analysis of these results indicates that explosions are aspherical for many GRBs.

Incurring Carbon Debts in Biofuel Production

Although biofuels have the potential to reduce CO_2 emissions, secondary effects of biofuel production must also be considered, such as how much CO_2 is released by the conversion of land to the production of biofuel stock. **Fargione *et al.*** (p. 1235, published online 7 February) analyze the carbon balance of the conversion of a variety of carbon-rich land types to food-based biofuel croplands and find that the carbon debt incurred by the conversion process can be as much as 420 times that of the annual greenhouse gas emission reductions that result from the displacement of fossil fuels from the energy generation process. Biofuels made from waste biomass, or grown on abandoned agricultural lands, can avoid most, or even all, of that carbon debt, however. **Searchinger *et al.*** (p. 1238; published online 7 February) have modeled greenhouse gas emissions in the production of corn-based ethanol. Instead of generating a roughly 20% reduction in greenhouse gases, as typically is claimed, emissions would approximately double during the first 30 years of implementation and create an emission increase that would take more than 160 years to recoup.

An Atomic View of Current Flow

The magnetic properties of ultracold atom clouds can be used as minute compass needles for the detection of small changes in magnetic field. As current flows through a wire, scattering of the electrons is usually confined to short length scales, and long-range ordering would not necessarily be expected. However, **Aigner *et al.*** (p. 1226) report a surprising finding using cold atom magnetometry to study the flow of current in polycrystalline gold wires. Ordered current fluctuations occur along the length of the wire angled at 45° to the current flow. They interpret and model the observed patterns as arising from scattering of the electrons around defects.

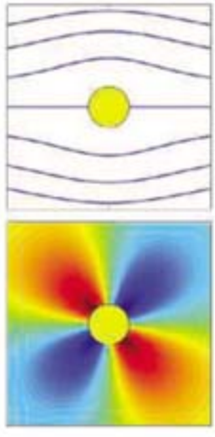

CREDITS (TOP TO BOTTOM): BIOMEDICAL GRAPHICS/THE SCRIPPS RESEARCH INSTITUTE; AIGNER *ET AL.*

Imaging a Tight Squeeze

One form of controlled nuclear fusion uses high-energy lasers to compress small capsules of hydrogen to densities and temperatures where fusion reactions can occur. Achieving optimum compression will require measurements of the shape and distribution of matter during the implosion, as well as an understanding of how local electromagnetic fields might affect the fusion plasma. **Rygg *et al.*** (p. 1223; see the Perspective by **Norreys**) used proton beams to create images of imploding fusion targets that map out the density and field distribution as a function of time during compression. The maps show unusual structures in the plasma that consist of filaments and strong radial electric fields that have a clear influence on the implosion dynamics.

Exosome Assembly Pathway

Exosomes are vesicles of endocytic origin that are released into the extracellular environment after fusion of multivesicular endosomes with the plasma membrane. **Trajkovic *et al.*** (p. 1244; see the Perspective by **Marsh and van Meer**) found that the exosomal cargo segregates together with lipid-raft components into distinct microdomains on the endosomal membrane. The transfer of these microdomains into the lumen of the endosome did not depend on the function of the known intravesicular budding ESCRT (endosomal sorting complex required for transport) involved in the degradative pathway, but required ceramide. Exosomes were enriched in ceramide, and exosome formation was sensitive to the inhibition of neutral sphingomyelinases. In giant unilamellar liposomes, addition of sphingomyelinase was sufficient to induce the inward budding of lipid rafts into a liposome. Thus, lipid rafts may act as collecting devices for

Continued on page 1159

Continued from page 1157

the lateral segregation of cargo in the limiting membrane of endosomes, and the formation of ceramide from sphingomyelin within these microdomains could trigger membrane budding into the multivesicular endosome.

Synthetic Bacterial Chromosomes

The synthesis of genomes de novo will provide a powerful tool for understanding the basic biology of living organisms and designing genomes for medical and environmental applications. **Gibson *et al.*** (p. 1215, published online 24 January; see the Perspective by **Endy**) have assembled the complete 580,076–base pair genome of *Mycoplasma genitalium*, starting from cassettes of 5 to 7 kilobases in size. The synthetic genome contained short "watermark" sequences at intergenic locations. Although it was possible to do some of the assembly in vitro, the larger fragments were assembled (that is, quarter genomes assembled into halves and wholes) by recombination in yeast.

Explaining Polarized Growth Patterns

The ability of certain cells to grow in a polarized fashion has been studied for many years, but the mechanisms involved in the process, particularly in plant cell systems, remain unclear. **Takeda *et al.*** (p. 1241) report the discovery of a positive feedback mechanism that regulates the development of a polarized cell shape in the commonly studied model plant, *Arabidopsis thaliana*. The positive feedback system is generated by the local interaction of Ca^{2+} and reactive oxygen species in root hair cells and is central to the maintenance of active growth at spatially restricted sites during polarized cell elongation.

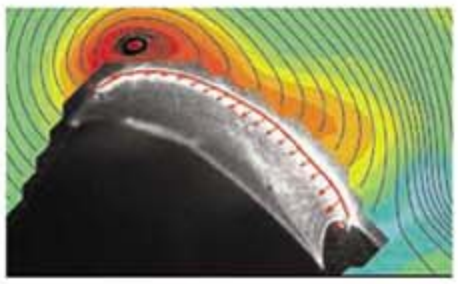

CREDIT: MUIJRES *ET AL.*

Bat Flight Plan

Recent work has found that bat wings generate very high lift coefficients at low flight velocities. However, the aerodynamic mechanism responsible for this excess lift has remained obscure. **Muijres *et al.*** (p. 1250) have visualized and measured the air flow above the wing surface of actively flying bats. The main lift-enhancing mechanism observed is a leading-edge vortex, which stays attached to the wing throughout the downstroke. The same unsteady mechanism is also responsible for high lift generation in insects.

Memory Breakdown

The phenomenon of memory reconsolidation has made people question the traditional view that long-term memories become more stable and resistant to perturbation with time. Reconsolidation indicates that memory change is a continuous process and that change is initiated by retrieval experiences themselves. However, the cellular events and mechanisms underlying this phenomenon have not been clear. **Lee *et al.*** (p. 1253, published online 7 February) provide evidence for degradation of postsynaptic proteins in hippocampal synapses thought to participate in the formation of contextual fear memories. Blockade of this degradation is accompanied by blockade of the retrieval-induced reorganization of the original memories. Thus, reconsolidation is like a breakdown of original memories while new elements are incorporated by new protein synthesis.

The phenomenon of memory reconsolidation has made people question the traditional view that long-term memories become more stable and resistant to perturbation with time. Reconsolidation indicates that memory change is a continuous process and that change is initiated by retrieval experiences themselves. However, the cellular events and mechanisms underlying this phenomenon have not been clear. **Lee *et al.*** (p. 1253, published online 7 February) provide evidence for degradation of postsynaptic proteins in hippocampal synapses thought to participate in the formation of contextual fear memories. Blockade of this degradation is accompanied by blockade of the retrieval-induced reorganization of the original memories. Thus, reconsolidation is like a breakdown of original memories while new elements are incorporated by new protein synthesis.

Dissecting Function in the Living Brain

Because the brain is composed of many interconnected cell types in close proximity, it is not easy to determine the precise function of any one class. Existing methods such as lesions or pharmacological inhibition are relatively crude, and their effects cannot reliably be used to eliminate the contribution of one cell type. Even genetic approaches, which can be targeted to certain cells, have only been used to inhibit one receptor subtype, and the deficits are often present throughout development, confounding interpretation. **Nakashiba *et al.*** (p. 1260, published online 24 January) constructed a tetanus-toxin–based, triple-transgenic mouse that allows reversible inhibition of all the synaptic activity of one type of cell in the hippocampus, the CA3 pyramidal cell. When the CA3 hippocampal cells were silenced, the mice could still learn a spatial task but could not recall certain memories or perform rapid learning tasks.

Donald Kennedy is the Editor-in-Chief of *Science*.

On the Way Out

AS I WRITE, I HAVE JUST A WEEK OR SO LEFT AS EDITOR-IN-CHIEF OF *SCIENCE*. IT IS ONE OF those mixed-emotions moments. I'm leaving some wonderful colleagues, which is painful, but on the other hand, my friend Bruce Alberts gets the opportunity to work with them. He deserves the splendid help they will give him, and they will have a leader who understands science, enjoys the deep respect of the community, and led it brilliantly as president of the National Academy of Sciences for a dozen years. So *Science* and the American Association for the Advancement of Science (AAAS) are the beneficiaries of a fine appointment. A profile of Bruce (p. 1199) explains why we are in such good hands. Meanwhile, I need to hurry and clean up any loose ends before he asks about them.

I had thought of celebrating this transition by designating some parting gifts to leave Bruce and my colleagues in science. Before getting to problem solutions, enemies lists, and the like, my first gift to Bruce is of Tiffany quality: the Editorial and News staffs he will inherit. Colin Norman in News and Monica Bradford as the Executive Editor are superb professionals, and the staffs they lead are as able and committed as their equivalents in any place I've ever been. Alan Leshner has been a great colleague and friend, and Beth Rosner and her staff have held off the recession. I hope to stay in contact with many of them.

In return for that, I want to beg Bruce to let me write the occasional editorial. His own passions for science, education, and public policy will fill that space elegantly, but I want a chance to poach a little whenever some outrage exceeds my tolerance level. He understands this need of mine, and I am grateful. At the same time, I must bequeath him some volunteers—including distinguished public servants—who will send him editorials they hope *Science* will publish. Some of these will be good, but he should be wary. It's always wise to ask if the proposed piece will be written by the Secretary of Whatever or by some staffer.

The world is full of questions about peer review. A few of our authors have occasionally believed that some reviewer has deliberately stalled a paper or even appropriated an idea. I would like to present the scientific community with some encouragement about this process. We have seen few supportable instances of bad behavior by reviewers, despite occasional claims. Of course peer review is not perfect. It has missed a couple of spectacular frauds, and in a few cases, has approved papers that later turned out to be wrong. But I know of no better process. Neither am I convinced that we should establish a system to press authors for authentication so intensely that it threatens the trust that has characterized our community.

I hope Bruce will not have to deal with an environment in which scientists who work for the U.S. government are controlled by public relations "minders" or by Assistant Secretaries appointed to ensure that science follows policy instead of the other way around. The Union of Concerned Scientists, having fought against this practice for years, has now produced a Bill of Rights for government scientists, designed to liberate federal researchers from practices that had become routine over the two terms of the Bush Administration. This won't be a gift but a duty, because *Science* will have to be alert to identify new cases that the Bill of Rights is designed to prevent.

Finally, I wish I could give my successor some release from the obligations of hearing appeals at *Science*. That requires deciding, negotiating, or rejecting differences that arise between authors and editors; or authors and peer reviewers; or authors contending about priority, or the correctness of another's finding, or delivering material reported in a *Science* paper to another author. Here's the best I can do, Bruce. Be as fair as you can, sympathize with anger, confess institutional error when appropriate, and be firm. And when the disappointed complain to members of the AAAS Board, remember to smile!

– Donald Kennedy

10.1126/science.1156805

EDITED BY GILBERT CHIN AND JAKE YESTON

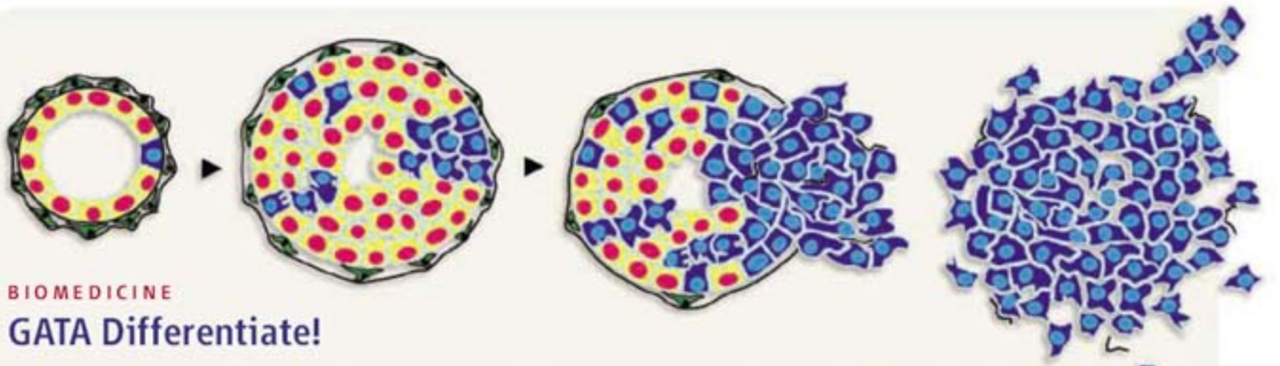

BIOMEDICINE

GATA Differentiate!

Because most cancer deaths are due to metastatic disease, there is great interest in developing therapies that would prevent cells in a primary tumor from undergoing the changes that confer the capacity to disseminate, or that would reverse such changes. Tumors that are destined to disseminate and metastasize display molecular markers that distinguish them from less aggressive cells, but it is not clear if these molecules play a causal role in tumor metastasis, and hence would be suitable drug targets.

Kouros-Mehr *et al.* have explored the role of one intriguing predictive marker in human breast cancer, a transcription factor called GATA-3 that is required for the differentiation and proper function of normal mammary tissue. Breast tumors with low expression levels of GATA-3 typically are poorly differentiated, have a higher metastatic potential, and are associated with a worse clinical outcome than are tumors with high levels of GATA-3. Studying a mouse model of breast cancer, the authors found that GATA-3 expression and markers of differentiated epithelial cells (red-yellow) were lost very early in tumor progression and that this loss was likely due to the expanded growth of GATA-3–negative mammary stem cells (blue). Importantly, when they reintroduced GATA-3–positive cells into later-stage breast tumors, the tumors became more differentiated and showed a reduced capacity to disseminate. These results indicate that GATA-3 is not only a marker but also a causal factor in tumor metastasis, and that drugs activating GATA-3 itself or the molecules that regulate it could form the basis of differentiation therapy for breast cancer. — PAK

Cancer Cell **13**, 141 (2008).

PLANT SCIENCE

Constructing a Scaffold

Plant cells partition at cytokinesis by forming a new cell wall. These walls are composed of interpenetrating networks of the polysaccharides cellulose and pectin and of (hydroxy)proline-rich glycoproteins, notably the extensins. Cannon *et al.* show by electron microscopy that the *Arabidopsis* mutant *rsh* is defective in cell wall assembly and that the defect is likely due to the absence of the *rsh*-encoded extensin protein, AtEXT3. This protein contains 11 identical amphiphilic motifs that, besides being rich in hydroxyproline, contain an isodityrosine (Idt) cross-link motif (YXY) and an HYS motif. In vitro, extensin peroxidase catalyzed tyrosine cross-linking between purified AtEXT3 monomers and led to the inference that the monomers were offset such that intermolecular cross-linking occurred between Idt and HYS, rather than between two Idt motifs. Atomic force microscopy imaging shows that AtEXT3 forms a dendritic network displaying both end-on and lateral adhesion. The alternating hydrophilic and hydrophobic modules of AtEXT3 may induce like-to-like self-association with cross-linking stabilizing the network and favoring a staggered alignment that would permit two-dimensional growth. The authors suggest that such a positively charged extensin network may serve as a template for the orderly deposition of negatively charged pectin during cell wall assembly. — VV

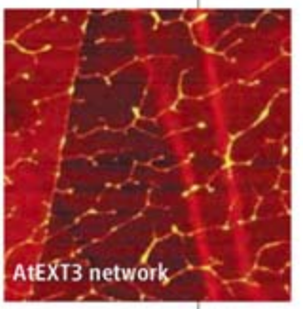

Proc. Natl. Acad. Sci. U.S.A. **105**, 2226 (2008).

APPLIED PHYSICS

Glimpsing Tiny Live Wires

The realization of molecular electronics requires reproducible methods for creating devices in which conduction occurs through individual molecules. Current methods rely on the fabrication of many devices to prove statistically that a single-molecule junction has been realized, but knowledge of the specific chemical environment of the conducting molecules tends to be limited, complicating the interpretation of the data. Ward *et al.* present a method for simultaneous electron transport measurements and single-molecule sensing using surface-enhanced Raman spectroscopy (SERS) on nanometer-scale structures (nanogaps) bridged by individual molecules. The metal electrodes that are used as contacts to the molecules also function as plasmonic antennae, resulting in an enormously enhanced vibrational signal. In about 1 in 10 junctions, changes in conductance with time correlate closely with changes in the SERS signal, supporting a link between electron transport and single-molecule conformational changes. The relation between conductance and SERS spectra remains complex, but steadily improving theoretical analyses paired with such measurements should shed light on the fundamental mechanisms at play. — JFU

Nano Lett. **8**, 10.1021/nl073346h (2008).

MOLECULAR BIOLOGY

Motoring Inside the Nucleus

The highly conserved protein actin not only functions as a critical cytoplasmic actor in cell shape and movement, but also, as shown recently, has a nuclear role in regulating gene expression. The

CREDITS (TOP TO BOTTOM): KOUROS-MEHR *ET AL.*, *CANCER CELL* **13**, 141 (2008); CANNON *ET AL.*, *PROC. NATL. ACAD. SCI. U.S.A.* **105**, 2226 (2008)

frequent companion of cytoplasmic actin is the motor protein myosin; therefore, it is not surprising that a myosin isoform (NM1) can be found in the nucleus. Ye *et al.* have examined the contributions of nuclear actin and myosin to transcription and find that NM1 and oligomeric (possibly filamentous) actin cooperate in the transcription of ribosomal RNA genes by RNA polymerase I. A series of experiments demonstrated that NM1 adenosine triphosphatase activity was necessary and that the cyclic actin-myosin interaction observed in skeletal muscle was likely to occur in the nucleus as well. The authors suggest that actin and myosin may collaborate in driving RNA polymerase and its target genes together. — BAP

Genes Dev. **22**, 322 (2008).

MATERIALS SCIENCE

A Graded Improvement

Refractive index is a key parameter to consider in selecting materials for optics and photonics applications, as it determines the extent of reflection and refraction when light impinges on an interface. Unfortunately, optimal choice of this parameter often necessitates compromising other material properties. Kim *et al.* show that they can conveniently tailor the refractive index of a single material—the transparent conductor indium tin oxide (ITO)—for device applications. Using oblique angle deposition, they are able to grow porous films consisting of arrays of oriented rods. The porosity can be controlled by changing the angle of the ITO vapor flux, thus tuning the refractive index from a bulk value of 2.19 to below 1.3. The authors exploit this tunability to grow a six-layer gradient coating on a light-emitting diode (LED), in which the ITO acts as both a coating and a conducting layer. By gradually reducing the refractive index, they eliminate almost all Fresnel reflection and thereby improve the output of the LED by 24% compared to a device made with a bulk ITO layer. — MSL

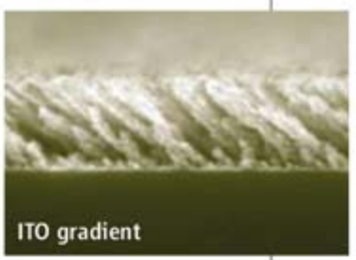
ITO gradient

Adv. Mater. **20**, 801 (2008).

CHEMISTRY

Picking O over N

In general, amines react more rapidly with carbonyl electrophiles than do alcohols. Lipase enzymes manage to invert this tendency and efficiently catalyze ester formation even in the face of a nearby nitrogen group striving to form an amide. Artificial catalysts have been less successful for this purpose though, and laboratory amino ester syntheses therefore often require wasteful N protection and deprotection steps. Ohshima *et al.* have now prepared a tetranuclear zinc cluster that bucks this trend and affords selectivity along the same lines as the enzymes. At loadings as low as 1.25 mole percent, the oxophilic catalyst gives 82 to 99% yields of the ester in reactions of methyl benzoate with a range of terminal alkyl amino alcohols. Similarly, ester selectivities higher than 90:1 are observed when equal concentrations of various amines and alcohols compete intermolecularly. The authors posit a mechanism that entails dual activation of the alcohol and electrophile by cooperative Zn centers. — JSY

J. Am. Chem. Soc. **130**, 10.1021/ja073578i (2008).

Science Signaling AAAS

<< A Receptor for Neurotrophins

Integrins are dimeric cell surface receptors composed of α and β subunits and interact with the extracellular matrix (ECM) to promote cell adhesion and survival. There are 18 α and 8 β subunits in mammals, and at least 24 heterodimers have been described. Given this complexity, it is not surprising that integrins have been observed to interact with molecules other than those in the ECM. For example, $\alpha_9\beta_1$, a widely distributed integrin, interacts with several classes of ligands, including ECM constituents (tenascin, thrombospondin 1, and osteopontin), metalloproteases (ADAM12 and 15), and vascular endothelial growth factor. Staniszewska *et al.* report that integrin $\alpha_9\beta_1$ also binds to the neurotrophins NGF, NT3, and BDNF. They found that an $\alpha_9\beta_1$–transfected colon cancer cell line adhered to mouse NGF, human recombinant NGF, BDNF, or NT3 with the same efficiency as to VCAM1, a known $\alpha_9\beta_1$ ligand. Adherence was blocked by an $\alpha_9\beta_1$-specific antibody and by a snake venom protein that selectively antagonizes $\alpha_9\beta_1$. Human recombinant NGF bound to $\alpha_9\beta_1$ with a K_d of about 5 nM, which is similar to the strength of the interaction between NGF and the low-affinity receptor $p75^{NTR}$. The responses of the transfected cells to NGF included proliferation (involving extracellular signal–regulated kinases 1 and 2) and migration (involving paxillin). — NRG

J. Cell Sci. **121**, 504 (2008).

CREDIT: KIM *ET AL.*, *ADV. MATER.* 20, 801 (2008)

www.sciencemag.org

Science

1200 New York Avenue, NW
Washington, DC 20005
Editorial: 202-326-6550, FAX 202-289-7562
News: 202-326-6581, FAX 202-371-9227
Bateman House, 82-88 Hills Road
Cambridge, UK CB2 1LQ
+44 (0) 1223 326500, FAX +44 (0) 1223 326501

Subscription Services For change of address, missing issues, new orders and renewals, and payment questions: 866-434-AAAS (2227) or 202-326-6417, FAX 202-842-1065. Mailing addresses: AAAS, P.O. Box 96178, Washington, DC 20090-6178 or AAAS Member Services, 1200 New York Avenue, NW, Washington, DC 20005

Institutional Site Licenses please call 202-326-6755 for any questions or information

Reprints: Author Inquiries 800-635-7181
Commercial Inquiries 803-359-4578

Permissions 202-326-7074, FAX 202-682-0816

Member Benefits AAAS/Barnes&Noble.com bookstore www.aaas.org/bn; AAAS Online Store http://www.apisource.com/aaas/ code MKB6; AAAS Travels: Betchart Expeditions 800-252-4910; Apple Store www.apple/eppstore/aaas; Bank of America MasterCard 1-800-833-6262 priority code FAA3YU; Cold Spring Harbor Laboratory Press Publications www.cshlpress.com/affiliates/aaas.htm; GEICO Auto Insurance www.geico.com/landingpage/go51.htm?logo=17624; Hertz 800-654-2200 CDP#343457; Office Depot https://bsd.officedepot.com/portalLogin.do; Seabury & Smith Life Insurance 800-424-9883; Subaru VIP Program 202-326-6417; VIP Moving Services http://www.vipmayflower.com/domestic/index.html; Other Benefits: AAAS Member Services 202-326-6417 or www.aaasmember.org.

science_editors@aaas.org	(for general editorial queries)
science_letters@aaas.org	(for queries about letters)
science_reviews@aaas.org	(for returning manuscript reviews)
science_bookrevs@aaas.org	(for book review queries)

Published by the American Association for the Advancement of Science (AAAS), *Science* serves its readers as a forum for the presentation and discussion of important issues related to the advancement of science, including the presentation of minority or conflicting points of view, rather than by publishing only material on which a consensus has been reached. Accordingly, all articles published in *Science*—including editorials, news and comment, and book reviews—are signed and reflect the individual views of the authors and not official points of view adopted by AAAS or the institutions with which the authors are affiliated.

AAAS was founded in 1848 and incorporated in 1874. Its mission is to advance science and innovation throughout the world for the benefit of all people. The goals of the association are to: foster communication among scientists, engineers and the public; enhance international cooperation in science and its applications; promote the responsible conduct and use of science and technology; foster education in science and technology for everyone; enhance the science and technology workforce and infrastructure; increase public understanding and appreciation of science and technology; and strengthen support for the science and technology enterprise.

Information for Authors

See pages 634 and 635 of the 1 February 2008 issue or access www.sciencemag.org/about/authors

EDITOR-IN-CHIEF **Donald Kennedy**
EXECUTIVE EDITOR **Monica M. Bradford**
DEPUTY EDITORS **R. Brooks Hanson, Barbara R. Jasny, Katrina L. Kelner**
NEWS EDITOR **Colin Norman**

Editorial supervisory senior editor Phillip D. Szuromi; **senior editor/perspectives** Lisa D. Chong; **senior editors** Gilbert J. Chin, Pamela J. Hines, Paula A. Kiberstis (Boston), Marc S. Lavine (Toronto), Beverly A. Purnell, L. Bryan Ray, Guy Riddihough, H. Jesse Smith, Valda Vinson, David Voss; **associate editors** Jake S. Yeston, Laura M. Zahn; **online editor** Stewart Wills; **associate online editors** Robert Frederick, Tara S. Marathe; **book review editor** Sherman J. Suter; **associate letters editor** Jennifer Sills; **editorial manager** Cara Tate; **senior copy editors** Jeffrey E. Cook, Cynthia Howe, Harry Jach, Barbara P. Ordway, Trista Wagoner; **copy editors** Lauren Kmec, Peter Mooreside; **editorial coordinators** Carolyn Kyle, Beverly Shields; **publications assistants** Ramatoulaye Diop, Chris Filiatreau, Joi S. Granger, Jeffrey Hearn, Lisa Johnson, Scott Miller, Jerry Richardson, Brian White, Anita Wynn; **editorial assistants** Carlos L. Durham, Emily Guise, Patricia M. Moore, Jennifer A. Seibert; **executive assistant** Sylvia S. Kihara; **administrative support** Maryrose Madrid

News senior correspondent Jean Marx; **deputy news editors** Robert Coontz, Eliot Marshall, Jeffrey Mervis, Leslie Roberts; **contributing editors** Elizabeth Culotta, Polly Shulman; **news writers** Yudhijit Bhattacharjee, Adrian Cho, Jennifer Couzin, David Grimm, Constance Holden, Jocelyn Kaiser, Richard A. Kerr, Eli Kintisch, Andrew Lawler (New England), Greg Miller, Elizabeth Pennisi, Robert F. Service (Pacific NW), Erik Stokstad; **intern** Elsa Youngsteadt; **contributing correspondents** Jon Cohen (San Diego, CA), Daniel Ferber, Ann Gibbons, Robert Irion, Mitch Leslie, Charles C. Mann, Virginia Morell, Evelyn Strauss, Gary Taubes; **copy editors** Rachel Curran, Linda B. Felaco, Melvin Gatling; **administrative support** Scherraine Mack, Fannie Groom; **bureaus** New England: 207-549-7755, San Diego, CA: 760-942-3252, FAX 760-942-4979, Pacific Northwest: 503-963-1940

Production director James Landry; **senior manager** Wendy K. Shank; **assistant manager** Rebecca Doshi; **senior specialists** Jay Covert, Chris Redwood; **specialist** Steve Forrester; **Preflight director** David M. Tompkins; **manager** Marcus Spiegler; **specialist** Jessie Mudjitaba

Art director Kelly Buckheit Krause; **associate art director** Aaron Morales; **illustrators** Chris Bickel, Katharine Sutliff; **senior art associates** Holly Bishop, Laura Creveling, Preston Huey, Nayomi Kevitiyagala; **associate** Jessica Newfield; **photo editor** Leslie Blizard

***Science* International**

Europe (science@science-int.co.uk) **editorial: international managing editor** Andrew M. Sugden; **senior editor/perspectives** Julia Fahrenkamp-Uppenbrink; **senior editors** Caroline Ash, Stella M. Hurtley, Ian S. Osborne, Stephen J. Simpson, Peter Stern; **editorial support** Deborah Dennison, Rachel Roberts, Alice Whaley; **administrative support** John Cannell, Janet Clements, Jill White; **news: europe news editor** John Travis; **deputy news editor** Daniel Clery; **contributing correspondents** Michael Balter (Paris), John Bohannon (Vienna), Martin Enserink (Amsterdam and Paris), Gretchen Vogel (Berlin); **intern** Elizabeth Quill

Asia Japan Office: Asca Corporation, Eiko Ishioka, Fusako Tamura, 1-8-13, Hirano-cho, Chuo-ku, Osaka-shi, Osaka, 541-0046 Japan; +81 (0) 6 6202 6272, FAX +81 (0) 6 6202 6271; asca@os.gulf.or.jp; **asia news editor** Richard Stone (Beijing: rstone@aaas.org); **contributing correspondents** Dennis Normile (Japan: +81 (0) 3 3391 0630, FAX 81 (0) 3 5936 3531; dnormile@gol.com); Hao Xin (China: + 86 (0) 10 6307 4439 or 6307 3676, FAX +86 (0) 10 6307 4358; cindyhao@gmail.com); Pallava Bagla (South Asia: +91 (0) 11 2271 2896; pbagla@vsnl.com)

Africa Robert Koenig (contributing correspondent, rob.koenig@gmail.com)

EXECUTIVE PUBLISHER **Alan I. Leshner**
PUBLISHER **Beth Rosner**

Fulfillment Systems and Operations (membership@aaas.org); **director** Waylon Butler; **customer service supervisor** Pat Butler; **specialists** Laurie Baker, Latoya Casteel, LaVonda Crawford, Vicki Linton; **data entry supervisor** Cynthia Johnson; **specialists** Tarrika Hill, Erin Layne, Sheila Thomas

Business Operations and Administration director Deborah Rivera-Wienhold; **assistant director, business operations** Randy Yi; **senior financial analysts** Michael LoBue, Jessica Tierney; **financial analyst** Nicole Nicholson; **rights and permissions: administrator** Emilie David; **associate** Elizabeth Sandler; **marketing director** John Meyers; **marketing managers** Allison Pritchard, Darryl Walter; **marketing associates** Aimee Aponte, Alison Chandler, Mary Ellen Crowley, Marcia Leach, Julianne Wielga, Wendy Wise; **international marketing manager** Wendy Sturley; **marketing executive** Jennifer Reeves; **marketing/member services executive** Linda Rusk; **site license sales director** Tom Ryan; **sales manager** Russ Edra; **sales and customer service** Mehan Dossani, Iquo Edim, Kiki Forsythe, Catherine Holland, Phillip Smith, Philip Tsolakidis; **electronic media: manager** Lizabeth Harman; **project manager** Trista Snyder; **assistant manager** Lisa Stanford; **senior production specialist** Walter Jones; **production specialists** Nichele Johnston, Kimberly Oster

Advertising director worldwide ad sales Bill Moran

Product (science_advertising@aaas.org); **consumer & sponsorship sales manager** Tina Morra: 202-326-6542; **midwest** Rick Bongiovanni: 330-405-7080, FAX 330-405-7081; **west coast/w. canada** Teola Young: 650-964-2266; **east coast/e. canada** Christopher Breslin: 443-512-0330, FAX 443-512-0331; **uk/europe/asia** Michelle Field: +44 (0) 1223-326-524, FAX +44 (0) 1223-325-532; **japan** Mashy Yoshikawa: +81 (0) 33235 5961, FAX +81 (0) 33235 5852; **senior traffic associate** Deiandra Simms

Commercial Editor Sean Sanders: 202-326-6430

Classified (advertise@sciencecareers.org); **us: recruitment sales manager** Ian King: 202-326-6528, FAX 202-289-6742; **inside sales manager: midwest/canada** Daryl Anderson: 202-326-6543; **northeast** Alexis Fleming: 202-326-6578; **southeast** Tina Burks: 202-326-6577; **west** Nicholas Hintibidze: 202-326-6533; **sales coordinators** Erika Foard, Rohan Edmonson, Shirley Young; **international: sales manager** Tracy Holmes: +44 (0) 1223 326525, FAX +44 (0) 1223 326532; **sales** Marium Hudda, Alex Palmer, Alessandra Sorgente; **sales assistant** Louise Moore; **japan** Mashy Yoshikawa +81 (0)3 3235 5961, FAX +81 (0)3 3235 5852; **advertising production operations manager** Deborah Tompkins; **senior production specialists** Robert Buck, Amy Hardcastle; **senior traffic associate** Christine Hall; **publications assistant** Mary Lagnaoui

AAAS Board of Directors **retiring president, chair** John P. Holdren; **president** David Baltimore; **president-elect** James J. McCarthy; **treasurer** David E. Shaw; **chief executive officer** Alan I. Leshner; **board** John E. Dowling, Lynn W. Enquist, Susan M. Fitzpatrick, Alice Gast, Linda P. B. Katehi, Cherry A. Murray, Thomas D. Pollard, Kathryn D. Sullivan

AAAS
ADVANCING SCIENCE, SERVING SOCIETY

FLYING HIGH

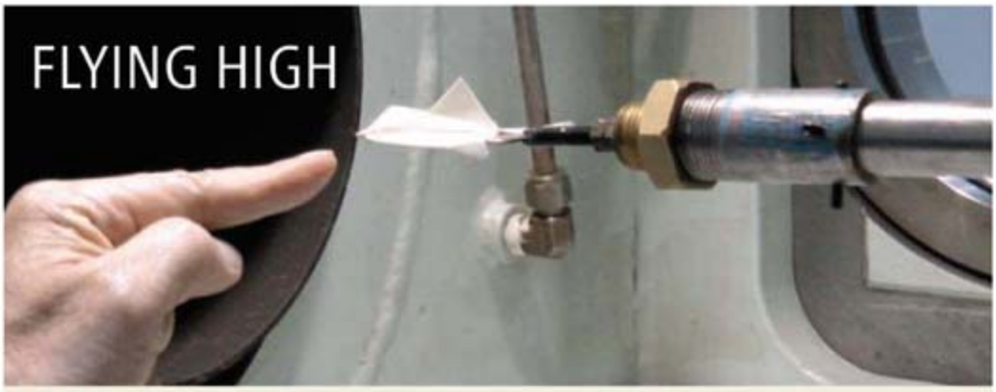

Paper-folding enthusiasts in Japan want to push the envelope by launching 100 small paper planes from the International Space Station.

The Japan Origami Plane Association came up with the idea in the late 1990s. Their plan got its first scientific test last month, when a team demonstrated that a 7-cm-long, 5-cm-wide model of the space shuttle made from heat-resistant paper could survive Mach 7 (about 8500 km/h) wind speeds and 200°C temperatures in the Hypersonic and High-Enthalpy Wind Tunnel at the University of Tokyo.

Shinji Suzuki, an aerospace scientist at the university who conducted the tests, hopes the project will help designers of lightweight aircraft and inspire schoolchildren to study science and engineering. Suzuki figures that he'll need a few years to convince NASA that the project meets its safety standards. If the agency approves, astronauts will launch 20-cm-long planes carrying multilingual messages with instructions to return any that reach Earth safely and are recovered. Suzuki acknowledges that many may perish after landing in the ocean, but he says one safe return would constitute a success.

Bumpy Bandage

Taking cues from the toes of geckos is proving a strategy worth sticking to. The lizards, which can run upside down and hang by a single toe, have inspired intense study of the physiological and physical properties that keep them from falling, as well as the development of a dry adhesive.

Now a team of engineers, chemists, and physicians has fashioned a waterproof, biodegradable tape made with an elastic polymer they invented and shaped to mimic the nanotopography of the gecko's foot pads. The polymer gets its "cling" from rows of tiny pillars on its surface, which is coated with a sugar-based glue.

The researchers hope to make internal bandages to help repair gut ulcers, for example, or to deliver time-released drugs. By varying the shape, size, and angle of the pillars, they can tailor the tape's adhesive properties to suit the target tissue, says chemical engineer Jeffrey Karp of Harvard Medical School in Boston. Karp and colleagues described the new bandage online 18 February in the *Proceedings of the National Academy of Sciences*.

The polymer's pillars are no match for a gecko's, says gecko-toe expert Kellar Autumn of Lewis and Clark College in Portland, Oregon. But he adds that the work "is very exciting because it suggests that gecko adhesives will have broad application in medicine."

Hang Gliders

Colugos have gliding down to a fine art, soaring from tree to tree like furry kites. Because they are nocturnal and elusive, however, nobody knew much about how they do it—until a group of researchers sneaked up on a few of them in Singapore and glued small sensor-filled packs to their backs.

The tree-dwelling mammals—thought to be the closest living relatives of primates—are about the size of small cats and live in the rain forests of Southeast Asia. To see how gliding works, biologists from the University of California, Berkeley, and the National University of Singapore captured colugos in the wild and outfitted them with backpacks weighing less than 30 grams each that continuously recorded the animals' movements.

Five colugos wore the packs for about a week, logging 200 glides of distances ranging from 2.5 meters to 150 meters before the glue gave out. The data showed that colugos leap most forcefully to launch the longest glides and alight softly. The longer the glide, the softer the landing, the team reported online this month in the *Proceedings of the Royal Society B*.

Biologist John Scheibe of Southeast Missouri State University in Cape Girardeau says the study is exciting because of its natural setting. Although there is much to learn about the evolution of gliding, Scheibe says the colugo research "puts an important piece of the jigsaw puzzle into place."

Manx Monitors

Microsoft has a new target audience: Manx shearwaters. The software giant's research arm is teaming up with the University of Oxford, U.K., and Freie Universität in Berlin, Germany, to monitor these nocturnal sea birds with wireless sensors, work that may yield new information about climate change.

Manx shearwaters, burrow-dwelling birds that resemble miniature albatrosses, breed on small islands off the coasts of Britain and Ireland. They spend most of their lives at sea, migrating to South America in the winter and traveling hundreds of miles to feast on herring and other small fish. Past studies of the elusive birds required ecologists to trek over slippery terrain for kilometers in the dark.

But researchers at Microsoft Research Cambridge plan to change all that by placing wireless sensors outside 50 burrows on Skomer Island off the coast of Wales. Scientists will monitor the birds' burrows and keep tabs on their whereabouts off the island with global positioning system tracking devices. The Manx shearwater's dependence on distinct but diverse habitats makes it an ideal study species for environmental changes that affect its habitat.

Marine ecologist John Croxall of Birdlife International says the team has "opened new avenues that inform us about the threats these birds face."

CREDITS (TOP TO BOTTOM): COURTESY OF SHINJI SUZUKI; HILARY BYRNES; ROBIN FREEMAN

EDITED BY YUDHIJIT BHATTACHARJEE

<< Two Cultures

NANOREALISM. Most artists labor for a lifetime without seeing their work hang in the Museum of Modern Art (MoMA) in New York City. But Keith Schwab (left), a physicist at Cornell University, has made it into MoMA without trying with an image in a current exhibition, "Design and the Elastic Mind."

The exhibition grew out of a series of salons starting in late 2006 for artists, designers, and scientists organized by Paola Antonelli, a senior curator at MoMA, and Adam Bly, founder of *Seed* magazine. Antonelli says she was struck by the aesthetic combination of form and function in a micrograph of a clover-shaped nanodevice that Schwab presented at one of the gatherings.

Schwab, who with Michael Roukes of the California Institute of Technology used the device to probe the quantum limit of heat flow, isn't taking his moment at the top of the art world too seriously. "It's not like the artists are sitting there thinking, 'This is the best nanodevice I've ever seen!' " he says. The exhibit runs through 12 May.

PIONEERS

BRIDGING THE GAP. Growing up in Washington state, Erin Fletcher frequently crossed the infamous Tacoma Narrows Bridge, which was rebuilt after a wind-induced collapse that occurred in 1940. Watching a film clip of the disaster inspired her to become a civil engineer. Now she designs highway sound barriers and bridges for a company.

Fletcher is one of a dozen female engineers featured on engineeryourlife.org, a new Web site hosted by the U.S. National Academy of Engineering. Its goal is to interest more college-bound girls in becoming engineers and to narrow the gender imbalance—roughly 4 to 1 in favor of men—in undergraduate enrollments. "The site shows that engineers are real people, that we have a good time in our jobs," Fletcher says. "We're doing important work, but we're not goofy and dorky and weird."

NONPROFIT WORLD

MONOPOLIZING MALARIA. Arata Kochi, the outspoken and at times undiplomatic head of the malaria program at the World Health Organization (WHO), is getting worried about the increasing clout of the biggest philanthropy in the world.

In a November 2007 memo to WHO Director-General Margaret Chan that was recently leaked to *The New York Times*, Kochi complains that the $39 billion Bill and Melinda Gates Foundation is effectively locking up malaria scientists in a "cartel" that stifles dissenting views. Moreover, the foundation is usurping WHO's policy-setting role, Kochi warns. The memo was recently circulated to other department heads at WHO, the newspaper reported.

Others too, are grumbling about the foundation's growing influence. Its new plan to eradicate malaria (*Science*, 7 December 2007, p. 1544) is "worrisome" because it preempted the authority of the World Health Assembly (comprised of WHO member countries), says an official at another global health organization who asked not to be identified.

But some Gates grantees disagree. Entomologist Willem Takken of Wageningen University in the Netherlands says Kochi's memo seems to be born out of "frustration" that a more action-oriented player with much deeper pockets has arrived on the scene.

Got a tip for this page? E-mail people@aaas.org

CREDITS (TOP TO BOTTOM): KEITH SCHWAB/CORNELL AND MICHAEL ROUKES/CALTECH; AP; COURTESY OF NSFC

Three Q's

BEIJING—The budget of the National Natural Science Foundation of China (NSFC) has doubled to $617 million in the past 5 years under the presidency of biologist **Chen Yiyu**. Last month, Chen was appointed to a second 5-year term at the agency, which funds research that has been peer-reviewed by outside scientists. NSFC's budget is expected to climb to $747 million this year.

Q: Is there enough good research in China to justify such large increases?
Overall, the level of science is still low. Last year, we received approximately 73,800 proposals and approved 14,700. But even among the approved projects, relatively few are of high quality. My priority is not to improve the success rate but to spend more on the best projects.

Q: NSFC recently set up joint funds with Sinopec, China's main oil company, and Baosteel. This is a radical departure from the old model.
So is our peer-review evaluation system, and that's our biggest success! Until about 5 years ago in China, we did not appreciate the connection between basic research and industrial development. Now we do, but industry thinks all the intellectual property should belong to them. We are negotiating with the companies now.

Q: China has recently been plagued by misconduct cases. How vigilant is NSFC?
We will openly criticize those who misbehave, and we send staff to investigate misconduct allegations. On one hand, we try to crack down on misconduct. But on the other hand, we try to create a healthy atmosphere for good science.

Eyes on the lunar prize
1170

Q&A with Germany's science minister
1172

SCIENCE EDUCATION

Florida Standards Support Evolution—With a Twist

Florida scientists declared victory last week after the state Board of Education approved science standards that for the first time explicitly embrace the teaching of evolution. But antievolution activists are claiming that the vote bolsters their position that evolution is a "just a theory" and therefore unproven. Such is life on the front lines of the continuing battle over teaching evolution in U.S. schools.

The basis for the dueling claims is a last-minute change by state school officials to a document drafted by an advisory committee made up of scientists, educators, and the public. In lieu of evolution, the standards now refer to "the scientific theory of evolution." State education officials say the new wording was intended to appease conservatives without compromising on accuracy. To be consistent, officials applied the same wording to every other scientific concept mentioned in the standards, for example, changing "photosynthesis" to "the scientific theory of photosynthesis."

The changes were made after state Representative Marti Coley phoned in during a 4 February conference call to the board and asked that the word "theory" be added to the draft standards. Mary Jane Tappen, director of the education department's Office of Mathematics and Science, then talked with members of the standards writing committee and other scientists. The additional words may make the document "cumbersome," she admits, "but some of us felt the document got better."

On 19 February, the board voted 4 to 3 to approve the revised version. Two members who voted with the majority—Linda Taylor and Kathleen Shanahan—had asked that the word "theory" be included. But two who voted against adopting the standards—Roberto Martinez and Akshay Desai—said they were angered by the last-minute rewording. "What's going on here is an effort by people who are opposed to evolution to water down our standards," Martinez said before casting his vote.

Nobelist Harold Kroto, a chemistry professor at Florida State University (FSU) in Tallahassee who helped rally public support for the standards, believes the new language allows scientists and teachers to make a clear distinction between scientific and unscientific theories. "The original standards were fine, but this might actually be better in the long run," he says. "The phrase 'scientific theory' gives us leverage to differentiate between theories that are supported by evidence and those that aren't." The simple addition of "theory" would have been disastrous, he adds.

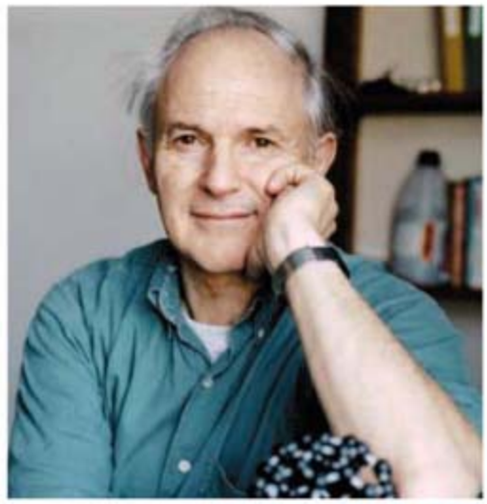

Different standards. Nobelist Harold Kroto and Florida legislator Marti Coley disagree on what new science standards say about evolution.

That's not how some conservatives see it, however. Coley issued a press release soon after the board's vote "applauding" the decision "to teach evolution as a scientific theory, not a scientific fact as had been earlier proposed." Coley says the standards now are "inclusive of a variety of viewpoints."

Some of the 23 individuals on the standards writing committee who had expressed concerns about last-minute changes seem satisfied with the final wording. "Our hackles went up when we heard of the request to add 'theory' " just to the references to evolution, says Sherry Southerland, a science education professor at FSU. "But we felt that putting the language throughout the standards would take care of that concern."

Tappen believes that the new standards leave no room for the teaching of alternative ideas about how life came to be, at least not in a science class. "Theories that are not scientific may be discussed in a humanities or a comparative religion course," she says. But the difference may not be clear to everyone, concedes FSU evolutionary biologist Joseph Travis. "If somebody wants to say a particular religious idea is a scientific theory, that's another issue."

The change failed to appease board member Donna Callaway, who had been pushing for an amendment to allow the teaching of alternatives to evolution. And the Seattle, Washington–based Discovery Institute, which advocates teaching students to question evolution, called the new wording "an impotent change." An analysis of the new standards posted on its blog carried this headline: "Florida State Board Tricked Into Meaningless 'Compromise' to Retain Dogmatism."

Hard-liners unhappy with the standards don't intend to let the matter rest. In a 21 February interview published in the *Florida Baptist Witness*, an organ of the Florida Baptist State Convention, the speaker of the state House of Representatives, Republican Marco Rubio, said he and other House leaders are considering introducing legislation to allow teachers to teach criticisms of evolution.

Callaway says she would support such an effort. "People have asked me why I don't question math concepts or grammar," she explained to *Science*. "I tell them, 'Those things have nothing to do with life. Evolution is personal, and it affects our beliefs.' "

–YUDHIJIT BHATTACHARJEE

CREDITS (TOP TO BOTTOM): COURTESY OF H. KROTO; MEREDITH HILL/FLORIDA HOUSE OF REPRESENTATIVES

Martian squeeze 1174

Five years of H5N1 1178

PEER REVIEW

NIH Urged to Focus on New Ideas, New Applicants

Advisers to the U.S. National Institutes of Health in Bethesda, Maryland, outlined a near-final plan to rescue the overburdened NIH peer-review system last week. They want NIH to go for a sweeping overhaul—one that would speed reviews, make the system more inviting, and nudge it to favor new ideas. One way to do this, they say, is to streamline a process that now encourages scientists to keep revising grant applications until they wear down resistance. Researchers seem to like the proposed changes, although some say NIH ought to test them first.

This analysis began last summer when NIH Director Elias Zerhouni asked for ideas to help NIH cope with system overload and reviewer burnout. The agency is receiving a record number of applications—about 80,000 are expected in 2008—at a time when its budget is stagnant. Zerhouni formed two advisory committees, one internal at NIH and the other external, and asked them to figure out how to fund "the best science … with the least administrative burden," he said last week at a teleconference meeting of his Advisory Committee to the Director (ACD). Many of the ideas adopted by the two groups were described in a preliminary report last year (*Science*, 14 December 2007, p. 1708).

One of the combined panel's fundamental recommendations is to avoid having proposals routinely revised and resubmitted as many as two times. These "amended applications" tend to be put in the queue in front of new applications, and there is a sense that "last chance" applications may be favored, the panel found. "It's a system that awards persistence over brilliance sometimes," Zerhouni said. "We really want to change that."

Instead, the panel says study sections should stamp some applications "not recommended for resubmission" during the first review. These quick rejections might run about 20%, external group co-chair Keith Yamamoto of the University of California, San Francisco, told *Science*. Proposals that make it past this first barrier but are not ranked among the best could also face tougher scrutiny. The panel would do away with the category of "amended" applications and have all submissions considered as "new." A study section now devoted to rebuttals of reviews would be eliminated; instead, the grant writer would simply incorporate any responses into a fresh application.

In addition, the panel recommends specific tweaks of review criteria and procedures. NIH should shorten its 25-page application, the advisers say, and focus more on impact and innovation and de-emphasize methods and preliminary data. Study sections should rate all proposals, even rejected ones, on five criteria such as impact so that people will know where they stand. The panel also suggests another way to reduce ambiguity: In addition to giving scores, study sections should rank all applications from first to last. For better quality, the number of reviewers for each proposal should be doubled from two to four or more.

The panel's charges included helping NIH spend its money more effectively. Noting that a small fraction of investigators hold multiple grants, the panel says NIH should "ensure optimal use of NIH resources" by requiring investigators to devote at least 20% of their effort to each grant. This might limit most researchers to three or four grants.

Zerhouni has said that a top objective is to give more help to new investigators. The panel suggests that NIH consider putting first-timers on a separate track, using generalists rather than specialists to review their proposals. To encourage more high-risk science, the panel suggests that NIH devote at least 1% of its basic investigator research grants to mechanisms such as the Pioneer Award, which is based on an investigator's track record rather than a specific research project. That could mean 300 to 400 awards per year for these risk takers, more than five times the current number, Yamamoto says.

Some ideas did not make it into the final report, such as whether to set a maximum length for applications. This was "hotly discussed and debated," said Lawrence Tabak, director of the National Institute of Dental and Craniofacial Research, who co-chaired both the internal and external working groups; the panel decided to let NIH figure it out. The panel also scrapped some ideas for motivating reviewers, such as extending the length of their grants, which could have led to a "stampede," Yamamoto says. Instead, the aim is to attract reviewers by "making the process better."

These ideas drew mostly positive reactions from the full ACD during last week's telephone call, although panel member Mary Beckerle of the University of Utah, Salt Lake City, cautioned that NIH needs to try some experiments first. The panel has "come up with lots and lots of good ideas," agrees Yale University cell biologist Thomas Pollard, who was not part of the meeting. "The question is which will work in practice." The panel planned to submit its final report this week, and Zerhouni says he will form an NIH implementation team within 4 to 6 weeks.

–JOCELYN KAISER

SIX NIH PEER-REVIEW RECOMMENDATIONS

- ✓ Mark some applications "not recommended for resubmission."
- ✓ Amended applications considered as "new"—omitting rebuttals of criticism.
- ✓ Rate all applications by specific criteria and rank to reduce ambiguity.
- ✓ Shorter application with focus on impact and innovation, less on methods and preliminary data.
- ✓ Require at least 20% of effort go to grant, to limit principal investigators with multiple grants.
- ✓ Consider separate review for new investigators.

New order. Two working groups proposed changes that would streamline NIH peer review.

SOURCE: NIH

SPACE EXPLORATION

New Prize Sends Old Hands On Flights of Lunar Discovery

As a legendary designer of communications satellites, Harold Rosen doesn't need to spend his ninth decade figuring out how to land a cheap probe that can maneuver and send back pictures from the moon's surface. But when Google announced last year that it was joining with the nonprofit X Prize Foundation to sponsor the $30 million Google Lunar X Prize, the National Medal of Technology winner decided to dust off an idea for a tubular, spinning payload that had been "in the back of my head" for decades. "We think we have the team to win it, and we're raring to go," says the spry aerospace engineer, who at 82 stays in shape by swinging on metal rings at the beach outside his home in southern California.

So far, Rosen's crew consists of volunteers—his wife, Deborah Castleman, a former satellite systems engineer; a brother and a grandson; and a handful of colleagues from the aerospace industry who jointly hold 130 patents. But Rosen hopes that the contest's publicity will attract companies willing to bankroll the entire effort, from design to delivery. And he thinks he can do it for the price of the winner's pot of $20 million.

Nine other teams have also stepped to the starting line in what Google's Tiffany Montague characterizes as "a new commercial moon race" for lunar industries and science. Competition organizer Peter Diamandis says that the $10 million awarded in 2004 as part of the Ansari X Prize to send a privately built, crewed spacecraft to the edge of the atmosphere leveraged nearly $100 million in related spending. He also hopes that the contest will "inspire a new generation" of students, who then translate their excitement about space into science and technology careers.

The Soviet Luna 24 mission in 1976 was the last robotic mission to the moon. The cost of following up on that feat has been prohibitively expensive: NASA's recently announced lunar orbital, called GRAIL, is priced at $375 million. Although the cash prize is far less, Montague says it is "an incentive, not meant to cover development costs."

Some of the contestants are hoping that their lunar missions will lead to deals with the media or with companies hoping to extract minerals or other resources. "For me, it's a business plan contest," says space entrepreneur Robert Richards of team Odyssey Moon, which is based in the United Kingdom's Isle of Man. Richards sees the race as just one step toward selling "small-scale robotic missions to deliver scientific and technology missions."

Even the recognized front-runner in the competition has a long way to go. The principals in Astrobotics, a collaboration between Raytheon (rocketry, navigation), Carnegie Mellon University (robotics), and the University of Arizona (space cameras, vehicle testing), have raised $1.5 million toward what the group estimates will be $100 million that it needs for its four-wheeled, pillbox-shaped rover mission. A focus on television and other media dollars has led to some unique engineering requirements, says University of Arizona planetary scientist Dante Lauretta. "Our media people are saying you can't have the rover look that boxy," he says only half-jokingly. Engineers will also need to make sure that the rover will ▶

SCIENTIFIC MISCONDUCT

Chemist Found Responsible for Ethical Breaches

This time it's chemistry's turn. After a series of high-profile scientific misconduct cases in stem cell biology and physics, an Indian chemistry professor has been punished by his university for committing unethical practices involving what appear to be dozens of recent papers, including plagiarizing data in an article submitted last year to an analytical chemistry journal. In the wake of the investigation, four Elsevier journals have retracted 13 papers written by Pattium Chiranjeevi, a professor of chemistry at Sri Venkateswara University (SVU) in Tirupati, India, and at least one other publication is reviewing pending submissions from Chiranjeevi or published articles he has written.

India's University Grants Commission is weighing a ban on any research grants; a university official says that, to date, Chiranjeevi has not received funding from any government agency. The university has decreed that he cannot hold an administrative position or mentor students. Although he has not been fired, he has been denied some pay raises. The investigation was completed last summer, but the case only came to light last week in an article in *Chemical & Engineering News*.

On-line Electrochemical Oxidation of Cr(III) for the Determination of Total Cr by Flow Injection-Solid Phase Spectrophotometry

Shiro MATSUOKA,[*] Yu NAKANO,[**] Ki TAKEHARA,[**] Sobiyo SAKUDO,[***] and Kunihisa YOSHIMURA[**]

On-line Electrochemical Oxidation of As(III) for the determination of total As by Flow Injection-Solid Phase Spectrophotometry

P.Subrahmanyam, B.Krishna Priya, B. Jayaraj* and P.Chiranjeevi**

Abstract

As on line oxidation method was developed for the determination of ultra-trace As(III) in natural water and urine samples using a flow electrolysis cell. This method was successfully applied to the determination of the total As concentration by flow injection-solid phase spectrophotometry (FI-SPS) using diphenylthiocarbazide (DPTC) as a

Doublespeak. A reviewer of a paper (*above*) spotted its similarity to one already in the literature (*top*), setting off the investigation. Chiranjeevi denies submitting the paper.

In an interview with *Science*, Chiranjeevi said that the charges against him are "baseless and not correct." He blames colleagues and journal editors for creating "this nuisance" and says that he plans to take action in an "international court of justice."

The university began its investigation after a peer reviewer discovered that a Chiranjeevi paper submitted to *Analytica Chimica Acta* (*ACA*) was nearly identical to a 2006 paper published by other authors in a different journal. Purnendu K. Dasgupta, an *ACA* editor and chemist at the University of Texas, Arlington, notified Duvvuru Gunasekar, then the chair of SVU's chemistry department.

In a summary of its findings, an internal three-member university panel concluded that Chiranjeevi "followed unethical and fraud practices in publishing research papers. Some parts of his research work were found to be fake." The summary, a copy of which has been obtained by *Science*, also notes that Chiranjeevi cited the use of

Topping it off. Aerospace pioneer Harold Rosen hopes a spinning design will spell victory for his lunar lander.

be able to snap a "self-portrait with the [corporate] logos in focus," he says, one of the contest's media-savvy rules.

It's not just glamour shots they're after. "Science isn't a level-one requirement," says Lauretta. "But you know us, we're scientists. Once we have a spacecraft on the moon, we are going to want to do science." New regolith formations and boulder distributions are among the features he's hoping to explore.

Although the $5 million bonus for photographing humanmade remnants of previous lunar missions may be a publicity gimmick, it also promises to focus attention on the important technological problem of carrying out precision landing. NASA's Mars rovers, Spirit and Opportunity, lacked such guidance systems. Instead, they bounce-landed on the Red Planet using giant air bags. To land near the historic Apollo 11 site on the Sea of Tranquility, for example, will require new technology.

Astrobotics will use Raytheon's adapted missile-guidance technology. "We don't want to land on the flag or the boot prints," says Lauretta. Mastering such landing skills "could revolutionize planetary science" for future missions, he predicts. (Scientists often have to avoid geologically exciting landing sites because they're too small; precise navigation could allow landing in tight areas.)

Rosen is taking another approach. He thinks the inherent stability of his spinning design, which he has modeled with a skate wheel and bobby pins, will obviate the need for expensive hardware. And he hopes that chasing the prize will be good for his health, too. "I thrive on it. [It] keeps me mentally alert."

–ELI KINTISCH

equipment that does not exist at SVU, copied material from other articles, and included "unjustified" co-authors.

"It's just amazing what this guy did," says Gary Christian, a professor emeritus of chemistry at the University of Washington, Seattle, and one of two editors-in-chief of *Talanta*, an analytical chemistry journal published by Elsevier. "This one is unprecedented in scope." Christian led an investigation that has prompted the journal to retract five papers from Chiranjeevi that it published between 2003 and 2007.

None of Chiranjeevi's recent work is thought to have broken much new scientific ground. "This is real low-profile stuff, specialized analytical techniques," says G. Bruce Wiersma, an ecologist at the University of Maine, Orono, and an editor for *Environmental Monitoring and Assessment*, which recently published several articles by Chiranjeevi. Springer, the journal's publisher, "is still in the process of dealing with" those articles, Wiersma says. Six other articles in press have since been "suspended," Wiersma adds.

The full scope of the falsified papers may never be known. Although the university has not said how many papers it examined, the summary concludes that "a large number of publications (66) in a short span of time, 2004–2007, without proper equipment, lead to the suspicion about the genuineness of the work." It cast further doubt on many of them, stating that the majority included co-authors whose involvement raised questions.

Nandula Raghuram, secretary of the Society for Scientific Values in Delhi, a nongovernmental organization that investigates cases of scientific misconduct in India, praises SVU's response, calling it "a breath of fresh air." He says Indian administrators too often look the other way to avoid bringing embarrassment to their schools. Raghuram says it's critical that the country set up and fund an independent watchdog group to monitor and investigate scientific misconduct cases.

But Rajagopala Chidambaram, chief scientific adviser to the Indian government, believes that there are too few scientific misconduct cases to warrant a full-time oversight body. Any alleged misconduct, he says, is best resolved by the universities and journals themselves. Varada Reddy, current chair of SVU's chemistry department, says, "No further action is envisaged against Chiranjeevi."

–ROBERT F. SERVICE

With reporting by Pallava Bagla in New Delhi, India.

CREDITS (TOP TO BOTTOM): DEBORAH CASTLEMAN; NIH

SCIENCESCOPE

NIH Grants: How Low Can You Go

A closely watched sign of health in U.S. biomedical science funding may hit a new low this year. The success rate for researchers seeking grants from the U.S. National Institutes of Health (NIH) is expected to drop from 21% in 2007 to 19% in 2008 (see graph), according to data in this month's 2009 presidential budget request. The falling numbers are the result of a one-two punch: NIH's budget has been held flat since 2003 while applications for grants have increased. The 2007 success rate, calculated by dividing the number of new awards by the number of reviewed applications, was already the lowest since 1970.

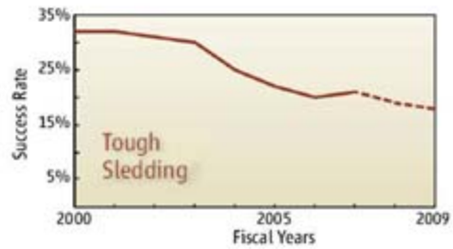

But dropping below the 20% mark is "a big deal," says Howard Garrison, public affairs director for the Federation of American Societies for Experimental Biology in Bethesda, Maryland. "It's scary for lots of established investigators. It's devastating for younger investigators." Next year could be even worse. The projected success rate is 18% if Congress follows the president's request for no raise for NIH.

–JOCELYN KAISER

Thai Drug Rule Under Review

Thailand's new health minister has ordered a review of a controversial government decision that broke patents on several medicines, allowing the country to make or import generic versions of the drugs. Health activists had welcomed the policy, adopted last year by Mongkol Na Songkhla, health minister in the government installed after the September 2006 coup. He ordered compulsory licenses on two AIDS drugs—efavirenz and lopinavir/ritonavir—and clopidogrel, a heart medication (*Science*, 8 June 2007, p. 1408). Just before the elected government took power earlier this month, Mongkol also issued licenses for four anticancer drugs: docetaxel, erlotinib, imanitib, and letrozole.

New health minister Chiya Sasomsub said last week that the review will examine the legal basis for compulsory licensing. Health activists are up in arms and have vowed to take the government to court if licenses are suspended.

–RICHARD STONE

ANNETTE SCHAVAN INTERVIEW

German Science Takes an International View

BERLIN—Many scientists were skeptical when Annette Schavan was named Germany's research and education minister in 2006. Her scientific credentials were limited: With a Ph.D. in theology, she directed the Roman Catholic Church's university scholarship program before serving as education and culture minister in the state of Baden-Württemberg. Since taking office, however, Schavan has presided over increasing research budgets and resolved the decade-long quarrel over a German National Academy of Sciences. She discussed Germany's latest science policy developments with *Science*. Her comments have been edited for length.

–GRETCHEN VOGEL

Q: This month, the Bundestag debated changing Germany's stem cell law. You worked for the Catholic Church for much of your career. You surprised some observers when you supported expanding the number of human embryonic stem (ES) cell lines.

A.S.: For me, the decisive argument was that it is exactly those researchers who are working on alternatives [to embryo-derived stem cells] who need to use the knowledge gained from human ES cells.

For me personally, it was a long road and a difficult decision. I believe that for the long term, we need regenerative medicine without the use of embryos. Otherwise, the more successful the development of treatments, the more embryos researchers will need. And for me, that is difficult to reconcile, because the ethics of healing and the ethics of protecting life are not alternatives but are two sides of the same coin.

Q: What do you think will happen in the vote next month?

A.S.: It is a vote of conscience, and many members of parliament are struggling with their position. So I don't want to predict how it will turn out. But no matter what, in recent weeks, science and politics have had a very positive dialogue with each other. Politics has taken science seriously, and scientists have taken politics seriously.

Q: German stem cell scientists have complained that the current law makes it difficult for them to cooperate in international projects, because they are not allowed to work with new cell lines even outside Germany. What do you say to them?

A.S.: The bills under consideration include the clarification of the legal situation that should fit the needs of international collaborations. The point is not controversial except for those who want to ban all research. [The bill Schavan cosponsors stipulates that any restrictions apply only to work within Germany—Ed. Note]

Q: You also surprised many observers with your announcement last year that the Leopoldina should be Germany's National Academy. What prompted that decision?

A.S.: Most importantly, I believe Germany needs to seize the chance it has to play a larger role in the international research agenda. We have excellent research facilities and excellent researchers. At the moment, there is broad political support here for increased investment in research. In climate change questions, for example, we want to be very active internationally. For that, we need a single contact for the academies in other countries.

Second, I want the discussion between science and politics to be intensified. More and more, scientific knowledge is absolutely necessary for responsible decision-making. Therefore, I find it important to have one institution that is the contact for political leaders and that can also bring issues to the attention of politicians that they haven't yet considered.

Q: Germany's new law regulating genetically modified (GM) crops disappointed many scientists, especially because it mandates a public database of locations of all transgenic crops and still leaves researchers potentially liable for any escaped pollen. Yet you praised it as a step forward for German research. What does it improve?

A.S.: The question for the GM law is whether the glass is half-full or half-empty. I can certainly understand the criticism. The public discussion is still very concerned with the possible risks—as was once the case with recombinant gene technology. We from the side of research speak more about the opportunities. And the goal of the law was to achieve an advance for research—for example, we have simplified the application process for experimental plantings—while at the same time ensuring a high measure of safety for the public and the environment.

We need to bring along those who have worries. That's why I said it was an improvement even when I would have wished for more. For example, you have to understand that if you call the [GM crop] database into question, you give the impression of trying to hide something. … I think it is a good compromise.

Q: Last week, the government announced a new strategy for "internationalizing" German science, including setting up "German Science Centers" around the world. What do you hope to accomplish?

A.S.: We want to intensify the relationships between German scientists and the international science community, … and we want to send the message that science policy is an important part of our foreign policy. For example, I was in Africa a few weeks ago, and there is a real need to strengthen the role of science in international development work. We need to figure out with people in developing countries how to develop local excellence in research that also contributes to development. I always have in the back of my head the sentence: "The new word for peace is development." And science and research are keys for development.

It's also about making sure Germany has a big enough piece of the global brain circulation. Germany will be especially affected by demographic developments. We are an aging society that should have an interest in attracting young talent from all over the world.

CREDIT: FRITZ REISS/AP PHOTO

RESEARCH FUNDING

Philip Morris Pulls the Plug on Controversial Research Program

Philip Morris has ended a controversial 8-year-old program that supported research at dozens of U.S. universities. The tobacco company's decision removes a major factor behind a recent decision by the University of California (UC) to monitor the flow of such support into the 10-campus system.

"It's a big shift," says K. Michael Cummings, head of the Tobacco Control Program at the Roswell Park Cancer Institute in Buffalo, New York. He accuses Philip Morris—the largest tobacco-industry sponsor of U.S. academic studies—of having supported "bogus" research. Now, he says, the company is retreating from a public relations fiasco. UC and other universities have been fighting internal battles for years about whether to ban tobacco-industry money, leading to "unseemly" coverage in the news, he says. Philip Morris spokesperson William Phelps, who confirmed last week that the company has ended its external research program, defended the quality of the research. He says that future support will be aimed at studies on "reducing the harm of smoking." He declined to say how much would be spent at universities.

Launched in 2000, the Philip Morris External Research Program (PMERP) has funded 470 research proposals at about 60 U.S. medical schools, according to the company. Studies have included examining the molecular basis of atherosclerosis and gene expression in lung tumors. But critics have charged that PMERP was no different from earlier, discredited Philip Morris programs—and had the same goal of confusing the public about the dangers of smoking (*Science*, 26 April 1996, p. 488).

The company notified grantees last September that it would no longer fund new research through PMERP. But the news only spread to the larger academic community after UC President Robert Dynes, in a 5 February letter, reminded UC chancellors to stringently review tobacco-sponsored research funding, as per a resolution adopted by UC's governing body in September. In an aside, he also noted that Philip Morris, "the only known current tobacco industry sponsor of University of California research," has shut down its external research program.

The effect of the decision on academic science remains unclear. At UC alone, 23 grants were funded by Philip Morris as of fiscal year 2006–2007, for a total of $16 million. James Enstrom, an epidemiologist at UC Los Angeles (UCLA) who uses Philip Morris money, says it means a change in the way things are done in his lab. "It's just something I have to deal with," he says.

But bioengineer and anti-tobacco crusader Stanton Glantz of UC San Francisco says not to count Philip Morris out of the academic game just yet. He cites a $6 million Philip Morris grant recently obtained by UCLA researcher Edythe London to study addiction, which Glantz says was not funded through PMERP. In Philip Morris's new strategy, funding may also go to studies of "reduced harm" products, such as spitless tobacco, at least some of which will be done in-house. Cummings doesn't buy the efficacy of such products, but he says ending PMERP is a "positive move."

–DAVID GRIMM

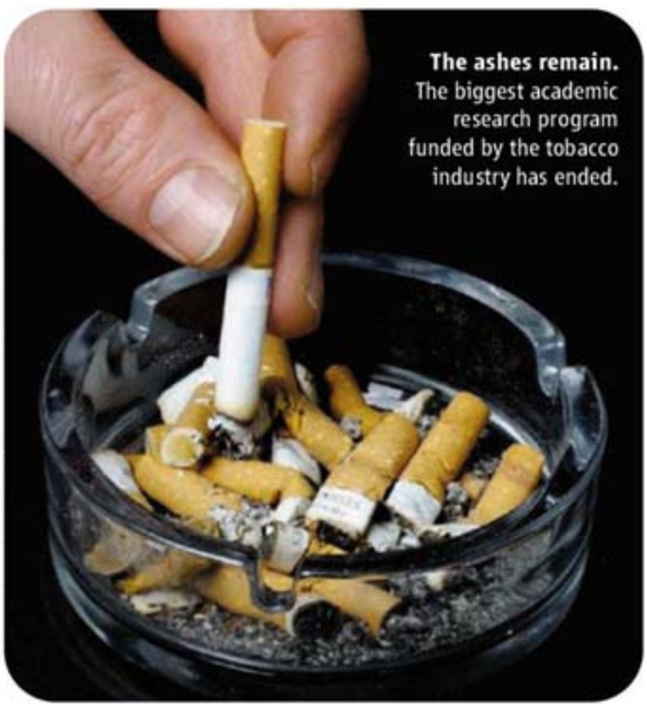

The ashes remain. The biggest academic research program funded by the tobacco industry has ended.

CREDITS (TOP TO BOTTOM): JPL/ESA; SIEWERT FALKO/DPA/LANDOV

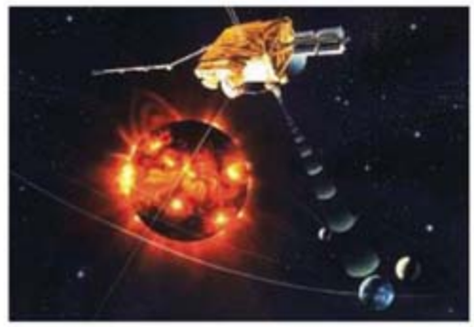

A Good Death

At 17, Ulysses is ancient in spacecraft years, so the announcement last week that the $1.15 billion joint NASA–European Space Agency mission will end within weeks was not too surprising. Neither was the cause: freezing to death as the spacecraft's radioisotope electrical generator inevitably winds down. "Ulysses is a terrific old workhorse," says project scientist and mission manager Richard Marsden, himself a 30-year veteran of the solar system–probe project. In its 6-year looping orbit, Ulysses has studied everything from the solar wind blowing from the sun's poles to interstellar dust and gas crossing Jupiter's orbit. Now the space agencies can start saving the $8 million per year in Ulysses operations costs and consider their next billion-dollar mission. –RICHARD A. KERR

DNA Database for Indian Tigers

NEW DELHI—With India's tigers on the ropes, the Department of Biotechnology plans to create a national DNA database to better ascertain the number of individuals left in the wild. Last week, the Indian government pegged the tiger population at 1411—less than half the number estimated in 2002 (*Science*, 22 February, p. 1027). Experts attribute the decline to poaching, human encroachment, and habitat loss. Under the $250,000, 2-year project, individual tigers will be identified from variations in mitochondrial and nuclear DNA collected from scat and hair samples. "Due to the tiger's cryptic and secretive behavior, it is not possible to enumerate and monitor its populations through direct observations," says the project's lead investigator, Lalji Singh, a molecular biologist at the Centre for Cellular and Molecular Biology in Hyderabad.

In addition to making population estimates more credible, he says, DNA could help law enforcement officials crack down on poaching. Qamar Qureshi, a wildlife biologist at the Wildlife Institute of India in Dehradun, says that although the technique "sounds promising," the cost of analyzing each sample—about U.S. $65—could be prohibitive over the long run. –PALLAVA BAGLA

War of the Worlds?

Despite the prospect of a sample-return mission, some researchers worry that the golden age of Mars science may be on the wane as NASA shifts its focus to Earth and Jupiter or Saturn

IT WOULD BE THE MOST AMBITIOUS AND expensive planetary science effort ever undertaken, with the promise of spectacular results. Yet when NASA science chief Alan Stern last month announced that the space agency is backing a mission to collect rocks and soil from Mars and bring them back to Earth, many planetary researchers reacted with dismay rather than joy. "This could destroy the short-term exploration program," warns planetary scientist James Head III of Brown University.

Make no mistake—Head and nearly every other Mars researcher dearly want to get their hands on martian samples. But they also noticed that the plan laid out in NASA's 2009 budget request (*Science*, 8 February, p. 714) would cut projected spending on Mars by half over the next 5 years. As a result, many scientists fear that NASA is abandoning a carefully plotted and extraordinarily successful research endeavor on the Red Planet in exchange for promises of an expensive mission far in the future.

An expert panel assembled at the request of White House budget officials to vet the plan concludes that it doesn't hold water. "You have to come clean," says planetary scientist Philip Christensen of Arizona State University, Tempe, who chaired the panel. "Either you fund the program, or you accept the fact that it will be significantly reduced for the next decade."

Christensen laid out the panel's conclusions at a 20 February meeting of the Mars Exploration Program Analysis Group in Monrovia, California, with Stern sitting in the front row. The agency's science chief insists that the new plan is sound and that the community is needlessly worked up about the proposed changes. "No missions have been canceled—none, zero, zip, nada," he told *Science*. "The Mars program is really healthy," he adds, noting that NASA might even hold a competition soon for a new Discovery mission that could be devoted to Mars.

Stern's assurances at the gathering, however, did not quell the anxiety among Mars researchers in the room. "I don't think many people accept this budget," said astrobiologist Bruce Jakosky of the University of Colorado (UC), Boulder.

That skepticism is the latest sign of a crisis afflicting the $4.6 billion science program that Stern inherited last spring. He intends to increase spending on earth science, start a $3 billion project to send a probe to the Jupiter or Saturn system, and begin building a series of lunar robots. The earth science effort addresses appeals from Congress and the U.S. National Academies to put more resources into monitoring

CREDIT: NASA-JPL

Mars mirage? Researchers fear that an international mission to collect samples and return them to Earth is unlikely to happen by 2020.

global climate change. The second follows another recommendation from the National Academies. And the third is part of a White House–backed push to focus on the moon in preparation for human landings.

Stern is trying to cater to all these constituencies without any growth in his overall budget, which encompasses earth and planetary sciences, astrophysics, and heliophysics, the study of the sun and its effects (see graph, p. 1176). And he's doing it at an agency with a $17.3 billion budget that is dominated by a costly effort to replace the space shuttle. In addition, Stern must cope with the unpleasant news of a $165 million overrun in the $1.6 billion Mars Science Laboratory (MSL) scheduled for launch next year. "Alan is trying to do the right thing by offering something to keep everyone happy," says UC Boulder planetary scientist Frances Bagenal, who is co-investigator on the New Horizons mission to Pluto, which Stern leads. "But it's impossible."

The robotic Mars effort has lived a charmed life ever since a group of scientists suggested in a 1996 research paper that a martian meteorite found in Antarctica contained signs of past life (*Science*, 16 August 1996, p. 924). That claim, although it has garnered little scientific support, generated strong political backing for a Mars exploration program. As a result, NASA has launched a mission every 26 months, when Mars and Earth are favorably aligned.

The effort has included some spectacular failures, such as the loss of an orbiter and a lander in 1999. But their rover successors, Spirit and Opportunity, continue to return data after 4 years on the surface, and Mars Odyssey has been in orbit since 2001. In May, the small Phoenix Scout spacecraft is scheduled to land on Mars's northern plains and begin a search for complex organic molecules in the ice-rich region.

"We've produced wonderful science on a reasonable budget," says Head. "And there is tremendously synergistic science going on, from atmospheric to mineralogy studies." Adds Jakosky, who heads one of the two competing efforts for the next Scout mission: "Scientists, NASA, Congress, the OMB [Office of Management and Budget], and the public all agreed this was a first-rate program." Researchers say it's a mistake to put the program in a lower gear just as they are on the verge of answering fundamental questions about the planet.

CREDITS (TOP TO BOTTOM): NASA-JPL; NASA-JPL

"Suck it up"

Impressive science is no guarantee of future support from a cash-strapped NASA, however. Microgravity researchers, earth scientists, and astrophysicists have been living for the past several years with lowered expectations. NASA's 2009 budget request to Congress diverts money from three of the four space science areas to the earth sciences, reflecting growing worries about global warming and sharp criticism of NASA's earth science program in a report last year from the National Academies' National Research Council (NRC). But more money for science as a whole is not in the cards. "You're only going to get so much," NASA Administrator Michael Griffin warned scientists in characteristically blunt fashion at an 11 February briefing at the National Science Foundation. "Suck it up and live with it."

Within planetary science, outer-planets researchers are itching for a mission of their own. "It's time to take a break from Mars and work on other things," says Bagenal, who also chairs NASA's outer-planets advisory group. A mission to Jupiter's moon Europa has been put off twice in recent years because of its cost. Given the high priority assigned to such a mission in an influential 2003 NRC report, Stern is backing a $3 billion spacecraft destined either for the jovian system or for Saturn's moons Titan and Enceladus with a launch by 2017. A decision on the destination is slated for later this year.

In order to bolster earth sciences and fly an outer-planets mission, however, NASA will have to divert funds from Mars. As recently as last fall, the agency planned to spend about $600 million annually through 2013 on the Mars program, with a slow rise to nearly $700 million by 2020. That was to pay for construction and launch of an astrobiology field lab that would land on the martian surface or two midsize rovers in 2016, as well as other as-yet-undefined efforts.

Under the new plan, spending on Mars would nosedive to $300 million in 2010, then inch upward to $414 million by 2013. Stern maintains that the dip in the next few years mostly reflects completion of MSL and moving back the launch of the next Scout mission from 2011 to 2013. The Mars budget would not grow significantly until at least 2016, according to a 13 February briefing by Doug McCuistion, director of the Mars Exploration Program. Only later in the next decade does projected funding shoot up to $1 billion by 2020 as work begins in earnest on the sample-return mission.

Christensen's panel says that fiscal plan won't fly. "The phasing is just wrong," says Christensen. "Our assessment is that it just won't work." Preparing to launch a sample return by the end of the decade would require a big boost in spending earlier in the decade. The group determined that NASA would have to cancel everything after MSL—including the 2013 Scout and the 2016 missions—to fly a sample return by the second half of the next decade. Stern, meanwhile, has slapped an $800 million cost cap on the 2016 mission, which he acknowledges would rule out the complex astrobiology field lab. Several scientists say that cap might also eliminate the rovers.

An alternative scenario would preserve the Scout mission and move the sample return back to 2022. But that would require using a poor orbital trajectory and create a dozen-year gap in U.S. landings on Mars, notes planetary scientist Lars Borg of Lawrence Livermore National Laboratory

ROAD TO THE RED PLANET

2008
- Phoenix

2009
- Mars Science Laboratory >>

2011
- No mission scheduled

2013
- Scout mission (MAVEN or TGE)

2016
- Astrobiology field lab
  or
- Two midsize rovers

2018
- Mars sample return
  (Rover to collect samples)

2020
- Mars sample return
  orbiter to retrieve samples >>

2022
- Sample-receiving facility opens

Countdown. NASA's exploration schedule for Mars makes use of a 26-month launch opportunity.

in California. "Everything is on the table," says Borg, calling the new plan a radical change in direction by NASA.

The Mars program's most daunting problems, however, are in the short term. The $165 million overrun in MSL, a car-sized roving suite of instruments designed to gather extensive data on martian soil and rocks, is due to increased manufacturing costs for the technologically complex lab and the need for double shifts to meet the scheduled launch window, say agency officials. To save money, project managers have already pruned MSL of a spare radioisotope power system, replaced a surface removal tool with a simpler brush, and reduced the zoom capability of one of the cameras. Stern says he has no plans to cancel MSL but that NASA could postpone the fall 2009 launch date until 2010 or 2011 if technical problems are not resolved by this summer.

No free sample

Stern concedes that anything beyond 2013 is "notional" and adds that the disagreement represents "normal scientific community debate." But he is eager to begin planning a sample-return mission, an idea that has been proposed periodically since the early 1980s. It would be extraordinarily complex, involving launch vehicles, a Mars landing system, an Earth return vehicle, a Mars lander, a Mars ascent vehicle, a rover, an Earth-reentry system, and a sample-receiving and -curation facility on Earth. It is also likely to rank high when planetary scientists put together their next long-term plan.

Early estimates put the overall cost of such an ambitious mission at $5 billion to $6 billion. Stern says that NASA can contribute no more than $3 billion, and he hopes to attract another $1 billion or so from Europe—which is eager to participate—and possibly Japan. The cost would be lower if the mission brought back rocks collected by previous landers, such as MSL or the 2013 European ExoMars.

Toward that end, Stern has pushed to add a sample cache to MSL, with money from his own office's reserves. A pricier approach would involve a rover equipped with a drill that could range over the martian landscape for 2 years until an orbiter arrived to carry the samples back to Earth. The rover could pick up individual samples as small as 5 grams and gather as much as 500 grams to be returned to Earth.

A quick grab, however, lacks appeal for many researchers, who have been able to study meteorites ejected from Earth's neighbor. "We already have Mars samples; it's not really worth it to scoop up a couple of rocks," says Brown University planetary scientist John Mustard, who chairs the advisory group that met with Stern last week. "If we make the investment to do such an extraordinarily ambitious project, you should have a big science payoff."

Mustard says the Mars community is enthusiastic about conducting the current planned missions followed by the more ambitious version of sample return: "That's the right program; it's exciting and scientifically justified." But he wonders if Stern's plan is realistic. "We just don't see how you connect the dots." To do a sample return by 2018 and 2020, he notes, NASA would have to spend large sums to tackle the stickiest technological challenges early, at a time when the $3 billion outer-planets mission will be absorbing the lion's share of the planetary science budget.

"No missions have been canceled—none, zero, zip, nada. … The Mars program is really healthy."

—ALAN STERN, NASA

With their eye on that long-delayed mission, some researchers say that reducing the near-term Mars budget wouldn't be such a tragedy. The Mars community, notes Bagenal, "has a huge flagship in MSL" and "is already swamped with data they've not had the time or money to analyze."

The tension over how to spend planetary science's limited pot could spill over onto Capitol Hill this year. Last year, astrophysicists persuaded lawmakers to ignore NASA's vehement objections and reinstate funding for the Space Interferometry Mission (SIM)—an effort to find Earth-sized planets in other star systems. Griffin and Stern sharply warned astrophysicists that their other projects will suffer as a result of the cost of restoring SIM.

Mars advocates possess even more political muscle, as well as grassroots backing throughout the country. The 2008 NASA spending bill pointedly notes that the appropriations committees "strongly support a robust Mars exploration program with a rate of at least one mission at every [26-month] opportunity." But leaders in the community so far are treading carefully. "It's important to step back and look at the big picture," says planetary scientist Richard Binzel of the Massachusetts Institute of Technology in Cambridge, who also chairs the Division of Planetary Sciences at the American Astronomical Society. "We have to look at the health of the overall program." Bagenal pledges to work to "get the community behind a unified solar system program," whereas Mustard insists that "we don't want to turn this into a tomato-throwing contest."

Stern says that his primary goal "is to have a balanced program." For now, that means rejiggering the Mars effort to survive the current budget crunch. "Whether Alan has hit the right balance is something we will see going forward," says Stephen Mackwell of the Lunar and Planetary Institute in Houston, Texas. "But there is no question there will be winners and losers."

–ANDREW LAWLER

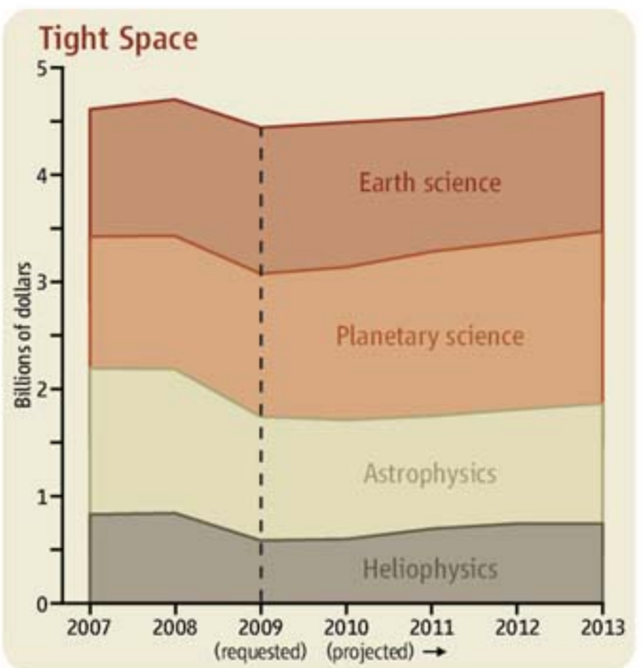

Tight space. An essentially flat budget through 2013 will mean stiff competition among the four pieces of NASA's science directorate.

CREDIT: COURTESY OF NASA; SOURCE: NASA

RESEARCH FUNDING

Are Epigeneticists Ready For Big Science?

NIH's hefty boost of U.S. epigenomics efforts has Europe wondering where it fits in

For Peter Jones, this next week is critical. He and his colleagues at the University of Southern California in Los Angeles are putting the finishing touches on their plan to map epigenomes, the myriad of chemical modifications of human DNA and its associated proteins that influence gene activity. Jones hopes his team will become part of a newly announced $190 million, 5-year National Institutes of Health (NIH) epigenomics initiative. And he views NIH's funding as a way to jump-start an ambitious international epigenome project that he has championed since 2005. "The [international] project is huge, as huge as the Human Genome Project," says Margaret Foti, CEO of the American Association for Cancer Research (AACR).

Yet some who study epigenetics question NIH's strategy and whether the science is ready for a large-scale international project. "Some of us biochemists think we need to know more about [epigenetic marks] before we spend all this time mapping," says Jerry Workman, a molecular biologist at the Stowers Institute for Medical Research in Kansas City, Missouri.

Twenty years ago, most geneticists paid little mind to epigenetics. But cancer and stem cell research have gradually focused attention on these genome modifications. In a still-obscure manner, enzymes, transcription factors, and snippets of RNA converge on particular DNA sequences. They customize the expression of nearby genes, often by adding methyl, acetyl, or phosphorous groups to the DNA or the histone proteins surrounding the DNA. Methylation, for example, can silence a nearby gene and seems to be involved in some cancers. Increasingly, researchers are unearthing links between epigenetics and other diseases.

Until now, researchers have tackled epigenomics piecemeal, with different groups cataloging where on the genomes of particular cells certain epigenetic modifications occur. European researchers took the lead, for instance, setting up a Human Epigenome Consortium in 1999. In 2003, the Wellcome Trust Sanger Institute and a Berlin-based company called Epigenomics teamed up to identify the location of every methyl group bound to a human gene in an assortment of tissues (*Science*, 17 October 2003, p. 387). After going through three chromosomes, the project "fizzled," says Stephen Beck of Imperial College London, who headed the Sanger effort.

Recently, faster, cheaper technologies that can better pinpoint sites of epigenetic activity have emerged, encouraging a more comprehensive attack on the epigenome (*Science*, 25 May 2007, p. 1120). When Jones became AACR president in 2005, he made epigenomics a priority, assembling an international task force that proposed a worldwide Alliance for the Human Epigenome and Disease. AHEAD would finally bring various epigenetics projects under one umbrella and help standardize the bioinformatics and the research. AHEAD called for a pilot phase, but no international funding materialized.

However, epigenomics has been selected as one of NIH's two new Roadmap Initiatives for 2008. By year-end, NIH plans to award $50 million to three to five epigenome mapping centers in the United States and allocate $7.5 million for a bioinformatics center. Other grants will go toward the identification of new epigenetic "marks" along the genome and new technologies for mapping them.

Mapping all epigenetic modifications is more daunting than sequencing the human genome, as there is no single epigenome. Each cell type has its own array of epigenetic marks. NIH's new initiative will likely characterize stem cells, progenitor cells, and differentiated cells from a variety of tissues. The effort "will have to make a tradeoff between how many epigenomes are analyzed and to what detail," says Kazu Ushijima of the National Cancer Center Research Institute in Tokyo.

Those who advocate a slower approach note that so many epigenetic marks exist—in some places, there can be many on each histone—that it's difficult to know which meaningfully influence gene expression. In addition, "there's a lot of unknown modifications on histones that have not been characterized, and for all we know, they might be the most important," says Workman. Kevin Struhl, a molecular biologist at Harvard Medical School in Boston, is also critical of the NIH initiative, arguing that more attention needs to be paid to the regulatory proteins that home in on target DNA and enable these chemical modifications. A focus on simply mapping histone modifications and DNA methylation "doesn't strike me as a good expenditure," he says.

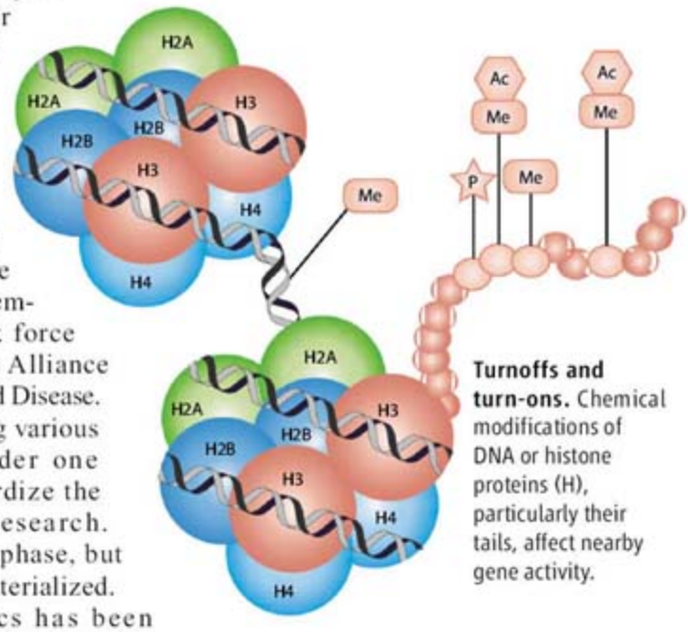

Turnoffs and turn-ons. Chemical modifications of DNA or histone proteins (H), particularly their tails, affect nearby gene activity.

Nor is it clear that the NIH effort will draw in the international community. Henk Stunnenberg of Radboud University in Nijmegen, the Netherlands, complains that Europeans are being left out, as there was little time for them to team up with U.S. groups to apply for the NIH money. Even Jones admits that he's been so busy preparing his grant that his global emphasis has fallen by the wayside, temporarily. But many agree in principle that an international epigenome project is still worth pursuing. "I think it would be wonderful," says Rolf Ohlsson, a molecular biologist at the University of Uppsala, Sweden. "It will be extremely counterproductive to do the same thing on both sides of the ocean."

–ELIZABETH PENNISI

CREDIT: SCIENCE SIGNALING, A. M. BODE, Z. DONG, INDUCIBLE COVALENT POSTTRANSITIONAL MODIFICATION OF HISTONE H3. SCI STKE 2005, RE4 (2005)

Nowhere to hide. Lightweight transmitters enable satellite tracking of migratory birds and the flu viruses they carry.

CREDIT: N. BATBAYAR/MONGOLIA WSCC

AVIAN INFLUENZA

Flu Virus Research Yields Results But No Magic Bullet for Pandemic

As concerns wane that the bird flu strain H5N1 will spark a global pandemic, scientists are warning that the virus, perhaps less of a threat, is here to stay

BANGKOK—Just a couple of years ago, scientists, public health officials, and journalists were nervously tracking every move of the deadly H5N1 avian influenza virus, fearing that a few simple mutations might give it the ability to spread readily among humans, sparking a global pandemic that could kill tens of millions. But since alarms were sounded when the virus started spreading in earnest among birds in late 2003, the dreaded pandemic hasn't come. "I'm less worried about this virus than I was 5 years ago," says virologist Robert Webster of St. Jude Children's Research Hospital in Memphis, Tennessee.

But H5N1 hasn't gone away—and increasingly, say scientists, the virus appears to be here to stay. "H5N1 is going to be with us for a long time," says Les Sims, a veterinary consultant based in Palm Cove, Australia, continuing to devastate poultry flocks and posing an ongoing threat to human health.

In 2007, the virus surfaced in poultry flocks in eight new countries as widely separated as Bangladesh, Poland, and Ghana. Outbreaks returned in 23 countries stretching from Japan to the United Kingdom; in Indonesia and Nigeria, in particular, they are now more or less continuous. Although the number of human cases and deaths declined by 25% compared with 2006, Nigeria, Laos, and Pakistan had their first human cases last year, and Indonesia, the hardest-hit country, reported 42 cases and 32 deaths. As long as the virus is circulating in birds, experts warn, there will continue to be sporadic human cases, and most of them will be fatal.

Research is providing insights into how the virus spreads and the viral mutations that might be needed for H5N1 to infect humans more easily, as was evident at a recent meeting here.* "The spinoff is a better understanding of flu viruses in general," says microbiologist Peter Palese of Mount Sinai School of Medicine in New York City.

But David Fedson, a vaccine expert and former executive at Aventis Pasteur now based in Sergy Haut, France, worries that these advances, although valuable, are not doing much to help prepare for an influenza pandemic. He and others believe a pandemic is inevitable, whether it is caused by H5N1 or another flu strain that has yet to emerge. "Nobody has a clue [how] to take some of these findings from the lab and turn them into something that addresses public health," laments Fedson.

* "Bangkok International Conference on Avian Influenza 2008," 23–25 January, Bangkok, Thailand.

Out of the wild

One continuing uncertainty is whether wild birds are "victims or vectors" of H5N1, says wildlife health specialist Scott Newman of the Food and Agriculture Organization (FAO) of the United Nations in New York City. Poultry trading is the primary means of spreading the virus. But the role wild birds play in long-distance spread is still unclear, says Newman. Several groups are studying the question both in the lab and in nature, taking advantage of new lightweight transmitters that enable satellite tracking of migratory species.

Nicolas Gaidet of the French Agricultural Research Centre for International Development in Montpellier, France, described one of the most ambitious efforts. The group, which includes researchers from FAO, the U.S. Geological Survey, Italy's Istituto Zooprofilattico Sperimentale delle Venezie, and others, collected cloacal, tracheal, and fecal samples from more than 11,000 birds in 19 countries in eastern Europe, the Middle East, and Africa in 2006 and 2007. The researchers fitted some of the migratory birds with transmitters. Overall, 2% of the birds were carrying influenza viruses, says Gaidet, and that number rose to 14% in certain species.

The group did not find any living wild birds infected with H5N1, which is in line with other surveys. That suggests that H5N1, which is lethal to many types of wild birds, may kill its victims before they travel far. The team did, however, find four birds in Nigeria carrying an H5N2 virus that genetic analysis indicates would be highly pathogenic to chickens. One, a white-faced whistling duck, subsequently flew 650 kilometers and is still apparently healthy. "This is the first time anyone has found a bird carrying a highly pathogenic virus over a great distance," Gaidet says.

At the meeting, researchers also described progress in understanding how avian influenza viruses mutate into human pandemic strains. Previous work had shown that the viruses' hemagglutinin protein, a surface protein that comes in 16 subtypes, preferentially binds to a host cell receptor known as alpha 2,3; human viruses prefer alpha 2,6. Evidence suggests that a mutation affecting hemagglutinin binding is necessary for an avian influenza virus to switch to a human virus. Whether additional mutations are needed is not known.

Mikhail Matrosovich of the Institute of Virology at Philipps University in Marburg,

Germany, is trying to answer that question by working with the 1968 H3N2 pandemic virus. The hemagglutinin protein of that virus differs from its putative avian ancestor by seven amino acid substitutions. Two of these had been linked to the receptor-binding preference of the hemagglutinin. To find out the role of the other five substitutions, Matrosovich's group is creating viruses with various combinations of the mutations and testing how well they bind and replicate in cultures of human airway epithelium cells. The team took the pandemic virus and switched the two mutations associated with binding preference back to their avian version. As expected, this engineered virus replicated far less efficiently in human cells than the pandemic virus did.

The biggest surprise, says Matrosovich, is that the virus with the avianlike binding protein grew at all in human cells. "These [findings] do not support the quite-common theory that there are no receptors for avian viruses in the human airway," Matrosovich says. Another virus construct, with the two binding mutations of the pandemic strain left intact but the remaining five substitutions reworked to their avian state, replicated much less efficiently than the pandemic strain as well, suggesting that these substitutions might also be needed for conversion to a pandemic virus, a finding likely to apply to all avian viruses.

Preliminary results from similar studies of changes in the neuraminidase protein common to the 1918, 1958, and 1967 pandemic viruses suggest that mutations in that protein also play a role in giving a virus pandemic capabilities, Matrosovich says.

Evidence that viruses need multiple mutations to adapt to human hosts might seem reassuring. But Prasert Auewarakul, a virologist and physician at Mahidol University in Bangkok, warned that viruses can adapt quickly. His group sequenced viruses retrieved from three fatal human H5N1 cases and found that genomic domains associated with hemagglutinin binding specificity were mutating far more frequently than other areas, indicating evolutionary pressure for the avian virus to adapt to its new host species. Another site with evidence of rapid change was associated with a protein involved in enabling avian influenza viruses, which thrive at the 40°C temperatures found within birds, to replicate efficiently at the lower 33°C temperature of the human body. Auewarakul notes that all three patients died 1 to 3 weeks after the onset of illness. "This tells us that the virus is evolving very quickly inside the human body," he concludes.

An ounce of prevention

Public health authorities hope an effective vaccine will prevent human H5N1 infections altogether. Numerous groups have reported advances in vaccines, including, for instance, novel ways of making one vaccine protect against several different flu strains and using adjuvants to stretch precious vaccine supplies. But Fedson notes that these advances might ameliorate but don't solve the bottleneck of current vaccine production, which requires incubating the virus in an enormous number of chicken eggs, a time-consuming and expensive process that requires biosecure facilities, a highly trained work force, and long lead times. Fedson calculates that with existing vaccine production capacity and the use of an adjuvant, 9 months after a pandemic virus appears there is likely to be only enough vaccine for 700 million people. "Pandemic vaccination is not going to be a realistic possibility in the near future for more than 85% of the world's people who live in countries that don't have vaccine companies," he adds.

Responding to that challenge, Linda Lua of the Australian Institute for Bioengineering and Nanotechnology at the University of Queensland in Brisbane presented "a radically different vaccine process" that doesn't use eggs. Instead of working with the entire virus, they select a part of a viral structural protein recognized by the human immune system. They then build these protein bits into viruslike particles for use as vaccines. "There is no genetic material," says Lua, which means that the particles are noninfectious; this in turn avoids the need for high-level biosafety production facilities.

"It's a pretty simple process," Lua says. The protein is produced in a bacterial-fermentation process, purified, and then chemically processed into viruslike particles. Lua says they deliberately developed a manufacturing process within the capabilities of some of the more advanced developing countries, such as Thailand and Vietnam. "It is an Asian solution for an Asian problem," Lua says. Anton Middelberg, a chemical engineer at the institute, says that once a pandemic strain appears, whether it is H5N1 or another flu subtype, they could identify target proteins and start production in 1 to 2 weeks. A plant small enough to load into a cargo plane and take to an airport near an outbreak site would be capable of producing about 500,000 doses of vaccine a week. "We can have a rapid response for pandemic influenza using this technology," Lua says. Fedson called the work "extraordinarily exciting."

Middelberg says they "tackled the manufacturing issues first" and are now seeking partners to move into animal testing. He adds that viruslike particle vaccines for hepatitis and human papillomavirus are already on the market and that other groups have gotten promising results with a viruslike particle vaccine against flu in mice. Provided they find a partner and funding, it would take "a few years" to have the process ready to go.

That is cold comfort to Michael Osterholm, a public health specialist at the University of Minnesota, Minneapolis, who warns that every day brings the world closer to the next pandemic. "We don't know if it's going to be H5N1, but there will be another pandemic," he says.

–DENNIS NORMILE

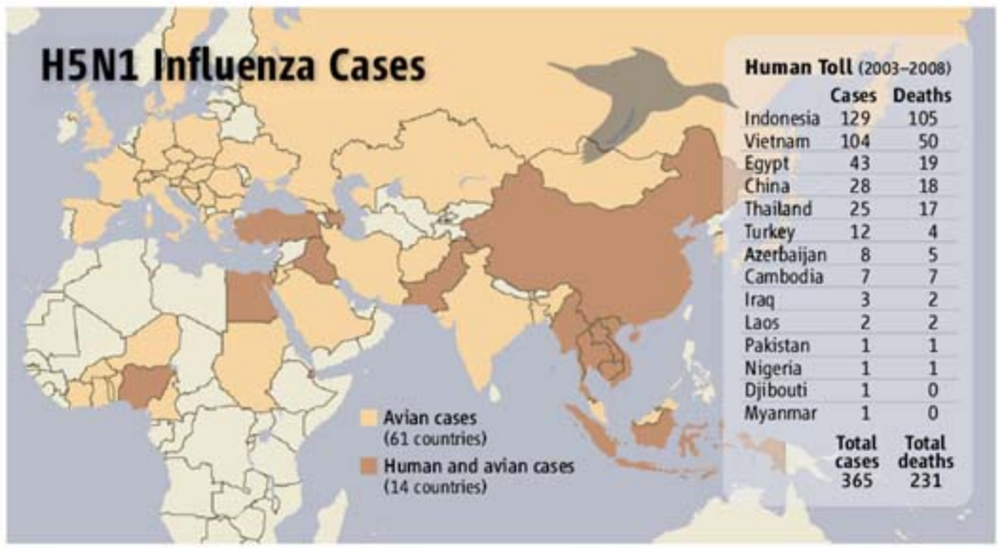

Still on the move. Although not headline news, in 2007 the H5NI virus spread to poultry flocks in eight new countries and returned in 23 others stretching from Japan to the United Kingdom while human cases continued to mount.

SOURCE: WHO AND OIE (WORLD ORGANISATION FOR ANIMAL HEALTH); 21 FEBRUARY 2008

ATOMIC PHYSICS

Insights Flow From Ultracold Atoms That Mimic Superconductors

They're the technological progeny of famed Bose-Einstein condensates. But chilly gases called Fermi condensates are proving even richer in new physics

In 1995, experimenters unveiled the coolest thing ever seen in atomic physics. Using lasers and electromagnetic fields, they chilled gases of certain atoms, known collectively as bosons, to within a millionth of a degree of absolute zero to coax them into a single quantum wave, giving the gas bizarre new properties. Known as a Bose-Einstein condensate (BEC), that atomic tsunami had been predicted 70 years earlier; its discoverers won a Nobel Prize in 2001.

Then in 2004, physicists pulled off a tougher trick by making other atoms, known as fermions, behave like the electrons in a superconductor, which pair and waltz along without resistance. Merely producing such a "Fermi condensate" was a more impressive feat, many researchers argued. But was it as important as the discovery of BECs? All agreed that that depended on what grew out of it. Fermi condensates could open new realms of research—or prove a conceptual dead end.

Now, only 4 years after they first were made, Fermi condensates are exceeding expectations. BECs have been used to make atom lasers and stop light dead, but Fermi condensates may be more fruitful, physicists say. "One of the biggest impacts of BECs is that they provided the technology and tools to do fermions," says Wolfgang Ketterle, an experimenter at the Massachusetts Institute of Technology (MIT) in Cambridge and co-winner of the Nobel Prize for BECs. "I see a lot of deeper conceptual issues" with fermions.

Like the electrons in a superconductor, the paired atoms flow without resistance to form a "superfluid." By tuning the tugs between atoms, researchers are mapping a new landscape of superfluidity. The gases are also providing insights into other forms of matter, such as the soup of fundamental particles called quark-gluon plasma that filled the infant universe and has been recreated at particle colliders.

Experiments with ultracold fermions might even crack the mystery of high-temperature superconductivity, says Randall Hulet, an experimenter at Rice University in Houston, Texas. "The promise is still enormous," he says. "There's much more to be done than has been done already."

Atoms, social and otherwise

Atoms are either joiners or loners, depending on how they spin. And that depends on how many protons, neutrons, and electrons they contain. If an atom has an even number of parts, as rubidium-87 does, its spin is a multiple of an iota known as Planck's constant. That makes it a boson, and any number of identical bosons can squeeze into one quantum wave. So when physicists chill rubidium-87 gas to below a millionth of a kelvin, the atoms pile into the lowest energy wave to make a superfluid BEC.

Atoms with an odd number of protons, neutrons, and electrons are far less gregarious. Known as fermions, they have an extra half-serving of spin, and a law of nature says that two identical fermions cannot occupy the same quantum state. So when fermions get cold, they stack one each into the lowest energy waves like so many plates in a cupboard (see figure, below).

Fermions can still form a superfluid, however. For example, in a superconductor, electrons (also fermions) fill two energy stacks: one for electrons spinning one way and another for electrons spinning the opposite way, as particles with opposite spins are in different states. Vibrations in the material then attract the electrons to one another, allowing opposite-spinning electrons to form loose, overlapping "Cooper pairs." At low temperature, there isn't enough energy about to break up the pairs, so they flow without hindrance.

Physicists aimed to mimic that effect in gases containing atoms spinning two different ways, to make them flow without resistance and show other weird quantum effects. To draw the atoms together, they apply a magnetic field. The field then produces a "Feshbach resonance" that greatly increases the interactions between the atoms.

Progress came in quick steps. In November 2003, Rudolf Grimm of the University of Innsbruck, Austria, and colleagues formed diatomic molecules of lithium-6 and produced a molecular BEC (*Science*, 14 November 2003, p. 1129). Three months later, Deborah Jin and her team at JILA, a laboratory run by the U.S. National Institute of Standards and Technology and the University of Colorado, Boulder, adjusted the magnetic field to create looser Cooper pairs of potassium-40 atoms and achieve a Fermi condensate (*Science*, 6 February 2004, p. 741). In 2005, Ketterle proved that a Fermi condensate is a superfluid by spinning one and observing a telltale pattern of tiny whirlpools called vortices (*Science*, 24 June 2005, p. 1848).

Fermi condensates don't behave exactly as expected, Jin says. "The superfluid didn't turn out to be like an ordinary superconductor," she says. "It's more like a high-temperature superconductor, but it's not really that,

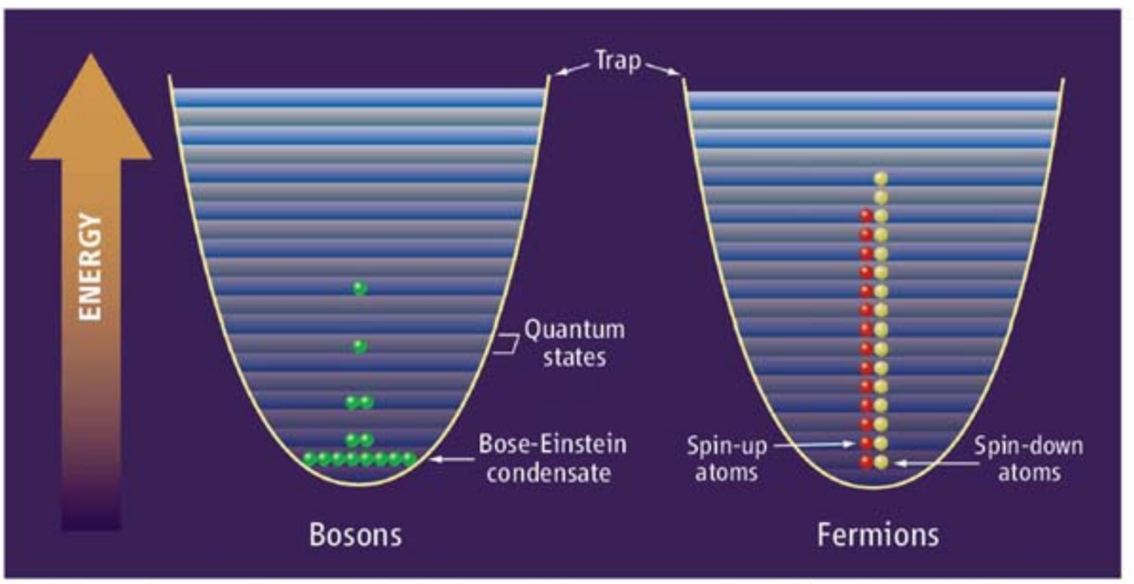

La différence. Bosons crowd into a single spatially extended quantum wave to flow without resistance. Fermions stack into the waves but then can pair to flow freely.

either." That's because the atoms attract one another so strongly. If the electrons in a metal pulled as hard, superconductivity would set in at thousands of degrees.

Charting new territory

Ultracold atoms can be manipulated far more easily than electrons in a superconductor. So like kids playing with a radio, physicists are turning every knob on their experiments to see what happens.

For example, researchers have varied the ratio of atoms spinning in the two directions. Such experiments could lend insight into the hearts of neutrons stars, which contain different numbers of different kinds of quarks (which are also fermions). The imbalance throws standard theory out of kilter and could result in new types of superfluid, such as the so-called FFLO state that is patterned like striped cloth.

In December 2005, Ketterle and his team reported that in lithium-6, superfluidity vanished when the ratio of up spins to down spins exceeded 85:15. In contrast, Hulet and colleagues found that superfluidity endured to a ratio of 93:7, the highest they could measure. For ratios above 55:45, it appeared that an evenly paired superfluid core forced the excess spins to the edges of the gas puff, like unpaired dancers squeezed off a crowded dance floor (*Science*, 23 December 2005, p. 1892). Hulet's results for nearly equal ratios even seemed to leave room for an exotic superfluid.

The experiments sparked a heated debate, however. Ketterle argued that, in theory, superfluidity had to disappear if the ratio got too lopsided. He questioned the claim of a sharp "phase separation" between an evenly paired superfluid and the excess spins. But theorist Henk Stoof of Utrecht University in the Netherlands suggested that the MIT team simply didn't get their atoms cold enough to see the separation, which sets in below a so-called "tricritical point" (see figure).

That cloudy situation is clearing. Ketterle and team have used laser light to trace the three-dimensional distribution of spins in their gas puffs. At the lowest temperatures, they observed a sharp boundary between core and periphery, they reported in the 7 February issue of *Nature*. That suggests that the MIT group had reached very low temperatures all along. But it also shows that the atoms phase-separate, as the Rice group claimed.

Meanwhile, Stoof and others have calculated that the tricritical point should lie pretty much at the temperature and spin ratio that the MIT group says it does. "It looks kind of settled," Stoof says. All agree that the Rice experiments must be taken seriously, however. Hulet's team traps their atoms in a very long, thin trap, Stoof notes, and the trap's shape may play a role and even stabilize the superfluid core in some way.

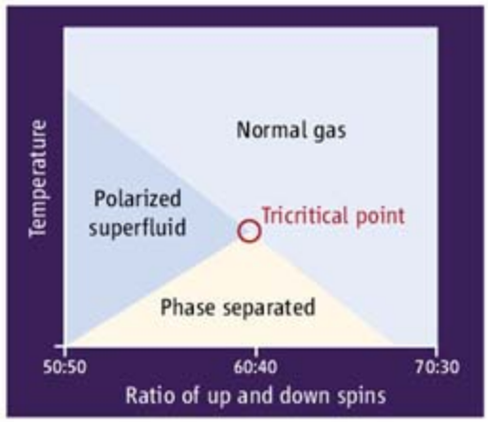

Terra nova. At lowest temperatures, a Fermi condensate separates into an evenly paired core and a shell of excess spins.

CREDIT: SHIN ET AL., *NATURE* 451, 689 (2007)

Quintessential fermions

Experimenters have also found extraordinary similarities between different types of cold atoms. In February 2007, John Thomas and colleagues at Duke University in Durham, North Carolina, traced how entropy varies with the energy in a lithium-6 gas. In April, theorist Peter Drummond of the University of Queensland in Brisbane, Australia, and colleagues showed that data for potassium-40, collected by JILA's Jin, lay along precisely the same curve.

Such "universal" thermodynamics arises because the atoms pull on one another so strongly that the details of their interactions cease to matter. But that means exactly the same relations should hold for hard-tugging quarks in a quark-gluon plasma or electrons in a high-T_c superconductor. "The big picture is that *all* strongly interacting fermions have to behave this way," Thomas says.

Universality has piqued the interest of nuclear physicists. They have created a quark-gluon plasma by smashing nuclei together at the Relativistic Heavy Ion Collider at Brookhaven National Laboratory in Upton, New York. A collision typically produces a cigar-shaped droplet of the 2-trillion-degree plasma, which expands oddly—much faster widthwise than lengthwise. Measuring that "elliptic flow," researchers have shown that the plasma is a nearly perfect liquid with almost no viscosity.

A cloud of fermionic atoms expands in the same strange way. Setting a puff of lithium-6 jiggling, Thomas found that its viscosity was nearly as low as the plasma's. The precise origins of that similarity remain to be determined, says nuclear theorist Krishna Rajagopal of MIT. "Nature is trying to tell us something," he says. "There is clearly some universality between these two very different liquids."

Some researchers hope to make connections to the ultracold, ultradense nuclear matter within a neutron star. There, different types of quarks may pair like the atoms in an imbalanced Fermi condensate. But there are key differences, Rajagopal says. The atoms spontaneously form a paired core surrounded by unpaired atoms. Such phase separation isn't possible with electrically charged quarks, he says, because it would cause a massive buildup of charge. Instead, a neutron star may contain the theorized FFLO superfluid, says Rajagopal, who hopes experimenters can prove that it does exist, perhaps in extremely elongated atom clouds.

The ultimate superconductor

Perhaps the grandest goal is to explain high-T_c superconductors, which carry electricity without resistance at temperatures as high as 164 K and have defied explanation for 20 years.

The superconducting compounds contain planes of copper and oxygen atoms arranged in a square pattern. Electrons hop from copper to copper, avoiding each other because their charges repel but somehow pairing by interacting through their spins and magnetic fields. The mathematical formulation of this scheme, known as the Fermi-Hubbard model, is simple to describe but too complex to solve even with the best computers.

So physicists hope to simply simulate the thing with cold atoms. The idea is to load ultracold fermions into a corrugated pattern of laser light. The atoms would hop from bright spot to bright spot like the electrons hopping from copper to copper. "If you're given one goal you want to accomplish in the next 5 years, it's to produce in the lab a Hubbard model" that mimics high-T_c superconductivity, Ketterle says.

Several groups around the world are pushing to do just that. But it may not be as easy as some expect, says Tin-Lun "Jason" Ho, a theorist at Ohio State University in Columbus. To form a Fermi condensate, researchers chilled their atoms to a few billionths of a kelvin. To probe the Hubbard model, Ho says, they may have to reach a few trillionths of a degree.

Still, in just a few years, Fermi condensates have opened new vistas and forged connections between distant fields. Likely, important results will continue to flow.

–ADRIAN CHO

PALEOANTHROPOLOGY

Rocking the Cradle of Humanity

The nation of Ethiopia is seeking to leverage its past—including its most famous daughter, the hominid called Lucy—to help secure its future

ADDIS ABABA, ETHIOPIA—At the National Museum here, Stephanie Melillo sits within arm's reach of almost 5 million years of human evolution—literally. Crammed into a corner in a temporary lab, transferring notes penned in a battered yellow notebook to her computer, this Stanford University graduate student must move out of the way so researcher Timothy White can unlock the filing cabinet that houses the reconstructed teeth of the famed 4.4-million-year-old hominid, *Ardipithecus ramidus*. A second cabinet nearby contains the cranium called Herto, which at 160,000 years old is one of the oldest known modern humans, plus skulls of *Homo erectus* and *Homo rhodesiensis*, 1 million and 500,000 years old, respectively.

White, of the University of California, Berkeley, co-leader of a team that discovered many of these fossils, eagerly explains the bones' significance to visiting government officials while Melillo and other researchers from three continents jostle elbow to elbow, desperately trying to finish their work before their visit here ends. It's clear that the group needs more space and that these priceless fossils need a better home. "We're coiled up here like a spring ready to explode," White complains.

In a few months, however, White and other researchers should each have their own office during their stays in Ethiopia, while the hominids rest in cushioned vaults. Even as Melillo works and White talks, hammering and other construction noises outside their windows herald the impending opening of the museum's new research center. Built with $10 million from the Ethiopian treasury, it is symbolic of a burst of scientific enterprise from a country besieged with AIDS, periodic famine, and, occasionally, armed conflict.

Kenya once held the world's attention for its contributions to understanding human evolution. But Ethiopia has its own cache of ancient treasures, and its leaders hope to use them to advance both the country's image and the science within its borders. "We want to catch up with the rest of the world," says Mohammoud Dirrir, minister of culture and tourism.

Not just the national museum but also universities and outreach efforts are expanding, in hopes of building Ethiopia's internal scientific capacity, encouraging research, and developing tourism. As part of its millennium celebration (Ethiopia follows the Egyptian Coptic calendar, in which this is the year 2000), the government hosted an international meeting* last month to foster links between research and development. For researchers, "everything is more positive, welcoming," says paleoanthropologist and native Ethiopian Sileshi Semaw of Indiana University, Bloomington. "Everyone is realizing our work is important."

Many obstacles exist. Ethiopia still lacks the funds and skilled teachers needed to realize its vision of being a scientific leader in Africa. And tourism and outreach sometimes conflict with research. Despite protests from scientists, the Lucy skeleton is now on tour in the United States. But there is optimism as well. The government and scientists "are now working together very well," says White. "We need to build on this collaboration as we move forward together."

Move to modernize

Working in Ethiopia hasn't always been so amicable. When Emperor Haile Selassie was overthrown in the 1970s, researchers were kicked out and the search for fossils suspended for several years. Even after White and others were allowed back in, the government paid little mind to their discoveries. But today, Lucy's discoverer, Donald Johanson of Arizona State University in Tempe, calls Ethiopia "Africa's most promising country to expanding our knowledge of the past." His project in Hadar in the Afar region of eastern Ethiopia is one of about 25 active paleontological or archaeological field sites in the country (see map, p. 1183). All fossils and artifacts unearthed stay in the country; once researchers leave the

* "International Conference on Transforming the Might of a Century-Long Research Output into Development," 12–15 January, Addis Ababa, Ethiopia.

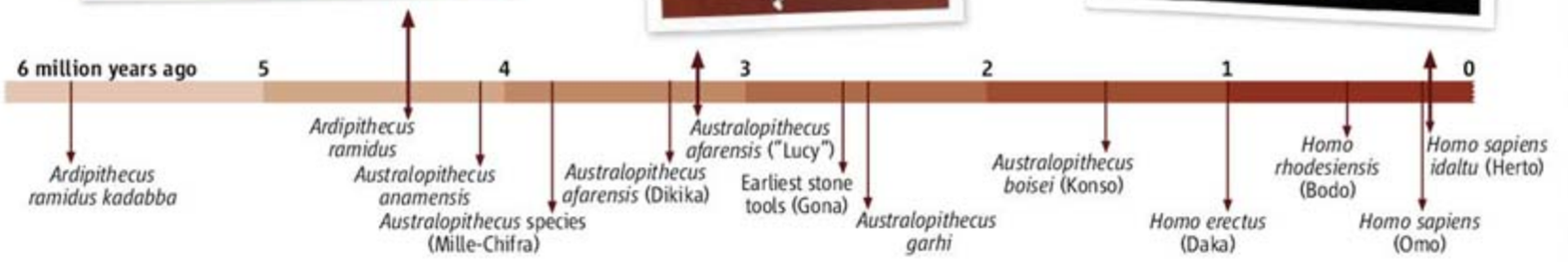

Step by step. Ethiopia is home to fossils representing many stages of hominid evolution from *Ardipithecus* to *Homo sapiens*.

CREDITS (LEFT TO RIGHT): T. D. WHITE/BRILL ATLANTA; THE CLEVELAND MUSEUM OF NATURAL HISTORY; D. L. BRILL/BRILL ATLANTA

field, they must go directly to the museum to drop off their finds, even if it means a late-night rendezvous with caretakers.

So it is no surprise that the museum is bursting. For decades, researchers squeezed into the former governor's residence; a small lab building was added in 1982 with funds from the U.S. National Science Foundation. But space remained tight. Some decades-old specimens are still wrapped in the newspaper or even the dried grass they were delivered in, waiting to be processed. "If two or three teams showed up at the same time, it was very hard to work," Johanson recalls.

Then in 2003, that lab was razed to make way for a six-story, modern structure that includes a two-floor library, a 500-person auditorium, and 200 rent-free offices, plus storage and study space for more than a million specimens. The three wings are devoted to paleontology and archaeology; art and history; and administrative, conservation, and educational spaces.

Although scheduled to open in the next few months, the building is still a dusty shell of concrete and glass, with unfinished wiring poking out of walls, ceilings missing tiles, and a gaping hole on the ground floor where a giant elevator is to go. The museum needs more than $5 million to outfit the new facility—there are almost no books for the library, for example—and less than $200,000 has been raised so far.

Foreign aid is helping: France is supplying furniture, and Japan may outfit the hominid spaces. Everyone involved is thrilled and not just with the prospect of more space. "It shows how much emphasis has been given [to research]," says Ethiopian native and paleoanthropologist Yohannes Haile-Selassie of the Cleveland Museum of Natural History in Ohio. "In a country that has a lot of needs, the government could have easily used that money for something else."

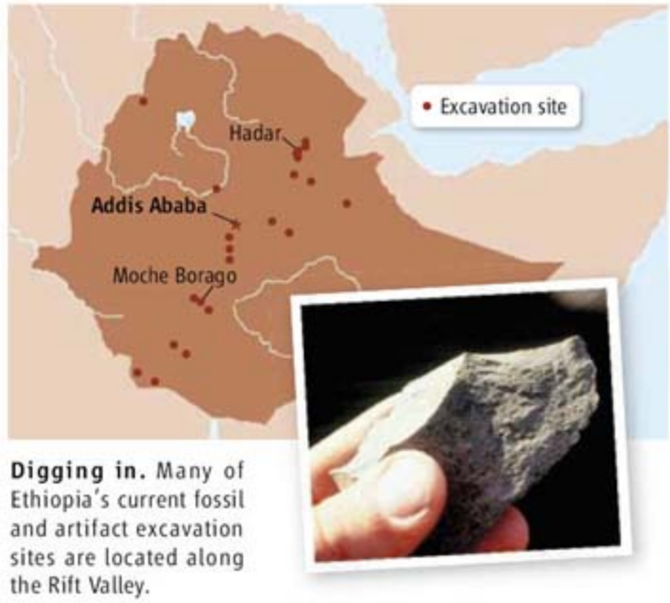

Digging in. Many of Ethiopia's current fossil and artifact excavation sites are located along the Rift Valley.

Beyond concrete and glass

But a six-story building that serves primarily as a second home to researchers from abroad is just the first step. "We must train more Ethiopians," says Berhane Asfaw, an Addis Ababa–based paleoanthropologist who often works with foreign teams. Toward that end, the Ethiopian government has about tripled the number of universities in the past 3 years and promised $10 million toward educating 10,000 master's students and 2000 Ph.D.s in the next 5 years. Addis Ababa University will shift its focus from undergraduate to graduate education.

Natural as well as applied sciences will get a boost, with new graduate programs sprouting up, including interdisciplinary ones key to fields such as paleontology. In the works are a botanical garden and a new natural history museum to promote research that is focused more on biology and earth sciences than is the national museum. And the goal for the next generation—unlike that of Haile-Selassie, Berhane Asfaw, and about a dozen other prominent Ethiopian researchers, all educated abroad (*Science*, 29 August 2003, p. 1178)—is to have "most of the training done in-house," says Araya Asfaw, dean of science at Addis Ababa University. The hope is to foster permanent research programs within Ethiopia that depend less on foreigners.

At the same time, "one of the most important things that needs to happen is the integration of tourism and science," says White. And that, too, is happening. National Geographic has pledged support for an educational center at the village nearest to Hadar, home of the 3.2-million-year-old Lucy. With better roads under construction, "it could easily be a destination spot for tourists," Johanson predicts. Exhibit plans are still taking shape, but there likely will be casts of Lucy and other fossil hominids, as well as photographs from the site.

Steven Brandt of the University of Florida, Gainesville, has similar visions for Moche Borago, an excavated cave an 8-hour drive southwest of Addis Ababa. Here, Brandt's team has dug up stone tools and other artifacts that help reveal the transition to complex societies about 50,000 years ago. Brandt hopes to set up a small research center at a local university, and he talks enthusiastically about the cave's potential as a stop-off, complete with displays and craft shops, for tourists heading to see native tribes farther south. "If he is committed [to that project]," says Yonas Beyene, research director at Ethiopia's Authority for Research and Conservation of Cultural Heritage, "it would be very much appreciated."

Researchers hope also to build another museum in or close to Addis Ababa devoted to human evolution, with an expected €10 million from the European Union, says Berhane Asfaw. The new museum will boost public outreach about hominids in a way the National Museum, with its limited exhibit space, cannot, he adds.

Are these goals a pipe dream? Maybe. Ethiopia faces an acute shortage of professors to teach graduate courses and at the moment can support little research by local scientists. "They have no money," says geologist Maurice Taieb of the Centre Européen de Recherche et d'Enseignement des Géosciences de l'Environnement in Aix-en-Provence, France.

Already, the government's decision to send Lucy abroad has raised the ire of some. Many Ethiopian and Western scientists argued that the skeleton was too fragile to travel (*Science*, 27 October 2006, p. 574). "Obviously, the Ethiopian government has made its own decisions on how to use Lucy in terms of tourism and economic gains," says Haile-Selassie, as the priceless bones are now on display in Houston, Texas. Lucy is scheduled to stay in the United States for several years, although no additional exhibitions are yet confirmed. Money earned by Lucy's travels will help improve the National Museum, says museum director Mamitu Yilma.

And even if, as Ethiopian officials hope, Lucy sparks a run of tourists visiting Ethiopia, Brandt worries about the fate of sites those tourists might want to see. Many sites are already vulnerable, he says, and better roads may destroy them or make them too accessible. "By opening up [to tourism], we can lose everything we have," agrees Berhane Asfaw.

Yet Seyoum Bereded, director of the Ethiopian Millennium National Festival Council Secretariat, is unfazed by these challenges, saying that science and tourism can be a compatible, and profitable, match. He's ready to push Ethiopian science into the 21st century. "If we have peace, we can do anything."

–ELIZABETH PENNISI

SOURCE: ARCCH; CREDIT: MICHAEL ROGERS

LETTERS

edited by Jennifer Sills

The Need to Cut China's Illegal Timber Imports

IN THE POLICY FORUM "CHINA'S FORESTRY REFORMS" (7 DECEMBER 2007, P. 1556), G. Wang and colleagues describe laudable steps to improve forest management and increase wood production in China. However, they fail to even mention China's burgeoning consumption of imported timber—much of it illegally harvested—and its profound implications for Chinese forestry and the global environment.

How has China managed to double its forested area while meeting its escalating domestic demands and becoming the world's largest exporter of timber products? The answer is that it relies massively on timber imports. Chinese imports quadrupled over the past decade from an estimated 12.5 to 45 million m^3 (*1*). Half of all traded timber in the world is now destined for China (*2*). China's timber supplies come from developing countries around the world, and it is overwhelmingly the biggest consumer of southeast Asian and Russian timber (*3*, *4*).

Unfortunately, the timber-exporting nations reap only modest benefits. Nearly all of the growth in Chinese timber imports has been in unprocessed logs, which provide few opportunities for local employment in timber-exporting nations (*1*). Moreover, most logs imported into China are effectively stolen, with no payment of government royalties to exporting nations or environmental control over harvest operations. At least 80% of Chinese timber imports from Brazil, Cambodia, Cameroon, Congo-Brazzaville, Equatorial Guinea, Gabon, Indonesia, Myanmar, Papua New Guinea, and the Solomon Islands are illegal, according to recent estimates, with somewhat lower values (50 to 60%) for Malaysia and Russia (*2*, *3*). Unprocessed logs are easy to acquire and smuggle, and corruption in the log trade is far more prevalent than that for processed forest products (*1*).

The rampant trade in illegal timber is promoting large-scale forest destruction, especially in the tropics. Poorly regulated timber operations degrade forests and provide a key economic impetus for road building (*5*), which greatly increases access to forests for slash-and-burn farmers, hunters, and land speculators that in turn destroy or severely degrade forests and their wildlife (*6*). This problem is especially severe in Indonesia, a biodiversity-rich nation that is currently losing ~2 million hectares of forest each year (*6*).

Of course, China is far from solely culpable for its insatiable appetite for imported timber (*7*). Its enormously profitable wood-products industry is largely driven by exports, which have grown 3.5-fold in the past decade (*2*). Exports to the United States and Europe have risen even faster over this period—by eight- and fivefold, respectively (*2*)—with the United States alone importing about $3.5 billion in illegal timber products (mostly furniture) from China annually (*3*). Such illegal imports will increase further if pending free-trade agreements are finalized between the United States and Asian countries (*8*). Chinese wood-products corporations will have little incentive to alter their predatory behavior so long as consumers in wealthy nations blithely continue buying their products.

Timber imports. Logging trucks ferry timber from Myanmar to China.

CREDIT: JEFFREY VINCENT

WILLIAM F. LAURANCE

Smithsonian Tropical Research Institute, Apartado 0843-03092, Balboa, Ancón, Panama. E-mail: laurancew@si.edu

References

1. R. Kozak, K. Canby, *Forest Trends*, issue 9 (October 2007).
2. T. Stark, S. P. Cheung, *Sharing the Blame* (Greenpeace International and Greenpeace China, 2006); www.illegal-logging.info/uploads/SHARING_THE_BLAME1.pdf.
3. Globaltimber, *China: Illegal Imports and Exports* (www.globaltimber.org.uk/Chinaillegalimpexp.htm, accessed 12 December 2007).
4. A. L. Mayer *et al.*, *Science* **308**, 359 (2005).
5. T. K. Rudel, *Tropical Forests: Regional Paths of Destruction and Regeneration in the Late Twentieth Century* (Columbia Univ. Press, New York, 2005).
6. W. F. Laurance, C. A. Peres, Eds., *Emerging Threats to Tropical Forests* (Univ. of Chicago Press, Chicago, 2006).
7. W. F. Laurance, *Tropinet* **18**, 1 (2007).
8. EIA/Telepak, *America's Free Trade for Illegal Timber* (Environmental Investigation Agency, Washington, DC, 2007); www.eia-international.org/files/news312-1.pdf.

Response

LAURANCE CHARGES THAT CHINA—AS A major timber importer—should play a role in mitigating the global problem of illegal logging. Illegal logging is widespread and extends far beyond the capabilities or responsibilities of a single country to resolve. For this reason, a number of international Forest Law Enforcement and Governance processes have been established. China is participating actively in these initiatives and is also working bilaterally with several countries (such as Indonesia) to help strengthen their forest law enforcement and governance.

The Chinese government recognizes that international wood smuggling is a major issue and has responded in a variety of ways, both nationally and internationally. As we

Plasma snapshots

1193

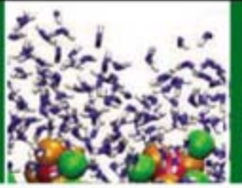

Salt and water

1197

mentioned in our Policy Forum, the commercial plantation program is one measure intended to reduce China's heavy reliance on wood imports by supplying 200 million m^3 of logs annually by 2015 (*1*). However, implementation of this program has been slow, plagued by inconsistent application of land-use laws and local corruption.

China is developing a national Forest Certification Standard and Chain of Custody process. This system should help ensure that those wishing to purchase wood products from China will be able to trace the origins of the wood. In 2007, the State Forestry Administration intensified its enforcement of national forest laws, fining or dismantling 3277 timber processing and trading venues involved in illegal activities (*2*).

Internationally, the Chinese government has worked jointly with its main trading partners to combat illegal logging and trade, signing several multi- and bilateral agreements in this area (*3*). China has also taken steps to reduce the smuggling of logs: It has banned direct imports of wood across the Myanmar border; issued Guidelines for Sustainable Forestry Management by Chinese Enterprises Operating Overseas (*4*); proposed an Asia-Pacific Network on Forest Rehabilitation and Sustainable Management (*5*); and imposed high taxes on solid wood products (such as a 5% tax on solid floor panels) to discourage the overconsumption of hardwood resources. On-the-ground action is also occurring at customs points. For example, in March 2006, Taiping Customs in Guangdong Province launched the "Woodpecker Action" against wood smuggling, which netted 53,592 m^3 of illegal wood and led to the arrest of 24 people in a single month (*6*).

Arguably, major responsibility rests with those nations exporting to China to regulate and monitor their own forests. These exporting countries are also developing countries, with local corruption, poor forest monitoring, and the need to raise export revenue. Illegal logging is most prevalent in developing countries, but even in more developed countries with stronger laws and monitoring, regulating for illegally imported logs is relatively new and difficult. Some sources estimate that as much as 10% of U.S. log imports are from illegal sources (*7*), and it was only in 2007 that the United States passed the Legal Timber Protection Act to regulate the importation of illegal logs (*8*).

The illegal wood trade is a global problem and requires coordinated regional and global responses. Continued expertise, funding, and constructive criticism are necessary to keep the pressure on China and other countries to make progress on environmental benchmarks. But vilifying China for its "predatory" behavior fails to recognize that the Chinese wood-products industry is only one part of a chain that extends from producer to consumer. It would be more constructive to recognize that as a developing country trying simultaneously to raise its people's living standards and improve its natural resources, China needs all the help it can get.

GUANGYU WANG,[1] JOHN L. INNES,[1]* SARA W. WU,[2] SHUANYOU DAI,[3] JIAFU LEI[3]

[1]Faculty of Forestry, University of British Columbia, Vancouver, BC V6T 1Z4, Canada. [2]World Forest Institute, Portland, OR 97221, USA. [3]State Forestry Administration, Beijing 100714, China.

*To whom correspondence should be addressed. E-mail: john.innes@ubc.ca

References and Notes

1. State Forestry Administration, *China Forestry Development Report* (China Forestry Publishing House, Beijing, 2001–06).
2. C. Zhiyong, "Going green good for global forest business," *China Daily*, 25 September 2007, p. 12 (www.chinadaily.com.cn/cndy/2007-09/25/content_6131309.htm).
3. These agreements include (i) the China-Russia cooperation agreement on Development of Forest Resources and Sustainable Forest Management; (ii) the MOU between SFA of China and MoF Indonesia to Combat Illegal Logging; (iii) The Third China-United States Strategic Economic Dialogues; and (iv) the China-EU Forest Enforcement and Governance Conference, Beijing, September 2007.
4. X. Lei, "China's efforts to make globalization green," *China Daily*, 2 November 2007, p. 10 (www.chinadaily.com.cn/opinion/2007-11/02/content_6224982.htm).
5. "Hu Jintao expounds China's stance on climate change at APEC meeting," *China View*, 9 September 2007 (http://news.xinhuanet.com/english/2007-09/09/content_6692083.htm).
6. Guangdong Anti-Smuggling Office, *Study on Smuggling Wood in Furniture Industry* [in Chinese] (www.dsb.gd.gov.cn/ruizheng/Article/ShowArticle.asp?ArticleID=2152).
7. Environmental Investigation Agency, *No Questions Asked* (EIA, Washington, DC, 2007); www.eia-global.org/noquestionsasked_web.pdf.
8. H.R. 1497–110th Congress (2007): Legal Timber Protection Act, GovTrack.us (database of federal legislation); www.govtrack.us/congress/bill.xpd?bill=h110-1497.

Minding Controls in Curriculum Study

THE EDUCATION FORUM ON EARLY CHILDhood executive functions by A. Diamond *et al.* ("Preschool program improves cognitive control," 30 November 2007, p. 1387) reported an educational intervention congruent with the views of clinicians who believe that intellectual ability emerges from early emotional growth (*1*). Unfortunately, the conclusions drawn by Diamond *et al.* suffer from evidentiary weaknesses.

A study of this type must reduce differences between groups to those essential to the experimental intervention. Diamond *et al.* reported that teachers trained to use the executive function techniques (EFs) needed almost a year of work before they were proficient; it was not stated how long the comparison teachers took to achieve their criterion. Anxiety about an unfamiliar curriculum might have motivational effects, causing the EF teachers to be more attentive to children's behavior than a less anxious group, as the long-established inverted U-shaped motivational function predicts (*2*).

The evidence is also weakened by a vague description of the comparison intervention. It is possible that more frequent adult-child interactions occurred in the EF condition than in the other group. More frequent interactions could foster the attachment relationships within which young children are thought to do their best learning. This possibility is reminiscent of the "common factors" concept in the study of psychosocial interventions; some researchers have suggested that common factors influence efficacy more than specific techniques do (*3*). In the Diamond study, the common factors might be adult-child interactions, and such factors might be the effective causes of changes the report attributes to specific EF techniques.

JEAN MERCER

Department of Psychology, Richard Stockton College, Pomona, NJ 08057, USA.

References

1. S. I. Greenspan, S. Wieder, *Infant and Early Childhood Mental Health* (American Psychiatric Publishing, Arlington, VA, 2006).
2. R. M. Yerkes, J. D. Dodson, *J. Comp. Neurol. Psychol.* **18**, 459 (1908).
3. A. D. Reisner, *Psychol. Record* **55**, 377 (2005).

Response

IN HER LETTER, MERCER OFFERS TWO ALTERnative explanations, couched as criticisms, for the findings we reported in our Education Forum (30 November 2007, p. 1387).

Mercer proposed that until teachers became proficient at the Tools of the Mind (Tools) curriculum, anxiety about an unfamiliar curriculum might have caused them to be more attentive to children's behavior than teachers in the comparison program. Our data do not support that hypothesis. By Year 2, teachers in both curricula were proficient, and we found virtually no differences between children who were with these programs in both Years 1 and 2 or only in Year 2. If teacher anxiety accounted for any of the differences, one would have expected a difference in performance between children in Tools who were exposed to anxious teachers (in Year 1) and children in Tools who were not (children who only attended Year 2), but such differences were minor.

Teacher anxiety would likely have increased classroom stress levels, impairing children's ability to master executive function skills or academic content (*1*). Research on the "long-established inverted U-shaped motivational function" referred to by Mercer has consistently shown that although increased anxiety makes individuals more vigilant and attentive to danger signs, it impairs thinking, problem-solving, and interpersonal sensitivity (*2*, *3*).

Mercer also speculated that perhaps more frequent adult-child interactions occurred in Tools classrooms, which could have fostered attachment relationships. There is no evidence, however, that Tools increased the frequency of adult-child interactions, although it did improve their quality, possibly promoting close positive teacher-student relationships as Mercer suggests. We do not consider that a weakness of our study. Indeed, in supporting online materials (SOM), we said that such intermediate variables might mediate, or contribute to, the observed effects.

Mercer's second suggestion somewhat contradicts her first, for if teachers' anxiety were heightened, that would impair the development of positive relationships with students. A stressed or anxious teacher is less likely to be emotionally present for the children and more likely to snap at children for small transgressions.

I would also like to correct a possible misconception left by the first paragraph of Mercer's letter. As we stated in the SOM, pages 14 to 15, the beneficial effect of Tools on academic performance might be mediated by its beneficial effects on emotional growth, but we did not investigate, and have no evidence on, its effect on emotional development.

ADELE DIAMOND

Department of Psychiatry, University of British Columbia, Vancouver, BC V6N 3L6, Canada.

References

1. J. J. Blase, *Am. Educ. Res. J.* **23**, 13 (1986).
2. A. F. T. Arnsten, *Science* **280**, 1711 (1998).
3. S. J. Lupien *et al.*, *Brain Cognit.* **65**, 209 (2007).

Letters to the Editor

Letters (~300 words) discuss material published in *Science* in the previous 3 months or issues of general interest. They can be submitted through the Web (www.submit2science.org) or by regular mail (1200 New York Ave., NW, Washington, DC 20005, USA). Letters are not acknowledged upon receipt, nor are authors generally consulted before publication. Whether published in full or in part, letters are subject to editing for clarity and space.

EVOLUTION

Happening Now, Outdoors

Hanna Kokko

According to popular legend, the idea of evolution hit Darwin while he was watching small, blackish-brown finches on the Galápagos Islands, much like Newton suddenly understood gravity when an apple fell on his head. Neither story is historically accurate—Darwin did not even care to label the birds he collected according to island—but the finches carry Darwin's name to this day. They also continue to contribute to our understanding of evolution and speciation. In his 1994 book *The Beak of the Finch* (*1*), Jonathan Weiner popularized what we then knew about these dull-plumaged yet fascinating birds. Much of his account was based on work by Peter and Rosemary Grant (*2*). Fourteen years on, this Princeton-based couple presents their own accessible summary of their life's research in *How and Why Species Multiply*.

Darwin had the power to visualize how natural selection operates day after day, minute after minute, but he thought that its effects would only become evident over time spans too long to observe directly. How he would enjoy reading what the Grants have to offer us. Basic techniques, such as banding all individuals, locating their nests, and measuring their beaks (and of course other body parts), yield considerable insight into the processes that create biodiversity. Simply put, large beaks crush big seeds more efficiently, but large-beaked finches are at disadvantage when their food is restricted to small seeds. The Galápagos regularly experience large fluctuations in climate, largely controlled by El Niño events, and the vegetation changes accordingly. Prolonged droughts (times when seeds are large and tough) can be followed by rampant rain (which leads to the dominance of plants with small seeds), and the finches dutifully follow. After more than 30 years of study, the finches' morphologies differ from those of their ancestors. Each climate change has shifted beak shapes and body sizes as predicted.

Such morphological changes demonstrate adaptation through natural selection, but the book's focus is on speciation and adaptive radiation. The Grants divide that process into three steps: initial colonization, divergence, and formation of a barrier to interbreeding at secondary contact. Repetitions of this sequence on various islands have given rise to the 14 or so current finch species. (The exact number is open to debate, which in itself is a sign of ongoing speciation.) The authors explain the scientific hypotheses involved in each step with admirable clarity, and I found only a few occasions where they perhaps erred on the side of oversimplifying theoretical predictions. (For example, competitive exclusion doesn't necessarily predict that of two near-identical species the first to arrive in an area will always resist invasion by the latter.) Yet the book's real strength is not theory but data.

Shifting to coexist. Large cactus finch (*Geospiza conirostris*) is intermediate in beak form and body size between large ground finch (*G. magnirostris*) and cactus finch (*G. scandens*) where both are absent (on Española) and more like cactus finch where large ground finch is present (on Genovesa).

CREDIT: PETER GRANT AND ROSEMARY GRANT/COURTESY PRINCETON UNIVERSITY PRESS

The reviewer is at the Department of Biological and Environmental Science, Division of Ecology and Evolution, University of Helsinki, 00014 Helsinki, Finland. E-mail: hanna.kokko@helsinki.fi

How and Why Species Multiply
The Radiation of Darwin's Finches

by Peter R. Grant and B. Rosemary Grant

Princeton University Press, Princeton, NJ, 2008. 272 pp. $35, £19.95. ISBN 9780691133607. Princeton Series in Evolutionary Biology.

The authors deliver tests of theory at a pace that nearly deceives the reader into believing that data collection was smooth and effortless. Want to know what happens to genetic diversity when a new population is founded? Just look at data files from 1982. Three males and two females of the large ground finch (*Geospiza magnirostris*) started a breeding population on Daphne Major, an island already inhabited by medium ground finches (*G. fortis*) and cactus finches (*G. scandens*). A genetic bottleneck (predicted by theory) was observed, but then, throughout the 1990s, new immigrants kept arriving. Instead of simply passing through, as before, they now stayed to breed on the island. Moreover, they were not a random sample of populations elsewhere, but significantly more heterozygous. This helped to swamp the effects of the bottleneck. So, the data suggested a modification of the original theory.

Interested in what happens when finches themselves are uncertain which species they belong to? Again, the Grants have relevant data: the fate of birds who accidentally learn the wrong species's song (which happens, for example, to those nestlings whose father dies during the nestling stage while the nearest singer is a different species). Imprinting indeed then leads to hybridization in the next generation, which allows detailed inferences about the murky phase of speciation before species identities have crystallized.

The Grants' account makes exciting and lucid reading. Among those who should take note are doubters of "old-fashioned" research methods who marvel at the prospects of genomics in the lab and wonder what use bird bands have in modern science. The authors consider evo-devo, too: the signaling molecules involved in beak development are known, as are differences in gene expression

between species of small- and large-beaked finches. But surely this would only count as trivia if not put in the context of evolution on the Galápagos: volcanic activity, followed by the arrival of a small flock of unremarkable-looking birds, and subsequently a plethora of interactions involving climate, vegetation, competition, song, mate choice, hybridization, etc. That context is where we start to understand what all the details mean. If doing so requires 30 years of bird banding, one hopes funding agencies recognize that.

How and Why Species Multiply ends with a sobering thought: "These are exciting times to be a geneticist: the world of genetics is expanding. At the same time the world's undisturbed environments are shrinking. If we are to take full advantage of genetic discoveries made inside organisms, we need to conserve the environments outside them." Does anything need to be added? Perhaps the book's penultimate sentence: "Nothing in evolutionary biology makes sense except in the light of ecology."

References

1. J. Weiner, *The Beak of the Finch: A Story of Evolution in Our Time* (Knopf, New York, 1994).
2. P. R. Grant, *Ecology and Evolution of Darwin's Finches* (Princeton Univ. Press, Princeton, NJ, 1986).

10.1126/science.1154815

HISTORY OF TECHNOLOGY

Tilting at a Myth

David L. Morton Jr.

Most of us remember Alexander Graham Bell for just one thing, although he had a varied and successful career studying human speech, experimenting with aviation, and even helping to found *Science*. Yet Bell's claim to have invented the telephone has been repeatedly challenged since the day he patented it in 1876. Historians have gathered around one or another of these competing claimants over the years, hoping to "set the record straight." But among the various "fathers" of the telephone, none has attracted more disciples than Elisha Gray, once a well-known inventor and the founder of the company that would become Western Electric but today largely forgotten. After a long hiatus in revisionist works on the telephone's birth, science journalist Seth Shulman has produced a new rendition, and he brings to it some tantalizing bits of fresh evidence and his considerable talent for writing engaging prose.

Gray and Bell filed documents at the U.S. Patent Office for nearly identical inventions on the very same day in 1876. When Gray, under advisement, abandoned his claim, Bell was given the patent and went on to glory. On subsequent review, it was revealed that Bell's initial patent specification covered only an improvement to the telegraph, but this document was hastily edited at the last minute to include voice communication. Gray's invention, on the other hand, was centered on the idea of transmitting the human voice by wire. Bell had indeed given thought (as many had before him) to voice telegraphy, but allegations emerged that a patent examiner had given Bell confidential information about the Gray invention. Indeed, the Bell patent's description of a telephone "transmitter" was strikingly similar to Gray's still-unpatented device. Subsequent legal proceedings against Bell carried on well into the 1880s before finally being settled in Bell's favor, but those bent on "exposing" Bell's crime have never given up. Shulman's contribution to the debate, besides reviving it, is to add some suggestive bits of evidence that do seem to reinforce one's suspicion that Bell's patented ideas were not his own.

The Telephone Gambit
Chasing Alexander Graham Bell's Secret
by Seth Shulman
Norton, New York, 2008. 256 pp. $24.95, C$27.50. ISBN 9780393062069.

Shulman blames historians for not correcting the persistent myth that Bell invented the telephone in his Boston lab with the assistance of Thomas Watson. However, it is clear from Shulman's own footnotes that historians have done a more than thorough job of investigating this matter. Although Bell's leading biographer, the late Robert V. Bruce, decided not to support Gray's position (*1*), perhaps that is understandable given the lack of decisive evidence in Gray's favor. Even Shulman must admit in the end that he cannot unequivocally prove Bell's guilt.

To those who already know how this story unfolds and to those involved in researching the history of technology, the more fascinating aspects of *The Telephone Gambit* have more to do with the author than either Bell or Gray. Shulman's book is part history, part personal narrative. He tells the story of the way he discovered this historical episode and what he thought about as he researched it. Shulman worked on his book as a guest of the prestigious Dibner Institute, a library devoted to the history of science and technology, and he recounts how he sought the advice of colleagues and tested his ideas all along the way.

Yet one wishes the company of professional historians would have helped him avoid falling into a classic trap. The book provides a detailed account of how one researcher lost his objectivity and adopted a partisan position in interpreting ambiguous historical data. Equally interesting, in a wincing sort of way, is Shulman's account of the progress of his research program, which resembles nothing so much as an enthusiastic graduate student investigating a potential thesis topic. One anticipates the inevitable discovery that the story has been done already, but Shulman never reaches that point. To anyone who has ever been in his situation (or advised someone doing historical research), it a fascinating thing to read. Morbidly fascinating perhaps.

Ultimately, Shulman misinterprets historians as his enemy, when it is popular culture that perpetuates the myth of Bell as the telephone's sole inventor. But if demonstrating that Bell probably stole Gray's idea were going to change cultural memory, it would have already done so. Further, the belief that finding the true point of origin of an invention explains much about the subsequent history of a technology is outmoded. Today's historians of technology seek to place inventions and the process of invention within the broader sweep of history. Establishing who arrived at the telephone first does not help us understand the vast importance of the commercially successful telephone system. This constellation of many inventions was devised neither by Bell nor Gray, but by an army of others who will likely never receive much recognition. The strong public fascination with certain inventors is not likely to go away, however, and many will be delighted with Shulman's lively account of the Bell-Gray scandal. But it is equally unlikely that *The Telephone Gambit* will accomplish its mission to alter the iconic memory of the tinkering, bearded Aleck Bell, shouting "Watson...!" in a half-fictitious garret laboratory.

Reference

1. R. V. Bruce, *Bell: Alexander Graham Bell and the Conquest of Solitude* (Little, Brown, Boston, 1973).

10.1126/science.1154816

The reviewer, the author of *Sound Recording: The Life Story of a Technology*, is at the College of Architecture, Georgia Institute of Technology, 247 4th Street, Atlanta, GA 30332–0155, USA. E-mail: david.morton@coa.gatech.edu

INQUIRY LEARNING

Integrating Content Detail and Critical Reasoning by Peer Review

Classroom lectures by experts in combination with journal clubs and Web-based discussion forums help graduate students develop critical reasoning skills.

Ravi Iyengar,[1]* Maria A. Diverse-Pierluissi,[1] Sherry L. Jenkins,[1] Andrew M. Chan,[2] Lakshmi A. Devi,[1] Eric A. Sobie,[1] Adrian T. Ting,[3] Daniel C. Weinstein[1]

Students working toward Ph.D.'s develop deep expertise in their areas of research through thesis work and interactions with advisers. Students must also develop broad knowledge in related areas to formulate research questions and to identify appropriate technologies in areas not encountered during their thesis research. Breadth of training will become increasingly critical for long-term success as biomedical research becomes ever more interdisciplinary and multidisciplinary. Graduate students also need to learn how to participate in and respond to peer review to become effective professionals. Learning the balance between breadth and depth and participating effectively in peer review are interrelated educational issues.

Breadth of training is obtained during the didactic part of the graduate program in advanced courses and journal clubs that use the primary literature. Typically, these formats use synchronous teaching-learning methods (*1*) that are valuable because they enable direct interactions and immediate feedback between the teachers and students. However, a time-limited session greatly reduces the possibility for students to critically evaluate and integrate information. Often the discussion is between the student and the teacher with limited, if any, sustained interactions between the students. In addition, there is little opportunity for the students to reflect on and respond to comments from the teacher or their peers. Technology-based approaches can be used to address these issues in inquiry learning (*2*). Web technologies such as threaded discussion forums are asynchronous formats that overcome the limitations of synchronous sessions. Because asynchronous discussions allow students to respond to a topic at any time, this feature encourages more thoughtful and in-depth responses (*3*, *4*). Moreover, as the peer-review process for publications and grants uses a similar asynchronous format, we felt this format would be useful for providing students with peer-review experience. Teaching effective peer-review skills is challenging (*5*, *6*) because of the many subtleties that must be considered (see table below, right). We felt that making evaluation of peer review an integral part of an advanced course could enable students to learn an essential professional skill.

Assessing students for breadth of knowledge and peer-review skills also poses challenges. Typical exams in advanced courses ask students to evaluate and design experiments. These exams, however, do not assess key aspects of graduate training, including the student's ability to apply ideas from one field to another, to choose among multiple technologies to answer a specific question, to comment effectively on a peer's approach, or to respond to criticisms of one's own thinking. These deficiencies arise for two reasons: (i) Lack of feedback and responses: Once the exam is handed in, the teacher grades the exams. However, the student cannot respond to the teacher's comments, and the teacher does not evaluate the student for her or his ability to understand and respond to constructive criticisms. (ii) Lack of peer interactions: In the typical exam format, each student deals individually with the teacher and has no knowledge of how his or her peers are thinking, much less the opportunity to comment on and respond to answers by peers. Yet scientists learn from peer interactions and are evaluated by their peers throughout their research careers.

We organize and teach an advanced course on cell signaling systems for second-year graduate students. The course, which began in 1988, originally focused on cell surface signaling molecules (heterotrimeric guanine nucleotide–binding proteins or G proteins). Over the years, as our knowledge of signaling pathways and biological processes has grown, the course has increasingly reflected facets of neuroscience, microbiology, immunology, pharmacology, and cell and developmental biology. This breadth has presented us with challenges and opportunities. Specifically, the breadth of student interests is valuable in peer interactions, because the comments made by the other students can provide useful perspectives that complement and enhance those of the instructors.

Advanced Course in Cell Signaling

Lectures, which cover the major signaling pathways in mammalian cells, are taught by researchers with expertise in the area and are developed from primary literature (*7*). Four discussion forums, in which journal articles are discussed in depth, are interspersed among the lectures. A persistent issue has been evaluating students' understanding of the journal club articles. In 2005, we introduced a format that used classroom presentation and discussion followed by written student responses to questions posted by the lecturer (*8*). Although this format evaluated how each student had understood the papers, the lack of teacher-student feedback and peer interactions in the asynchronous mode precluded prolonged and potentially thoughtful discussions. To address this deficiency, for the final exam we used a Web-based forum that was designed to elicit peer interactions (*9*). In response to the teacher's questions, each student selected a primary publication and described in 200 to 500 words how the experiments in the paper answered the question. The first set of answers was posted on the Web using *Science*'s Signal Transduction Knowledge Environment (STKE) Discussion Forum, identifying students by numbers to maintain anonymity. Each student then wrote brief (less than 250 words), anonymous commentaries on two other students' answers. The original answer and the two commentaries

EFFECTIVE PEER-REVIEW SKILLS

- Identify and evaluate what is new.
- Make criticism constructive and respectful.
- Distinguish between content and style.
- Define terminology; avoid jargon.
- Justify statements with references and logical arguments.

[1]Department of Pharmacology and Systems Therapeutics, [2]Department of Oncological Sciences, and the [3]Immunology Institute, Mount Sinai School of Medicine, New York, NY 10029, USA.

*Author for correspondence. E-mail: ravi.iyengar@mssm.edu

were evaluated to determine each student's final grade. Although the peer commentary feature worked well, this format did not allow students to reply to the critiques and to modify their responses accordingly.

Integrating Journal Clubs, Web Discussion Forums, and Exams

When the course was offered in 2007 (*10*), we integrated the journal clubs, discussion forums, and exams. Each of the four journal clubs was led by two faculty members. Recent primary publications relevant to lectures in the previous section were selected by the faculty and posted on the Web. Students were required to answer several questions related to the papers before the discussion forum. During the classroom session, the teachers called on the students to explain the figures and tables in the papers. This was followed by an open discussion of the papers and the posted questions. The teachers then provided individual written critiques of students' written answers, and students revised their answers to respond to the critiques. The revised answers were posted on the Web with anonymity maintained. The students then posted brief comments on two of their peers' answers using their student number as an identifier. For each of the four discussion forums each student received grades for the original answer, the revised answer, and the peer critiques (*10*).

The technology needed for this integrative project is relatively modest. In 2005, we had used the discussion forum in STKE. In 2007 we used the WebCT software platform from Blackboard Learning System (*11*). This program allows us to post the course contents, to run the discussion forums, and to set up Web links.

Web technologies were useful in assessing the depth and breadth of student knowledge. Because answers were relatively brief, students cited the appropriate literature to justify assumptions and specific experimental approaches. With hyperlinks to the cited references, the teachers could easily evaluate whether the students had understood the papers and used them appropriately. Addition and justification of referencing for the revised version of the answers became a useful tool to assess both integration of breadth and depth and ability to respond to peer review.

Outcomes

We had several major objectives from the student learning perspective: (i) to convey a historical perspective of the key experiments that established canonical signal transduction mechanisms, (ii) to engage the students substantively in a structured dialogue regarding current ideas and experiments, (iii) to enable the students to develop novel approaches to help integrate information, and (iv) to teach and evaluate participation in peer review. The use of team teaching, although challenging from a scheduling perspective, provides the students with a broad, yet personal, perspective of the development of research on the various signaling pathways. Integrating the lectures with classroom-based journal clubs and Web-based discussion forums has allowed us to achieve these goals. An unexpected benefit of the question-and-answer format was making the students aware of Web-based databases and bioinformatics tools useful for organizing information and designing experiments, resources often used by researchers.

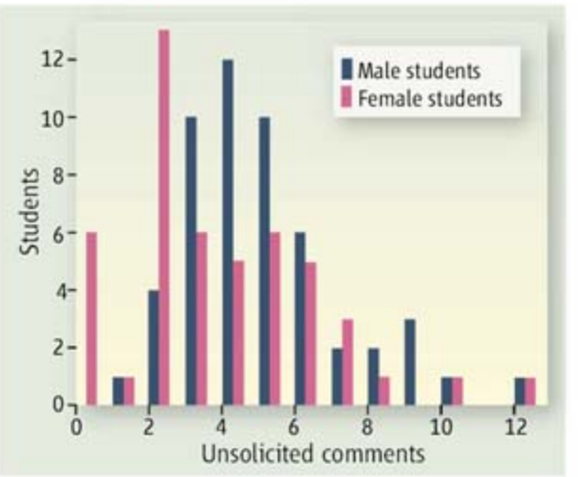

Distribution of the number of unsolicited comments made in classroom discussion forums by male and female students.

A valuable outcome of this integrative project was the ability to document and assess how students integrated breadth of knowledge with depth of reasoning. This was achieved by comparing the original and revised answers, as well as the references used in both answers. The commentaries on answers from their peers were also very useful in assessing the student's integrated learning capability. All of the faculty observed a difference between the classroom discussion, where students mostly did not challenge each others' comments, and the written Web postings where students were respectful but often quite critical of answers from their peers. Anonymity of the Web format and the time provided to think about the Web postings appear to contribute to this critical feedback between peers. We had a nearly even distribution of male and female students in a class of 25, but the female students on average made fewer unsolicited comments in class ($P = 0.03$; see graph, left). We observed only a weak correlation between the number of unsolicited comments made by a student in classroom discussion and the student's grade on the assignment ($R^2 = 0.15$; see SOM). These data gathered over the four discussion forums support our original concern that some of the top students do not speak up in class. The gender divide in voluntary journal club participation in an advanced course is disconcerting and merits further study.

We also examined the students' evaluations of the course, assessed using the school's standard survey instrument. We compared the overall course rating, exam format, and effectiveness of readings for this course to ratings for two other courses with similar formats except for the lack of asynchronous interactions. The cell signaling course ranked better in all three categories [table S1 (*16*)]. This integration project has appeared to work well both from the teachers' and students' perspectives and has struck a practical balance between student-teacher and student-student interactions. In the future, we feel a comparison between instructor critiques and peer critiques would be useful.

References and Notes

1. G. M. Johnson, G. H. Buck, paper presented at the Annual Conference of the American Educational Research Association, Chicago, IL, 9 to 13 April 2007; http://eric.ed.gov/ERICDocs/data/ericdocs2sql/content_storage_01/0000019b/80/28/08/16.pdf
2. D. C. Edelson, D. N. Gordon, R. D. Pea, *J. Learning Sci.* **8**, 391 (1999).
3. R. Branon, C. Essex, *TechTrends* **45**, 36 (2001).
4. M. Teikmanis, J. Armstrong, *Comput Nurs.* **19**, 75 (2001).
5. J. T. Lightfoot, *Adv. Physiol Educ.* **19**, 557 (1998).
6. W. H. Guilford, *Adv. Physiol Educ.* **25**, 167 (2001).
7. R. Iyengar, M. Diverse-Pierluissi, D. Weinstein, L. A. Devi, *Sci. STKE* **2005**, tr3 (2005).
8. D. C. Weinstein, *Sci. STKE* **2005**, tr24 (2005).
9. R. Iyengar, M. Diverse-Pierluissi, D. Weinstein, L. Devi, *Principles of Cell Signaling and Biological Consequences: Final Forum*, *Sci. STKE* (Forum as seen February 2008); http://stke.sciencemag.org/cgi/forum-display/short/stke_el;357.
10. Supporting online materials include the syllabus for the Spring 2007 course, the instructions for the journal club Web-discussion forum, statistical analysis, and survey results. Examples of student answers, teacher critiques; and student comments on the Web can be found at (*12*).
11. Blackboard and WebCT, www.blackboard.com/webct.
12. S. L. Jenkins *et al.*, *Sci. Signal.* **1**, tr2 (2008).
13. The development of this integration project is part of the educational program supported by the Predoctoral Training Grant T32GM062754 from the National Institute of General Medical Sciences, NIH. We thank N. Gough for her encouragement and support over the last 2 years in developing the lectures for the Web and the use of the STKE discussion forum in 2005. We also thank M. Schindler for help with use of the WebCT program and T. Krulwich for her comments on the manuscript.

Supporting Online Material

www.sciencemag.org/cgi/content/full/319/5867/1189/DC1

10.1126/science.1149875

CELL BIOLOGY

No ESCRTs for Exosomes

Two pathways within endosomes use specific protein complexes or membrane domains to direct cargo for degradation or secretion from cells.

Mark Marsh[1] and Gerrit van Meer[2]

Exosomes are small (50 to 100 nm in diameter) membrane-bound vesicles released by a variety of cells. Originally proposed to discard excess transferrin receptor from reticulocytes during red blood cell formation (*1*), exosomes are now thought to play key roles in cell-to-cell communication, antigen presentation, and in the pathogenesis of retroviral infections (including HIV) and prion diseases (*2*–*4*). However, how exosomes are formed has not been clear. On page 1244 in this issue, Trajkovic *et al.* (*5*) provide intriguing insights into exosome formation, making these microvesicles a bit less mysterious but raising many new questions about their biogenesis.

An early view was that exosomes are formed by invagination of the membrane of endosomes (see the figure) to produce intraluminal vesicles, thus rendering these organelles multivesicular bodies (*6*, *7*). Exosomes are then secreted when these multivesicular bodies fuse with the plasma membrane and release their content (*6*). A more recent view holds that exosomes can also form at the plasma membrane in some cell types (*8*). The link between exosomes and multivesicular bodies was strengthened by the discovery of the ESCRT (endosomal sorting complex required for transport) machinery (*9*). This highly conserved set of protein complexes recognizes membrane proteins that are modified with ubiquitin molecules and thus marked for sorting to lysosomes (either as functional components of lysosomes or as substrates for lysosomal proteolysis). ESCRT complexes sort these cargoes to specific domains of endosomes and regulate both the inward invagination of these membrane regions and the scission of invaginated membrane buds to form intraluminal vesicles. Cells that lack components of the ESCRT machinery often have fewer multivesicular bodies or fewer intraluminal vesicles in multivesicular bodies, and fail to deliver cargo to lysosomes (*7*). The ESCRT machinery is also required to complete the topologically related (budding of membrane vesicles away from the cytoplasm) assembly of various enveloped RNA viruses (*10*), including HIV, and to mediate the abscission reactions that complete mammalian cell division (*11*).

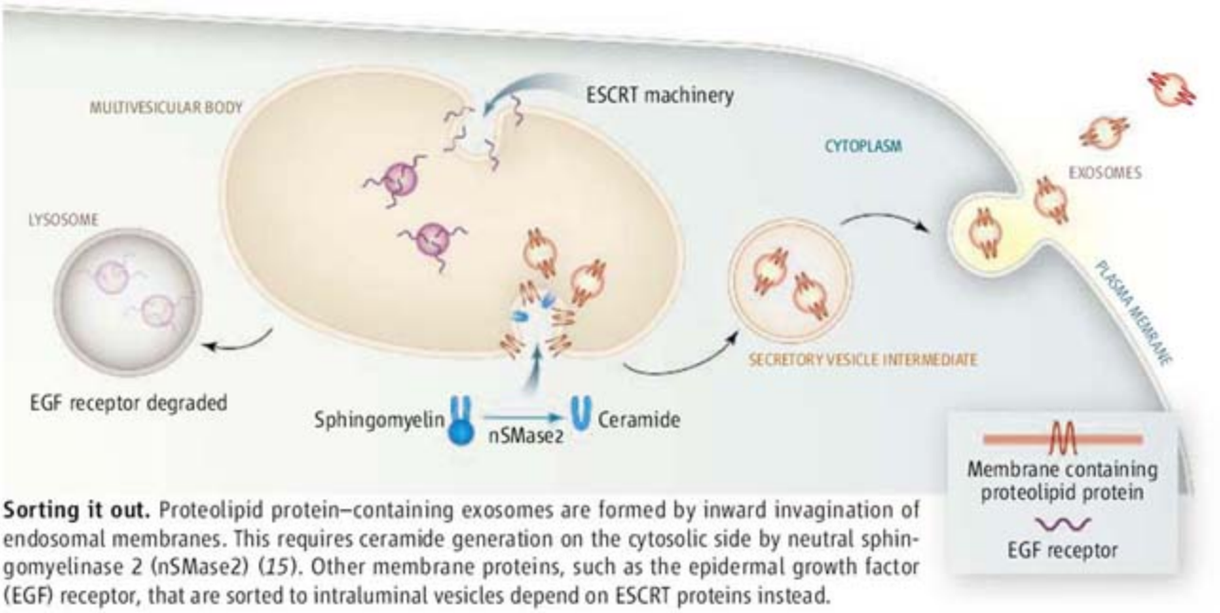

Sorting it out. Proteolipid protein–containing exosomes are formed by inward invagination of endosomal membranes. This requires ceramide generation on the cytosolic side by neutral sphingomyelinase 2 (nSMase2) (*15*). Other membrane proteins, such as the epidermal growth factor (EGF) receptor, that are sorted to intraluminal vesicles depend on ESCRT proteins instead.

It was thus not unreasonable to conjecture that the ESCRT machinery would also be involved in the similar process of exosome formation. Indeed, an ESCRT-associated protein (AIP1/Alix) interacts with transferrin receptors during exosome formation in reticulocytes (*12*). ESCRT proteins are also recruited to proposed sites of exosome formation in lymphocytes (*8*) and are found in exosomes (*3*, *5*). A regulatory role in intraluminal vesicle formation was also suggested based on the inhibition of inward budding in liposomes by the ESCRT protein Alix (*13*). Nevertheless, the role of the ESCRT machinery in exosome formation has remained unclear.

Trajkovic *et al.* used an oligodendrocyte cell line (myelinating cells of the central nervous system) to study the formation and release of exosomes containing proteolipid protein. Proteolipid protein is a major component of myelin, the lipid-rich membrane that oligodendrocytes use to enwrap and insulate axons. They find that formation of proteolipid protein–containing exosomes does not require ESCRT machinery. By contrast, sorting of the epidermal growth factor receptor to lysosomes in these cells is inhibited by depletion of ESCRT components or expression of a dominant-negative form of an ESCRT protein (Vps4).

Morphological analysis of the oligodendrocyte endosomes shows that proteolipid protein segregates into membrane domains that are distinct from domains containing cargo destined for ESCRT-mediated sorting to lysosomes. Trajkovic *et al.* show through mass spectrometric analysis that secreted proteolipid protein–containing exosomes purified from cell culture medium are enriched in ceramide, a lipid produced from the membrane lipid sphingomyelin by sphingomyelinases. Disrupting the expression of neutral sphingomyelinase 2 (nSMase2) by RNA interference or the use of specific inhibitors reduced secretion of proteolipid protein–containing exosomes. Moreover, when Trajkovic *et al.* added a bacterial sphingomyelinase to liposomes containing domains with different degrees of fluidity, budding occurred specifically from the "raft"-like lipid phase. This led them to

[1]Cell Biology Unit, MRC Laboratory for Molecular Cell Biology and Department of Cell and Developmental Biology, University College London, Gower Street, London WC1E 6BT, UK. E-mail: m.marsh@ucl.ac.uk [2]Membrane Enzymology, Bijvoet Center/Institute of Biomembranes, Utrecht University, Padualaan 8, 3584 CH Utrecht, Netherlands. E-mail: g.vanmeer@uu.nl

suggest that ceramide-induced aggregation of lipid microdomains leads to domain-induced inward budding of intraluminal vesicles, perhaps promoted by the cone-shaped structure of ceramide (see the figure).

The observations of Trajkovic *et al.* raise several questions. Morphological experiments indicate that both proteolipid protein–containing exosomes and epidermal growth factor receptor–containing intraluminal vesicles can be formed within the same endosome. Is this the case, or are there functionally distinct populations of endosomes that generate different intraluminal vesicles (*14*)? Also, if both types of vesicles are present in the same multivesicular body, they must somehow be sorted to ensure that only the exosomes are secreted. It is also not clear whether all exosomes are formed through the same molecular mechanism, or if different mechanisms are used for different types of exosome cargo. The Trajkovic *et al.* study shows that secretion of the tetraspanin CD63, another exosome-associated membrane protein, is also blocked by a sphingomyelinase inhibitor, but not by a dominant-negative ESCRT component. If the ceramide-based process is the primary mechanism for exosome formation, it would seem that ESCRT-dependent enveloped viruses have usurped the lysosomal sorting and abscission machinery for assembly, though the idea that the budding of some viruses involves raft domains could also indicate that a combination of the two processes is used.

The presence of ceramide in exosomes may imply its direct role in the lipid-phase organization of the endosomal membrane, whereby the ceramide-enriched phase ends up in the budding vesicle. This is supported by the presence of proteolipid protein—a typical membrane raft component—in exosomes. However, without knowing the lipid composition of the endosomal membrane, one cannot conclude that exosomes originate from a specific membrane domain. Also, without knowing the transbilayer organization or ceramide concentration in the endosomal membrane, the extrapolation of model membrane experiments remains problematic. Whatever the molecular mechanism by which a change in lipid composition drives vesicle budding, the process is likely to be regulated. The present work suggests that a better understanding of lipid metabolism may provide new vistas in exosome research.

References

1. B. T. Pan, R. M. Johnstone, *Cell* **33**, 967 (1983).
2. B. Fevrier *et al.*, *Proc. Natl. Acad. Sci. U.S.A.* **101**, 9683 (2004).
3. W. Stoorvogel *et al.*, *Traffic* **3**, 321 (2002).
4. S. J. Gould, A. M. Booth, J. E. Hildreth, *Proc. Natl. Acad. Sci. U.S.A.* **100**, 10592 (2003).
5. K. Trajkovic *et al.*, *Science* **319**, 1244 (2008).
6. B. T. Pan, K. Teng, C. Wu, M. Adam, R. M. Johnstone, *J. Cell Biol.* **101**, 942 (1985).
7. S. Urbe *et al.*, *J. Cell Sci.* **116**, 4169 (2003).
8. A. M. Booth *et al.*, *J. Cell Biol.* **172**, 923 (2006).
9. M. Babst, *Traffic* **6**, 2 (2005).
10. E. Morita, W. I. Sundquist, *Annu. Rev. Cell Dev. Biol.* **20**, 395 (2004).
11. J. G. Carlton, J. Martin-Serrano, *Science* **316**, 1908 (2007).
12. C. Geminard, A. De Gassart, L. Blanc, M. Vidal, *Traffic* **5**, 181 (2004).
13. H. Matsuo *et al.*, *Science* **303**, 531 (2004).
14. I. J. White *et al.*, *EMBO J.* **25**, 1 (2006).
15. M. Tani, Y. A. Hannun, *J. Biol. Chem.* **282**, 10047 (2007).

10.1126/science.1155750

MATERIALS SCIENCE

New Materials at a Glance

Depositing materials on a substrate at a glancing angle can create new and unusual structures.

Michael J. Brett[1,2] and Matthew M. Hawkeye[1]

Through precise engineering of structure on the nanoscale, researchers can endow a material with remarkably different properties from those of the bulk. A major effort in nanotechnology research is the development of a toolbox of processing techniques for nanostructure fabrication. Recently, materials scientists have looked at glancing angle deposition (GLAD) as an important tool for this task. In this technique, materials are deposited on surfaces at a highly oblique angle, resulting in a flexible and straightforward method of producing nanostructured and porous thin-film materials in unusual configurations.

GLAD is a combination of traditional thin-film vacuum deposition and carefully controlled substrate motion (*1*). During standard film deposition, a stream of vapor-phase atoms strikes a perpendicular substrate. In GLAD, the substrate is tilted far from perpendicular, such that the atoms arrive obliquely. As the atoms condense on the substrate, they agglomerate into microscopic clumps or nucleation sites. Line-of-sight shadowing prevents atoms from condensing in the region immediately behind each nucleus (see the figure, top panel); thus, atoms deposit only on the tops of nuclei (*2*). As deposition continues, the nuclei develop into columnar structures that are oriented toward the vapor source. Increasing the substrate tilt leads to greater separation between columns and a more porous structure.

We can add a new degree of control by rotating the substrate, which changes the apparent location of the vapor source from the perspective of the growing columns. Because the columns grow toward the vapor source, the growth direction of the columns can be controlled. Using the appropriate substrate movements, we can sculpt the columns into different geometries such as chevrons (abrupt 180° rotations), helices (slow continuous rotation), and vertical posts (rapid continuous rotation).

The ability to control the column orientation throughout the thickness leads to a particularly interesting application of GLAD. A tilted column will exhibit optical birefringence: Incident light will experience a different refractive index depending on whether the light is polarized parallel or perpendicular to the column axis (*3*, *4*). Because the optical properties are linked to the orientation of the columns, sculpting the columns into helical shapes will cause the optical properties to vary periodically throughout the thickness of the film. Light will therefore see a periodic medium, creating a polarization-dependent optical diffraction effect analogous to that seen in some liquid crystals (*5*, *6*). Circularly polarized light of the same handedness as the structure will be reflected, whereas the other circular polarization state will pass through. This polarization discrimination acts as a circular polarization filter and could be implemented in display technologies. For such technology to be adopted, efficient polarizers must be developed. Toward this goal, Hodgkinson *et al.* have worked to maximize the birefringence of columnar structures and improve the optical performance of helical films (*7*, *8*).

The ability to create separated columnar

[1]Department of Electrical and Computer Engineering, University of Alberta, Edmonton, Alberta T6G 2V4, Canada. E-mail: brett@ece.ualberta.ca [2]National Research Council of Canada, National Institute for Nanotechnology, Edmonton, Alberta T6G 2E1, Canada.

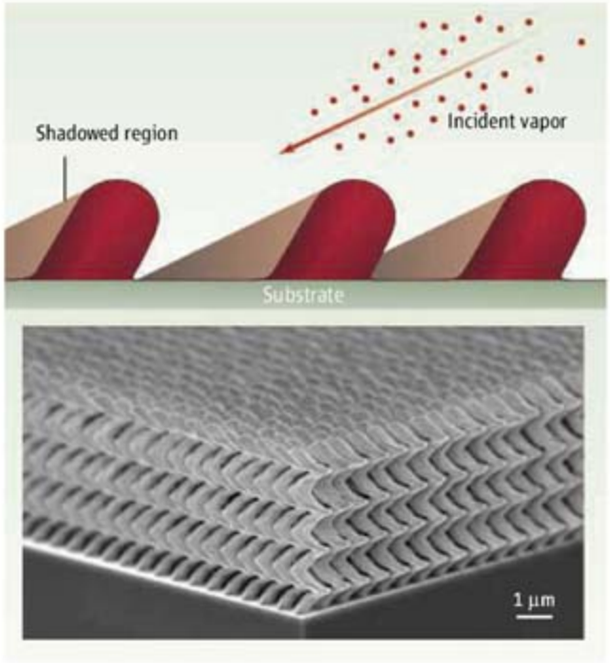

Oblique strategies. (**Top**) A conceptual view of column growth. Incident vapor atoms are blocked from the shadowed regions by the developing columns. As a result, deposition is restricted to the tops of the nuclei, which grow toward the vapor source. (**Bottom**) Scanning electron microscope image of a microstructured surface. By rotating the substrate, silicon columns have been sculpted into a square spiral configuration. Such an arrangement is useful for photonic crystal devices.

microstructures with GLAD also leads to novel devices. For instance, there is an obvious visual similarity between a film of helical columns and a bed of springs. The microstructured helices also exhibit the mechanical spring behavior of their macroscopic counterparts (*9*). Electrically controlled squeezing of microhelices has been elegantly demonstrated. By passing a current through cobalt-coated silicon helices, Singh *et al.* induced an attractive force between adjacent coils and compressed the structure (*10*). Dice *et al.* sandwiched helices between aluminum layers in a parallel-plate capacitor arrangement (*11*). Charging the plates creates an electrostatic force and squeezes the microsprings. The ability to actuate such small structures could find use as stand-alone resonant devices or when integrated into microelectromechanical systems (MEMS).

The GLAD process allows the fabrication of submicrometer columnar structures over a macroscopic area in a single processing step. Because the nucleation process is stochastic, the columns grow randomly over the surface. For the majority of applications, it is not detrimental to have randomly arranged columns. Certain devices, however, have stringent requirements on column location and uniformity. In the three-dimensional photonic crystal architecture proposed by Toader and John (*12*), identical square spiral columns must be arranged in a tetragonal lattice. To defeat the randomness inherent in the nucleation process, the substrate is patterned (via lithographic techniques) with a seed nuclei template before deposition. Properly spaced, these seeds initiate the shadowing process and columns grow at the seed site only (*13*, *14*). Control over the planar arrangement of columns is therefore achieved, as is greater uniformity among the columnar structures (see the figure, bottom panel). Following this procedure, Jensen and one of us (M.J.B.) demonstrated the existence of a three-dimensional photonic band gap in the important telecommunications window near the infrared 1.6-μm wavelength (*15*). With GLAD, we can precisely fabricate complex structures over large areas, making it competitive with other photonic crystal fabrication techniques.

A major advantage of the GLAD process is its compatibility with many materials. Dielectrics, metals, semiconductors, and organic materials capable of fabrication by physical vapor deposition are suited to the GLAD process for engineering microstructure. However, applications requiring high surface area and porosity can make use of the many materials generated by simpler chemical means. GLAD will find its niche in devices requiring both a porous material and a precisely engineered microscale architecture.

References

1. M. M. Hawkeye, M. J. Brett, *J. Vac. Sci. Technol. A* **25**, 1317 (2007).
2. H. König, G. Helwig, *Optik* **6**, 111 (1950).
3. L. Holland, *J. Opt. Soc. Am.* **43**, 376 (1953).
4. T. Motohiro, Y. Taga, *Appl. Opt.* **28**, 2466 (1989).
5. A. Lakhtakia, W. S. Weiglhofer, *Proc. R. Soc. London Ser. A* **448**, 419 (1995).
6. K. Robbie, M. J. Brett, A. Lakhtakia, *Nature* **384**, 616 (1996).
7. I. Hodgkinson, Q. H. Wu, *Adv. Mater.* **13**, 889 (2001).
8. L. De Silva, I. Hodgkinson, *J. Vac. Sci. Technol. A* **25**, 1118 (2007).
9. C. Gaire, D.-X. Ye, T.-M. Lu, G.-C. Wang, R. C. Picu, *J. Mater. Res.* **23**, 328 (2008).
10. J. P. Singh *et al.*, *Appl. Phys. Lett.* **84**, 8657 (2004).
11. G. D. Dice, M. J. Brett, D. Wang, J. M. Buriak, *Appl. Phys. Lett.* **90**, 253101 (2007).
12. O. Toader, S. John, *Science* **292**, 1133 (2001).
13. D.-X. Ye, T.-M. Lu, *Phys. Rev. B* **76**, 235402 (2007).
14. C. M. Zhou, D. Gall, *Appl. Phys. Lett.* **90**, 093103 (2007).
15. M. O. Jensen, M. J. Brett, *Opt. Express* **13**, 3348 (2005).

10.1126/science.1153910

PHYSICS

Complexity in Fusion Plasmas

Peter A. Norreys

Images of imploding fusion plasmas reveal complex electric and magnetic field structures.

The November 2007 report by the United Nations Intergovernmental Panel on Climate Change concluded that the changes in climate worldwide were most likely due to rising greenhouse gas emissions. Strategies are urgently needed to reduce these emissions, and there is a clear need for nonpolluting, environmentally safe alternatives to the burning of fossil fuels for electricity generation. One possibility is fusion energy, where the by-products of the thermonuclear reaction are helium and neutrons. Among the proposals for fusion energy, reactions in laser-compressed plasmas have garnered substantial attention and resources. The plasma produced this way, however, can be complex and unstable. On page 1223, Rygg *et al.* have found a way to make detailed images of the density and electric field structures in these extreme environments (*1*), information that is necessary for better control of the reactions.

Research over the past 50 years has shown that achieving energy gain from fusion reactions (that is, more energy out than in) is a lot more difficult than was originally envisaged. The principal reason is that the fusion fuel has to be heated to

Central Laser Facility, Rutherford Appleton Laboratory, Chilton, Oxfordshire OX11 0QX UK. E-mail: p.a.norreys@rl.ac.uk

Fast ignition. In the fast ignition approach to inertial confinement fusion (from top to bottom), symmetrically arranged lasers first compress the spherical fuel target to high density. Then another laser focused on the tip of a gold cone generates energetic electrons that heat the hot spot in the compressed fuel to ignition temperatures.

temperatures of a hundred million degrees centigrade so that the ions have sufficient kinetic energy to overcome the repulsive electrostatic barrier and their nuclei can fuse. The combined mass of the fusion products is lower than that of original fuel, and the difference is given out as kinetic energy of the fusion products.

Clearly, no vessel can withstand these temperatures, so the fuel has to be confined in some manner to prevent contact with the reactor walls. One method is to confine the fusion fuel at relatively low densities by means of strong magnetic fields for a long time—the magnetic confinement fusion approach (*2*). An alternative, inertial confinement fusion, relies on the compression of a hollow, millimeter-sized shell containing the fusion fuel to ultrahigh densities, either directly with a symmetrical array of nanosecond-duration laser pulses (*3*) or indirectly by placing the shell inside a radiation cavity, converting the laser energy to soft x-rays, and using that radiation to drive the implosion (*4*). One can think of these two alternative approaches to fusion energy as being analogous to the conventional furnace and the internal combustion engine.

At the start of the laser pulse in direct drive, the electric field strength at the surface of the pellet is enormous—many millions of volts per centimeter. The material is ionized within one or two oscillations of the laser electric field. The ionized electrons and ions—or plasma—are heated to millions of degrees centigrade, and pressures of millions of atmospheres are generated. The plasma then rapidly expands into the vacuum, and momentum conservation demands that the shell starts to implode—the rocket effect. Eventually, the internal pressure prevents further compression of the fuel (at the stagnation point) and a fusion burn ignites and propagates through the compressed fuel.

The direct- and indirect-drive approaches rely on ignition by a central spark generated by the collapse of a number of accurately timed shock waves at the center of the fuel at stagnation. Matter is heated to higher temperatures behind the shock front, and thus a considerable amount of energy is needed to compress the material to the ultrahigh densities needed for fusion energy gain.

"Fast ignition" is a less mature approach but has received considerable worldwide interest since it was first proposed by Tabak *et al.* (*5*). The scheme allows the separation of fuel compression and the heating of the spark region to ignition temperatures (see the figure). It relies on the generation of a large number of MeV electrons when a petawatt laser pulse is focused into the tip of a cone placed very close to the stagnation point (*6*, *7*). The fast electrons do not have far to propagate, and they heat the matter to the ignition temperature so quickly that the plasma does not have time to respond.

The real beauty of the idea is that the symmetry requirements are relaxed and higher gain can be obtained for less drive energy. However, the exact degree of uniformity needed for the compression of the fuel for direct-drive fast ignition remains an issue. In their remarkable new observations, Rygg *et al.* have compressed cone-attached hollow shell targets. They used 36 beams of the OMEGA laser facility at the University of Rochester to drive the implosions. Radiographs were made using monoenergetic proton fusion products generated in a second implosion target, placed 1 cm away. They unequivocally show that magnetic field structures of 60 T are generated between the ablation front (where the material is evaporated) and the critical density surface (where the laser energy is either absorbed or reflected), with a modulation period of ~150 μm. They also show for the first time that there is an electric field generated as a result of a pressure gradient near the ablation front.

The authors attribute the magnetic field structures to a hydrodynamic instability that is seeded during the early stages of the implosion (caused by plasma density variations) or to the development of instabilities caused by heat flow. It is not clear at this stage which is the answer; more experiments are needed to clarify the generation mechanism. If the magnetic field is due to the early stage hydrodynamic instability, then the new method of "adiabat pulse-shaping" may be able to mitigate the effects (*8*). This new method has recently been shown to work for fully symmetrically irradiated targets. The idea is to irradiate the pellet with a short, intense laser pulse that creates a shock that propagates through the outer shell but whose strength decreases as it progresses. It has the effect of lowering the ablation front density while increasing the ablation velocity and shell thickness, thereby reducing the growth of the hydrodynamic instability. If the heat-flow instabilities are the cause, then other solutions must be considered. Whatever the outcome, Rygg *et al.* have developed a powerful new tool to study the growth and structure of these fields and strategies to reduce them.

References

1. J. R. Rygg *et al.*, *Science* **319**, 1223 (2008).
2. ITER project, www.iter.org.
3. J. Nuckolls, L. Wood, L. Thiessen, G. Zimmerman, *Nature* **239**, 139 (1972).
4. J. Lindl, *Phys. Plasmas* **2**, 3933 (1995).
5. M. Tabak *et al.*, *Phys. Plasmas* **1**, 1626 (1994).
6. R. Kodama *et al.*, *Nature* **412**, 798 (2001).
7. R. Kodama *et al.*, *Nature* **418**, 933 (2002).
8. C. D. Zhou *et al.*, *Phys. Rev. Lett.* **98**, 025004 (2007).

10.1126/science.1155621

CHEMISTRY

An Enlightening Structure-Function Relationship

Mutation and structural data elucidate distinct mechanisms by which different antibodies bind and induce luminescence of dye molecules.

Bruce A. Armitage[1] and Peter B. Berget[2]

Small-molecule cofactors are widely used in biological systems to augment or alter the function of a biomolecular partner. For example, cofactors participate in electron-transfer reactions catalyzed by redox enzymes. In 2000, Simeonov *et al.* inverted this paradigm, reporting a system in which proteins (specifically, monoclonal antibodies) acted as cofactors for activating the fluorescence of a small molecule (a *trans*-stilbene derivative) (*1*). The resulting complexes have since been used to make fluorescent biosensors for various analytes. On page 1232 of this issue, Debler *et al.* (*2*) reveal a fascinating relation between the structure of the antibody-stilbene complex and the mechanism by which emission is enhanced.

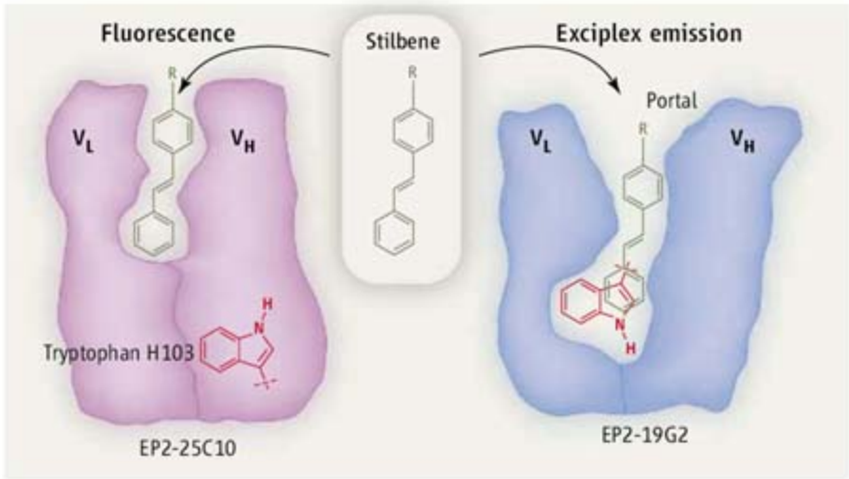

Structure and function. The same fluorogenic dye molecule is bound by two antibodies in different ways, leading to different emission mechanisms and colors. (**Left**) The EP2-25C10 antibody binds the dye in a shallow pocket, and purple fluorescence is enhanced due to the conformational constraints. (**Right**) The EP2-19G2 antibody binds the dye in a much deeper pocket that allows π stacking with a tryptophan residue. An exciplex is formed after excitation, and charge recombination leads to blue luminescence.

The original paper (*1*) and a subsequent report from the same group (*3*) yielded a catalog of antibody-stilbene complexes emitting blue, purple, or green wavelengths of light. In most cases, the monoclonal antibody simply provided a constrained environment to inhibit photoisomerization of the stilbene (*4*), leading to strong fluorescence. The exception was the blue-emitting complex. Here, steady-state and time-resolved experiments indicated that enhanced emission resulted not only from constraining the dye, but also from the formation of an excited-state complex. A crystal structure suggested that this "exciplex" forms between the stilbene and a π-stacked tryptophan residue (Trp^{H103}) located at the deepest point in the binding pocket.

Debler *et al.* have now mutated residues in the stilbene-binding pocket and analyzed the impact on the emission properties. As expected, mutation of Trp^{H103} to phenylalanine (Trp^{H103} → Phe) eliminated exciplex emission without reducing the affinity of the protein for stilbene. In contrast, a Tyr^{L34} → Phe mutant retained exciplex emission, albeit with lower intensity. In the crystal structure of the complex, Tyr^{L34} lies perpendicular to the stilbene and evidently helps to hold it in place stacked against Trp^{H103}. Presumably, replacing the tyrosine OH with an H in phenylalanine sufficiently alters the structure to weaken exciplex formation.

In an exciplex, some charge transfer takes place between the two components; in the extreme case, complete transfer of an electron yields a contact radical ion pair (*5*). This property of exciplexes introduces a subtle but important point: Because the ion pair is an excited-state species, emission results from charge recombination, as opposed to simple relaxation of a locally excited state.

To elucidate the mechanisms by which stilbene luminescence is activated by the two types of antibodies, the authors turned to high-resolution structural analysis of antibody-stilbene cocrystals. In the exciplex-forming antibody, EP2-19G2, the hydrophobic stilbene-binding pocket is deep within the antibody, between the V_H and V_L domains (see the figure, right panel). The Trp^{H103} that forms the exciplex is highly conserved and normally participates in contacts between two domains that stabilize the antibody fold. For this amino acid to form an exciplex with the stilbene, the interface between the two domains must rearrange. This interdomain distortion generates a surface depression that creates a portal to the deep binding pocket [see figure 2B in (*2*)].

The crystal structures of the green and purple antibody-stilbene complexes, which do not show exciplex emission, reveal a binding pocket that is also quite hydrophobic but at least 0.6 nm shallower. There is no distortion of the V_H/V_L interface and no surface depression or portal to the stilbene-binding pocket [see the figure, left panel, and figure 2A in (*2*)]. With no long portal in the green and purple antibodies, stilbene is unable to approach the Trp^{H103}, and no exciplex emission occurs.

EP2-19G2 has been used in several biosensor applications, including fluorescent labeling of DNA that was modified with stilbene dyes (*6*), high-throughput screening of chiral catalysts (*7*), discrimination of small-molecule stereoisomers (*8*), and detection of mercury (*9*). These sensors exploit the unique structural features of the antibody, i.e. the depth and shape of the portal leading to the stilbene-binding pocket.

Other biomolecules such as nucleic acid aptamers (*10*) and single-chain variable-fragment antibodies (scFvs) (*11*) can selectively bind fluorogenic dyes and enhance their fluorescence by a factor of more than 1000. Because there is no evidence for exciplex formation, these cases are analogous to the green and purple antibody-stilbene complexes. In the case of the scFvs that bind thiazole orange and malachite green, considerable spectral tuning and improved binding affinity was generated through directed evolution (*11*). This approach could be used to generate stilbene-binding scFvs with improved affinity, higher fluorescence quantum yields, or more diverse colors. Such modified biomolecules could find applications in fluorescence imaging and sensing.

[1]Department of Chemistry and Molecular Biosensor and Imaging Center (MBIC), Carnegie Mellon University, Pittsburgh, PA 15213, USA. E-mail: army@cmu.edu
[2]Department of Biological Sciences and MBIC, Carnegie Mellon University, Pittsburgh, PA 15213, USA. E-mail: berget@cmu.edu

The discovery of the exciplex-forming antibody was fortuitous in that immunization and in vivo selection were based solely on binding to the stilbene antigen, not on activation of emission. Methods that allow direct selection of luminescent scFvs—for example, by flow cytometry (*11*)—would be more efficient and might even allow discrimination between normal fluorogenic and exciplex-forming scFvs as a result of the different emission properties expected for such protein-dye complexes.

References

1. A. Simeonov *et al.*, *Science* **290**, 307 (2000).
2. E. W. Debler *et al.*, *Science* **319**, 1232 (2008).
3. F. Tian *et al.*, *Angew. Chem. Int. Ed.* **45**, 7763 (2006).
4. J. Saltiel, Y.-P. Sun, in *Photochromism: Molecules and Systems*, H. Dürr, H. Bouas-Laurent, Eds. (Elsevier, New York, 1990), pp. 64–162.
5. S. L. Mattes, S. Farid, *Science* **226**, 917 (1984).
6. G. F. Kaufmann *et al.*, *Angew. Chem. Int. Ed.* **44**, 2144 (2005).
7. M. Matsushita *et al.*, *Angew. Chem. Int. Ed.* **42**, 5984 (2003).
8. H. Matsushita *et al.*, *Mol. Biosyst.* **1**, 303 (2005).
9. M. Matsushita, M. M. Meijler, P. Wirsching, R. A. Lerner, K. D. Janda, *Org. Lett.* **7**, 4943 (2005).
10. J. R. Babendure, S. R. Adams, R. Y. Tsien, *J. Am. Chem. Soc.* **125**, 14716 (2003).
11. C. Szent-Gyorgyi *et al.*, *Nat. Biotechnol.* **26**, 235 (2007).

10.1126/science.1155093

GENOMICS

Reconstruction of the Genomes

Advances in DNA sequencing and synthesis technologies are making it possible to read and write entire genomes.

Drew Endy

"I am the family face; flesh perishes, I live on, projecting trait and trace through time to times anon, and leaping from place to place over oblivion." So starts the poem *Heredity* by Thomas Hardy, whose protagonist personifies the observation that all life exists through a process of direct descent from one generation to the next. Scientifically, the replication and propagation of genetic material, as DNA or RNA, is the primary mechanism by which each generation transmits the instructions underlying the traits and traces of their offspring. On page 1215 of this issue, Gibson *et al.* (*1*) bypass nature's constraint of direct descent by combining information and raw chemicals to construct the entire set of genetic material, or genome, encoding a bacterium (see the figure). This first construction of a genome encoding a self-reproducing organism heralds important opportunities in both genetics and biotechnology, highlights the need for improved DNA construction technology, and reinforces the value of ongoing public discussion of the impacts of making organisms easier to engineer.

Gibson *et al.* used a multistage process to construct the genome of *Mycoplasma genitalium*. First, information defining the 582,970–base pair (bp) DNA sequence of the genome to be synthesized was obtained from a computer database and divided into shorter sections, or cassettes of DNA up to ~7000 bp long. Commercial DNA suppliers then constructed these cassettes. Raw chemicals derived from sugar cane were combined to synthesize specific oligonucleotides, short fragments of DNA up to several hundred base pairs long (*2*). The suppliers then combined subsets of oligonucleotides to produce the requested cassettes (*3*). Gibson *et al.* used a hierarchical scheme to assemble, check, and, as needed, repair ever-longer DNA fragments, eventually producing the full-length genome.

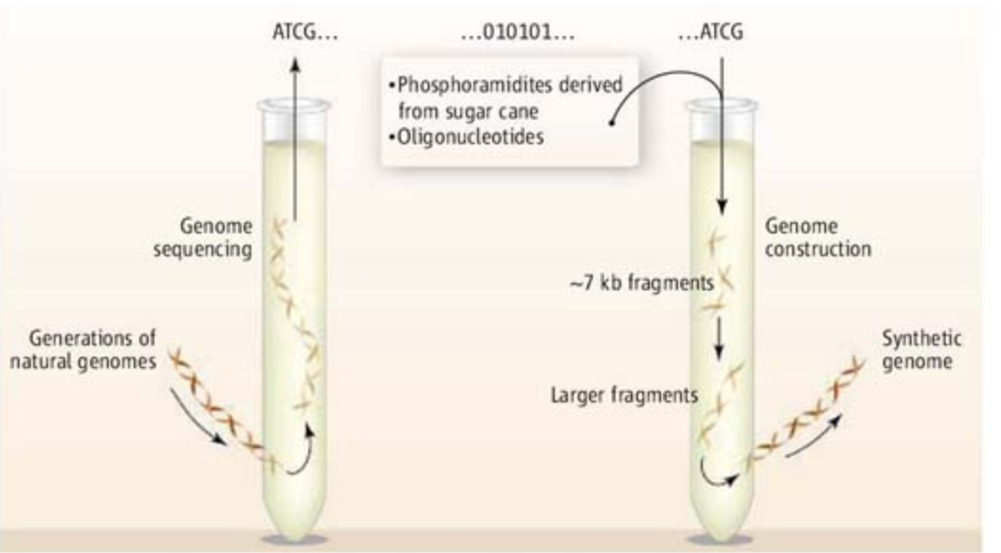

Genome construction. DNA sequencing technology decodes the genome of an organism. DNA synthesis and genome construction technologies enable the opposite process. Bacterial genomes can be built from DNA sequence information and raw chemicals.

Given that all life is encoded by genetic material, ongoing and future advances in DNA synthesis and genome construction technology will be important. For example, the U.S. National Institutes of Health is estimated to spend ~$1.5 billion annually supporting the manual manipulation of DNA (*4*). Such work consumes most of the experimental effort for many biologists and biological engineers, a hidden opportunity cost that is harder to quantify. Moreover, the required slavish mastery of ad hoc methods and tedious tools for DNA manipulation discourages most students and researchers in fields such as physics, electrical engineering, and computer science from exploring biomedical and biotechnology research. Thus, an improved ability to provide any DNA molecule quickly, reliably, and economically would enhance and expand life sciences and engineering research (*5*), and might well become the goal of well-coordinated public research programs. Unfortunately, no such programs exist today.

Meanwhile, consider that most early discoveries of genetically encoded functions depended on analysis of the linkage between natural or randomly generated mutations and phenotypes (*6*), a powerful approach akin to blindly smashing many cars with a hammer and then determining which broken parts matter by attempting to drive each machine. Over the past 30 years, the invention (*7*) and development (*8*) of DNA sequencing technology have provided a complementary approach for discovering genetic functions. By comparing DNA sequence information from different organisms, researchers can

Biological Engineering Department, Massachusetts Institute of Technology, Cambridge, MA 02139, USA. E-mail: endy@mit.edu

CREDIT: ADAPTED FROM DREW ENDY

now identify sequences that have remained relatively constant throughout millions of years of evolution (*9*). The presence of a DNA sequence across distantly related organisms implies that disruption of the sequence via an evolutionary "hammer" would have produced a deleterious effect on the organism, and thus the conserved sequence likely encodes an important function.

However, two additional approaches are needed to confirm and exhaustively identify all functions encoded by a natural DNA sequence. Specific DNA sequences thought to affect phenotypes must be purposefully changed and the expected effect confirmed. Also, seemingly irrelevant DNA sequences must be removed, disrupted, or otherwise modified and shown to be unnecessary. To date, the application of these additional approaches has been limited to short DNA sequences (*10*) or well-studied organisms (*11*). In developing their genome construction methods, Gibson *et al.* are hoping to more readily explore whether genes that can be individually disrupted (*12*) might also be disrupted in combination. Going forward, the ability to implement many simultaneous and directed changes to natural DNA sequences (*13*) and to build and test synthetic systems (*14*) will give researchers a powerful new "hammer" for constructing how life works.

The 582,970-bp "synthetic" genome produced by Gibson *et al.* also unequivocally demonstrates that it is now possible to construct the genomes for all known human viruses, including strictly regulated pathogens (such as smallpox), from publicly available DNA sequence data, methods, and materials. For now, the process of genome construction, as well as the production of an infectious agent given a newly synthesized but inert genome, requires highly skilled experts and considerable resources (Gibson *et al.* must still demonstrate that their synthesized genome will encode a living bacterium). In the meantime, recent international efforts to establish and coordinate best safety and security practices among competing DNA suppliers can be celebrated and improved (*15*). And, new efforts might focus on developing professional societies and improved standards of practice among biological engineers.

References

1. D. G. Gibson *et al.*, *Science* **319**, 1215 (2008); published online 24 January 2008 (10.1126/science.1151721).
2. Y. Sanghvi, *A Roadmap to the Assembly of Synthetic DNA from Raw Materials*, http://hdl.handle.net/1721.1/39657 (2007).
3. S. J. Kodumal *et al.*, *Proc. Natl. Acad. Sci. U.S.A.* **101**, 15573 (2004).
4. H. Bügl *et al.*, *A Practical Perspective on DNA Synthesis and Biological Security*, http://dsspace.mit.edu/bitstream/1721.1/40280/1/PPDS.pdf (2006).
5. D. Baker *et al.*, *Sci. Am.* **294**, 44 (June, 2006)
6. F. W. Studier, R. Hausmann, *Virology* **39**, 587 (1969).
7. F. Sanger *et al.*, *Proc. Natl. Acad. Sci. U.S.A.* **74**, 5463 (1977).
8. R. Carlson, *Biosecur. Bioterror.* **1**, 203 (2003).
9. G. Bejerano *et al.*, *Science* **304**, 1321 (2004).
10. T. D. Schneider, G. D. Stormo, *Nucleic Acids Res.* **17**, 659 (1989).
11. A. W. Murray, J. W. Szostak, *Nature* **306**, 189 (1983).
12. C. A. Hutchison *et al.*, *Science* **286**, 2165 (1999).
13. L. Y. Chan *et al.*, *Mol. Syst. Biol.* **1**, 2005.0018 (2005).
14. M. B. Elowitz, S. Leibler, *Nature* **403**, 335 (2000).
15. H. Bügl *et al.*, *Nat. Biotechnol.* **25**, 627 (2007).

10.1126/science.1155749

CHEMISTRY

Getting Specific About Specific Ion Effects

Recent studies are shedding light on the mechanisms that drive the properties of salt solutions.

Douglas J. Tobias and John C. Hemminger

Have you noticed that "lite" salt, which is a mixture of KCl and NaCl, tastes slightly different from ordinary table salt, which is essentially pure NaCl? If so, then you have experienced a specific ion effect. Such effects are ubiquitous in chemical and biochemical processes involving salt solutions and have traditionally been attributed to the influence of the salt ions on the structure of water. Yet, a surge of recent research has provided compelling evidence that we should instead think about these phenomena in terms of specific ion interactions with surfaces and influences on hydrophobic interactions (*1*–*5*).

In the 1880s, Hofmeister and co-workers investigated the relative ability of different salts to precipitate proteins from blood serum and egg whites (*6*). The work resulted in the following ranking for anions: $SO_4^{2-} > F^- > HPO_4^{2-} > CH_3COO^- > Cl^- > Br^- > NO_3^- > I^- > ClO_4^- > SCN^-$. Ions on the left side of this Hofmeister series salt out (precipitate) solutes, whereas ions on the right salt in (dissolve or denature) solutes. An analogous series can be constructed for cations. Similar trends have been found in many solution properties (*7*, *8*), including surface tensions, chromatographic selectivity, colloid stability, and protein denaturation temperatures. It is widely held that Hofmeister series reflect specific ion effects on the long-range structure of water: Ions on the left are structure makers, ions on the right structure breakers.

Two recent studies (*1*, *2*) mount a strong case against this structure maker/breaker concept. Smith *et al.* (*1*) analyzed Raman spectra of water OH vibrations in potassium halide solutions. The position of the band centers and the line shapes of OH vibrational spectra are sensitive to details of the hydrogen-bonding network. Spectra of fluoride solutions are slightly blue-shifted compared with neat water, whereas solutions of the heavier halides are red-shifted. These effects were previously explained in terms of the structure-making and -breaking abilities of these ions. Using Monte Carlo simulations, Smith *et al.* show that the different halide ions do produce spectroscopically distinct changes to water hydrogen bonding, but these perturbations are largely confined to the first solvation shell. This result is consistent with an earlier spectroscopic study of the dynamics of halide ion solvation shells (*9*).

Mancinelli *et al.* found contradictions in the structure maker/breaker concept in a neutron diffraction study of NaCl and KCl solutions (*2*). According to the conventional Hofmeister series for cations, both Na^+ and K^+ are water-structure breakers. Yet, the analysis of the diffraction data suggested that, whereas water molecules are more orientationally disordered around the K^+ ion, Na^+ is more tightly solvated and more disruptive to water-water correlations.

Clues to more accurate explanations for specific ion effects are emerging from studies of the behavior of ions near interfaces.

Department of Chemistry and Atmospheric Integrated Research for Understanding Chemistry at Interfaces (AirUCI) Environmental Molecular Sciences Institute, University of California, Irvine, Irvine, CA 92697, USA. E-mail: dtobias@uci.edu; jchemmin@uci.edu

For example, molecular dynamics simulations have predicted that the propensity for anions to adsorb to the air-water interface follows an inverse Hofmeister series ($SO_4^{2-} < NO_3^- < I^-$) (see the first figure) and is correlated with specific ion effects on surface tensions and surface potentials (*10*). These predictions have been confirmed by spectroscopic measurements (*11*–*14*). The results suggest that specific ion effects could reflect differences in the hydration of ions near surfaces (for example, the air-water interface or biomolecular surfaces) compared to the bulk solution.

This hypothesis was supported by recent studies. In a thermodynamic surface-bulk partitioning model, Pegram and Record (*3*) have found a good correlation between the propensity of ions to adsorb to the air-water interface and the effect of these ions on processes that involve protein surface hydration. Consistent with this analysis, Chen *et al.* have provided experimental evidence for changes in the hydration of ions when they interact with protein-like polymers at the air-water interface (*4*). In the case of cations, Pegram and Record did not find a similar correlation, probably because cations do not adsorb to the bare air-water interface (*3*). Inorganic cations are generally excluded from the air-water interface (*10*) and sit below the surface even in the presence of strongly adsorbing anions, such as I^- (see the first figure, bottom panel). However, recent x-ray photoemission experiments and molecular dynamics simulations have shown that surfactants containing polar groups can draw cations into the interfacial layer (*15*) (see the second figure).

About 10 years ago, Baldwin argued that specific ion effects on protein stability could be described in terms of the ability of ions to salt in the polar peptide group and salt out the nonpolar side chains (*16*). At first glance, it seems plausible that salting-out ions strengthen hydrophobic interactions, whereas salting-in ions decrease them. Yet, a recent study suggests that specific ion effects on hydrophobic interactions are more complicated (*5*). In simulations of hydrophobic solutes in salt solutions, the propensity of the solutes to aggregate (salt out) increased with increasing ion charge density, as expected. However, ions of low charge density could induce salting out or salting in, depending on concentration. Low-charge-density ions can form complexes with the hydrophobic species, forming micelle-like aggregates at low ion concentration and soluble, surfactant-like complexes at high ion concentration. Thus, salt effects on hydrophobic interactions result from a subtle balance of ion-solute and ion-water interactions.

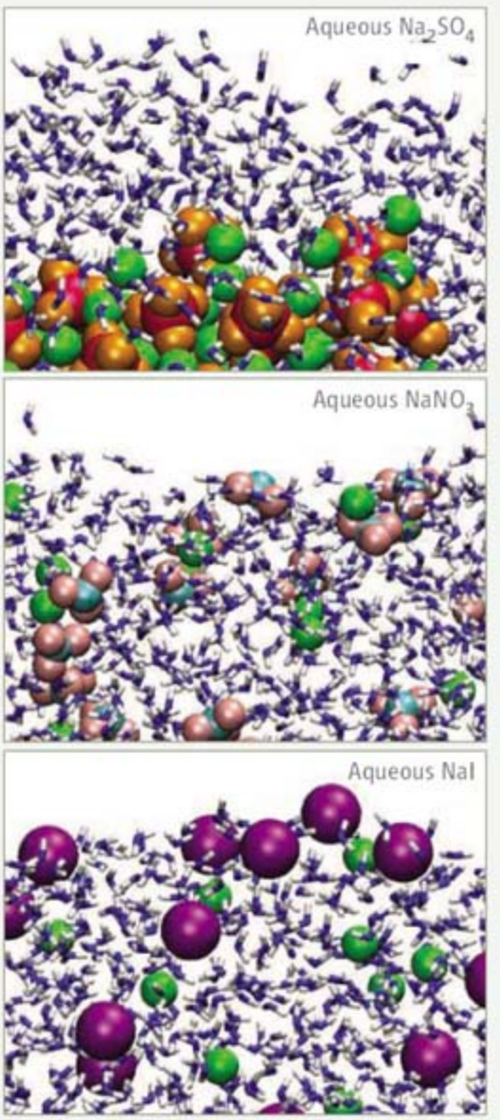

Specific ion effects at the air-water interface. In snapshots from molecular dynamics simulations of air-solution interfaces of aqueous solutions (*10, 11, 18*), some ions accumulate near the interface, whereas others avoid the interface. Atom colors: Water O, blue; Na, green; S, magenta; sulfate O, orange; N, cyan; nitrate O, pink; I, purple.

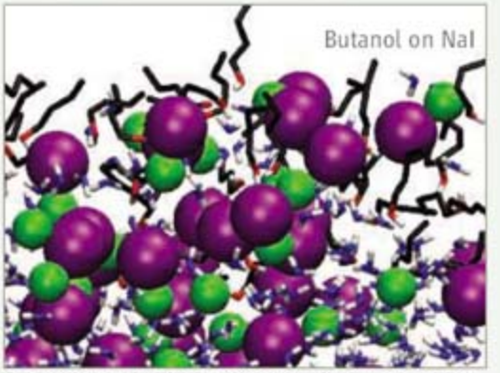

Specific interactions between ions and surfactants (*15*). The large enhancement of anions over cations at the interface in neat aqueous NaI (see the first figure, bottom panel) is suppressed when the surfactant butanol is present (this figure). Coloring as in the first figure, except butanol C, black; butanol O, red.

The existence and widespread applicability of Hofmeister series suggest an underlying simplicity. Yet, specific ion effects continue to defy all-encompassing theories. Fruitful directions for further research include the exploration of salt effects on hydrophobic interactions and the characterization of specific ion interactions with polar groups. For complex solutes such as proteins in salt solutions, hydrophobic and electroselective interactions appear to be intertwined (*17*). Techniques are available for interface-specific experiments that directly probe specific ion interactions, coupled with appropriate theory and simulations. It looks like scientists will remain immersed in salt water for some time.

References and Notes

1. J. D. Smith, R. J. Saykally, P. L. Geissler, *J. Am. Chem. Soc.* **129**, 13847 (2007).
2. R. Mancinelli, A. Botti, F. Bruni, M. A. Ricci, A. K. Soper, *J. Phys. Chem. B* **109**, 13570 (2007).
3. L. M. Pegram, M. T. Record Jr., *J. Phys. Chem. B* **111**, 5411 (2007).
4. X. Chen, T. Yang, S. Kataoka, P. S. Cremer, *J. Am. Chem. Soc.* **129**, 12272 (2007).
5. R. Zangi, M. Hagen, B. J. Berne, *J. Am. Chem. Soc.* **129**, 4678 (2007).
6. F. Hofmeister, *Arch. Exp. Path. Pharmakol.* **XXV**, 1 (1888).
7. K. D. Collins, M. W. Washabaugh, *Quart. Rev. Biophys.* **18**, 323 (1985).
8. W. Kunz, P. Lo Nostro, B. W. Ninham, *Curr. Opin. Coll. Int. Sci.* **9**, 1 (2004).
9. A. W. Omta, M. F. Kropman, S. Woutersen, H. J. Bakker, *Science* **301**, 347 (2003).
10. P. Jungwirth, D. J. Tobias, *Chem. Rev.* **106**, 1259 (2006).
11. S. Gopalakrishnan, P. Jungwirth, D. J. Tobias, H. C. Allen, *J. Phys. Chem. B* **109**, 8861 (2005).
12. S. Gopalakrishnan *et al.*, *Chem. Rev.* **106**, 1155 (2006).
13. P. B. Petersen, R. J. Saykally, *Annu. Rev. Phys. Chem.* **57**, 333 (2006).
14. S. Ghosal *et al.*, *Science* **307**, 563 (2005).
15. M. J. Krisch *et al.*, *J. Phys. Chem. C* **111**, 13497 (2007).
16. R. L. Baldwin, *Biophys. J.* **71**, 2056 (1996).
17. L. Vrbka, P. Jungwirth, P. Bauduin, D. Touraud, W. Kunz, *J. Phys. Chem. B* **110**, 7036 (2006).
18. J. L. Thomas, M. Roeselová, L. X. Dang, D. J. Tobias, *J. Phys. Chem. A* **111**, 3091 (2007).
19. We thank the many co-workers and collaborators who have contributed to our research on specific ion effects. We acknowledge funding support from the AirUCI Environmental Molecular Sciences Institute (NSF grant CHE 0431312).

10.1126/science.1152799

PROFILE

Bruce Alberts, *Science*'s New Editor

Highlights from Alberts's life as a citizen-scientist make it clear that he is well prepared to lead the journal.

Marc Kirschner

In March, the editorship of *Science* passes to Bruce Alberts, professor of biochemistry and biophysics at the University of California, San Francisco (UCSF). He will make the 5000-mile round trip to *Science* at least once a month and oversee the weekly publication of the most prominent journal in science worldwide. It is a position with immense influence on the conduct of science.

The expectations are high for the new editor to set the highest intellectual and ethical standards for publication, and at the same time produce a journal that makes science exciting for the public. *Science* is expected to publish meaningful original work that stands the test of time—as well as analyses and commentaries that influence the political process, expose misdeeds and misunderstandings, represent the profession of science, foster education, advocate for science, and represent science as a source of enlightenment and hope for all people—and to be so fascinating that geologists will order another cup of coffee to read about microRNA and molecular biologists will skip a meeting to catch the newest article on planetary evolution. No one is fully prepared for such a job. Yet Bruce Alberts has made contributions of such variety and quality that we can be reassured that this position is in the best of hands.

Bruce's stellar career of public service may have obscured the brilliance of his scientific accomplishments. He received his Ph.D. in 1965 from Harvard University, studying DNA structure with Paul Doty. During postdoctoral training with Alfred Tissières in Geneva, he developed DNA affinity chromatography and was the first to isolate a single strand–specific DNA binding protein. As a young faculty member at Princeton University, he went on to purify all seven proteins required for DNA synthesis in bacteriophage T4 and reconstitute the process—an extraordinary accomplishment. His experiments on DNA replication are a model of physical rigor and biological insight. Though a renowned professor, Bruce maintained an unassuming office, which doubled as a hallway, in the basement of the chemistry building. This would forever be his style, modest and self-deprecating. The department he helped build at Princeton University believed that everything in science was open to new understanding, and that chemistry, physics, and biology could come together in new ways. For the beleaguered young faculty, Bruce was a friend and a stern taskmaster. He invited interesting people to visit and talk, offering the young faculty chances to learn. I remember Bruce inviting Barbara McClintock to lecture on cytogenetics. I understood little of what she said; yet the impact of her enthusiasm and tireless intellect is still with me.

The Princeton department imploded in the mid-70s and Bruce was lured to UCSF. His leadership helped establish the institution as a great research center known also for its humanity, collegiality, concern for education, and broad appreciation of science. To those who thought that humanity and excellence in science were, if not mutually exclusive, at least mildly incompatible, Bruce proved them wrong. He infused his values into the high-octane world of academic science, and UCSF was the richer for it.

Although Bruce refocused his research in new directions, it was apparent that no laboratory or department could contain his commitment to public service centered on science policy and education. In the 1980s, Bruce and colleagues produced a radically new cell biology textbook that transformed the teaching of that subject. "Alberts," as the book is generally called, emphasized biophysical understanding, current experiments, and bold graphics. He has continued the leadership of that remarkable volume through five editions.

Bruce developed a deep commitment to elementary and high-school science education. He had empathy for teachers who struggled with difficult working conditions and he fumed about curricula that stressed rote memory and failed to convey the excitement of discovery. He launched the Science and Health Education Partnership, which pairs UCSF students, postdoctoral fellows, and faculty with public-school teachers. After two decades, many hundreds of UCSF volunteers and 80 to 90% of San Francisco's public schools are involved.

Bruce began participating at the national level through the National Academy of Sciences (NAS) as chair of the Board on Biology. He chaired the NAS committee that strongly endorsed a human genome project, a task that seemed impossible to some and undesirable to others. This, among other important roles, eventually led to his nomination for NAS president in 1993. It was hard for Bruce to leave his laboratory and students and embark on a career that would end his role as an experimental scientist.

Bruce's time at the NAS was multifaceted but can be characterized by two foci: education and international cooperation. Both are difficult to influence, but there were substantial milestones, such as forging the first national science curriculum standards for K-12 education and establishing the InterAcademy Council to bring impartial and informed scientific opinion to less developed countries. Bruce has traveled throughout the world to promote science and science education. He learned to embrace small victories and to lead by example, no matter what the effort.

Two years ago, Bruce finished his second and final term as NAS president and, with his wife Betty, returned home to San Francisco, surrounded by friends, children, and grandchildren—a nice picture for the sunset of a great career. But Bruce, with his limitless energy and commitment to important causes, plunged into teaching and revising the UCSF graduate program. He continued chairing the InterAcademy Council and became president of the American Society for Cell Biology. And at the urging of fellow scientists, he now has taken on the editorship of *Science*.

I know that when Bruce reads this profile, he will feel uncomfortable that I've excluded the contributions of so many others. But I think I may have omitted Bruce's greatest talent—his ability to inspire people to devote time for public causes and adopt them as their own. That is why there are so many people to acknowledge, and why, even after stepping down from the NAS presidency, Bruce keeps traveling so much. He told me that he wants to pay back many people for their services while he was NAS president. This time around, it's our turn to give our services enthusiastically to help Bruce Alberts maintain and expand *Science*'s role as a resource for science and a tool to promote the highest values of the profession.

10.1126/science.1155869

Harvard Medical School, Boston, MA 02215, USA. E-mail: marc@hms.harvard.edu

CREDIT: NATIONAL ACADEMY OF SCIENCES, WASHINGTON, DC

SCIENCE POLICY

Scientists "Uniquely Positioned" to Assist Climate Policy-Makers

As governments around the world search for ways to address rising greenhouse gas emissions, researchers should be ready to offer expert advice to lawmakers seeking a broad view of global climate change and its potential consequences, according to a distinguished panel of science policy advisers at a recent Capitol Hill briefing.

The panel, convened by AAAS and three other scientific societies on 11 January, drew more than 150 congressional staffers, think tank representatives, university faculty, and journalists spilling out of the briefing room in the Rayburn House Office Building. In front of a crowd eager for answers, the speakers discussed how scientists can assist policy-makers in their analysis of climate change proposals awaiting congressional debate.

"Funding scientists and their research is going to help answer questions like how much are humans responsible for global warming and what are the potential effects on our lives," said David Goldston, former staff director of the House Science Committee and a lecturer at Princeton University. "These are very important questions, and we need answers as we move forward."

"Scientists are uniquely positioned to help the public understand the dangers and help lawmakers make informed decisions about addressing climate change," agreed Michael Oppenheimer, the Albert G. Milbank Professor of Geosciences and International Affairs at Princeton University.

But Oppenheimer, Goldston, and the other panelists acknowledged the limits of scientific advice in crafting climate change policy, which will have to incorporate a wide set of political, economic, and social considerations beyond the scientific data, they said.

"Climate goals involve more than science, so in the end, policy-makers, not scientific institutions, should choose them," Oppenheimer said, although he also noted that it "may even be part of the scientist's professional obligation" to comment publicly on the implications of their research.

"Scientists do not hang up their citizenship when they enter a briefing room," agreed Stephen Schneider, a senior climatologist and professor at Stanford University. He stressed the need for scientists to support their public arguments by "clearly identifying which opinions are personal values and which are based on professional judgments."

(Left to right) Michael Oppenheimer, Stephen Schneider, David Goldston, and Ralph Cicerone

Although nearly all researchers agree that the Earth is in the midst of a human-caused warming period, no scientist can definitely state how hot it will get or predict exactly how the Earth will respond, Schneider cautioned. He compared the Earth's rate of warming to a carnival pinwheel—"the great greenhouse gamble," he quipped—with different-sized sections representing different average global temperature increases.

The largest section on the pinwheel chart, created by researchers at the Massachusetts Institute of Technology, represents the most likely outcome (22.5% likelihood) of a 2 to 2.5°C increase in temperature. The smallest slice of the pinwheel (a 3.8% likelihood) predicts an increase of more than 5°C.

Oppenheimer said policy-makers will have to respond to the consequences of higher temperatures in four main areas: access to water and food; human health in extreme climate conditions; ecosystems and species; and sea-level rise from ice sheet melting.

The exact nature of these challenges remains uncertain, however, and several panel speakers urged the U.S. Congress to support sharp increases in climate science research funding to fill in the details. Goldston singled out researchers at NASA Earth Science programs—"the biggest people in Earth observation and monitoring"—as a group that deserved an immediate budget increase.

By measuring climate changes in fragile regions, developing more powerful computer programs to improve climate predictions, and increasing satellite observation budgets, researchers can "accelerate scientific research to deliver more useful results," said Ralph Cicerone, president of the National Academy of Sciences, who also suggested that the scientific community evaluate a diverse portfolio of carbon mitigation strategies.

"There are also some really big bioengineering ideas that are not quite developed, nor fully articulated or peer-reviewed, so they are far from ready for implementation," Cicerone noted. "But we would be foolish not to look into them. The stakes are too high."

The American Geophysical Union, the American Meteorological Society, and the Pew Center for Global Climate Change cosponsored the briefing with AAAS.

—Benjamin Somers and Becky Ham

SCIENCE AND SOCIETY

Neureiter Receives Public Welfare Medal

Norman P. Neureiter, director of the AAAS Center for Science, Technology and Security Policy, has been awarded the 2008 Public Welfare Medal by the U.S. National Academy of Sciences for his lifelong efforts to encourage international cooperation in science and technology.

Established in 1914, the medal honors "extraordinary use of science for public good." The Academy commended Neureiter's work as the first science and technology adviser to the U.S. Secretary of State, at the White House's Office of Science and Technology Policy, and in the Foreign Service.

Neureiter is "elated" by the Academy's decision to recognize the importance of science and technology cooperation as a positive instrument of a constructive U.S. foreign policy.

"This kind of engagement can be one of the nation's most effective 'soft power' strategies for both addressing problems of global concern—such as food, energy, and climate change—and for building bridges of understanding to other countries," he said. "It is the ultimate win-win strategy."

Neureiter is the second current AAAS senior manager to receive the Public Welfare Medal: Shirley Malcom, director of Education and Human Resources at AAAS, was honored in 2003 for her lifelong efforts to make science available to those normally underrepresented in science careers.

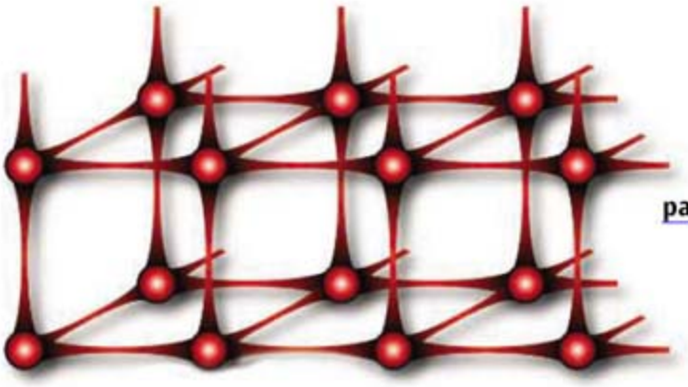

page 1211

INTRODUCTION

Quantum Wonderland

LIKE ALICE AND HER WONDERLAND, PHYSICISTS ALSO HAVE ACCESS TO TWO worlds: the classical and the quantum. Although both worlds are inhabited by the same two species, bosons and fermions, their behavior in either world can be remarkably different. The macroscopic or classical world is filled with the familiar and modeled with classical laws. Lowering the temperature sufficiently to enter the quantum world reveals that these species can interact in cooperative ways, giving rise to exotic phases of matter—quantum matter—not seen in the classical world. Here, things get interesting (and weird); solids, liquids, and electrons can flow without dissipation; exotic phases can emerge; fluctuations can be critical; and objects can be entangled and be in multiple places at once.

Many experimentalists and theorists have been exploring this quantum regime for some time now, studying how individual particles and ensembles of particles behave, in attempts to unravel the underlying physics producing these exotic properties and phases. Some others are heading straight to applications. The six Perspectives in this special section provide a taste of some of the topics that occupy the world of quantum matter.

With atoms trapped in a lattice of optical microtraps, Bloch (p. 1202) discusses how the ability to manipulate the magnitude and sign of the interaction between the atoms can provide a model system in which to explore the formation of the exotic phases seen in quantum gases, liquids, solids, and electronic and magnetic systems. Leggett (p. 1203) sets out the theoretical basics of such quantum systems, explaining how their behavior depends on which family of statistics (Bose-Einstein or Fermi-Dirac) the atoms belong to. Choosing the example of quantum criticality in fermionic systems, Zaanen (p. 1205) points out that the fermions and their statistical family are troublemakers. Trying to explain the complexity emerging from what are simple constituents, he tells us that our present mathematical toolbox is incapable of describing how these exotic electronic phases emerge and that new mathematical tools need to be developed. Another recent example of an observation in need of an explanation is the supersolid effect found in helium-4, where a solid crystal seems to move like a superfluid. Chan (p. 1207) presents the latest on this new phase and argues that imperfections in the crystal appear to be necessary for the effect to be seen. Communication is a vital technology in the classical world, and Walmsley (p. 1211) describes how developments made in the quantum world are carrying over to applications through the use of quantum optics in areas such as secure communication and cryptography. Lloyd (p. 1209) expands on the topic of communication and information, describing how quantum information can be considered as matter, as concrete as any of the matter we are familiar with in our classical world, and how theoretical ideas in quantum error correction will lend themselves to the realization of an operational quantum computer.

Outside the special section, Adrian Cho's story in News Focus (p. 1180) describes research in Fermi condensates, gases composed of fermionic atoms, which may help researchers model materials as diverse as high-temperature superconductors and the interiors of neutron stars.

So, armed with an Alice-like curiosity, let's take a short walk in this quantum landscape.

– IAN OSBORNE AND ROBERT COONTZ

CREDIT: I. A. WALMSLEY

Quantum Matter

CONTENTS

Perspectives

See also related News story page 1180

Science

PERSPECTIVE

Quantum Gases

Immanuel Bloch

Ultracold quantum gases are proving to be a powerful model system for strongly interacting electronic many-body systems. This Perspective explores how such atomic ensembles can help to unravel some of the outstanding open questions in the field.

When matter is cooled down close to zero temperature, particles can interact in a cooperative way and form novel states of matter with striking properties—superconductors, superfluids, or fractional quantum Hall liquids. Similar phenomena can now be observed in a dilute gas of atoms, five to six orders of magnitude less dense than the air surrounding us. Here, degenerate bosonic and fermionic quantum gases trapped in magnetic or optical traps are generated at temperatures in the nanokelvin regime (*1*). Whereas initial research concentrated on weakly interacting quantum states [for example, on elucidating the coherent matter wave features of Bose-Einstein condensates (BECs) and their superfluid properties], research has now turned toward strongly interacting bosonic and fermionic systems (*2*, *3*). In these systems, the interactions between the particles dominate over their kinetic energy, making them difficult to tackle theoretically but also opening the path to novel ground states with collective properties of the many-body system. This has given rise to the hope of using the highly controllable quantum gases as model systems for condensed-matter physics, along the lines of a quantum simulator, as originally suggested by Feynman (*4*).

Two prominent examples have dominated the research in this respect: (i) the transition from a superfluid to a Mott insulator of bosonic atoms trapped in an optical lattice potential (*5*–*7*) and (ii) the BEC–Bardeen-Cooper-Schrieffer (BCS) crossover of a two-component Fermi gas across a Feshbach resonance through which the magnitude and sign of the interactions between pairs of atoms can be tuned (*8*–*11*). In the first, a weakly interacting and superfluid gas of quantum degenerate bosons can be turned into an incompressible and insulating gas in a three-dimensional lattice of optical microtraps. The Mott insulator can be visualized as a many-body system in which strong repulsive interactions between the particles sort them into a perfectly ordered array and each lattice site is occupied by a single atom. In the second example, pairs of fermionic atoms can form bosonic composite particles when their interactions are tuned by Feshbach resonances. Such bosonic composites can themselves undergo Bose-Einstein condensation, thus fundamentally altering the properties of the many-body system. When a true two-body bound state exists between the particles, the composite bosonic particle is simply a molecule, albeit very large, whereas in the case of attractive interactions without a two-body bound state the composite pair can be seen to be related to a BCS-type Cooper pair, which can then undergo condensation. It is the possibility of changing almost all the underlying parameters dynamically and the ability to model the complex many-body quantum systems by first principles that have led to a surge in experimental and theoretical research.

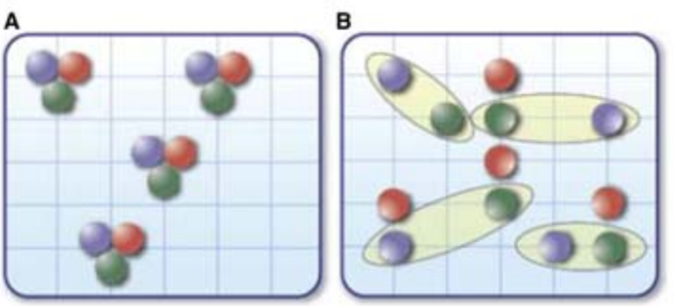

Fig. 1. Three-species fermionic atoms (red, green, and blue spheres) in an optical lattice can form two distinct phases when the interactions between the atoms are tuned. In the first case of strong attractive interactions between the atoms, they join as "trions" (**A**), whereas in the second case of weaker interactions, a color superfluid is formed (**B**), in which atoms pair up between only two species. The two phases have strong analogies to the baryonic phase (A) and the color superfluid phase (B) in quantum chromodynamics [see (*12*)].

What is next on the agenda? For fermionic systems with and without a lattice, researchers are trying to see whether they can pair up particles with very different mass ratios, such as lithium and potassium, or possibly even three different fermionic atomic species. This line of work is fueled by a theoretical prediction that such fermionic mixtures could show phases in which three fermions join to form a "trion" analogous to quarks forming baryonic matter or, alternatively, only two of the fermionic components pair to form a "color" superfluid (*12*) as in quantum chromodynamics (Fig. 1). For the case of two particles with highly different mass ratios, one hopes to observe exotic forms of superconductivity such as the Fulde-Ferrell-Larkin-Ovchinnikov superconducting phase (*13*, *14*), where particles condense into pairs with nonzero momentum. Early experiments have produced degenerate mixtures of two fermionic atomic species (*15*) and two fermionic species with an additional third bosonic component (*16*), and both are progressing quickly toward exploiting Feshbach resonances to control the interactions between the fermionic atoms.

For lattice-based systems, efforts are under way to explore the feasibility of using ultracold atoms as quantum simulators for strongly interacting many-body systems. For example, in the famous class of high-Tc superconductors, such as the CuO compounds, one observes that these form antiferromagnetically ordered ground states when undoped. Upon doping, and thereby changing the effective filling in the system, the antiferromagnetic order is destroyed and a superconducting phase with d-wave symmetry of the order parameter emerges (*17*) (Fig. 2). What exactly happens during the transition and how it can be described theoretically is currently a subject of heated debates and one of the fundamental unsolved problems in the field of condensed-matter physics. Cold-atom researchers are currently trying to determine whether they can help to resolve some of these issues (*18*). As a starting point, several groups are preparing to observe antiferromagnetically ordered states in two-component Fermi mixtures in an optical lattice. To achieve this, however, one needs to cool the many-body system to challenging temperatures T below the superexchange interaction energy J_{ex}, which characterizes the coupling strength between the spins of atoms on neighboring lattice sites. If the temperature is not low enough, thermal fluctuations would simply destroy the fragile magnetic order present in the ground state. Superexchange interactions form the basis of quantum magnetism in strongly correlated electronic media and can be described as an effective spin-spin interaction between the neighboring particles on a lattice (*19*). They are a result of virtual "hopping" events of particles to neighboring lattice sites, in which a particle tunnels to an adjacent site and then the same particle—or its neighbor—returns to the original lattice position. For two spin-polarized fermions, such hopping is suppressed by the Pauli principle, whereas for two fermions with opposing spin directions, the hopping is allowed and leads to

Johannes-Gutenberg Universität, 55118 Mainz, Germany. E-mail: bloch@uni-mainz.de

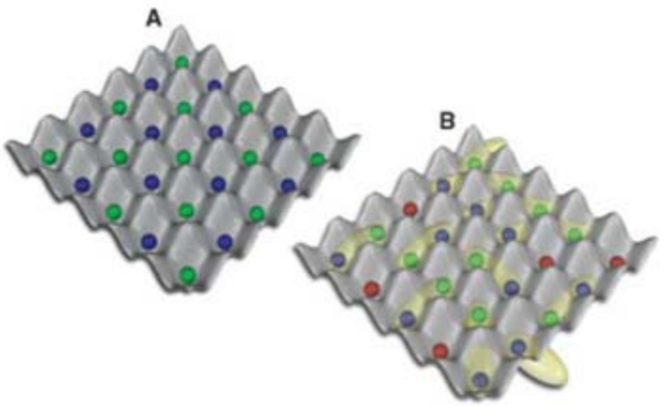

Fig. 2. For two-component Fermi gases (blue and green spheres) in an optical lattice, an antiferromagnetic ground state is expected at half-filling (**A**). Upon doping (red spheres), such an antiferromagnetic order is expected to be destroyed and, in some theories, a spin-liquid state emerges (**B**), which can form the basis for a high-Tc superconducting phase [see (*17*, *29*)]. Researchers with ultracold atoms are currently trying to establish both phases in the experiment.

a decrease of the total energy of the particles. For fermionic atoms, an antiferromagnetic orientation of the atoms with alternating spins is thus favorable over a ferromagnetic one. Exchange and superexchange interactions between ultracold atoms have been observed, showing that they can be controlled to a high degree and that their coupling strengths can be in the kHz range (*20*, *21*). The temperatures of the Fermi gases produced in the experiments so far also seem to be initially low enough to enter an antiferromagnetically ordered phase, such that one can expect to observe these phases in upcoming experiments (*22*). Whether the temperatures one needs are, however, already also low enough to observe a *d*-wave superconducting phase is unclear, especially as current theories do not permit a precise estimate of the critical temperature for entering the superconducting phase. By comparing to critical temperatures observed with typical high-Tc superconductors, one can estimate the required temperatures to be a fraction of the superexchange coupling. Progress in this direction might therefore be crucially linked to novel approaches for cooling the quantum gases to even lower temperatures in the lattice (*23*).

Control over the effective spin-spin interactions between neighboring atoms could also open up a new avenue for the simulation of quantum magnetism with cold atoms or molecules. Both atoms and molecules offer the ability to implement arbitrary spin Hamiltonians on a lattice (*24*). For atoms, the spin-spin interactions are generated by superexchange couplings (*25*, *26*), whereas for ultracold molecules the electric dipole-dipole interaction can mediate even stronger spin coupling between individual molecules on neighboring sites (*27*). Heteronuclear Feshbach molecules have recently already been formed in optical lattices; however, in order for them to possess a strong electric dipole moment, the molecules that are up to now created in highly excited vibrational states will have to be brought to the ground state in a controlled way. Laser spectroscopy in molecules could do exactly this: by using a single pulse or a sequence of two-photon Raman transitions, the high excitation energy could be removed and the molecules could be brought to the ground state. If all this can still be done in such a gentle fashion that does not heat the atoms and molecules too much, and whether one will be able to ultimately obtain a degenerate gas of heteronuclear molecules stable enough to carry out experiments, remain to be seen.

Finally, several research teams are currently trying to find ways to address and observe single atoms on single lattice sites (*28*). In the optical regime, this requires a demanding optical microscope, as the atoms in the lattice are only spaced by half a micrometer or less. However, if successful, one not only would be able to observe but also could control a spin system in two dimensions with 10,000 particles simultaneously in view, all with single-site and single-atom resolution. Observing dynamical evolutions in these systems, probing their spatial correlations, and finally implementing quantum information processing in such a truly large-scale system would offer exciting prospects for future research.

References

1. L. Pitaevskii, S. Stringari, *Bose-Einstein Condensation* (Oxford Univ. Press, Oxford, 2003).
2. D. Jaksch, P. Zoller, *Ann. Phys.* **315**, 52 (2005).
3. I. Bloch, J. Dalibard, W. Zwerger, http://arXiv.org/pdf/0704.3011.
4. R. P. Feynman, *Int. J. Theor. Phys.* **21**, 467 (1982).
5. M. P. A. Fisher, P. B. Weichman, G. Grinstein, D. S. Fisher, *Phys. Rev. B* **40**, 546 (1989).
6. D. Jaksch, C. Bruder, J. I. Cirac, C. W. Gardiner, P. Zoller, *Phys. Rev. Lett.* **81**, 3108 (1998).
7. M. Greiner, O. Mandel, T. Esslinger, T. W. Hänsch, I. Bloch, *Nature* **415**, 39 (2002).
8. C. A. Regal, M. Greiner, D. S. Jin, *Phys. Rev. Lett.* **92**, 040403 (2004).
9. M. W. Zwierlein *et al.*, *Phys. Rev. Lett.* **92**, 120403 (2004).
10. M. Bartenstein *et al.*, *Phys. Rev. Lett.* **92**, 120401 (2004).
11. T. Bourdel *et al.*, *Phys. Rev. Lett.* **93**, 050401 (2004).
12. A. Rapp, G. Zarand, C. Honerkamp, W. Hofstetter, *Phys. Rev. Lett.* **98**, 160405 (2007).
13. P. Fulde, R. A. Ferrell, *Phys. Rev.* **135**, A550 (1964).
14. A. I. Larkin, Y. N. Ovchinnikov, *Sov. Phys. JETP* **20**, 762 (1965).
15. E. Wille *et al.*, http://arXiv.org/pdf/0711.2916.
16. M. Taglieber, A.-C. Voigt, T. Aoki, T. W. Hänsch, K. Dieckmann, *Phys. Rev. Lett.* **100**, 010401 (2008).
17. P. A. Lee, N. Nagaosa, X.-G. Wen, *Rev. Mod. Phys.* **78**, 17 (2006).
18. W. Hofstetter, J. I. Cirac, P. Zoller, E. Demler, M. D. Lukin, *Phys. Rev. Lett.* **89**, 220407 (2002).
19. A. Auerbach, *Interacting Electrons and Quantum Magnetism* (Springer, Berlin, 2006).
20. M. Anderlini *et al.*, *Nature* **448**, 452 (2007).
21. S. Trotzky *et al.*, *Science* **319**, 295 (2008).
22. F. Werner, O. Parcollet, A. Georges, S. R. Hassan, *Phys. Rev. Lett.* **95**, 056401 (2005).
23. A. Greissner, A. J. Daley, S. R. Clark, D. Jaksch, P. Zoller, *Phys. Rev. Lett.* **97**, 220403 (2006).
24. M. Lewenstein *et al.*, *Adv. Phys.* **56**, 243 (2007).
25. L.-M. Duan, E. Demler, M. D. Lukin, *Phys. Rev. Lett.* **91**, 090402 (2003).
26. A. B. Kuklov, B. V. Svistunov, *Phys. Rev. Lett.* **90**, 100401 (2003).
27. A. Micheli, G. K. Brennen, P. Zoller, *Nat. Phys.* **2**, 341 (2006).
28. K. D. Nelson, X. Li, D. S. Weiss, *Nat. Phys.* **3**, 556 (2007).
29. P. W. Anderson, *Science* **235**, 1196 (1987).

10.1126/science.1152501

PERSPECTIVE

Quantum Liquids

A. J. Leggett

Quantum liquids are systems in which not only the effects of quantum mechanics but also those of the characteristic indistinguishability of elementary particles are important. The most spectacular of these are the systems of bosons (liquid ^{4}He, the Bose alkali gases), which undergo the phenomenon of Bose condensation, and the fermion systems (liquid ^{3}He, the electrons in some metals), which display the related phenomenon of Cooper pairing. I discuss these phenomena and the relation between them.

A quantum liquid may be defined as a many-particle system that shows not only the effects of quantum mechanics but also those of quantum statistics. As is well known, general considerations concerning the rotation group limit the possible values of total angular momentum that can be possessed by any "elementary" particle, or any compound system such as an atom made up of elementary particles, to $nh/2$ where n is an integer (including zero). If n is even, the particle or system in

Department of Physics, University of Illinois at Urbana-Champaign, Urbana, IL 61801, USA.

question is called a boson; if odd, a fermion. A famous theorem of quantum field theory, the spin-statistics theorem (*1*), then states that the total wave function of any many-particle system must be even under the interchange of all the coordinates of any two bosons of identical type, and odd under interchange of those of any two identical fermions. Formally, if i and j label two particles of the same species, and $\boldsymbol{r}_i\sigma_i$, etc., their space and spin (or other internal) coordinates, then we must have

$$\Psi(\boldsymbol{r}_1\sigma_1,\ \boldsymbol{r}_2\sigma_2\ldots,\ \boldsymbol{r}_i\sigma_i\ldots,\ \boldsymbol{r}_j\sigma_j\ \ldots\boldsymbol{r}_N\sigma_N) = \pm\Psi(\boldsymbol{r}_1\sigma_1,\ \boldsymbol{r}_2\sigma_2\ldots\boldsymbol{r}_j\sigma_j\ \ldots\boldsymbol{r}_i\sigma_i\ldots\boldsymbol{r}_N\sigma_N) \quad (1)$$

with the ± sign applying to bosons (fermions). In the special case of free particles that can occupy plane wave states with momentum $\boldsymbol{k}$, spin projection σ, and energy $\varepsilon_{k\sigma}$, the condition (Eq. 1) leads, for a collection of identical particles of a single species in thermal equilibrium at temperature $T = 1/k_B\beta$ (where k_B is Boltzmann's constant), to a single-particle distribution $n_{k\sigma}$ of the form

$$n_{k\sigma}(T, \mu) = [\exp\beta(\varepsilon_{k\sigma} - \mu) \mp 1]^{-1} \quad (2)$$

where μ is the chemical potential and the ∓ sign now refers to bosons (fermions). The distribution (Eq. 2) with the minus sign is known as the Bose-Einstein distribution and that with the plus sign as the Fermi-Dirac distribution; hence, bosons (fermions) are often said to satisfy Bose (Fermi) statistics. However, it needs to be emphasized that the "statistics" of Eq. 2 apply only to a very special case, whereas the requirement of Eq. 1 of symmetry or antisymmetry of the many-particle wave function is much more general. I will follow the inaccurate but conventional practice of referring to the consequences of Eq. 1 as those of (quantum) statistics.

A necessary condition to see nontrivial effects of Eq. 1 is that the system should show appreciable effects of quantum mechanics in the first place, i.e., should deviate appreciably from the behavior predicted by a purely classical description. Crudely speaking, this is likely to happen when the thermal energy k_BT falls below a typical single-particle excitation energy. For example, if we describe an insulating crystalline solid by the Einstein model, in which each atom vibrates in the potential field of its neighbors with a frequency ω_o, then the condition is about $k_BT \lesssim \hbar\omega_o$; a more sophisticated (Debye) model confirms this result, in the sense that (for example) the specific heat of a crystalline solid falls below the classical "equipartition" value of $3k_b$ per atom when $k_BT \lesssim \hbar\omega_D$, where the Debye frequency, ω_D, is of the same order as ω_o. More generally, a very rough order of magnitude for the temperature T_d at which quantum-mechanical effects begin to show up in an important way may be obtained by imagining each particle of mass m to move in a cage of side $a \sim n^{-1/3}$ (n = particle density) formed by its neighbors; because the typical single-particle excitation energy is then of order $\hbar^2/ma^2$, the criterion is

$$T_d \sim \frac{\hbar^2 n^{2/3}}{mk_B} \quad (3)$$

This criterion is approximately correct for liquids and gases (in the latter case, the temperature T_d, which can be estimated more rigorously from an analysis of Eq. 2, is often called the degeneracy temperature); it underestimates T_d somewhat for solids because there the effective size of the "cage" tends to be substantially less than the interatomic spacing. In any case, on putting in the values of n and m, it is clear that the condition $T \lesssim T_d$ is satisfied for electrons in any liquid or solid below the vaporization temperature and for atoms in any liquid or solid at cryogenic, but nowadays relatively easily attainable, temperatures; it can also be satisfied for ultracold atomic gases, as in these systems, although the density is many orders of magnitude smaller than that in a typical solid or liquid, the temperature is also much less.

However, although the criterion $T \lesssim T_d$ is certainly a necessary condition to see the effects of quantum statistics (i.e., the constraint Eq. 1), it is by no means sufficient. In fact, if we compare the behavior of a carbon crystal made of the "common" isotope ^{12}C (a boson) with that of one composed of the rare isotope ^{13}C (a fermion), the only difference is a trivial one associated with the slightly different masses. In order for the statistics to have an effect, it is essential that identical particles are able to change places. A nice example of this principle (*2*) is seen in the structure of the vibrational and rotational levels of diatomic molecules composed of chemically identical atoms, such as C_2: if we consider a heteronuclear molecule such as ^{12}C–^{13}C, then, because there is no question of exchange of "identical" particles, the constraint (Eq. 1) has no effect and all levels are allowed. If now we replace (for example) the ^{13}C atom by a second ^{12}C, we find that the vibrational levels are unaffected (except trivially, via the difference in reduced mass) but that the odd-angular-momentum rotational levels are missing! This underlines spectacularly the difference between a process such as rotation, in which the identical atoms physically change places, and one such as vibration where they do not. Note that for the "statistics" to have an effect it is not necessary that the two identical atoms ever occupy the same position at the same time. [For a more detailed discussion, see for example (*2*), section 1.1.]

Thus, a quantum liquid is a many-particle system in which (i) the temperature is less than or of the order of the T_d defined by Eq. 2 and (ii) the particles can change places relatively easily. As so defined, the category of quantum liquids includes the ultracold dilute atomic gases as a special case; however, because they are the subject of another essay in this issue (*3*), I will confine myself here to systems occurring at typical liquid or solid densities. The category then includes the electrons in metals, the two stable isotopes of helium (the only element that remains liquid under its own vapor pressure in the limit $T \to 0$), and if we are willing to leave the terrestrial sphere, the neutrons in neutron stars and possibly more exotic forms of matter such as quark stars.

Rather generally, the properties of any quantum liquid are likely to be quantitatively and even qualitatively different from those of the corresponding classical system; this has long been known in, for example, the case of the electrons in metals at temperatures of the order of room temperature ($T \ll T_d$), which are actually often described surprisingly well by the simple (Sommerfeld) model of noninteracting fermions, which leads to Eq. 2. However, the most spectacular manifestations of the effects of quantum statistics are associated with the phenomenon of Bose-Einstein condensation (BEC) and the related phenomenon of Cooper pairing occurring in Fermi systems. For a noninteracting gas of bosons described by the distribution of Eq. 2, a straightforward analysis originally carried out by Einstein (*4*) shows that below a temperature T_0 of the order of T_d a nonzero fraction of all the N particles, that is, a macroscopic number $N_0(T) \sim N$, occupies the lowest single-particle state (in free space, this is the zero-momentum state). It has long been believed that a similar phenomenon occurs, in thermal equilibrium, in a system of interacting bosons, provided that the interaction is overall positive (repulsive) and that it is just this that is happening in the "superfluid" (He-II) phase of the bosonic liquid ^4He. In recent years, direct evidence for BEC has been obtained in dilute ultracold atomic gases such as ^{87}Rb and ^{23}Na; these gases are actually confined in a harmonic trap, and in the absence of interactions BEC would show up as a much-enhanced ($N_0 \sim N$) population of the harmonic ground state, leading to a sharp spike in the density distribution around the origin. In real life, this spike is somewhat broadened by the repulsive interatomic interactions, but it can still be clearly seen in the experiments (*5*). An interesting feature of BEC in the atomic gases is that theory suggests, and experiment confirms, that it can occur even when the system is far out of thermal equilibrium and the macroscopically occupied state is thus strongly time-dependent.

In qualitative terms, the BEC state is characterized by the fact that a macroscopic number N_0 of particles are forced to occupy the same single-

particle state and thus to behave in exactly the same way [compare with (6)]. This property leads to a variety of spectacular effects, including the complex of phenomena known as superfluidity, which is observed to occur in the He-II phase of liquid ^{4}He, and a variety of interference phenomena, which it has become possible to observe in the ultracold atomic gases [(2), section 2.5].

Turning now to Fermi systems, we see from Eq. 2 that in this case the value of $\langle n_{k\alpha} \rangle$ can never exceed 1 (the Pauli principle), so that the direct analog of BEC certainly cannot occur. However, there is no reason why a complex made up of an even number of fermions (a boson) cannot undergo BEC (indeed, this is exactly what is happening in, for example, ^{87}Rb at ultralow temperatures), and in particular there is every reason to believe (compare below) that if two spin-1/2 fermions are coupled by an attractive interaction sufficiently strong to bind them into a spin-0 bosonic molecule, these molecules will indeed undergo BEC; such a scenario might be imagined to describe, for example, liquid D_2, if we could exclude crystallization. Imagine now that we gradually weaken the interfermion attraction to the point where (in the two-body problem) the molecule is no longer stable and even beyond. Can a sort of BEC still persist under these conditions? In their epoch-making work (7) in 1957, Bardeen, Cooper, and Schrieffer (BCS) showed that the answer is yes: A degenerate system of fermions with an arbitrarily weak attraction will, at sufficiently low temperatures (exponentially low compared to T_d), form "Cooper pairs," a sort of giant diatomic (or more accurately dielectronic, because BCS were dealing explicitly with the electrons in a metal), spin-0 molecules, and the latter will then in effect automatically undergo the phenomenon of BEC. In contrast to the case of (hypothetical) liquid D_2, however, the size of the "molecules" is now large compared with their average separation, so that the theory of Cooper pairing is quantitatively and even qualitatively quite different from that of BEC of tightly bound diatomic molecules.

When Cooper pairing occurs in an electrically neutral system of fermions such as liquid ^{3}He, the consequences are qualitatively similar to those of BEC in a bosonic system such as ^{4}He. Indeed, it is almost universally believed that the anomalous phases of liquid ^{3}He that occur below 3 mK (note this is $<<T_d \sim 1$ K), which show many of the manifestations of superfluidity, are indeed characterized by the onset of Cooper pairing. When the latter occurs in the electrically charged system of electrons in metals, the effects are even more spectacular: In particular, the metal in question will exhibit the two major effects characterizing superconductivity, namely, persistent flow of currents in a ring and the exclusion of magnetic flux (Meissner effect), which leads to the possibility, inter alia, of static magnetic levitation. Superconductivity, originally thought to be an intrinsically low-temperature effect, has in the past 20 years been observed to occur in a class of cuprate materials up to around half of room temperature; although the detailed explanation of this high-temperature superconductivity is still furiously debated, there seems little doubt that its fundamental origin lies in the phenomenon of Cooper pairing.

As explained above, it is somewhat natural to think of the phenomenon of Cooper pairing in a system of fermions with weak attraction on the one hand and BEC in the system of diatomic molecules formed from them on the other as opposite ends of the same spectrum, and it has long been speculated that by "tuning" the strength of the attraction one might be able to realize a continuous transition between the two situations; this is known as the "BEC-BCS crossover." In the past 4 years, by using the phenomenon of Feshbach resonance, it has become possible to study the BEC-BCS crossover experimentally in ultracold atomic gases, and it indeed appears to be continuous as tentatively predicted by theory: See the article by I. Bloch in this issue (3). Thus, we now have a very satisfying unification of the concepts of BEC in a bosonic system and Cooper pairing in a fermionic one.

References and Notes

1. R. F. Streater, A. S. Wightman, *PCT, Spin and Statistics and All That* (Benjamin, New York, 1964).
2. A. J. Leggett, *Quantum Liquids: Bose Condensation and Cooper Pairing in Condensed-Matter Systems* (Oxford Univ. Press, Oxford, 2006).
3. I. Bloch, *Science* **319**, 1202 (2008).
4. A. Einstein, *Abh. Preuss. Akad. Wiss.* **3**, 18 (1925).
5. M. R. Andrews *et al.*, *Science* **273**, 84 (1996).
6. Molecule of the Year for 1995, *Science* **270** (1995).
7. J. Bardeen, L. N. Cooper, J. R. Schrieffer, *Phys. Rev.* **108**, 1175 (1957).

8. This work was supported by the NSF under grant no. NSFDMR-03-50842.

10.1126/science.1152822

PERSPECTIVE

Quantum Critical Electron Systems: The Uncharted Sign Worlds

J. Zaanen

Phases of classical matter, such as solids and liquids, are ruled by emergence principles that are well understood. Although the same principles govern forms of quantum matter that have no secrets for physicists, such as the superfluids, having to deal with fermions and the associated Fermi sign problem shatters this analogy. This Perspective addresses the Fermion sign problem and describes experiments on metals undergoing quantum phase transitions exhibiting scale-invariant electronic behavior, a description of which is at odds with established quantum theory.

Ice is different from water, and water is different from steam, although these phases of matter are all made from the same water molecules. Countless numbers of molecules are required to make this work, and the various phases of matter are said to "emerge." Emergence is at its best when the transition between such phases is continuous and the system no longer has any sense of preference for one or the other phase. This lack of "executive power" has the consequence that the system spontaneously adopts the powerful symmetry of scale invariance. In this "critical state" the system looks on average the same, regardless of the amplification factor that is used to observe it (1).

The concept of emergence is so powerful that it transcends the classical-quantum divide, and this apparently includes the generation of scale invariance: Quantum critical states where quantum fluctuations drive a phase transition at zero temperature are now routinely observed (2–6). However, dealing with emergence in quantum physics requires one to consider the organizational principles of quantum statistics, as discussed by Leggett (7), whereby quantum particles are either bosons or fermions. Despite its underlying quantum properties, bosonic matter is ruled by the same emergence principles as classical matter (2). In stark contrast, Fermi statistics wreck this analogy, and the emergence principles governing fermionic matter are among the great mysteries of modern physics. Fortunately, experimentation can help: Electrons in solids are relatively easy to probe, and they form systems of countless numbers of strongly interacting fermions. The recently observed quantum phase transitions in a variety of metals (3–6) reveal that fermionic quantum matter can exhibit unexpected behavior: Particles tend to acquire an infinite mass, and the scale-invariant fermionic phases that take over appear to be the birthplace of new forms of stable quantum matter.

Regular matter is formed from a large number of quantum particles, electrons, quarks, and

Instituut-Lorentz for Theoretical Physics, Leiden University, Leiden 2333 CA, Netherlands. E-mail: jan@lorentz.leidenuniv.nl

so forth. To answer the question of where classical integrity comes from, we look to Feynman's path integral formalism (*2*), a rather pictorial view of the quantum world but one that does reproduce accurately all the known facts about quantum systems in equilibrium. Within this formalism, quantum systems resemble classical matter living in a higher-dimensional "Euclidean space-time" (Fig. 1) having an extra axis, "imaginary time" (our time times the square root of –1). The maximal duration of this imaginary time is the ratio of Planck's constant divided by temperature: When temperature is lowered, "more time is available" to see quantum behavior. The strength of the quantum fluctuations is analogous to temperature in classical physics, having the effect of "heating up" the "stuff" inside space-time. When temperature is lowered and the quantum fluctuations are sufficiently vigorous, this frozen quantum matter might melt. The resulting space-time liquid will appear to our eyes as, for instance, a superconductor. When this melting transition taking place in space-time at zero temperature generates scale invariance, the quantum critical state is realized.

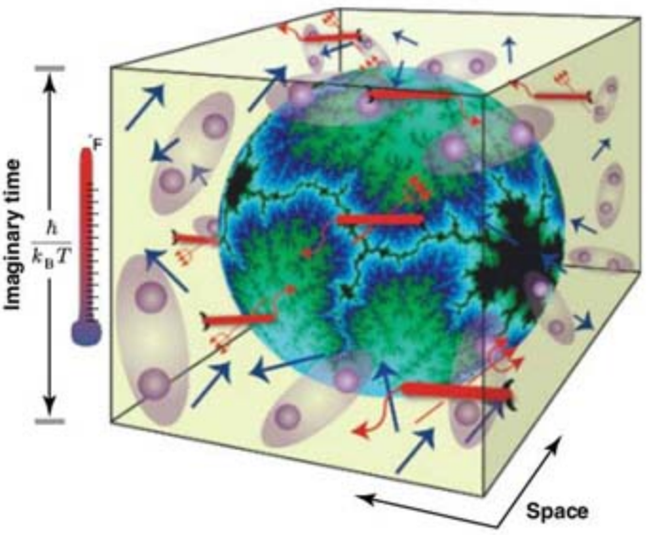

Fig. 1. Illustrating the Feynman path integral, the mathematical tool of choice to address emergence phenomena in many-particle quantum systems (*2*). Near a quantum phase transition, the world inside space-time turns scale-variant at shorter scales, like the Julia set of this cartoon, whereas at larger scales a stable form of quantum matter takes over. Dealing with fermions, the devilish minus signs obscure, however, any detailed understanding of these space-time worlds. The duration of imaginary time is determined by h (Planck's constant divided by 2π) and the product of Boltzmann's constant k_B and absolute temperature T.

These quantum critical states have in fact become quite ubiquitous in the laboratory. One variety is formed by the "designer quantum critical states," where the theorists have so much understanding that they can now guide the experimentalists to where to look. Prominent examples are the cold atoms and the spin systems, as highlighted by Bloch (*8*) and Lloyd (*9*). For bosons and some spin systems, the stuff filling up the space-time of the path integral is similar to classical matter, but this is not at all the case for fermions. The culprit for this deviation is the infamous "fermion sign problem." When fermions come into play, it turns out that in the statistics underlying the description of matter, one must deal with "negative probabilities," and this detaches the many-fermion problem from any classical analog. We have in fact no understanding at all of what is going on in space-time, because we need mathematics to look around and the sign problem is "NP hard" (*10*), meaning that the problem is mathematically unsolvable. The only fermionic substance that we can handle mathematically is the Fermi liquid, the state of electrons in normal metals. Although different from any form of classical matter, this state is at first sight deceptively simple: The electrons turn cooperatively into noninteracting "quasi-electrons" that only communicate via the Pauli exclusion principle. This pushes them into states of high quantum zero-point energy (*7*), and their average "Fermi energy" is typically on the order of 10,000 K in standard metals. This Fermi liquid is in fact a purely empirical construction. Although it is observed in experiments, theoretical physics has failed to explain its existence in general terms, despite countless attempts.

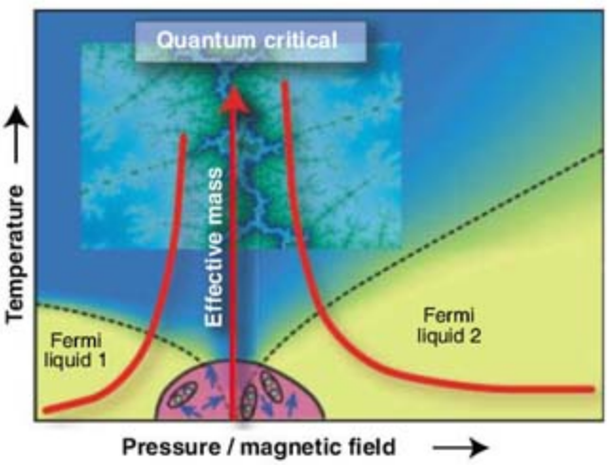

Fig. 2. Typical phase diagram observed in the heavy-fermion metals in the proximity of a quantum phase transition (*3*–*6*). The thermal phase transition to a magnetic state is driven to zero temperature by varying a magnetic field or pressure, and this is the anchor point of a regime of finite-temperature quantum critical fluid behavior fanning out for increasing temperature. The fermionic weirdness manifests itself through the effective mass of the quasi-electrons in the Fermi liquids on both sides, which increases without bound approaching the quantum phase transition. Invariably one finds that at a low temperature, an exotic superconductor (or even a quantum liquid crystal state) takes over at the last minute.

But electrons are also known to form "non–Fermi liquid" states, as can be found in metals containing rare earth, actinide, and transition metal ions (*3*–*6*). At ambient conditions, these show a phase transition to some magnetic state at a low temperature, and by applying pressure or magnetic fields, this transition can be driven to zero temperature. For example, in the diagram of pressure/magnetic field versus temperature (Fig. 2), one finds a V-shaped region anchored where the magnetic transition approaches zero temperature, and the regime inside the V shows the telltale signs of the quantum critical fluid. Actually, this fanning out of the quantum critical region for increasing temperature is just mapping out the "scale invariance geography" in space-time. When the system is close but not at the phase transition, it will show the physics of the stable phase at large scales (Fig. 1). However, upon zooming in, the system will forget its preferred state, and at a characteristic scale the system will reenter the scale-invariant regime. The increase of temperature is like the magnification factor of a microscope, and the V reveals that the scale where the system takes the decision to become a stable phase shifts to shorter times when one moves away from the quantum critical point.

But now the fermion signs hit hard: The experiments give away the workings of quantum scale invariance in space-time, but we have no clue whatever about the nature of the stuff creating the scale invariance! The stable states that are found outside the V in the proximity of the quantum phase transition are Fermi liquids, and because we have a phenomenological understanding of these states, they tell us something. When interactions are weak, one can do controlled calculations, and these reveal a peculiar Fermi liquid rule: The interactions between real electrons have the effect of increasing the mass of the quasi-electrons. This mass enhancement effect is quite modest when the calculations can be trusted, but in the approach to the metallic quantum phase transition, one finds that the effective mass of these quasi-electrons easily exceeds 1000 times the electron mass, to increase indefinitely upon getting closer and closer to the quantum critical point (*3*, *4*). Again the only hold we have is quantum scale invariance: The Fermi energy is a scale, but because the quantum critical state forbids any scale, it has to disappear. The Fermi energy is the average zero-point motion energy, and the only way to remove it is by making the mass of the quasi-electrons infinite!

Somehow there is something badly wrong with these infinitely heavy quasi-electrons. Nature seems to share this concern: Without exception, one observes that eventually some other stable quantum matter state takes over (Fig. 2). These phenomena are currently under intense investigation, and it is clear that they can be quite strange. Recently a quantum version of a liquid crystal was discovered (*5*) but generically strange forms of superconductivity were found (*3*, *4*), including a superconductor that appears to be indestructible by magnetic fields (*6*).

These observations beg for an explanation in terms of a triumphant mathematical theory, but the efforts of the theorists have gotten stuck in running variations on the established themes of bosonic matter and the Fermi liquid (*4*): One finds the fermion signs, in one or the other disguise, as the proverbial brick wall blocking any progress. The "heavy fermion" quantum criticality highlighted here is quite instrumental in forcing us to face the fact that there is still a vast quantum territory lying behind our intellectual horizon that awaits further exploration. The 20-year-long struggle of the physics community with superconductivity at high temperatures, as found in copper oxides, might well be rooted in the sign problem: Although the empirical situation is less clear, there are indications that this high-T_c superconductivity is born from a quantum critical state (*11*). But the fermion signs infest all of physics. In high-energy physics this is well recognized in the context of quark matter, but it might even be consequential in the most fundamental realms (*12*). The modern way of thinking about the ultimate origin of space-time (and everything else) has quantum emergence as a common denominator, but even string theory rests in this regard on intuitions originating in the earthly realms. There are plenty of fermions in such theories, but they are instinctively taken to be of the Fermi-liquid kind, and there is plenty of room for big surprises caused by the fermion signs at the very bottom.

References and Notes

1. J. Cardy, *Scaling and Renormalization in Statistical Physics* (Cambridge Univ. Press, Cambridge, 1996).
2. S. Sachdev, *Quantum Phase Transitions* (Cambridge Univ. Press, New York, 1999).
3. P. Coleman, A. J. Schofield, *Nature* **433**, 226 (2005).
4. H. von Löhneisen, A. Rosch, M. Vojta, P. Wölfle, *Rev. Mod. Phys.* **79**, 1015 (2007).
5. R. A. Borzi *et al.*, *Science* **315**, 214 (2007); published online 22 November 2006 (10.1126/science.1134796).
6. F. Levy, I. Sheikin, A. Huxley, *Nature Phys.* **3**, 460 (2007).
7. A. J. Leggett, *Science* **319**, 1203 (2008)
8. I. Bloch, *Science* **319**, 1202 (2008).
9. S. Lloyd, *Science* **319**, 1209 (2008).
10. M. Troyer, U. J. Wiese, *Phys. Rev. Lett.* **94**, 170201 (2005).
11. J. Zaanen, *Nature* **430**, 513 (2004) and references therein.
12. H. Georgi, *Phys. Rev. Lett.* **98**, 221601 (2007).
13. I thank F. Krueger for his work on the figures.

10.1126/science.1152443

PERSPECTIVE

Supersolidity

M. H. W. Chan

The observation of nonclassical rotational inertia (NCRI) by the torsional oscillator in 2004 gave rise to a renaissance in the study of solid helium-4. Recent theoretical and experimental studies found evidence that disorder in the solid plays a key role in enabling superfluidity. A recent experiment found a marked increase in the shear modulus that shares the same temperature and helium-3 impurity concentration dependence as that of NCRI. This correlation indicates that the onset of superfluidity requires the pinning and stiffening of the dislocation network by helium-3.

Shortly after the discovery of superfluidity in liquid ^{4}He (*1*, *2*), the possibility of the same phenomenon occurring in solid helium was raised by Wolfke (*3*). Careful theoretical consideration of the problem (*4*–*7*) suggested that the possible presence of quantum mechanically induced or zero-point lattice vacancies could facilitate such a "supersolid." In this scenario the superfluid fraction, which reaches 100% in liquid helium, may be immeasurably small. Nevertheless, the suggestion spurred considerable experimental effort in search of evidence for the supersolid phase. Other than some interesting anomalies in the ultrasound experiments (*8*), these efforts were unsuccessful (*9*). The situation changed in 2004 when we reported (*10*, *11*) superfluid-like behavior of solid helium samples housed within a torsional oscillator (TO).

In an ideal TO the resonant period is given by $2\pi(I/G)^{1/2}$, where G is the torsional spring constant of the torsion rod and I the rotational inertia of the torsion bob. We observed that below 200 mK, the resonant period of such an oscillator drops rather abruptly. A number of control experiments led us to conclude that the period drop was due to the solid ^{4}He confined inside the torsion bob oscillating with an effective moment of inertia I that is smaller than the high-temperature, classical value. This is known as nonclassical rotational inertia (NCRI), where $I(T) = I_{\text{classical}}[1 - f_s(T)]$ and $f_s(T)$ is the superfluid fraction (*7*). f_s becomes distinguishable from noise at an onset temperature, $T_0 \sim 200$ mK, and grows at first gradually and then more rapidly with decreasing temperature before saturating below ~50 mK (Fig. 1). We found $f_s \sim 1\%$ in the low-temperature limit for solid samples grown inside an annulus of 1 mm in width, as well as for those confined within porous structures having characteristic lengths from nanometers (*10*) to half a micrometer (*12*). The measured value of f_s is attenuated when the oscillation speed exceeds a value corresponding to several quanta of circulation, suggesting that the important excitations in the system are vortices. The phenomenon is immensely sensitive to ^{3}He impurities, even down to a concentration of x_3 in the 1 part per billion (ppb) level. The temperature at which f_s reaches half its saturated value, $T_{1/2}$, increases smoothly from 30 mK at $x_3 = 1$ ppb to 500 mK at $x_3 = 85$ parts per million (ppm) (*10*, *13*).

Department of Physics, Pennsylvania State University, University Park, PA 16802, USA. E-mail: chan@phys.psu.edu

A phenomenological model that captures a great deal of the experimental findings is the vortex liquid model proposed by Anderson (*14*). The attenuation of f_s with oscillation speed is attributed to the nonlinear susceptibility of the entangled collection of many thermally activated vortices. The ability of the vortices to move counter to the time-dependent superflow (relative to the cell's oscillation) results in the screening of the supercurrents. As the temperature is lowered, the motion and number of vortices are reduced so that f_s becomes finite. One prediction of the model is an increase in T_0 with increasing measurement frequency, and it was confirmed for the same sample (x_3 = 0.3 ppm) that $T_0 \sim 160$ mK at 496 Hz and $T_0 \sim 240$ mK at 1173 Hz (*15*).

The observation of NCRI has now been replicated in at least three other laboratories (*16*–*19*). Although the temperature dependence of $f_s(T)$ is entirely reproducible, its magnitude varies substantially. The low-temperature supersolid fraction ranges from as little as 0.015% to as much as 20%, the latter of which was reported by Rittner and Reppy in their studies of extremely narrow annuli (0.15 mm width) of solid helium (*17*). They also found f_s to be substantially reduced by thermally annealing the sample (*16*). The large variation in f_s, the effects of annealing, and the lack of evidence for zero-point vacancies (*20*) in the $T = 0$ limit support the theoretical consensus that superfluidity does not exist in a perfect crystal (*20*, *21*).

Three types of disorder have been considered to be responsible for the phenomenon: glassy regions, grain boundaries, and dislocation lines. Glassy regions have been proposed primarily because they lack crystalline order, thus making them more amenable for superfluidity. Indeed, a quantum Monte Carlo simulation (*22*) found that when disorder is quenched into the

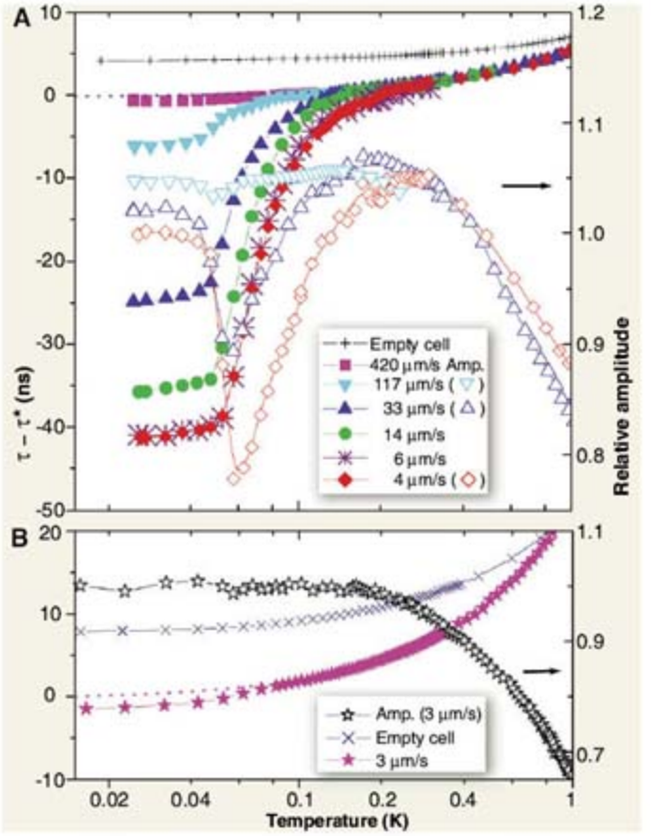

Fig. 1. (**A**) The period shift (left scale, filled symbols) and the relative oscillation amplitude (right scale, open symbols) of the TO for different maximum oscillation speeds as measured by Kim and Chan (*11*). The introduction of solid ^{4}He into the annular open space in the torsion cell increased the resonant period by 3012 ns. (**B**) The period shift was greatly reduced when measurements were carried out in a cell with a barrier inserted in the annulus. [Figure reproduced from (*11*)]

solid phase of ^{4}He it exhibits superfluid characteristics, indicating that NCRI may be the consequence of percolating "superglass" regions. The major difficulty with this idea is that such a glass phase has never been detected in x-ray or other diffraction studies, past or present. Results from a recent high-precision specific-heat study are also inconsistent with glassy behavior (*23*). Instead of the expected linear dependence on T for glasses, a peak with a maximum height of ~20 μJ/mol-K (2.5×10^{-6} k_B per ^{4}He atom, where k_B is Boltzmann's constant) is found. The peak is centered near 75 mK (T_0 of NCRI in 1 ppb ^{4}He) in all solid samples studied. This peak suggests that there is indeed a genuine thermodynamic phase transition separating the normal and the supersolid phases.

In the grain boundary model, it is proposed that liquid superfluid films flow along the interfaces of small crystalline grains and give rise to NCRI (*24*–*26*). This indicates that f_s scales with the total area of the grain boundaries. It is known that samples grown by the blocked capillary method, the method used in all but one TO experiment to date, commonly result in crystal grains with linear dimensions larger than 0.1 mm (*27*). In contrast, solid helium confined in porous Vycor glass (having a typical pore size of 7 nm) has a surface area per unit volume that is roughly 10^4 times as large, and yet f_s is on the same order (~1%) as that of many bulk solid samples.

Dislocation lines in solid ^{4}He form a three-dimensional network consisting of a vast number of dislocation segments and nodes, the latter of which are essentially immobile. Ultrasound measurements indicated that when an oscillating stress field is imposed, the dislocation segments vibrate with little or no damping below 1 K (*28*). The network is characterized by the total dislocation line length per unit volume, λ, and network loop length, L_N, between nodes. In single crystals it was found that $0.1 < \lambda^* L_N^2 < 0.3$, where $\lambda \sim 1 \times 10^6$ cm^{-2} and $L \sim 5$ μm. The dislocation lines can also be pinned by ^{3}He impurities that condense onto them (*29*). The average distance, L_3, between the ^{3}He atoms on a dislocation line is determined by the binding energy, $E_b/k_B \sim 0.5$ K (*13*, *29*, *30*), and the temperature. At a fixed x_3, there is a specific crossover from network pinning to impurity pinning when L_3 becomes shorter than L_N. The characteristic temperatures, such as T_0 and $T_{1/2}$, of samples of different x_3 are found to track the crossover temperature when impurity pinning dominates (*13*), implying that the appearance of NCRI is related to the stiffening of the dislocation network. A direct measurement of the shear modulus has recently confirmed this interpretation. Day and Beamish (*31*) found a marked increase (between 5 and 20%) of the shear modulus, μ, of solid helium (with $x_3 = 0.3$ ppm) below 250 mK. The temperature dependence of μ resembles that of f_s found in TO measurements. When the measurements were repeated with just 1 ppb of ^{3}He impurities, the increase in μ shifted to a lower temperature, consistent with the TO results (Fig. 2).

The stiffening of the dislocation network and the onset of NCRI are clearly related. However, there is as yet no understanding of how these phenomena are correlated. It has been suggested that the long-range phase coherence inherent in supersolidity requires a rigid dislocation network that is pinned by ^{3}He impurities (*13*, *31*). It has also been suggested that superflow takes place along the dislocation lines (*32*, *33*) and that supersolidity appears when these dislocation lines are cross-linked into a three-dimensional network. The problem with this latest idea is that typical densities of dislocations are three orders of magnitude too low to support $f_s \sim 1\%$, let alone 20%.

There is also the possibility of a more mundane connection between the two phenomena without invoking supersolidity. In a real TO, the resonant period depends on the exact dimensions, densities, and elastic moduli of all its constituent parts (*34*). The stiffening of solid helium inside the torsion cell will lead to an enhancement of the overall rigidity of the system and therefore lower the resonant period, mimicking mass decoupling. A careful simulation study by means of the finite element method of the annular TO used by us (*11*) indicates that the reduction in

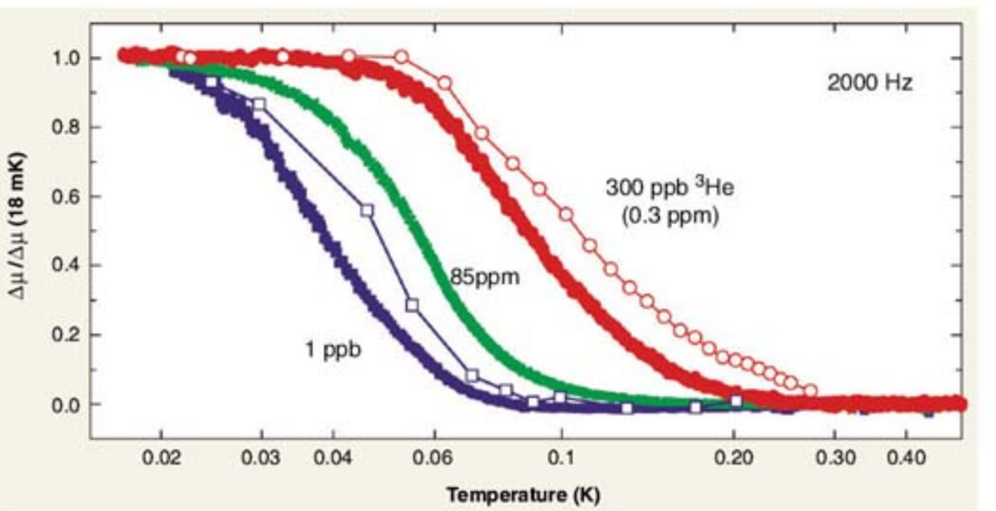

Fig. 2. Shear modulus anomaly in solid ^{4}He with 1 ppb, 0.3 ppm, and 85 ppm of ^{3}He impurities as measured by Day and Beamish (*31*). Changes in shear modulus, Δμ, have been scaled by the values at 18 mK in order to compare temperature dependence. Open circles with lines are similarly scaled NCRI data from TO measurements on 1 ppb (*27*) and 0.3 ppm (*11*) samples.

the resonant period (~10^6 ns) due to a 10% increase in μ of solid helium is less than 0.5 ppm or 0.5 ns (*35*). This decrease is a factor of 100 less than the period drop observed experimentally (Fig. 1). In addition, it is difficult to correlate dislocation stiffening to NCRI for solid helium confined in porous gold (*12*) and particularly in Vycor glass (*10*), because the dimensions of solid helium are much smaller than the micrometer-sized dislocation segments.

An important test that should clarify the relation and the possible causality of the two phenomena would be repeating both the shear modulus and TO experiments with the same sample of ultrahigh-purity ^{3}He. Ultrasound measurements indicate that the dislocation network in ultrahigh-purity ^{3}He, particularly in the high-pressure, hexagonal-close-packed (hcp) phase ($P > 10^7$ Pa), responds to isotopic impurities in much the same way as does hcp ^{4}He (*36*), the solid helium phase of current interest. A likely outcome would be the appearance of a similar increase in the shear modulus without any (or a greatly reduced) concomitant drop in the period of the TO because ^{3}He is a fermion. However, given the history of the last 3.5 years, there may well be other unforeseen surprises.

References and Notes

1. P. Kapitza, *Nature* **141**, 74 (1938).
2. J. F. Allen, A. D. Misener, *Nature* **141**, 75 (1938).
3. M. Wolfke, *Ann. Acad. Sci. Techn. Varsovie* **6**, 14 (1939).
4. L. Reatto, *Phys. Rev.* **183**, 334 (1969).
5. A. F. Andreev, I. M. Liftshitz, *Sov. Phys. JETP* **29**, 1107 (1969).
6. G. V. Chester, *Phys. Rev. A* **2**, 256 (1970).
7. A. J. Leggett, *Phys. Rev. Lett.* **25**, 1543 (1970).
8. J. M. Goodkind, *Phys. Rev. Lett.* **89**, 095301 (2002).
9. M. W. Meisel, *Physica B (Amsterdam)* **178**, 121 (1992).
10. E. Kim, M. H. W. Chan, *Nature* **427**, 225 (2004).
11. E. Kim, M. H. W. Chan, *Science* **305**, 1941 (2004).
12. E. Kim, M. H. W. Chan, *J. Low Temp. Phys.* **138**, 859 (2005).
13. E. Kim *et al.*, *Phys. Rev. Lett.* **100**, 065301 (2008).
14. P. W. Anderson, *Nature Phys.* **3**, 160 (2007).
15. Y. Aoki, J. C. Graves, H. Kojima, *Phys. Rev. Lett.* **99**, 015301 (2007).
16. A. S. C. Rittner, J. D. Reppy, *Phys. Rev. Lett.* **97**, 165301 (2006).
17. A. S. C. Rittner, J. D. Reppy, *Phys. Rev. Lett.* **98**, 175302 (2007).
18. A. Penzev, Y. Yasuta, M. Kubota, *J. Low Temp. Phys.* **148**, 677 (2007).
19. M. Kondo, S. Takada, Y. Shibayama, K. Shirahama, *J. Low Temp. Phys.* **148**, 695 (2007).
20. B. K. Clark, D. M. Ceperley, *Phys. Rev. Lett.* **96**, 105302 (2006).
21. See, for example, the review in (*37*).
22. M. Boninsegni, N. V. Prokof'ev, B. V. Svistunov, *Phys. Rev. Lett.* **96**, 105301 (2006).
23. X. Lin, A. C. Clark, M. H. W. Chan, *Nature* **449**, 1025 (2007).
24. E. Burovski, E. Kozik, A. Kuklov, N. V. Prokof'ev, B. V. Svistunov, *Phys. Rev. Lett.* **94**, 165301 (2005).
25. S. Sasaki, R. Ishiguro, F. Caupin, H. J. Maris, S. Balibar, *Science* **313**, 1098 (2006).
26. L. Pollet *et al.*, *Phys. Rev. Lett.* **98**, 135301 (2007).
27. A. C. Clark, J. T. West, M. H. W. Chan, *Phys. Rev. Lett.* **99**, 135302 (2007).
28. R. Wanner, I. Iwasa, S. Wales, *Solid State Commun.* **18**, 853 (1976).
29. I. Iwasa, K. Araki, J. Suzuki, *J. Phys. Soc. Jpn.* **46**, 1119 (1979).
30. M. A. Paalanen, D. J. Bishop, H. W. Dail, *Phys. Rev. Lett.* **46**, 664 (1981).
31. J. Day, J. R. Beamish, *Nature* **450**, 853 (2007).
32. S. I. Shevchenko, *Sov. J. Low Temp. Phys.* **13**, 61 (1987).
33. M. Boninsegni *et al.*, *Phys. Rev. Lett.* **99**, 035301 (2007).
34. Z. Nussinov, A. V. Balatsky, M. J. Graf, S. A. Trugman, *Phys. Rev. B* **76**, 014530 (2007).
35. A. C. Clark, J. D. Maynard, M. H. W. Chan, http://arxiv.org/abs/0711.3619v2 (2008).
36. J. R. Beamish, J. P. Franck, *Phys. Rev. B* **28**, 1419 (1983).
37. N. V. Prokof'ev, *Adv. Phys.* **56**, 381 (2007).

38. I acknowledge the NSF for support and J. R. Beamish, J. D. Maynard, J. D. Reppy, E. Kim, A. C. Clark, X. Lin, and J. T. West for informative discussions. I thank J. R. Beamish for providing Fig. 2.

10.1126/science.1155302

PERSPECTIVE

Quantum Information Matters

Seth Lloyd

This Perspective discusses the role that quantum information plays in determining the quantum-mechanical aspects of matter. Beginning with the entwined concepts of information and entropy, the article discusses how quantum information theory can supply us with novel concepts and techniques for understanding how matter behaves at the most microscopic of levels.

At first glance, the relationship between quantum information and quantum matter seems tenuous. Information is not very material: It is more concept than thing. Quantum information is even more ethereal than classical information. Matter, by contrast, is solid stuff, reliable and down to earth. The word for matter comes from the Latin *materia*: "wood for building, construction materials." Quantum matter is particularly solid: Quantum mechanics guarantees the stability of the elementary particles and atoms that make up the building blocks of nature. (A hydrogen atom constructed according to the laws of classical electromagnetism would explode in a burst of radiation in less than a trillionth of a second. A hydrogen atom constructed according to the laws of quantum mechanics can last the age of the universe.) Matter seems to be about energy and stability; when it comes to discussing its properties, why should quantum information matter?

Department of Mechanical Engineering, Massachusetts Institute of Technology, MIT 3-160, Cambridge, MA 02139, USA. E-mail: slloyd@mit.edu

In fact, when it comes to matter, quantum information matters a lot. First of all, information is not as immaterial as it might seem. By the end of the 19th century, the great statistical mechanicians Maxwell, Boltzmann, and Gibbs had firmly established that the physical quantity called entropy, which limits the efficiency of heat engines, was in fact a form of information—information about the microscopic motions of atoms and molecules. The very first paper about quantum matter, Planck's 1901 paper on black-body radiation, was also fundamentally about information and quantum mechanics (*1*). In that paper, Planck not only introduced his famous constant to establish the relationship between energy and frequency ($E = h\nu$), he also established the constant of proportionality between information (defined statistically) and entropy. This constant, now called Boltzmann's constant, $k_B = 1.3806503 \times 10^{-23}$ J/K, can be thought of as establishing the relationship between information and entropy: One bit corresponds to an amount of entropy equal to k_B times the logarithm of 2. Planck's paper established that the universe was, at bottom, digital.

Quantum information theory studies the consequences of the digital nature of the universe. Quantum computers are devices that store information at the level of individual quanta (photons, electrons, atoms, etc.) and process that information in a way that preserves quantum coherence (*2*). Quantum communication systems transmit information at the ultimate rates allowed by the laws of quantum mechanics. Although, as noted above, information has played an important role in quantum mechanics since the very beginning, quantum information theory as a distinct discipline is a young field. Before Shor's 1994 discovery that quantum computers could in principle factor large numbers and so break commonly used codes (*2*), quantum information mattered to only a handful of scientists.

During the 1960s and 1970s, Richard Feynman was involved in attempts to use classical digital computers to evaluate the consequences of quantum field theory. He observed that quantum mechanics was hard to program on a classical digital computer. The reason for this difficulty was straightforward: Quantum mechanics possesses a variety of strange and counterintuitive features, and features that are hard for human beings to comprehend are also hard for classical computers to represent at the level of individual classical bits. Consider that a relatively small quantum system consisting of a collection of 300 electron spins "lives" in $2^{300} \approx 10^{90}$ dimensional space. As a result, merely writing down the quantum state of the spins in a classical form as a sequence of bits would require a computer the size of the universe, and to compute the evolution of that state in time would require a computer much larger than that.

Fig. 1. This figure shows, in an impressionistic fashion, the state of a spin system performing an adiabatic quantum computation. The first panel shows the initial state of the spins. They are all aligned along the x axis by a strong magnetic field. The magnetic field is gradually turned off, and, at the same time, a "problem" Hamiltonian whose ground state encodes the answer to some hard problem is gradually turned on. In the center panel, both the magnetic field and the problem Hamiltonian are of equal strength, and the spins are in a fully entangled state. In the final panel, the magnetic field has gone to zero and the spins are in the ground state of the problem Hamiltonian. The answer to the problem can now be obtained by reading off the states of the spins with the convention that spin up = 0 and spin down = 1.

In 1982, Feynman noted that if one has access to a quantum-mechanical device for representing the state of the spins and for transforming that state, rather than a classical device, then the computation of the time evolution of such a system can be much more economical (*3*). Consider a collection of 300 two-level quantum systems, or qubits, one for each electron spin. Suppose that one sets up or programs the interactions between those qubits to mimic the dynamics of the collection of spins. The resulting device, which Feynman called a universal quantum simulator, will then behave as a quantum analog computer, whose dynamics form an analog of the spin dynamics. Since Feynman's proposal, researchers in quantum information have created detailed protocols for programming quantum analog computers, including reproducing the behavior of fermions (*4*, *5*) and gauge fields. Large-scale quantum simulators have actually been constructed out of crystals of calcium fluoride (*6*). Each crystal contains a billion billion spins, which can be programmed using techniques of nuclear magnetic resonance to simulate the behavior of a wide variety of solid-state systems. These solid-state quantum simulators have already revealed a variety of previously unknown quantum phenomena, including spin transport rates that are startlingly higher than the rates predicted by semiclassical theory.

The chameleon-like ability of quantum computers to change their behavior not only allows them to simulate other quantum systems but also gives rise to novel methods for solving computational problems. Many classically hard problems take the form of optimization problems—for example, the traveling salesman problem, in which one aims to find the shortest route connecting a set of cities. Such optimization problems can be mapped onto a physical system, in which the function to be optimized is mapped onto the energy function of the system. The ground state of the physical system then represents a solution to the optimization problem. A common classical technique for solving such problems is simulated annealing: One simulates the process of gradually cooling the system in order to find its ground state (*7*). However, simulated annealing is bedeviled by the problem of local minima, states of the system that are close to the optimal states in terms of energy but very far away in terms of the particular configuration of the degrees of freedom of the state. To avoid getting stuck in such local minima, one must slow the cooling process to a glacial pace in order to ensure that the true ground state is reached in the end.

Quantum computing provides a method for getting around the problem of local minima. Rather than trying to reach the ground state of the system by cooling, one uses a purely quantum-mechanical technique for finding the state (*8*). One starts the system with a Hamiltonian, or energy functional, whose ground state is simple to prepare (for example, "all spins are sideways"). Then one gradually deforms the Hamiltonian from the simple dynamics to the more complex dynamics, whose ground state encodes the answer to the problem in question. If the deformation is sufficiently gradual, then the adiabatic theorem of quantum mechanics guarantees that the system remains in its ground state throughout the deformation process. When the adiabatic deformation is complete, then the state of the system can be measured to reveal the answer.

Adiabatic quantum computation (also called quantum annealing) represents a purely quantum way to find the answer to hard problems (Fig. 1). How powerful is adiabatic quantum computation? The answer is nobody knows for sure. The key question is what is sufficently gradual deformation? That is, how slow does the deformation have to be to guarantee that the transformation is adiabatic? The answer to this question lies deep in the heart of quantum matter. As one performs the transformation from simple to complex dynamics, the adiabatic quantum computer goes through a quantum phase transition. The maximum speed at which the computation can be performed is gov-

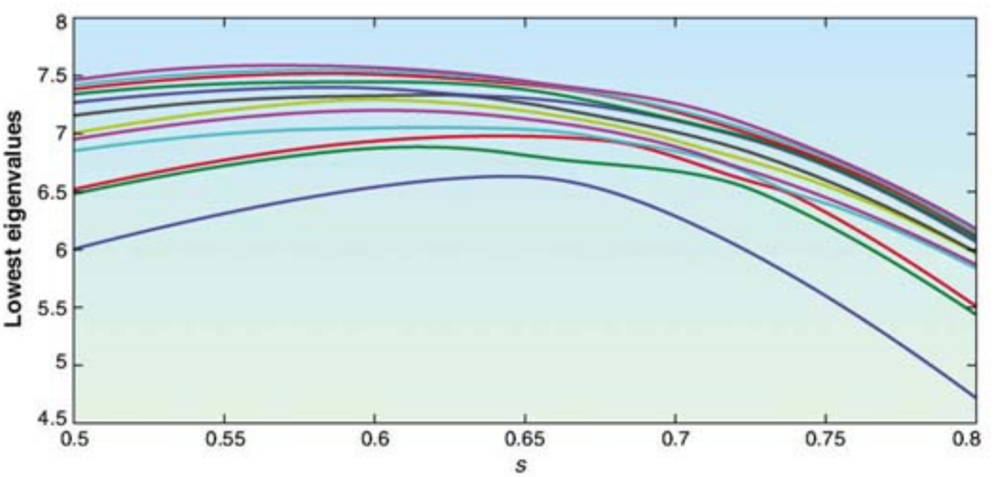

Fig. 2. The figure shows the 12 lowest energy levels of a 16-qubit quantum computer undergoing an adiabatic quantum computation. Over the course of the computation, the system's Hamiltonian goes from a simple form to a complex form whose ground state encodes an instance of a hard computational problem. The parameter s tells how simple or complex the Hamiltonian is. For s = 0.05, the Hamiltonian is relatively simple. At the point s = 0.8, the Hamiltonian is complex and its ground state encodes the answer to the problem. At the intermediate point s = 0.66, the Hamiltonian undergoes a phase transition between its simple and complex forms. At this point, the gap between the ground-state energy and the first excited-state energy reaches its minimum value and the state of the system is maximally entangled. The time it takes to perform the computation is inversely proportional to the size of this gap. Just how the gap scales with the size of the system is an open question in both quantum computation and the theory of quantum phase transitions.

erned by the size of the minimum energy gap of this quantum phase transition (Fig. 2). The smaller the gap, the slower the computation must be. The scaling of gaps during phase transitions (gapology) is one of the key disciplines in the study of quantum matter (*9*). Although scaling of the gap has been calculated for many familiar quantum systems, such as Ising spin glasses, calculating the gap for adiabatic quantum computers that are solving hard optimization problems seems to be just about as hard as solving the problem itself.

Few quantum computer scientists believe that adiabatic quantum computation can solve the traveling salesman problem. Nonetheless, there is good reason to believe that adiabatic quantum computation can outperform simulated annealing on a wide variety of hard optimization problems.

How do you build an adiabatic quantum computer? You need a quantum system that can be programmed to enact different Hamiltonians whose ground states instantiate the solutions to hard problems. The dynamics of the system must be sufficiently flexible to be adiabatically deformed from simple to complex Hamiltonians. Finally, you have to be able to measure the final state of the system to read out the answer to the problem.

Quantum systems found in nature are typically too inflexible or too uncontrollable to meet the requirements for adiabatic quantum computation. Human-made quantum systems, in contrast, can be designed to meet those specifications. The solution arises from one of quantum information processing's most significant contributions to the study of quantum matter: the demonstration of macroscopic quantum coherence. Macroscopic quantum coherence arises when a relatively macroscopic system, such as a supercurrent containing billions of electrons, is able to exhibit collective quantum behavior. In 2001, for example, two groups were able to put superconducting loops in a macroscopic quantum superposition of supercurrent flowing clockwise and counterclockwise simultaneously (*10*, *11*). (Don't try to visualize this phenomenon; it is one of those quantum effects mentioned above that resist all intuitive explanation.) In 2003, my colleagues and I designed superconducting circuits that used macroscopic quantum coherence to implement adiabatic quantum computation (*12*). Although 16-qubit and 28-qubit devices based on this design have been constructed, claims that adiabatic quantum computers can solve all sorts of hard problems in a completely quantum-mechanical fashion have yet to be borne out (*13*, *14*). Even if adiabatic quantum computers fail to solve hard problems, such devices still constitute artificial systems that, as Feynman envisaged, can simulate the behavior of strange computational quantum matter.

Quantum information offers a wide variety of techniques for understanding quantum matter. One of the primary contributions of the field is a detailed picture of the weird form of quantum correlation known as entanglement (*2*). Entanglement initially made its way into quantum mechanics as a particularly egregious example of a counterintuitive quantum phenomenon. (Einstein referred to it as "spukhafte Fernwirkung," or "spooky action at a distance.") Quantum information theory has shown that, far from being exotic, entanglement is ubiquitous. Entanglement underlies the stability of the covalent bond; entanglement is a key feature of ground states of solid-state systems (*15*); even the vacuum of space is entangled (*16*)! In fact, the Hawking radiation emerging from black holes can be thought of as a particularly exotic form of vacuum entanglement (*17*).

Over the past few decades, quantum information theory has transcended its earlier role as an esoteric study of the foundations of quantum mechanics, to become an integral part of the science of quantum matter in all its forms. As its relationship with the theory of quantum matter becomes more elaborate and more intimate, quantum information theory has the potential to unravel some of the deep mysteries of physics. For example, the connection of entanglement with Hawking radiation suggests that quantum information may have a key role to play in understanding quantum gravity. Meanwhile, quantum information theory has suggested a wide variety of fundamental experiments in quantum matter, such as the demonstration of macroscopic quantum coherence mentioned above (*10*, *11*). Unexpected connections have arisen between transport theory in quantum matter and quantum information theory: Hopping electrons might be able to discern winning strategies for chess or Go more efficiently than classical chess or Go masters (*18*), or the efficiency of photosynthesis might arise because excitons moving through photocenters effectively implement a quantum computer algorithm (*19*). Finally, if we can continue to realize Feynman's vision of quantum simulation, we may someday be able to simulate the behavior not only of electrons and elementary particles but of the universe itself (*20*). The fact that simulating the entire universe requires a quantum computer as big as the universe should not stand in our way!

References

1. M. Planck, *Ann. Phys.* **4**, 553 (1901).
2. M. A. Nielsen, I. L. Chuang, *Quantum Computation and Quantum Information* (Cambridge Univ. Press, Cambridge, 2000).
3. R. P. Feynman, *Int. J. Theor. Phys.* **21**, 467 (1982).
4. S. Lloyd, *Science* **273**, 1073 (1996).
5. S. Bravyi, A. Kitaev, *Ann. Phys.* **298**, 210 (2002).
6. C. Ramanathan, S. Sinha, J. Baugh, T. F. Havel, D. G. Cory, *Phys. Rev. A* **71**, 020303(R) (2005).
7. S. Kirkpatrick, C. D. Gelatt, M. P. Vecchi, *Science* **220**, 671 (1983).
8. E. Farhi, J. Goldstone, S. Gutmann, *Science* **292**, 472 (2001).
9. S. Sachdev, *Quantum Phase Transitions* (Cambridge Univ. Press, Cambridge, 1999).
10. C. H. van der Wal *et al.*, *Science* **290**, 773 (2000).
11. R. Friedman, V. Patel, W. Chen, S. K. Tolpygo, J. E. Lukens, *Nature* **406**, 43 (2000).
12. W. M. Kaminsky, S. Lloyd, in *Quantum Computing and Quantum Bits in Mesoscopic Systems*, B. Ruggiero, P. Silvestrini, A. Leggett, Eds. (Kluwer Academic, Netherlands, 2003), pp. 229–236.
13. P. Judge, "D-Wave's quantum computer ready for latest demo," CNET News.com, 7 November 2007 (www.news.com/D-Waves-quantum-computer-ready-for-latest-demo/2100-1010_3-6217842.html).
14. S. K. Moore, "Prototype commercial quantum computer demo'ed," *IEEE Spectrum Online*, 13 February 2007 (www.spectrum.ieee.org/feb07/comments/1710).
15. M. M. Wolf, G. Ortiz, F. Verstraete, J. I. Cirac, *Phys. Rev. Lett.* **97**, 110403 (2006).
16. M. Cramer, J. Eisert, M. B. Plenio, J. Dreissig, *Phys. Rev. A* **73**, 012309 (2006).
17. S. W. Hawking, *Nature* **248**, 30 (1974).
18. E. Farhi, J. Goldstone, S. Gutmann, preprint available at http://xxx.lanl.gov/abs/quant-ph/0702144.
19. G. S. Engel *et al.*, *Nature* **446**, 782 (2007).
20. S. Lloyd, *Phys. Rev. Lett.* **88**, 237901 (2002).

10.1126/science.1154732

PERSPECTIVE

Looking to the Future of Quantum Optics

Ian A. Walmsley

Light has provided both fundamental phenomenology and enabling technology for scientific discovery for many years, and today it continues to play a central role in fundamental explorations and innovative applications. The ability to manipulate light beams and pulses with the quantum degrees of freedom of optical radiation will add to those advances. The future of quantum optics, which encompasses both the generation and manipulation of nonclassical radiation, as well as its interaction with matter, lies in the rich variety of quantum states that is now becoming feasible to prepare, together with the numerous applications in sensing, imaging, metrology, communications, and information processing that such states enable.

The main attributes of quantum light that distinguish it from classical light are the nature of its fluctuations and of its correlations. These distinguishing features have been known for many years, and precise formulations of what constitutes nonclassical light were devel-

oped in the 1960s. However, the past decade has seen marked advances in our ability to prepare specific quantum states of light that elucidate these distinctions and make use of them. Developing this ability further—to increase the distance over which quantum correlations (or entanglement) may be distributed, to increase the number of light quanta (photons) that occupy these entangled states, and to understand how to characterize, store, and exploit those states—is the direction of future research.

Classical light has a certain degree of randomness to it, even though the intensity and phase of a classical light beam or pulse may both be very precisely defined. This is not so for a quantum light beam, the photon number and phase of which cannot both be specified simultaneously. One consequence is that the number of photons in a classical light pulse fluctuates, whereas, for a quantum pulse, it may not. Similarly, the amplitudes of a quantum light beam may be less noisy than those of its classical counterpart.

Classical light is also restricted in the types of correlations that separate beams may have. For example, two light beams may be highly correlated in their wavelength or direction, though each beam individually may not have a well-defined wavelength or direction, respectively. Similarly, the beams may be correlated in the conjugate variables of time or position, or in two orthogonal polarizations. The difference for quantum light is that there may be strong correlations in both pairs of conjugate degrees of freedom at the same time. That is, two light beams in a pure quantum state may be highly correlated in both their direction and their position or in both wavelength and time. This is an example of quantum entanglement.

There are important consequences stemming from the fact that only the joint properties of the two (or more) beams can be said to have definite values. A well-known example of this is in secure communications, for which entanglement is a key property that allows the presence of an eavesdropper to be detected (*1*, *2*). Entanglement among many photons in many different modes is now becoming possible, and optics provides a means to explore the rich structure and dynamics of these complex quantum states.

Today, it is possible to create a broad range of quantum states of light that have no classical analog. There are two main routes to achieve this. The first is to use single emitters, such as individual atoms or excitons (an electron-hole pair), to emit single photons (*3*–*5*) (Fig. 1, A and B). It is possible to use this approach to entangle two emitter atoms by detecting one or more photons from each, provided the apparatus is arranged so that it is impossible to tell from which atom the detected photon has come (*6*–*8*). It will be possible to "daisy chain" this procedure: thus, to arrange that large numbers of atoms, each of which are remote from the others, eventually become entangled, which leads to a highly nonclassical state of many atoms that is mediated by photons.

The integration of quantum optics with technologies such as ion and atom traps, and indeed photonic microstructured cavities and waveguides, provides a deterministic way to swap entanglement between light and matter. One important avenue will be the implementation of quantum memories for photons, which can store information coded in these "flying qubits" in long-lived matter states or "stationary qubits" (*9*–*12*). This is a key technology for quantum communications and computational networks (Fig. 2). Reading out quantum correlations from matter provides a creative approach to sensing and measurement: It may be used to probe the dynamics of complex entangled states of matter with minimal back-action on the atoms. A recent example of this shows how the extraordinarily strong coupling between individual atoms injected into an optical cavity and the microwave field inside the cavity may be used to implement a true quantum nondemolition detector for photons, one that does not absorb the photon in order to measure it (*13*).

A different avenue is that of quantum optomechanics. Recent work has shown that it is possible to cool mirrors in optical cavities with the light force associated with the beams contained in the cavity; effectively, the momentum fluctuations of the mirror are modified by its collisions with the photons (*14*, *15*). In principle, it is possible to produce nonclassical states of the mirror motion in this way; perhaps this will eventually enable us to understand how to entangle a light beam with a truly macroscopic object.

The second route to generating quantum light is by means of nonlinear optics, such as parametric downconversion (Fig. 1, C and D), in which a light beam at one frequency generates two new light beams (the signal and idler), each near half the frequency of the pump. The "splitting" of the pump photon into two siblings

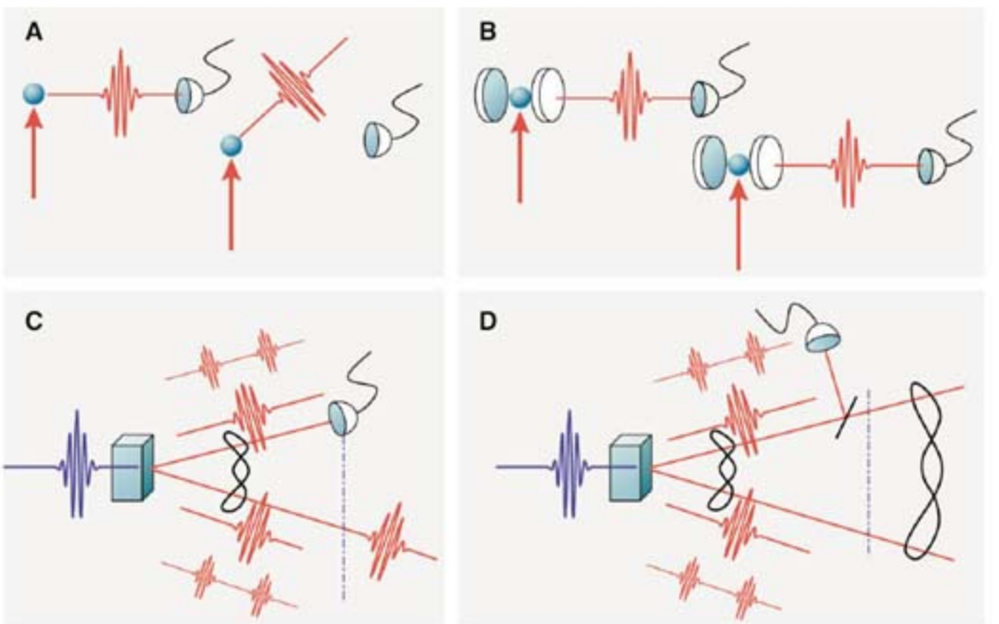

Fig. 1. Approaches to the generation of quantum light. (**A**) A single atom (or single semiconductor quantum dot or other quantum system containing a single electronic excitation), indicated by the sphere, is held in isolation. When it is excited by a laser (red arrow), it emits a single photon into the whole of space. Infrequently, the photon is emitted in the direction of a small photodector (hemispherical bucket). (**B**) A refinement of this approach, which determines the direction of photon emission, places the atom in an optical cavity, consisting of a pair of mirrors (discs). This approach to "shaping" the photons (so that they can be used with conventional optics and detectors) is called cavity quantum electrodynamics and is currently one of the most promising avenues to building multiatom and multiphoton nonclassical states. (**C**) The nonlinear optical process of parametric downconversion, in which a blue photon is split into a pair of red photons in the nonlinear optical microstructure (shaded cube). The signal and idler beams are quantum correlated (or entangled, as indicated by the black lasso) in their in-phase and in-quadrature amplitudes, in their time of generation and frequency, and in their position and direction, providing for the preparation of nonclassical states based on the detection of photons from one of the beams, such as "heralding" a single photon. (**D**) Conditional-state preparation may also increase the entanglement between signal and idler, if (for example) photons are subtracted from one of the beams. This is a component of entanglement distillation and enables Schrödinger cat–like states to be generated.

Department of Physics, University of Oxford, Clarendon Laboratory, Parks Road, Oxford OX1 3PU, UK. E-mail: walmsley@physics.ox.ac.uk

means that the signal and idler are highly entangled in photon number, in their amplitudes, in time-energy, and in position-direction. This provides several different capabilities. For example, it is possible to prepare new kinds of nonclassical states by means of conditional detection, such as one- and two-photon states (*16*), as well as "Schrödinger kitten" states—that is, states whose amplitudes have two distinct values at the same time—named for the famous "cat" that is simultaneously dead and alive (*17*). In terms of applications, fields that are specified by continuous variables such as amplitudes (as opposed to discrete variables such as photon number) have a very large information capacity. Further, even simple optical elements such as a beamsplitter (for example, a half-silvered mirror that combines two beams of light) can be used to entangle and disentangle the signal and idler beams, and photodetectors for amplitude may be very efficient. A goal for the near future is to demonstrate that the approach can be used to combine a large number of weakly entangled beams into a smaller number of highly entangled beams, a process known as entanglement "distillation" (*18*).

Conditional-state preparation based on detection, when combined with feedforward control, also forms the basis of an optical quantum computer (*19*). Here, future measurement sequences are determined by the outcomes of past measurements, enabling information processing with the use of complex entangled states prepared beforehand (*20*) (Fig. 2). Indeed, certain metrology can be brought to a precision of the tightest known quantum bound by this means (*21*). How far this can be pushed remains an open question.

A task for the immediate future is to make quantum states robust against the loss of photons, which is inevitable in propagating light over distance through optical systems (*22*). This would enable the distribution of entanglement over longer distances and address important questions regarding how entanglement scales in the presence of decoherence. Is it possible to find states of many photons or large amplitudes that do not decohere rapidly or that can be protected against noise by experimentally feasible control schemes?

In quantum optics, there is a symbiosis between innovative technology and science. Current exciting developments in optical technologies (such as materials, detectors, and lasers) and structures (such as waveguides, fibers, and photonic crystal microcavities) will play an increasingly important role in enabling the exploration of fundamental quantum phenomena and their applications in new technologies. The future of the field lies in the development of robust approaches for creating clean, pure-state quantum light beams and the precise control of their interaction with matter, both at the level of individual atoms and with macroscopic objects. Pushing this frontier will lead both to scientific discoveries, unraveling the enigmatic character of quantum correlations, and to innovative quantum technologies, many of which are yet to be envisioned.

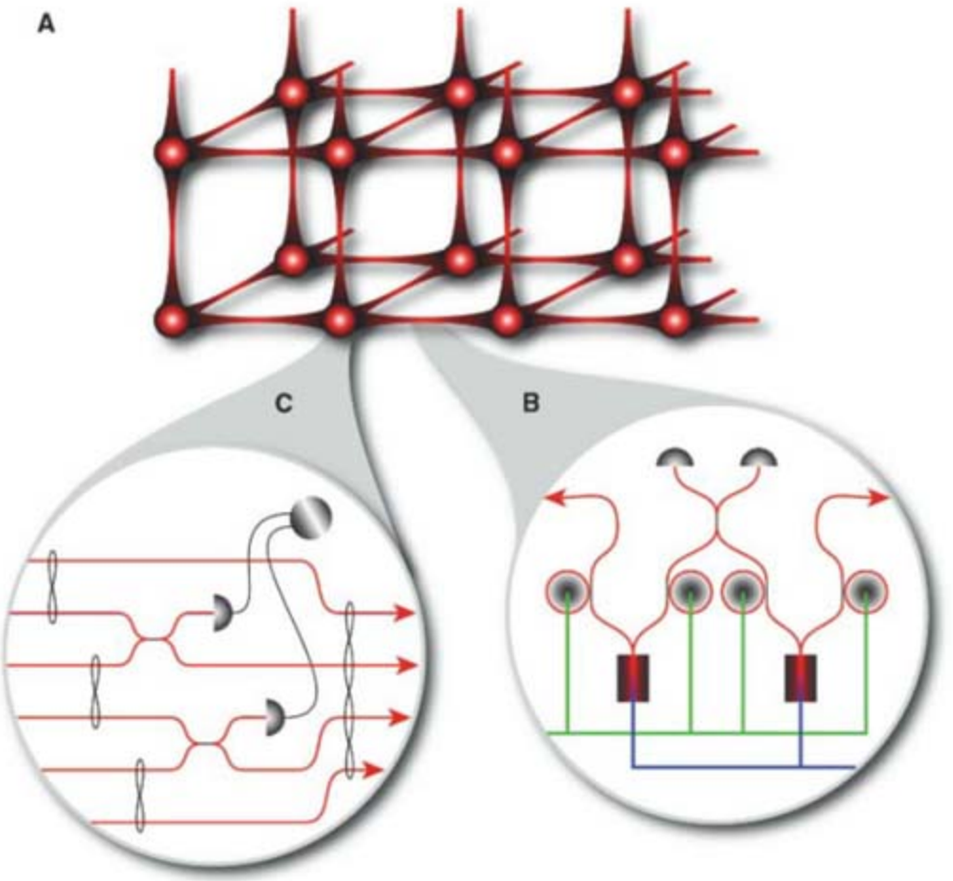

Fig. 2. A quantum network, as shown in (**A**), enables the generation of large-scale entanglement among many photons by means of feedforward. Sources of nonclassical light are distributed between the nodes of the network. The photons' quantum states generated by these sources are stored in quantum memories until required, illustrated in (**B**). The light is released into the network, and separate nodes are entangled by means of measurements on subsets of the photons, shown in (**C**), which herald the production of entangled quantum states among the other nodes. Classical communications are used to signal the network preparation and to control the operations that are then enacted on the output quantum states. This provides a possible scenario for building up many-photon entangled states over large distances. Aside from elucidating fundamental issues such as the robustness of scalability of entanglement, these networks will have applications in quantum communications, computation, and imaging.

References and Notes

1. N. Gisin, G. Ribordy, W. Tittle, H. Zbinden, *Rev. Mod. Phys.* **74**, 145 (2002).
2. A. Acin, N. Gisin, L. Masanes, *Phys. Rev. Lett.* **97**, 120405 (2006).
3. M. Hijlkema *et al.*, *Nat. Phys.* **3**, 253 (2007).
4. J. McKeever *et al.*, *Science* **303**, 1992 (2004).
5. R. M. Stevenson *et al.*, *Nature* **439**, 179 (2006).
6. S. Bose, P. L. Knight, M. B. Plenio, V. Vedral, *Phys. Rev. Lett.* **83**, 5158 (1999).
7. L. M. Duan, M. D. Lukin, J. I. Cirac, P. Zoller, *Nature* **414**, 413 (2001).
8. D. L. Moehring *et al.*, *Nature* **449**, 68 (2007).
9. M. Fleischhauer, M. D. Lukin, *Phys. Rev. A* **65**, 022314 (2002).
10. B. Julsgaard, J. Sherson, J. I. Cirac, J. Fiurášek, E. S. Polzik, *Nature* **432**, 482 (2004).
11. J. Nunn *et al.*, *Phys. Rev. A* **75**, 011401 (2007).
12. A. V. Gorshkov, A. Andre, M. Fleischhauer, A. S. Sorensen, M. D. Lukin, *Phys. Rev. Lett.* **98**, 123601 (2007).
13. S. Gleyzes *et al.*, *Nature* **446**, 297 (2007).
14. D. Vitali *et al.*, *Phys. Rev. Lett.* **98**, 030405 (2007).
15. D. Kleckner, D. Bouwmeester, *Nature* **444**, 75 (2006).
16. D. Achilles, Ch. Silberhorn, I. A. Walmsley, *Phys. Rev. Lett.* **97**, 043602 (2006).
17. A. Ourjoumtsev, R. Tualle-Brouri, J. Laurat, P. Grangier, *Science* **312**, 83 (2006).
18. D. E. Browne, J. Eisert, S. Scheel, M. B. Plenio, *Phys. Rev. A* **67**, 062320 (2003).
19. E. Knill, R. Laflamme, G. Milburn, *Nature* **409**, 46 (2001).
20. R. Prevedel *et al.*, *Nature* **445**, 65 (2007).
21. B. L. Higgins, D. W. Berry, S. D. Bartlett, H. M. Wiseman, G. J. Pryde, *Nature* **450**, 393 (2007).
22. W. Wasilewski, K. Banaszek, *Phys. Rev. A* **75**, 042316 (2007).
23. I acknowledge support from the European Commission through the Integrated Project Qubit Applications (QAP) and from the UK Engineering and Physical Sciences Research Council.

10.1126/science.1152495

Ubiquity of Biological Ice Nucleators in Snowfall

Brent C. Christner,[1]* Cindy E. Morris,[2] Christine M. Foreman,[3] Rongman Cai,[1] David C. Sands[4]

Aerosols play an integral role in climate by directly scattering or absorbing solar radiation, and indirectly these particles serve as condensation and ice nuclei in clouds. Ice formation in tropospheric clouds is required for snow and most rainfall. At temperatures > –40°C, ice formation is not spontaneous, and diverse substrates can act as catalysts of ice nucleation (*1*). Biological ice nucleators (IN) are the most active IN in nature, and some bacterial plant pathogens can catalyze ice formation at temperatures near –2°C. Although biological particles are important components of aerosols (*2*), existing technologies are unable to detect IN active at temperatures > –10°C (*3*), and the impact of biological IN on atmospheric processes remains ambiguous (*4*).

We examined the concentration and nature of IN active at temperatures > –10°C in 19 fresh snowfalls collected at mid- and high-latitude locations from October 2005 to June 2006 (*5*) and found the lowest cumulative concentration of IN at –9°C in Antarctic snowfall (four IN per liter of snow melt) and highest in samples from Montana and France (110 and 120 IN per liter, respectively). DNA-containing cells between 0.3 and 15 μm in diameter (1.5×10^4 to 5.4×10^6 cells per liter) accounted for <1% of the total particles in the snow samples (1.1×10^7 to 3.9×10^9 particles per liter), and the concentration of biological IN was independent of the particle and cell concentration (Fig. 1). The data presented in Fig. 1B are for the warmest temperature for which concentrations of IN could be calculated for all samples (–7°C), thereby facilitating comparison.

The activity of most known biological IN is mediated by proteins or proteinaceous compounds (*4*). Therefore, we reasoned that IN of biological origin would be inactivated by heat, whereas IN of mineral origin would not. Heat treatment inactivated 69% to 100% of the IN active at temperatures ≥ –7°C and ≤ –4°C (Fig. 1B). In bacteria, ice-nucleation activity depends on an intact cell wall and is conferred by a 120- to 180-kD protein embedded in the outer membrane (*6*). Disruption of the cell wall reduces ice-nucleation activity in bacteria (*7*). Hence, we postulated that lysozyme would decrease the ice-nucleation activity if bacteria were involved and found that 0 to 85% of the IN were susceptible to lysozyme (Fig. 1B). Incomplete hydrolysis and resistance to lysozyme could allow some bacterial cells to remain intact in the presence of lysozyme, and, therefore, our results are probably underestimating the concentration of bacterial IN in snowfall.

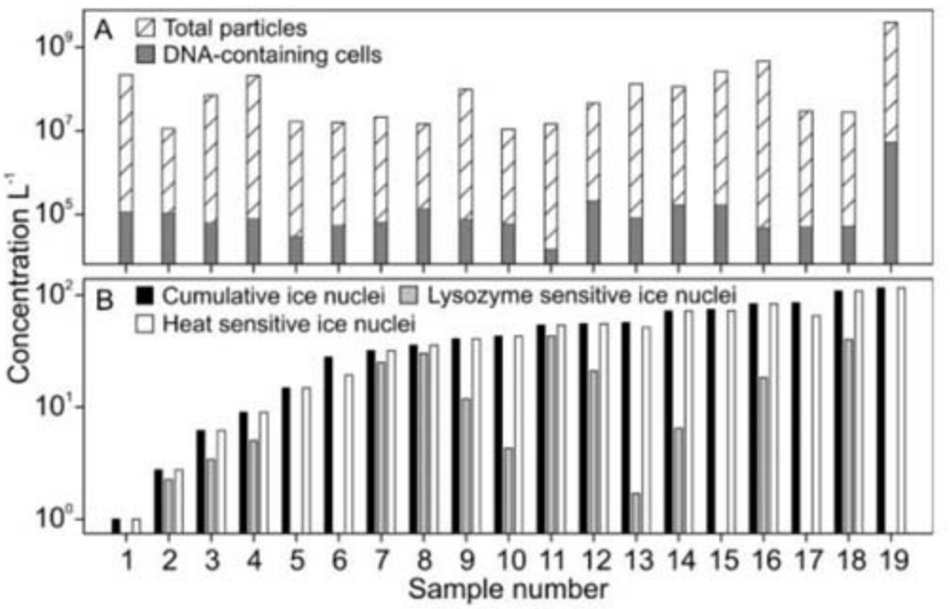

Fig. 1. Particle, cell, and freeze immersion IN concentrations in fresh snowfall collected from Montana, France, the Yukon, and Antarctica. (**A**) Quantity of particles and DNA-containing cells between 0.3 and 15 μm in diameter. (**B**) The cumulative concentration of IN (>0.2 μm) per liter of snow melt that were active at –7°C and sensitive to lysozyme and heat denaturation. From left to right, samples were ranked on the basis of increasing cumulative concentrations of IN. Samples 2, 5 to 8, 10 to 12, 17, and 18 were collected in the vicinity of Bozeman, Montana; samples 3, 9, 13 to 16, and 19 from the French Alps and Pyrenees in southern France, and samples 1 and 4 from Ross Island, Antarctica and the Wheaton Glacier, Yukon, respectively. See table S1 for numerical data and detail on sampling dates and site locations.

The samples analyzed were collected during seasons and in locations (e.g., Antarctica) devoid of deciduous plants, making it likely that the biological IN we observed were transported from long distances and maintained their ice-nucleating activity in the atmosphere. Assuming that all biological IN in the snow samples were DNA-containing cells, we estimate that about 0.4% of the cells in mid-latitude snowfalls were ice-nucleating active at temperatures between –7°C and –4°C. Although extrapolating the absolute composition and quantity of biological IN in clouds on the basis of concentrations in precipitation is difficult, our results indicate that these particles are widely dispersed in the atmosphere, and, if present in clouds, they may have an important role in the initiation of ice formation, especially when minimum cloud temperatures are relatively warm.

Biological IN were first described nearly 40 years ago (*1*); however, there are no estimates for the biological component of IN in the atmosphere. Our results reveal that biological IN active at warm temperatures are abundant in fresh snow samples and are ubiquitous in precipitation from worldwide locations. Unearthing a role for biological IN in the precipitation cycle has implications for deciphering feedbacks between the biosphere and climate, improving climate forecast models, and understanding atmospheric dissemination strategies of plant pathogens (*4*) and other microorganisms.

References and Notes

1. G. Vali, in *Biological Ice Nucleation and Its Applications*, R. E. Lee Jr., G. J. Warren, L. V. Gusta (American Phytopathological Society Press, St. Paul, MN, 1995), ch. 1.
2. R. Jaenicke, *Science* **308**, 73 (2005).
3. O. Möhler, P. J. DeMott, G. Vali, Z. Levin, *Biogeosciences* **4**, 1059 (2007).
4. C. E. Morris, D. Georgakapolous, D. C. Sands, *J. Phys. (Paris)* **121**, 87 (2004).
5. Materials and methods are available on *Science* Online.
6. H. Kawahara, *J. Biosci. Bioeng.* **94**, 492 (2002).
7. S. E. Lindow, E. Lahue, A. G. Govindarajan, N. J. Panopoulos, D. Gies, *Mol. Plant-Microbe Interact.* **2**, 262 (1989).

8. We thank F. Johnson, T. Leonard, S. Savage, M. Skidmore, and S. Trautman for collecting snow samples. This research was funded by a Louisiana State University faculty research grant awarded to B.C.C. and NSF grant OPP-0440943 to C.M.F.

Supporting Online Material

www.sciencemag.org/cgi/content/full/319/5867/1214/DC1
Materials and Methods
Table S1

27 August 2007; accepted 5 December 2007
10.1126/science.1149757

[1]Department of Biological Sciences, Louisiana State University, Baton Rouge, LA 70803, USA. [2]L'Institut Nationale de la Recherche Agronomique, Unité de Pathologie Végétale UR407, F-84140 Montfavet, France. [3]Center for Biofilm Engineering and Department of Land Resources and Environmental Sciences, Montana State University, Bozeman, MT 59717, USA. [4]Department of Plant Sciences and Plant Pathology, Montana State University, Bozeman, MT 59717, USA.

*To whom correspondence should be addressed. E-mail: xner@lsu.edu

Complete Chemical Synthesis, Assembly, and Cloning of a *Mycoplasma genitalium* Genome

Daniel G. Gibson, Gwynedd A. Benders, Cynthia Andrews-Pfannkoch, Evgeniya A. Denisova, Holly Baden-Tillson, Jayshree Zaveri, Timothy B. Stockwell, Anushka Brownley, David W. Thomas, Mikkel A. Algire, Chuck Merryman, Lei Young, Vladimir N. Noskov, John I. Glass, J. Craig Venter, Clyde A. Hutchison III, Hamilton O. Smith*

We have synthesized a 582,970–base pair *Mycoplasma genitalium* genome. This synthetic genome, named *M. genitalium* JCVI-1.0, contains all the genes of wild-type *M. genitalium* G37 except MG408, which was disrupted by an antibiotic marker to block pathogenicity and to allow for selection. To identify the genome as synthetic, we inserted "watermarks" at intergenic sites known to tolerate transposon insertions. Overlapping "cassettes" of 5 to 7 kilobases (kb), assembled from chemically synthesized oligonucleotides, were joined by in vitro recombination to produce intermediate assemblies of approximately 24 kb, 72 kb ("1/8 genome"), and 144 kb ("1/4 genome"), which were all cloned as bacterial artificial chromosomes in *Escherichia coli*. Most of these intermediate clones were sequenced, and clones of all four 1/4 genomes with the correct sequence were identified. The complete synthetic genome was assembled by transformation-associated recombination cloning in the yeast *Saccharomyces cerevisiae*, then isolated and sequenced. A clone with the correct sequence was identified. The methods described here will be generally useful for constructing large DNA molecules from chemically synthesized pieces and also from combinations of natural and synthetic DNA segments.

Mycoplasma genitalium is a bacterium with the smallest genome of any independently replicating cell that has been grown in pure culture (*1*, *2*). Approximately 100 of its 485 protein-coding genes are nonessential under optimal laboratory conditions when individually disrupted (*3*, *4*). However, it is not known which of these 100 genes are simultaneously dispensable. We proposed that one approach to this question would be to produce reduced genomes by chemical synthesis and introduce them into cells to test their capacity to provide the essential genetic functions for life (*4*, *5*). This paper describes a necessary step toward these goals—the complete chemical synthesis of a mycoplasma genome.

The actual synthesis and assembly of this genome presented a formidable technical challenge. Although chemical synthesis of genes has become routine, the only completely synthetic genomes so far reported have been viral (*6*–*8*). The largest previously published synthetic DNA that we are aware of is a 32-kb polyketide gene cluster (*9*). To accomplish assembly of the 582,970–base pair (bp) *M. genitalium* JCVI-1.0 genome, we needed to establish convenient and reliable methods for the assembly and cloning of much larger synthetic DNA molecules.

Strategy for synthesis and assembly. The native 580,076-bp *M. genitalium* genome sequence (*Mycoplasma genitalium* G37 ATCC 33530 genomic sequence; accession no. L43967) (*3*) was partitioned into 101 cassettes of approximately 5 to 7 kb in length (Fig. 1) that were individually synthesized, verified by sequencing, and then joined together in stages. In general, cassette boundaries were placed between genes so that each cassette contained one or several complete genes. This will simplify the future deletion or manipulation of the genes in individual cassettes. Most cassettes overlapped their adjacent neighbors by 80 bp; however, some segments overlapped by as much as 360 bp. Cassette 101 overlapped cassette 1, thus completing the circle.

Short "watermark" sequences were inserted in cassettes 14, 29, 39, 55 and 61. Watermarks are inserted or substituted sequences used to identify or encode information into DNA. This information can be either in noncoding or coding sequences (*10*–*12*). Most commonly, watermarking has been used to encrypt information within coding sequences without altering the amino acid sequences (*10*, *11*). We opted to insert watermark sequences at intergenic sites because synonymous codon changes may have substantial biological effects. Our watermarks are located at sites known to tolerate transposon insertions, so we expect minimal biological effects. They allow us to easily differentiate the synthetic genome from the native genome (*2*, *13*).

In addition to the watermarks, a 2514-bp insertion in gene MG408 (*msrA*), which includes an aminoglycoside resistance gene, was placed in

The J. Craig Venter Institute, Rockville, MD 20850, USA.

*To whom correspondence should be addressed. E-mail: hsmith@jcvi.org

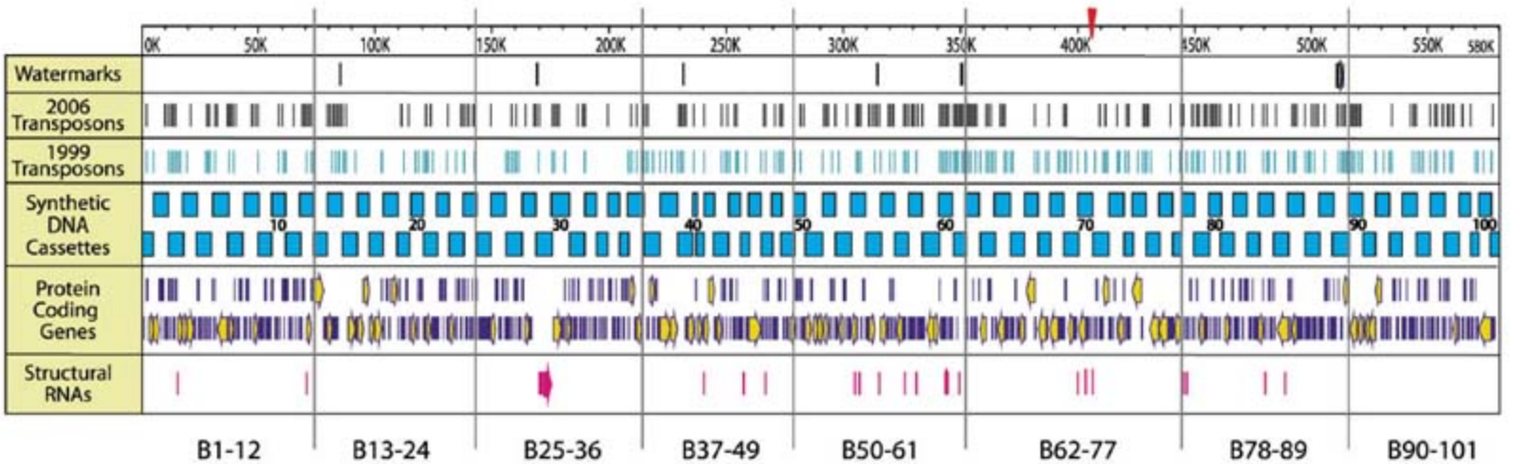

Fig. 1. Linear GenomBench (Invitrogen) representation of the circular 582,970-bp *M. genitalium* JCVI-1.0 genome. Features shown include locations of watermarks and the aminoglycoside resistance marker, viable Tn4001 transposon insertions determined in our 1999 and 2006 studies (*3*, *4*), overlapping synthetic DNA cassettes that comprise the whole genome sequence, 485 *M. genitalium* protein-coding genes, 43 *M. genitalium* rRNA, tRNA, and structural RNA genes, and B-series assemblies (Fig. 2). The red dagger on the genome coordinates line shows the location of the yeast/*E. coli* shuttle vector insertion. Table S1 lists cassette coordinates; table S2 has FASTA files for all 101 cassettes; table S3 lists watermark coordinates; table S4 lists the sequences of the watermarks.

cassette 89. It has been shown that a strain with this specific defect in this virulence factor cannot adhere to mammalian cells, thus eliminating pathogenicity in the best available model systems (*14*). The synthetic genome with all of the above insertions is 582,970 bp in length. Figure 1 is a map of the *M. genitalium* JCVI-1.0 genome showing various features such as genes, ribosomal and tRNAs, transposon insertions (*3*, *4*), watermark locations, and cassette positions.

Synthesis of DNA the size of our cassettes has become a commodity, so we opted to outsource their production, principally to Blue Heron Technology, but also to DNA2.0 and GENEART. The main challenges in this project were the assembly and cloning of synthetic DNA molecules larger than those previously reported. We planned a five-stage assembly as diagrammed in Fig. 2. In the first stage, sets of four neighboring cassettes were assembled by in vitro recombination and joined to a bacterial artificial chromosome (BAC) vector DNA to form circularized recombinant plasmids with ~24-kb inserts. For example, cassettes 1 to 4 were joined together to form the A1-4 assembly, cassettes 5 to 8 were assembled to form A5-8, and so forth. In the second stage, the 25 A-series assemblies were taken three at a time to form B-series assemblies. For example, B1-12 was constructed from A1-4, A5-8, and A9-12. This reduced the 25 A-assemblies to only 8 B-assemblies, each about 1/8 of a genome in size (~72 kb). In the third stage, the 1/8-genome B-assemblies were taken two at a time to make four C-assemblies, each approximately 1/4-genome (~144 kb) in size. These first three stages of assembly were done by in vitro recombination and cloned into *E. coli*. We encountered difficulties in carrying out the planned assembly and cloning of the half and whole synthetic genomes in *E. coli*. For this reason, the final assemblies were carried out in *S. cerevisiae* by transformation-associated recombination (TAR) cloning.

Assembly of synthetic cassettes by in vitro recombination. Figure 3 illustrates the reaction used for the first stage of assembly of the overlapping cassettes. Recombinant plasmids bearing the individual cassette DNA inserts were cleaved with the appropriate type IIS restriction enzymes, which cleave outside of their recognition site to one side, to release the insert DNA. After phenol-chloroform extraction and ethanol precipitation, the cassettes were used without removing vector DNA. The essential steps of the reaction are (i) the overlapping DNA molecules are digested with a 3′ exonuclease to expose the overlaps, (ii) the complementary overlaps are annealed, and (iii) the joints are repaired. Polymerase chain reaction (PCR) amplification was used to produce a unique BAC vector for the cloning of each assembly, with terminal overlaps to the ends of the assembly. Each PCR primer includes an overlap with one end of the BAC, a Not I restriction site, and an overlap with one end of the cassette assembly. Cassettes were assembled, four at a time, in the presence of the appropriate BAC vector. Because the *M. genitalium* JCVI-1.0 genome does not contain a Not I site, all of the assemblies can be released intact from the BAC.

For example, the assembly A66-69 was constructed by mixing together equimolar amounts of the four cassette DNAs and the linear PCR–

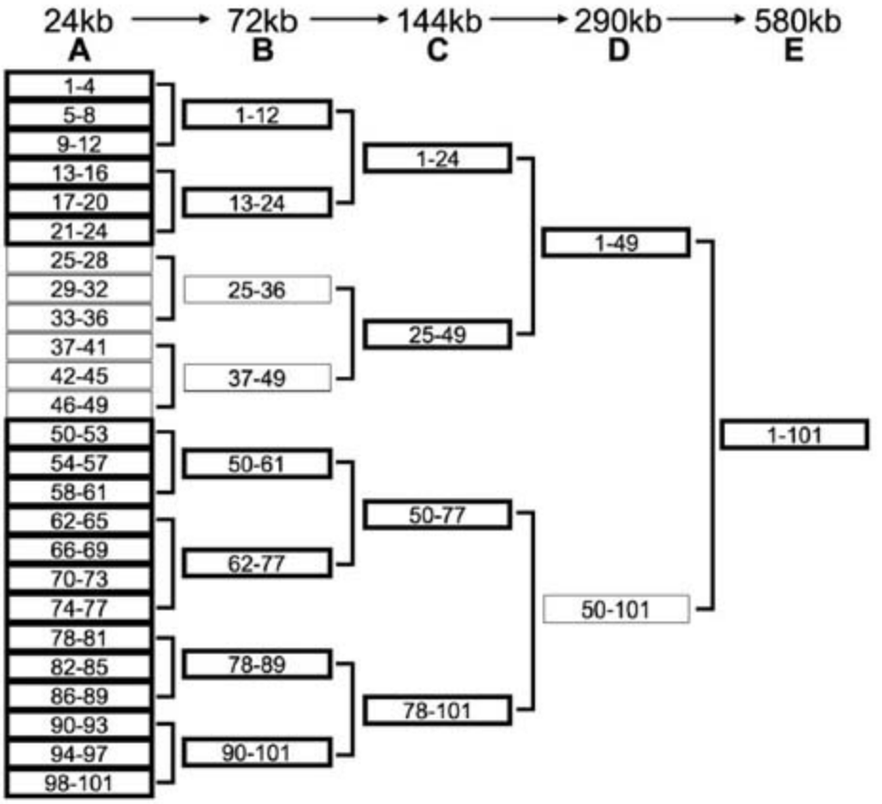

Fig. 2. A plan for the five-stage assembly of the *M. genitalium* chromosome. In the first stage of assembly, four cassettes are joined to make an A-series assembly approximately 24 kb in length (assembly 37-41 contained five cassettes). In the next stage, three A-assemblies are joined together to make a total of eight ~72-kb B-series assemblies (assembly B62-77 contained four A-series assemblies). The eighth-genome B-assemblies are taken two at a time to make quarter-genome C-series assemblies. These assemblies were all made by in vitro recombination (see Fig. 3) and cloned into *E. coli* using BAC vectors. Half-genome and whole-genome assemblies were made by in vivo yeast recombination. Assemblies in bold boxes were sequenced to verify their correctness. For the final molecule, the D-series half molecules were not employed. Rather, we assembled the whole molecule from the four C-series quarter molecules.

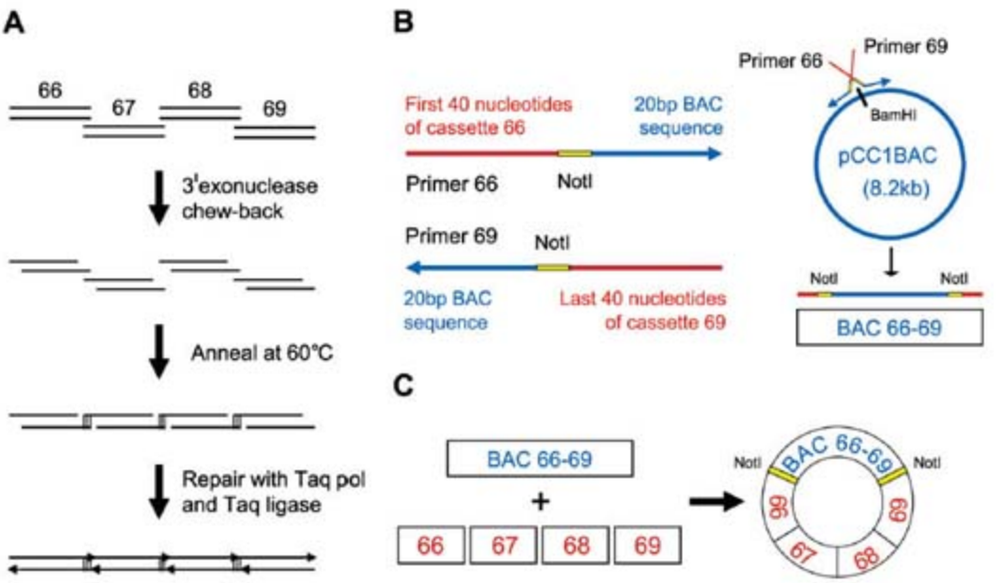

Fig. 3. Assembly of cassettes by in vitro recombination. (**A**) Diagram of steps in the in vitro recombination reaction, using the assembly of cassettes 66 to 69 as an example. (**B**) BAC vector is prepared for the assembly reaction by PCR amplification using primers as illustrated. The linear amplification product, after gel purification, is included in the assembly reaction of (A), such that the desired assembly is circular DNA containing the four cassettes and the BAC DNA as depicted in (**C**).

amplified BAC vector specific for this assembly, BAC 66-69, as described above (Fig. 3) (*13*). The 3′ ends of the mixture of duplex vector and cassette DNAs were then digested to expose the overlap regions using T4 polymerase in the absence of 2′-deoxyribonucleoside-5′-triphosphates (dNTPs). The T4 polymerase was inactivated by incubation at 75°C, followed by slow cooling to anneal the complementary overlap regions. The annealed joints were repaired using Taq polymerase and Taq ligase at 45°C in the presence of all four dNTPs and nicotinamide adenine dinucleotide (NAD). [See the supporting online material for details of the assembly reaction (*13*)].

Samples of the assembly reactions were subjected to field inversion gel electrophoresis (FIGE) to evaluate the success of the assembly (Fig. 4) (*13*). Additional samples were electroporated into *E. coli* EPI300 (Epicentre) or DH10B (Invitrogen) cells and plated on LB agar plates containing 12.5 μg/ml chloramphenicol. Colonies appeared after 24 to 48 hours. A-series assembly reactions generally yielded several thousand colonies. B- and C-series assembly reactions generally yielded several hundred colonies. Colonies were picked and BAC DNA was prepared from cultures using an alkaline lysis procedure. The DNA was then cleaved with Not I and analyzed by FIGE to verify the correct sizes of the assemblies. Typically, more than 90% of the A-series and 50% of the B- and C-series clones contained a BAC with the correct insert size. Clones with the correct size were preserved as frozen glycerol stocks. Some of the cloned assemblies were sequenced to ascertain the accuracy of the synthesis as indicated by bold boxes in Fig. 2.

The 25 A-series assemblies and all the larger assemblies were cloned in the pCC1BAC vector from Epicentre (Fig. 3). The pCC1BAC clones could be propagated at the single-copy level in EPI300 cells and then induced to 10 copies per cell according to the Epicentre protocol. Induced 100-ml cultures yielded up to 200 μg of BAC DNA. The assembly inserts in the BACs were immediately flanked on each side by a Not I site such that cleavage efficiently yielded the insert DNA with part of the Not I site attached at each end (the *M. genitalium* genome has no Not I sites). When the Not I–flanked assemblies were used in higher assemblies, the 3′ portion of the Not I site (2 nucleotides) was removed by the chew-back reaction. The 5′ portion of the Not I site produced a 6-nucleotide overhang after annealing, but the overhang was removed during repair by the Taq polymerase 5′ exonuclease activity (Fig. 5).

B-series assemblies were constructed from Not I–digested A-series clones, and C-series assemblies were constructed from Not I–digested B-series assemblies. It was generally not necessary to gel-purify the inserts from the cleaved vector DNA because, without complementary overhangs, they were inactive in subsequent reactions. FIGE analyses of the assembly reactions for A66-69, B50-61, and C25-49 are shown in Fig. 4, A to C. Figure 4D shows a FIGE analysis of the sizes of these cloned inserts.

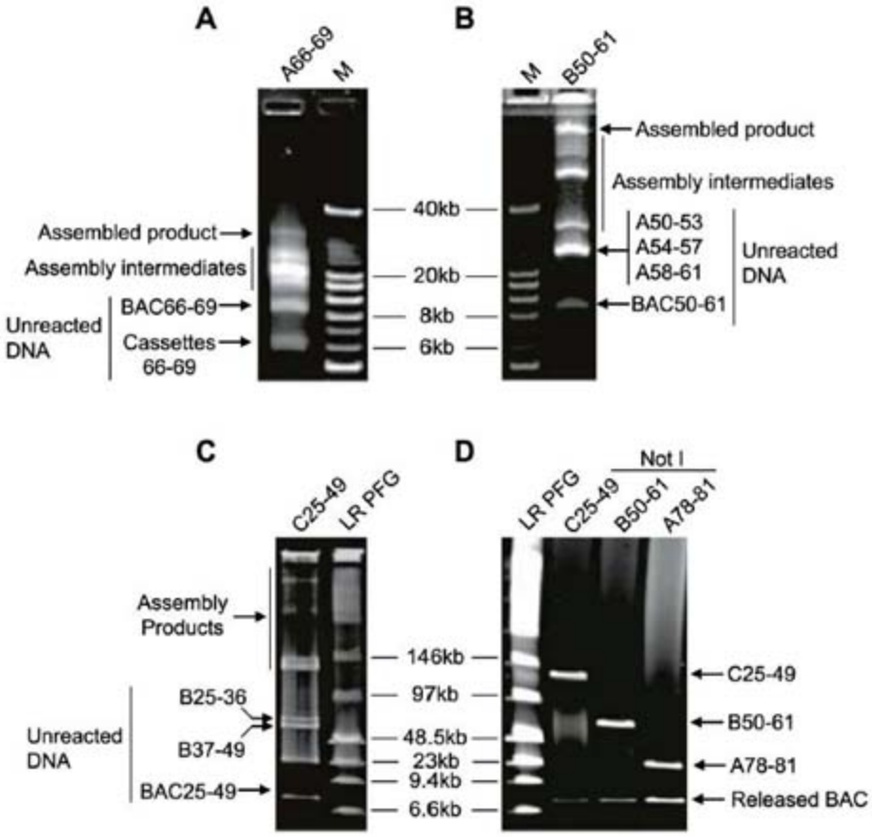

Fig. 4. Gel electrophoretic analyses of selected examples of A-, B-, and C-series assembly reactions and their cloned products. (**A** to **C**) A 10-μl sample of the chew-back assembly reactions for A66-69 (A), B50-61 (B), and C25-49 (C) was loaded onto a 0.8% Invitrogen E-gel (A and B) or onto a 1% BioRad Ready Agarose Mini Gel (C), then subjected to FIGE using the U-5 program (A and B) or the U-9 program (*13*) (C). See (*13*) for FIGE parameters. (**D**) Sizes of the Not I–cleaved assemblies were determined by FIGE analysis as in (C). The DNA size standards were the 1-kb extension ladder (M; Invitrogen) and the low-range PFG marker (LR PFG; NEB). Bands were visualized with a BioRad Gel Doc (A and B) or using an Amersham Typhoon 9410 Fluorescence Imager (C and D). Unreacted cassette, A-series, B-series, and BAC DNA, incomplete assembly products, and full-length assembly products are indicated.

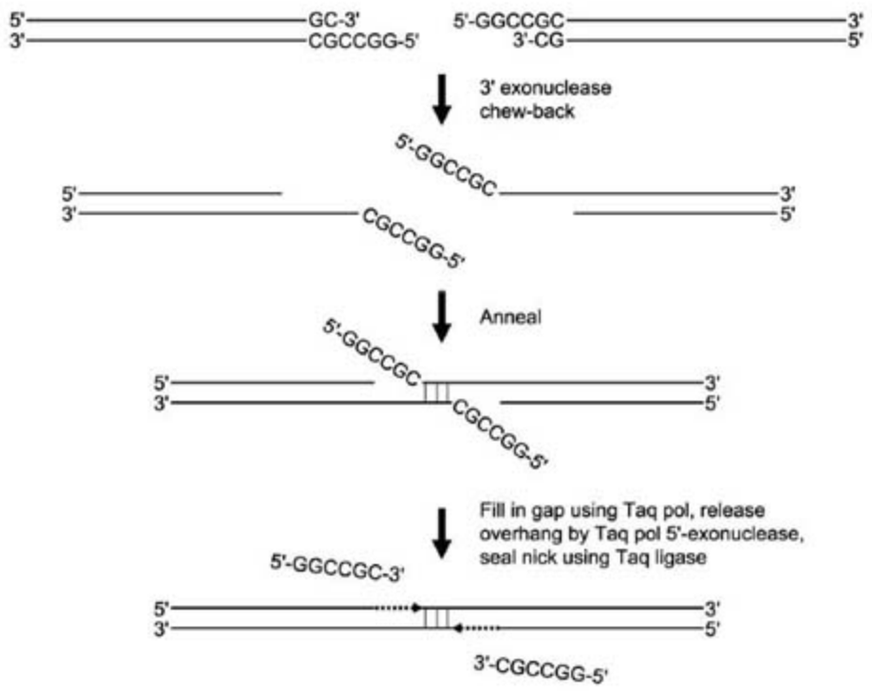

Fig. 5. Repair of annealed junctions containing nonhomologous 3′ and 5′ Not I sequences. The 3′ GC nucleotides are removed during the chew-back reaction. In the repair reaction the 5′-GGCCGC Not I overhangs are removed by the 5′-exonuclease activity contained in the Taq polymerase.

Assembly by in vivo recombination in yeast. We were unable to obtain half-genome clones in *E. coli* by the in vitro recombination procedure described above. We suspected that larger assemblies were simply not stable in *E. coli*. We had already experienced difficulty in maintaining the C78-101 clone except in Stbl4 *E. coli* cells (Invitrogen). Thus, we turned to *S. cerevisiae* as a cloning host. Yeast will support at least 2 Mb of DNA in a linear centromeric yeast artificial chromosome (YAC) (*15*) and has been used to clone sequences that are unstable in *E. coli* (*16*).

Linear YAC clones are usually constructed by ligation of an insert into a restriction enzyme cloning site (*17*). An improvement on this method uses cotransformation of overlapping insert and vector DNAs into yeast spheroplasts, where they are joined by homologous recombination (Fig. 6A). This produces circular clones and is known as TAR cloning (*18*). A TAR clone, like a linear YAC, contains a centromere and thus is maintained at chromosomal copy number along with the native yeast genome. However, unlike linear YACs, circular TAR clones can be readily separated from the linear yeast chromosomes.

To assemble quarter genomes into halves and wholes in yeast, we used the pTARBAC3 vector (*19*). This vector contains both YAC and BAC sequences (Fig. 6B). The vector was prepared using a strategy similar to the one described above for BAC vectors, but longer, 60 bp, overlaps were generated at the termini (*20*). In TAR cloning, recombination is stimulated by a factor of about 20 at double-stranded breaks (*21*). Thus, we integrated the vector at the cleaved intergenic BsmB I site in C50-77. This resulted in the elimination of the four bases of the BsmB I 5′ overhang. The DNA to be transformed consisted of six pieces (one vector, two fragments of quarter 3, and quarters 1, 2, and 4). To obtain a full-sized genome as an insert in pTARBAC3, a single yeast cell must take up all six pieces and assemble them by homologous recombination.

Transformation of the yeast cells was performed using a published method (*22*). Vector and inserts were transformed at approximately equimolar amounts. Transformants were screened first by PCR and then by Southern blot with mycoplasma-specific probes (*13*). Positive clones were tested for stability by Southern blotting of subclones. Based on these assays, at least 17 out of 94 transformants screened carried a complete synthetic genome. One of these clones, sMgTARBAC37, was selected for sequencing.

TAR cloning was also performed with each of the four sets of two adjacent quarter genomes, as well as with a mixture of C1-24, C25-49, and C50-77. DNAs from transformants of these various experiments were isolated and electroporated into *E. coli* (*23*). In this way, we obtained BAC clones of the sizes expected for D1-49, D50-101, and assemblies 25-77 and 1-77. Of these, D1-49 was chosen for sequencing, and it was correct. Our lack of success in obtaining these clones directly by in vitro recombination may have been due to inefficient circularization of large DNA molecules or to breakage during the handling of the DNA before transforming *E. coli*.

Recovery of the synthetic *M. genitalium* genome from yeast and confirmation of its sequence. A 600-kb YAC is about 5% of the total DNA in a yeast cell. To enrich sMgTARBAC37 for sequencing, we used a strategy of total DNA isolation in agarose, selective restriction digestion of yeast host chromosomes, and electrophoretic separation of these linear fragments from the large, relatively electrophoretically immobile circular molecules (*13*). Figure 6 shows the size and purity of the sMgTARBAC37 DNA that was used to prepare a library for sequencing. The sMgTARBAC37 DNA was sequenced by the random shotgun method to ~7X coverage. The sequence exactly matched our designed genome and can be accessed at GenBank accession number CP000925.

Error management. Our objective was to produce a cloned synthetic genome 582,970 bp in length with exactly the sequence we designed. This was not trivial, because differences (errors) between the actual and designed sequence can arise in several ways. An error could be present in the sequence that was supplied to the contractors. The contractors could produce cassettes with errors. Errors could occur during repair of the assembly junctions. Propagation of assemblies in *E. coli* or yeast could lead to errors. In the latter two instances, errors could occur at a late stage of the assembly. At various points during the ge-

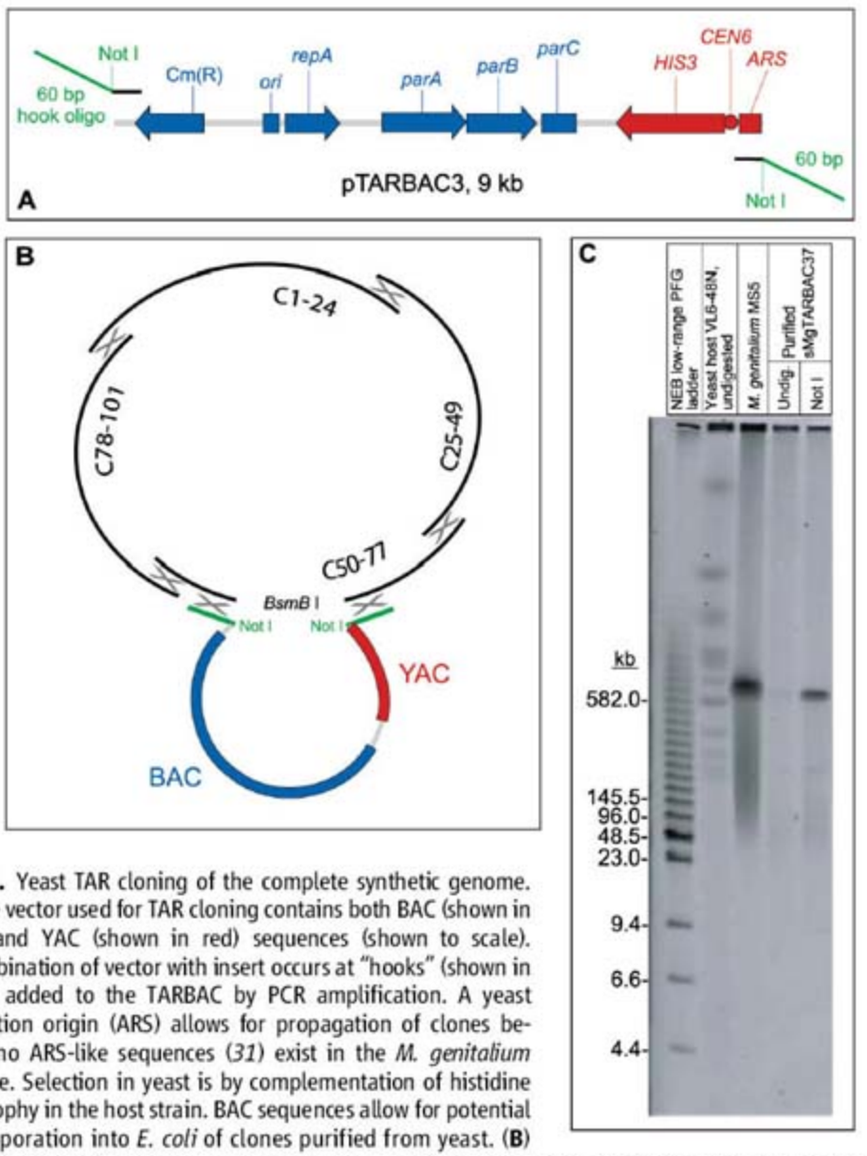

Fig. 6. Yeast TAR cloning of the complete synthetic genome. (**A**) The vector used for TAR cloning contains both BAC (shown in blue) and YAC (shown in red) sequences (shown to scale). Recombination of vector with insert occurs at "hooks" (shown in green) added to the TARBAC by PCR amplification. A yeast replication origin (ARS) allows for propagation of clones because no ARS-like sequences (*31*) exist in the *M. genitalium* genome. Selection in yeast is by complementation of histidine auxotrophy in the host strain. BAC sequences allow for potential electroporation into *E. coli* of clones purified from yeast. (**B**) *M. genitalium* JCVI-1.0 quarter genomes were purified from *E. coli*, Not I–digested, and mixed with a TARBAC vector for cotransformation into *S. cerevisiae*, where recombination at overlaps from 60 to 264 bp combined the six fragments into a single clone. The TARBAC was inserted into the BsmB I site in C50-77. (**C**) CHEF gel analysis of the complete synthetic genome clone sMgTARBAC37. Size markers are the low-range pulsed field gel marker (NEB), the host yeast strain VL6-48N (*32*), undigested, and the native *M. genitalium* MS5 (*14*) genome, which contains an insertion disrupting the MG408 gene. Purified sMgTARBAC37 from the preparation used for sequencing is shown both undigested and Not I digested. The Not I digest releases the 583-kb synthetic *M. genitalium* genome from the vector. The undigested sample confirms the circularity of the clone, because a 592-kb circle was too large to electrophorese into the gel. A small fraction of the clone was broken, and these linear molecules were detected by a faint signal.

nome assembly, clones were sequenced (Fig. 2). Most of the assemblies were exactly correct; however, in our *E. coli* clones, we encountered at least one example of each of the error types described above. Several errors were repaired by rebuilding assemblies, but in some cases other methods were used.

During sequence verification of the C50-77 quarter molecule, two single-bp deletions were detected. One was traced back to a synthesis error in cassette 65, and a corrected version was supplied by the contractor. An error in cassette 55 resulted from an incorrect sequence transmitted to the contractor. This cassette was corrected by replacing a restriction fragment containing the error with a newly synthesized fragment. C50-77 was then reassembled and sequenced. The two errors were corrected, but two new single-base substitution errors appeared. Taq polymerase misincorporation in a joint region likely caused one of these errors. The other remains unexplained but could have arisen during propagation in *E. coli*. One final reassembly yielded the correct quarter molecule that was used to assemble the whole chromosome.

Concluding remarks. We designed, chemically synthesized, and assembled the entire *M. genitalium* JCVI-1.0 chromosome, which is based on *M. genitalium* G37, and cloned it in yeast. This construct is more than an order of magnitude larger than previously reported chemically synthesized DNA products (*9*). The final product is built from ~10^4 synthetic oligonucleotides, each ~50 nucleotides in length, and is the largest chemically synthesized molecule of defined structure of which we are aware.

Very large nonsynthetic constructs have previously been produced from bacterial genomic DNA using in vivo methods. Itaya *et al.* (*24*) developed a method for cloning megabase-sized segments of DNA into the *Bacillus subtilis* genome using the natural transformation system of this bacterium. They cloned almost all of the *Synechocystis* PCC6803 genome as a set of four separate ~800- to 900-kb fragments into the *B. subtilis* chromosome by a reiterated "inch worm" process to generate a composite genome. Using a similar approach, this group recently reported the assembly and cloning of PCR products into an extrachromosomal vector (*25*). Holt *et al.* (*26*) have described how one might reassemble a fragmented donor genome from *Haemophilus influenzae* piecewise into *E. coli* using, for example, lambda Red recombination. All these methods used sequential stepwise addition of segments to reconstruct a donor genome within a recipient bacterium. The sequential nature of these constructions makes such methods slower than the purely hierarchical scheme that we employed (Fig. 2). Other approaches have been proposed that could use hierarchical assembly strategies (*27*).

The Itaya (*24*) and Holt (*26*) groups found that the bacterial recipient strains were unable to tolerate some portions of the donor genome to be cloned, for example, ribosomal RNA (rRNA) operons. In contrast, we found that the *M. genitalium* rRNA genes could be stably cloned in *E. coli* BACs. We were able to clone the entire *M. genitalium* genome, and also to assemble the four quarter-genomes in a single step, using yeast as a recipient host. However, we do not yet know how generally useful yeast will be as a recipient for bacterial genome sequences.

For the assembly of our synthetic genome, we used both in vitro and in vivo recombination methods. The efficiency of our in vitro procedure declined as the assemblies became larger. We were able to obtain quarter-genome, but not half-genome, clones using the in vitro methods described above. Some of the larger products in the half-genome reactions appeared to be concatamers that formed in preference to circles. In addition, large BACs (>100 kb) transform *E. coli* less efficiently. Sheng *et al.* (*28*) found that a 240-kb BAC transformed less efficiently by a factor of 30 than an 80-kb BAC in the same recipient strain of *E. coli*.

To complete the assembly, we turned to in vivo yeast recombination. Previous work had established that relatively large segments (>100 kb) of the human genome can be cloned in a circular yeast vector if the vector carries terminal homologies ("hooks") that flank the human genome segment (*18*). If yeast is cotransformed with a mixture of vector and high molecular weight human DNA, clones containing the human DNA segment are obtained. Recombination is stimulated by breaks at the point of homology. We surmised that our overlapping pieces, each of which has terminal 80-bp homologies to adjacent pieces, might be efficiently assembled and then joined to overlapping vector DNA by the transformation-associated recombination mechanism in yeast (*20*). We found that two quarters could be efficiently cloned to produce half genomes in the yeast vector. More surprisingly, four quarters, one of which had been cleaved at the vector insertion point, could be recombined and cloned to yield whole genomes. This implies that some of the competent yeast cells are capable of taking up as many as six separate DNA molecules and recombining them into a circular DNA molecule. This raises the question: How many pieces can be assembled in yeast in a single step? The ability to assemble many pieces of DNA in a single reaction could be very useful for generation of combinatorial genome libraries. In the future, it may be advantageous to make greater use of yeast recombination to assemble chromosomes.

We are currently using a TARBAC vector to propagate the synthetic chromosome in yeast. We do not know whether this vector might interfere with the production of viable cells by transplantation (*5*), nor do we know whether the genomic location of the vector could affect viability. It may be necessary to alter the vector sequences or even to excise the vector before transplantation.

The methods described here have advantages compared with those previously described for constructing large DNA molecules, either chemically synthesized or natural. Large in vitro DNA assemblies (>30 kb) have used type IIS restriction enzymes to generate unique sticky ends on the components of the assembly, which are then joined by ligation [for example, see (*9*, *29*)]. As the pieces to be assembled grow larger, it becomes increasingly difficult to find a type IIS enzyme that does not cleave within the piece. Our method is not limited to type IIS enzymes. We can use enzymes that cleave infrequently, for example type II enzymes with eight base recognition sites (e.g., Not I; see Figs. 3 and 5) or enzymes with even greater specificity [e.g., homing endonucleases; see New England Biolabs (NEB) catalog]. Instead of type IIS sticky end ligation, our method uses in vitro recombination of overlaps between the ends of the fragments to be assembled. A chew-back and anneal method (Fig. 3) similar to the first step of the assembly reaction described here was used to simultaneously assemble and clone up to nine small overlapping DNA fragments (275 to 980 bp) into a plasmid vector (*30*). The second-step repair reaction included in our method (*13*) greatly increases the efficiency of cloning of large assemblies (>50 kb).

Nothing in our methodology restricts its use to chemically synthesized DNA. It should be possible to assemble any combination of synthetic and natural DNA segments in any desired order by designing PCR primers to generate appropriate overlaps between them.

In closing, we wonder whether use of the UGA codon to code for tryptophan in mycoplasmas, rather than for termination as in the "universal" code, contributed to our success in cloning the synthetic *M. genitalium* JCVI-1.0 genome. This may make cloning in *E. coli* and other organisms less toxic because most *M. genitalium* proteins will be truncated. If so, then it should be possible to synthesize other genome constructions using this same code. The genome would then need to be installed, for example, by transplantation (*5*), in a cytoplasm that can properly translate the UGA to tryptophan. To generalize on this phenomenon, it might be possible to use other codon changes as long as there is a receptive cytoplasm with appropriate codon usage.

Note added in proof: While this paper was in press, we realized that the TARBAC vector in our sMgTARBAC37 clone interrupts the gene for the RNA subunit of RNase P (rnpB). This confirms our speculation that the vector might not be at a suitable site for subsequent transplantation experiments.

References and Notes

1. S. D. Colman, P. C. Hu, W. Litaker, K. F. Bott, *Mol. Microbiol.* **4**, 683 (1990).
2. C. M. Fraser *et al.*, *Science* **270**, 397 (1995).
3. J. I. Glass *et al.*, *Proc. Natl. Acad. Sci. U.S.A.* **103**, 425 (2006).
4. C. A. Hutchison *et al.*, *Science* **286**, 2165 (1999).
5. C. Lartigue *et al.*, *Science* **317**, 632 (2007).
6. K. J. Blight, A. A. Kolykhalov, C. M. Rice, *Science* **290**, 1972 (2000).
7. J. Cello, A. V. Paul, E. Wimmer, *Science* **297**, 1016 (2002).
8. H. O. Smith, C. A. Hutchison 3rd, C. Pfannkoch, J. C. Venter, *Proc. Natl. Acad. Sci. U.S.A.* **100**, 15440 (2003).

9. S. J. Kodumal *et al.*, *Proc. Natl. Acad. Sci. U.S.A.* **101**, 15573 (2004).
10. M. Arita, Y. Ohashi, *Biotechnol. Prog.* **20**, 1605 (2004).
11. D. Heider, A. Barnekow, *BMC Bioinformatics* **8**, 176 (2007).
12. B. Shimanovsky, J. Feng, M. Potkonjak, in *Revised Papers from the 5th International Workshop on Information Hiding* (Springer-Verlag, Berlin, 2003).
13. Materials and methods are available as supporting material on *Science* Online.
14. S. Dhandayuthapani, M. W. Blaylock, C. M. Bebear, W. G. Rasmussen, J. B. Baseman, *J. Bacteriol.* **183**, 5645 (2001).
15. P. Marschall, N. Malik, Z. Larin, *Gene Ther.* **6**, 1634 (1999).
16. N. Kouprina *et al.*, *EMBO Rep.* **4**, 257 (2003).
17. D. T. Burke, G. F. Carle, M. V. Olson, *Science* **236**, 806 (1987).
18. V. Larionov, N. Kouprina, J. Graves, M. A. Resnick, *Proc. Natl. Acad. Sci. U.S.A.* **93**, 13925 (1996).
19. C. Zeng *et al.*, *Genomics* **77**, 27 (2001).
20. V. N. Noskov *et al.*, *Nucleic Acids Res.* **29**, E32 (2001).
21. S. H. Leem *et al.*, *Nucleic Acids Res.* **31**, e29 (2003).
22. N. Kouprina, V. N. Noskov, V. Larionov, *Methods Mol. Biol.* **349**, 85 (2006).
23. G. A. Silverman, *Methods Mol. Biol.* **54**, 65 (1996).
24. M. Itaya, K. Tsuge, M. Koizumi, K. Fujita, *Proc. Natl. Acad. Sci. U.S.A.* **102**, 15971 (2005).
25. M. Itaya, K. Fujita, A. Kuroki, K. Tsuge, *Nat. Methods* **5**, 41 (2008).
26. R. A. Holt, R. Warren, S. Flibotte, P. I. Missirlis, D. E. Smailus, *Bioessays* **29**, 580 (2007).
27. T. Knight, "Idempotent Vector Design for Standard Assembly of Biobricks" (MIT, Cambridge, MA, 2003).
28. Y. Sheng, V. Mancino, B. Birren, *Nucleic Acids Res.* **23**, 1990 (1995).
29. B. Yount, M. R. Denison, S. R. Weiss, R. S. Baric, *J. Virol.* **76**, 11065 (2002).
30. M. Z. Li, S. J. Elledge, *Nat. Methods* **4**, 251 (2007).
31. C. S. Newlon, J. F. Theis, *Curr. Opin. Genet. Dev.* **3**, 752 (1993).
32. V. Larionov, N. Kouprina, G. Solomon, J. C. Barrett, M. A. Resnick, *Proc. Natl. Acad. Sci. U.S.A.* **94**, 7384 (1997).
33. We thank J. Mulligan for his interest in our work and expediting cassette synthesis by Blue Heron Technologies, S. Vashee and R.-Y. Chuang for many helpful discussions about the manuscript, and J. Johnson and T. Davidsen for assistance with GenBank submissions. Additionally, we thank the Larionov laboratory at NIH for their gifts of yeast strains and TAR cloning expertise. The bulk of the work was supported by Synthetic Genomics, Inc. J.C.V. is Chief Executive Officer and Co-Chief Scientific Officer of Synthetic Genomics, Inc., a privately held entity that develops genomic-driven strategies to address global energy and environmental challenges. H.O.S. is Co-Chief Scientific Officer and on the Board of Directors of Synthetic Genomics, Inc. C.A.H. is Chairman of the Synthetic Genomics, Inc., Scientific Advisory Board. All three of these authors hold Synthetic Genomics, Inc., stock.

Supporting Online Material

www.sciencemag.org/cgi/content/full/1151721/DC1
Materials and Methods
Fig. S1
Tables S1 to S4
References

15 October 2007; accepted 11 January 2008
Published online 24 January 2008;
10.1126/science.1151721
Include this information when citing this paper.

REPORTS

Asphericity in Supernova Explosions from Late-Time Spectroscopy

Keiichi Maeda,[1,2,3]* Koji Kawabata,[4] Paolo A. Mazzali,[2,5,6] Masaomi Tanaka,[7] Stefano Valenti,[8,9] Ken'ichi Nomoto,[1,6,7] Takashi Hattori,[10] Jinsong Deng,[11] Elena Pian,[5] Stefan Taubenberger,[2] Masanori Iye,[12] Thomas Matheson,[13] Alexei V. Filippenko,[14] Kentaro Aoki,[10] George Kosugi,[15] Youichi Ohyama,[16] Toshiyuki Sasaki,[10] Tadafumi Takata[17]

Core-collapse supernovae (CC-SNe) are the explosions that announce the death of massive stars. Some CC-SNe are linked to long-duration gamma-ray bursts (GRBs) and are highly aspherical. One important question is to what extent asphericity is common to all CC-SNe. Here we present late-time spectra for a number of CC-SNe from stripped-envelope stars and use them to explore any asphericity generated in the inner part of the exploding star, near the site of collapse. A range of oxygen emission-line profiles is observed, including a high incidence of double-peaked profiles, a distinct signature of an aspherical explosion. Our results suggest that all CC-SNe from stripped-envelope stars are aspherical explosions and that SNe accompanied by GRBs exhibit the highest degree of asphericity.

Massive stars (≳10 solar masses) end their lives when the nuclear fuel in their innermost region is consumed; lacking sufficient internal pressure support, they can no longer withstand the pull of gravity. Their core then collapses to a neutron star or a black hole. Gravitational energy from the collapse produces an explosion that expels the rest of the star in what is observed as a supernova (SN).

CC-SNe are classified (*1*) by how much of the stellar envelope is present at the time of the explosion (*2*). Stars that retain their H envelope produce SNe with a H-rich spectrum, classified as type II. On the other hand, stars that have lost all or most of the H envelope produce CC-SNe that are known as stripped-envelope (or stripped) SNe. These include, in a sequence of increasing degrees of envelope stripping, type IIb (He-rich but still showing some H), type Ib (He-rich, no H), and type Ic (deprived of both H and He). Some type Ic SNe (hereafter broad-lined SNe Ic) show very broad absorption features in optical spectra obtained within a few weeks after the explosion; these features are produced by material moving at a velocity > 0.1 c (c is the speed of light), probably as the result of an explosion characterized by a kinetic energy (E_K) larger than the canonical value of ~10^{51} erg (*3*). The most energetic broad-lined SNe Ic can reach $E_K \gtrsim 10^{52}$ erg [hereafter hypernovae (HNe) or gamma-ray burst HNe (GRB-HNe)] (*4*) and can be associated with GRBs (*5*). Figure 1 summarizes the relation between E_K and the mass of ^{56}Ni that powers the optical light of stripped CC-SNe (*6*).

An important unsolved question concerns how the gravitational energy of the collapse is turned into the outward motion of the SN explosion. Most recently proposed scenarios involve aspherical explosions (*7*–*11*). Therefore, mapping the explosion geometry can be illuminating. It is especially critical to establish whether the explosion geometry is similar for all CC-SNe or at least for different subclasses (GRB-HNe, broad-lined SNe Ic, normal-energy SNe, or stripped versus type II SNe).

Some evidence for asymmetric explosions was obtained from the polarization detected in several SNe II (*12*) and SNe Ib/c (*13*) and in the broad-lined SN Ic 2002ap (*14*–*16*). However, because there are still few such detections, no systematic study exists.

[1]Institute for the Physics and Mathematics of the Universe (IPMU), University of Tokyo, Kashiwa-no-ha 5-1-5, Kashiwa City, Chiba 277-8582, Japan. [2]Max-Planck-Institut für Astrophysik, Karl-Schwarzschild-Strasse 1, 85741 Garching, Germany. [3]Department of Earth Science and Astronomy, College of Arts and Science, University of Tokyo, Tokyo 153-8902, Japan. [4]Hiroshima Astrophysical Science Center, Hiroshima University, Hiroshima 739-8526, Japan. [5]National Institute for Astrophysics–Osservatorio Astronomica di Trieste, Via G. B. Tiepolo 11, 34143 Trieste, Italy. [6]Research Center for the Early Universe, School of Science, University of Tokyo, Tokyo 113-0033, Japan. [7]Department of Astronomy, School of Science, University of Tokyo, Tokyo 113-0033, Japan. [8]Department of Physics, University of Ferrara, I-44100 Ferrara, Italy. [9]European Organization for Astronomical Research in the Southern Hemisphere, Karl-Schwarzschild-Strasse 1, 85741 Garching, Germany. [10]Subaru Telescope, National Astronomical Observatory of Japan (NAOJ), 650 North A'ohoku Place, Hilo, HI 96720, USA. [11]National Astronomical Observatory, Chinese Academy of Sciences, 20A Datun Road, Chaoyang District, Beijing 100012, China. [12]Division of Optical and Infrared Astronomy, NAOJ, Osawa 2-21-1, Mitaka, Tokyo 181-8588, Japan. [13]National Optical Astronomy Observatory, Tucson, AZ 85719, USA. [14]Department of Astronomy, University of California, Berkeley, CA 94720-3411, USA. [15]Atacama Large Millimeter/Submillimeter Array Project, NAOJ, Mitaka, Tokyo 181-8588, Japan. [16]Department of Infrared Astrophysics, Institute of Space and Astronomical Science, Japan Aerospace Exploration Agency (JAXA), 3-1-1 Yoshinodai, Sagamihara, Kanagawa 229-8510, Japan. [17]Astronomy Data Center, NAOJ, Mitaka, Tokyo 181-8588, Japan.

*To whom correspondence should be addressed. E-mail: maeda@ea.c.u-tokyo.ac.jp

The best way to investigate a SN's inner ejecta geometry is through late-time spectroscopy. At $\gtrsim$ 200 days after the explosion, expansion makes the density of the ejecta so low that optical photons produced anywhere in the ejecta escape without interacting with the gas. At these epochs, the SN spectrum is nebular, showing emission lines mostly of forbidden transitions. Because the expansion velocity is proportional to the radius of any point in the ejecta, the Doppler shift indicates where the photon was emitted. A photon emitted from the near side of the ejecta is detected at a shorter (blueshifted) wavelength, and a photon emitted from the far side of the ejecta is detected at a longer (redshifted) wavelength. The late-time nebular emission profiles thus probe the distribution of the emitting gas within the SN ejecta. This strategy is particularly effective for stripped CC-SNe, because we can look directly into the oxygen core.

Analysis of the late-time spectra of the GRB-HN SN Ic 1998bw (*17*) and of the broad-lined SN Ic 2003jd (*18*) provided evidence that these objects shared a similar, bipolar explosion. However, we viewed SN 1998bw on-axis, and SN 2003jd sideways. This seems consistent with the fact that SN 1998bw was associated with a GRB, whereas SN 2003jd was not, and suggests that if SN 2003jd also produced a GRB, this was missed because of its orientation [(*18*), but see (*19*) for concerns].

We obtained late-time spectra of stripped CC-SNe to study their morphology and quantify their properties. Our data were obtained mostly with the Faint Object Camera and Spectrograph (*20*) on the 8.2-m Subaru telescope and with the Focal Reducer and Low-Dispersion Spectrograph 2 on the European Southern Observatory (ESO) Very Large Telescope (VLT). Additional data are from (*21*). The strongest emission line in stripped CC-SNe is [O I] λλ6300, 6363. Despite being a doublet, it behaves like a single transition if the lines are sufficiently broad ($\gtrsim$0.01 *c*), because the red component is weaker than the blue one by a factor of 3 [supporting online material (SOM) text].

Because at epochs more than 200 days after the explosion the ejecta are transparent to line emission and radiation transfer is unimportant (SOM text), we selected spectra obtained at least 200 days after discovery to build an unbiased data set. Additionally, we did not include HNe discovered through an associated GRB, to avoid bias in the viewing angle. The selection procedure and possible biases are discussed in (*22*). Our sample (table S1) is the largest published data set to date of stripped CC-SNe at such late epochs. Figure 2 shows the spectra of the 18 SNe in our sample. Among them, 13 are presented here for the first time.

The observed [O I] λλ6300, 6363 emission profiles can be compared with the prediction of various explosion models. We used three representative models from (*23*): one extremely aspherical (BP8), one mildly aspherical (BP2), and one spherical (BP1).

In the spherical model, ^{56}Ni is confined in a central high-density region with an inner hole and is surrounded by a low-density O-rich region (*24*). This results in a single-peaked but flat-topped [O I] profile, independent of the orientation.

On the other hand, the bipolar model (*24*–*26*) is characterized by a low-density ^{56}Ni-rich region located near the jet axis, where the jets convert stellar material (mostly O) into Fe-peak elements, and by a high-density disklike structure composed of unburned O-rich material, because the jet expands laterally only weakly (*17*, *24*) (fig. S1). The [O I] profile in a bipolar model depends on both the degree of asphericity and the viewing angle (*23*, *27*) (SOM text and fig. S1). If a bipolar SN explosion is viewed from a direction close to the jet axis, the O-rich material in the equatorial region expands in a direction perpendicular to the line of sight, and the [O I] emission profile is observed to be sharp and single-peaked. On the other hand, for a near-equatorial view, the profile is broader and double-peaked. The best fit to the light curve and the spectra of the GRB-HN SN 1998bw was obtained with model BP8 (*23*, *27*).

For the degree of asphericity of this model, the [O I] profile should switch from single- to double-peaked near a viewing angle $\theta \approx 50°$ measured from the jet direction (fig. S2). The predicted frequency of double-peaked [O I] is thus ~64%, in the absence of bias in the orientation. For a less aspherical model, the fraction of double peaks is reduced: Model BP2 shows double peaks only for $\theta \gtrsim 70°$ and has a double-peak fraction of ~34%. With this variety of [O I] profiles, statistics (Table 1) can be used to constrain the degree of asphericity and remove the uncertainty in the viewing angle.

Figure 3 shows the [O I] emission profiles for our sample. Out of 18 SNe, 5 (SNe 2003jd,

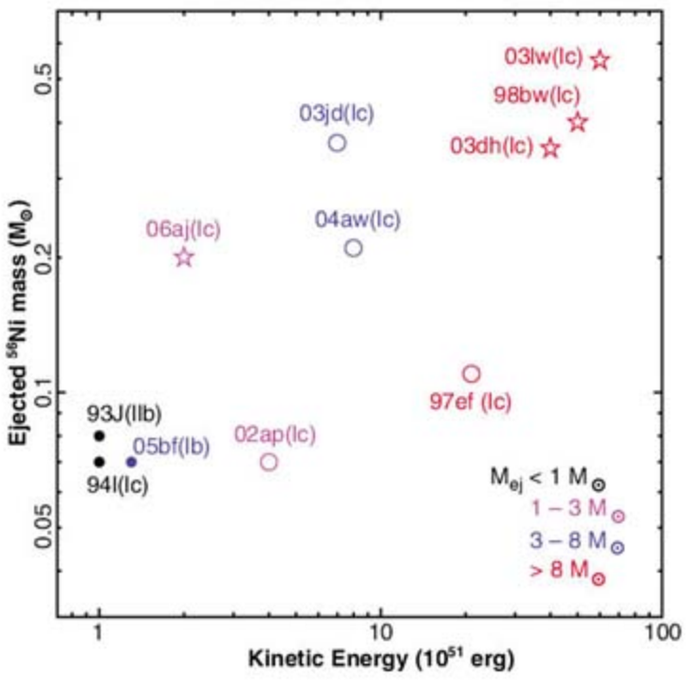

Fig. 1. Relation between E_K and the mass of ejected ^{56}Ni [$M(^{56}$Ni)] of stripped CC-SNe (SOM text). Colors indicate the ejecta mass (M_{ej}). For SN IIb 1993J and SN Ib 2005bf, the ejecta mass after subtraction of the He envelope mass is shown as M_{ej}, to compare with SNe Ic, which lack the He envelope. SNe associated with GRBs or an x-ray flash (XRF) are indicated by stars, and broad-lined SNe Ic without GRBs or XRFs by open circles. Other (normal) stripped CC-SNe are shown as dots.

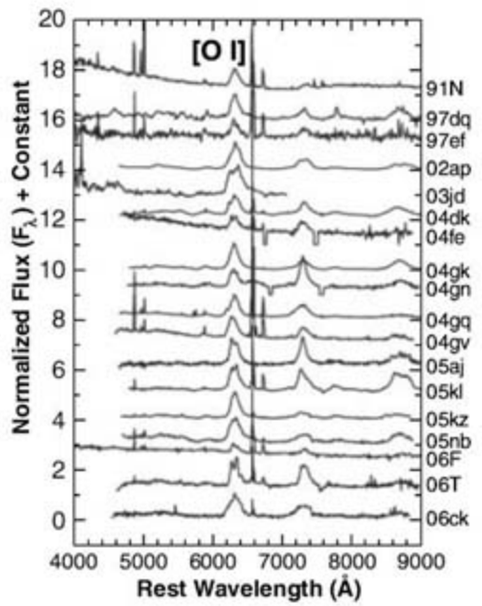

Fig. 2. Nebular spectra of the SNe in the sample used in this study. Narrow lines (such as Hα at 6563 Å) originate from a diffuse superposed H II region, not from a SN. The spectra of SNe 1991N, 1997dq, and 1997ef are from (*21*). The other spectra were obtained with the Subaru telescope, except for SN 2006F, which was taken by the VLT (*22*). Spectra were de-redshifted by means of the redshift obtained from the observed wavelength of the narrow Hα emission if possible; otherwise, the redshift of the nucleus of the host galaxy was adopted. For presentation, the flux is arbitrarily scaled and shifted vertically. The strongest emission line (dashed line) is [O I] λλ6300, 6363. The feature at ~7300 Å is [Ca II] λλ7291, 7324 contaminated by several emission lines: [O II], [Fe II], and [Ni II].

2004fe, 2005aj, 2005kl, and 2006T) clearly show double-peaked [O I] profiles. Four others (SNe 1997dq, 2004 gn, 2005kz, and 2005nb) are apparently transitional objects with flat-topped or mildly peaked [O I] profiles, and there is a marginal detection of double peaks in some cases. The remaining nine SNe exhibit single-peaked profiles. For illustrative purposes, the observed profiles are compared with model predictions in Fig. 3.

The line profiles are well reproduced by the bipolar explosion model, assuming different viewing angles. Although detailed fits are not unique for individual objects, this uncertainty does not affect the bulk statistics (single- versus double-peaked): The presence of double-peaked [O I] profiles is not predicted in spherical models, and their fraction yields a secure estimate of the number of aspherical SNe viewed sideways, assuming that the sample is unbiased in orientation. The high incidence of double-peaked profiles is an important discovery: Double-peaked [O I] was previously reported only for SN Ic 2003jd (*18*) and SN Ib 2004ao (*28*). The observed fraction of double-peaked profiles, (5 to 9)/18 = 28 to 50%, median ~39%, is consistent with all stripped CC-SNe being mildly aspherical, like model BP2.

On the other hand, the observed fraction does not support the possibility that all stripped CC-SNe are extremely aspherical explosions like SN 1998bw (model BP8), as then we would expect an even larger fraction of double-peaked [O I] profiles: According to our Monte Carlo simulations with randomly oriented viewing directions, the observed number should be 7 to 16 out of 18 SNe with 99% confidence level and 10 to 13 with 70% confidence level. Alternatively, about half of all stripped CC-SNe may have asphericity as large as that of GRB-HNe, with a double-peak incidence of ~64% (model BP8), with the remaining half being approximately spherical and yielding the bulk of the single-peaked profiles. With a larger SN sample, we could look in more detail at [O I] profiles as functions of the degree of asphericity and orientation and more fully explore these scenarios.

Although our sample is still small, we can look for statistical differences between GRB-HNe, broad-lined SNe Ic, and other stripped CC-SNe. In our sample, six SNe are broad-lined (non-GRB) SNe Ic (SNe 1997ef, 1997dq, 2002ap, 2003jd, 2005kz, and 2005nb), and the rest are probably normal stripped CC-SNe. The observed fraction of double-peaked [O I] is 33% (1 out of 3 SNe) for broad-lined SNe Ic and 36% (4 out of 11) for the others, if SNe with transitional [O I] profiles (Fig. 3) are excluded. Within the statistical uncertainty, caused especially by the small sample of broad-lined SNe Ic, there is no difference between the two groups. Both are consistent with the predictions of model BP2 and show too few double-peaked profiles for model BP8. This suggests that on average, broad-lined, non-GRB SNe Ic are less aspherical than GRB-HNe and are morphologically closer to normal stripped CC-SNe.

Broad-lined, non-GRB SNe Ic typically have smaller E_K than GRB-HNe (Fig. 1). There has been speculation that broad-lined, non-GRB SNe Ic might be intrinsically similar to GRB-HNe but viewed off-axis, leading to apparently smaller E_K. Although this may still be true for a small subset of them, the moderate asphericity inferred for this group suggests that broad-lined, non-GRB SNe Ic are probably intrinsically different from GRB-HNe.

On the other hand, asphericity is not a special feature of GRB-HNe but rather a generic property of stripped CC-SNe. Both broad-lined and normal stripped CC-SNe have a moderate degree of asphericity. All stripped CC-SNe probably share to some extent a common explosion mechanism that generates the same kind of asphericity, with GRB-HNe probably the most aspherical.

Our result offers an important insight into the theory of SN explosions. The most popular models for high- and low-energy CC-SNe are in fact different: black hole formation and the production of a jet in HNe and perhaps broad-lined SNe Ic (*29*) and delayed neutrino heating from the proto–neutron star for normal SNe (*30*). In the former case, the explosion is probably initiated along the axis of rotation and/or magnetic field (*10*, *11*, *29*), whereas in the latter case, some asphericity may be generated by hydrodynamic instabilities (*7*–*9*). The result supports recent theoretical scenarios of the SN explosion, which suggest that an important role in the collapse is played by hydrodynamic instability, rotation, or magnetic fields.

Recently, Modjaz *et al.* (*31*) showed another sample of late-time spectra of stripped CC-SNe. Their conclusions are similar to ours. One SN in their sample (SN 2004ao with double-peaked [O I]) could be added to our sample according to our selection criteria. It increases the frequency of double-peaked events, but it does not change our conclusions within the uncertainties.

Table 1. Fraction of double-peaked [O I] SNe.

Model	Dividing angle*	Fraction†
Spherical	–	0%
BP2	~70°	~34%
BP8	~50°	~64%
Observed	–	39 ± 11%

*The viewing angle (θ_0 measured from the jet direction) which divides the [O I] profile; i.e., single-peaked if $\theta < \theta_0$ and double-peaked if $\theta_0 \leq \theta \leq 90°$. †Fraction of SNe showing double-peaked [O I].

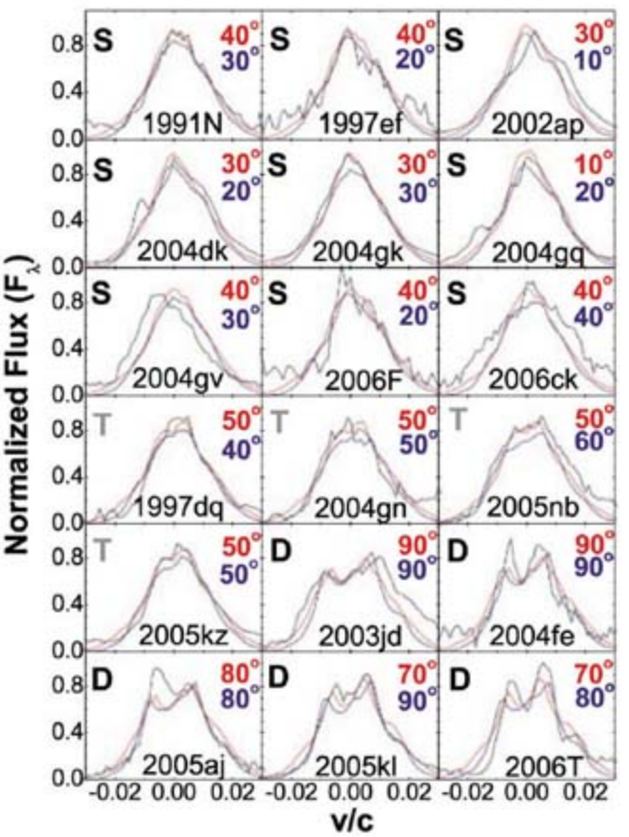

Fig. 3. Observed [O I] λλ6300, 6363 emission-line profiles (black curves), classified into characteristic profiles: single-peaked (denoted by S, top nine SNe), transition (T, middle four SNe), and double-peaked (D, bottom five SNe). For presentation, model predictions of the bipolar model (*23*) with different viewing directions are shown for model BP8 (red curves, with the direction denoted by the red text) and for the less aspherical model BP2 (blue). The models shown here have smaller expansion velocities (corresponding to $E_K \approx$ a few × 10^{51} erg) than the one applied to SN 1998bw ($E_K \gtrsim 10^{52}$ erg) (*23*). The separation between the two peaks in the double-peaked cases is ~0.01 *c* to 0.02 *c*, which is much larger than the wavelength resolution in the observations (~10 Å, corresponding to 0.0015 *c*).

References and Notes

1. A. V. Filippenko, *Annu. Rev. Astron. Astrophys.* **35**, 309 (1997).
2. K. Nomoto, K. Iwamoto, T. Suzuki, *Phys. Rep.* **256**, 173 (1995).
3. P. A. Mazzali *et al.*, *Astrophys. J.* **572**, L61 (2002).
4. K. Iwamoto *et al.*, *Nature* **395**, 672 (1998).
5. T. J. Galama *et al.*, *Nature* **395**, 670 (1998).
6. K. Nomoto *et al.*, *Il Nouvo Cimento* **121B**, 1207 (2007).
7. J. M. Blondin, A. Mezzacappa, C. DeMarino, *Astrophys. J.* **584**, 971 (2003).
8. R. Buras, M. Rampp, H.-Th. Janka, K. Kifonidis, *Astron. Astrophys.* **457**, 281 (2006).
9. A. Burrows, E. Livne, L. Dessart, C. D. Ott, J. Murphy, *Astrophys. J.* **655**, 416 (2007).
10. K. Kotake, H. Sawai, S. Yamada, K. Sato, *Astrophys. J.* **608**, 391 (2004).

11. S. G. Moiseenko, G. S. Bisnovatyi-Kogan, N. V. Ardeljan, *Mon. Not. R. Astron. Soc.* **370**, 501 (2006).
12. D. C. Leonard *et al.*, *Nature* **440**, 505 (2006).
13. L. Wang, D. A. Howell, P. Höflich, J. C. Wheeler, *Astrophys. J.* **550**, 1030 (2001).
14. K. S. Kawabata *et al.*, *Astrophys. J.* **580**, L39 (2002).
15. D. C. Leonard, A. V. Filippenko, R. Chornock, R. J. Foley, *Pub. Astron. Soc. Pac.* **114**, 1333 (2002).
16. L. Wang, D. Baade, P. Höflich, J. C. Wheeler, *Astrophys. J.* **592**, 457 (2003).
17. K. Maeda *et al.*, *Astrophys. J.* **565**, 405 (2002).
18. P. A. Mazzali *et al.*, *Science* **308**, 1284 (2005).
19. A. M. Soderberg, E. Nakar, E. Berger, S. R. Kulkarni, *Astrophys. J.* **638**, 930 (2006).
20. N. Kashikawa *et al.*, *Pub. Astron. Soc. Jpn.* **54**, 819 (2002).
21. T. Matheson, A. V. Filippenko, W. Li, D. C. Leonard, J. C. Shields, *Astron. J.* **121**, 1648 (2001).
22. Data and methods are available as supporting material on *Science* Online.
23. K. Maeda, K. Nomoto, P. A. Mazzali, J. Deng, *Astrophys. J.* **640**, 854 (2006).
24. K. Maeda, K. Nomoto, *Astrophys. J.* **598**, 1163 (2003).
25. A. M. Khokhlov *et al.*, *Astrophys. J.* **524**, L107 (1999).
26. A. I. MacFadyen, S. E. Woosley, A. Heger, *Astrophys. J.* **550**, 410 (2001).
27. K. Maeda, P. A. Mazzali, K. Nomoto, *Astrophys. J.* **645**, 1331 (2006).
28. M. Modjaz *et al.*, *Astron. J.*, http://arxiv.org/abs/astro-ph/0701246 (2008).
29. A. I. MacFadyen, S. E. Woosley, *Astrophys. J.* **524**, 262 (1999).
30. H. A. Bethe, J. R. Wilson, *Astrophys. J.* **295**, 14 (1985).
31. M. Modjaz, R. P. Kirshner, P. Challis, preprint available at http://arxiv.org/abs/0801.0221 (2008).
32. The data were collected at the NAOJ Subaru telescope. The additional data were from the ESO VLT under ESO program 078.D-0246. K.M. and M.T. have been supported by the Japan Society for the Promotion of Science (JSPS). E.P. and P.M. acknowledge financial support from PRIN MUIR 2005 and PRIN INAF 2006. K.N. is supported by a JSPS Grant-in-Aid for Scientific Research (18104003 and 18540231). J.D. is supported by the National Natural Science Foundation of China (grant no. 10673014). A.V.F. is supported by NSF grant AST-0607485.

Supporting Online Material

www.sciencemag.org/cgi/content/full/1149437/DC1
Methods
SOM Text
Figs. S1 and S2
Table S1
References

20 August 2007; accepted 17 January 2008
Published online 31 January 2008;
10.1126/science.1149437
Include this information when citing this paper.

Proton Radiography of Inertial Fusion Implosions

J. R. Rygg,[1]* F. H. Séguin,[1] C. K. Li,[1] J. A. Frenje,[1] M. J.-E. Manuel,[1] R. D. Petrasso,[1]† R. Betti,[2] J. A. Delettrez,[2] O. V. Gotchev,[2] J. P. Knauer,[2] D. D. Meyerhofer,[2] F. J. Marshall,[2] C. Stoeckl,[2] W. Theobald[2]

A distinctive way of quantitatively imaging inertial fusion implosions has resulted in the characterization of two different types of electromagnetic configurations and in the measurement of the temporal evolution of capsule size and areal density. Radiography with a pulsed, monoenergetic, isotropic proton source reveals field structures through deflection of proton trajectories, and areal densities are quantified through the energy lost by protons while traversing the plasma. The two field structures consist of (i) many radial filaments with complex striations and bifurcations, permeating the entire field of view, of magnetic field magnitude 60 tesla and (ii) a coherent, centrally directed electric field of order 10^9 volts per meter, seen in proximity to the capsule surface. Although the mechanism for generating these fields is unclear, their effect on implosion dynamics is potentially consequential.

Identification and characterization of the physical phenomena associated with dynamic, extreme states of matter—such as those of high–energy-density physics (*1*, *2*) found in inertial fusion (*3*, *4*), laboratory astrophysics (*2*, *5*), and laser-plasma interaction physics (*6*)—are of fundamental scientific importance. A novel method of diagnosing inertial fusion implosions has resulted in the characterization of two distinct electromagnetic field configurations that have potentially consequential effects on implosion dynamics. This method also makes possible the quantitative study of the temporal evolution of capsule size and areal density.

The method involves radiography with a pulsed (0.1 ns), monoenergetic (15.0 MeV), quasi-isotropic proton source (*7*, *8*). Fields are revealed in radiographs through deflection of proton trajectories, and areal densities are quantified through the energy lost by protons while traversing the plasma. The imaged samples are inertial confinement fusion (ICF) capsules of the fast-ignition (FI) variety (*9*, *10*), initially 430 μm in radius, imploded by 36 laser beams that deposit 14 kJ of energy in a 1-ns pulse (*8*).

For electricity generation (*3*, *4*) and for studies of extremely high–energy-density physics in the laboratory (*1*, *2*), ICF seeks to release copious energy by igniting a compressed pellet of fusion fuel. Fuel compression to densities of 300 g/cm^3 or higher will be achieved by energy deposition onto the surface of a fuel capsule over nanosecond time scales, either by laser light (direct drive) or by x-rays generated in a cavity by laser light (indirect drive). Ignition and energy gain will occur in a central hot spot, or, in the FI scheme, by the extremely rapid (picosecond-scale) deposition of additional energy, either directly onto the compressed pellet (*9*) or along the axis of a cone that keeps the path clear of plasma ablated from the pellet surface (*10*).

The 15-MeV (fig. S1), monoenergetic proton radiography applied herein was recently used by Li *et al.* in a different context to investigate fields generated by laser-foil interactions (*11*, *12*). Mackinnon *et al.* (*13*) used a broad-band, non-isotropic proton source to study six-beam implosions, though they did not observe either striated or coherent field structures. In addition, earlier workers, using optical techniques largely sensitive to density perturbations, observed very-fine-scale radial filaments and jets (*14*, *15*) in targets driven by one to four laser beams. However, the character of these structures is qualitatively different in several ways from the striations described in this report [see supporting online material (SOM) text].

In the reported experiments (Fig. 1), cone-in-shell FI targets were radiographed before and during implosion, 1.56 ns after the start of the

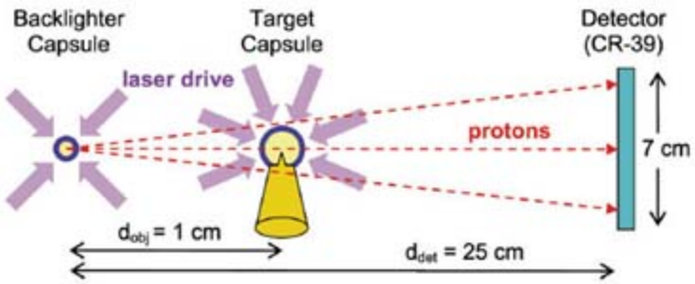

Fig. 1. Schematic of the experimental setup. A short (130-ps), monoenergetic (energy linewidth $\Delta E/E$ < 3%), quasi-isotropic pulse of 15.0-MeV D^3He fusion protons is generated by laser implosion of a backlighter capsule filled with D_2 and ^3He gas. The ~3×10^8 protons emitted from the 45-μm full width at half maximum source region interact with matter and electromagnetic fields in a cone-in-shell capsule implosion. The position and energy of every proton reaching the detector are individually recorded on CR-39, encoding the details of the matter and field distributions surrounding the target capsule.

[1]Plasma Science and Fusion Center, Massachusetts Institute of Technology, Cambridge, MA 02139, USA. [2]Laboratory for Laser Energetics, University of Rochester, Rochester, NY 14623, USA.

*Present address: Lawrence Livermore National Laboratory, Livermore, CA 94551, USA.
†To whom correspondence should be addressed. E-mail: petrasso@psfc.mit.edu

laser drive (Fig. 2), shortly after the end of the acceleration phase (*4*). The radiographs were taken perpendicular to the Au cone axis. Figure 3 shows the experimental results (which are also characteristic of many implosions without cones). Because the detector records proton fluence and energy, Fig. 3 shows images illustrating the spatial distributions of both proton fluence and mean proton energy.

Five important features are apparent in these images. First, the character of the isotropic and monoenergetic proton source is reflected in the uniform background of Fig. 3, A and C. Second, a complex filamentary structure is seen in the fluence image of Fig. 3B. The uniform energy seen outside the capsule in Fig. 3D demonstrates that the fluence striations are due to electromagnetic deflection rather than to scattering through plasma density filaments. Third, substantial plasma blowoff from the cone casts a much wider shadow as the capsule is imploded. Fourth, a significant enhancement of the proton fluence at the center of the imploded target (Fig. 3B) suggests the presence of a radially directed, focusing electric field. Finally, radial compression of the capsule by a factor of two is seen in Fig. 3D. The basic repeatability of the field structure and capsule compression was demonstrated by radiographs taken at the same relative time but on different implosions.

In the radiographic images, field structure is studied by means of the spatial distribution of proton fluence. The proton-path–integrated electric (E) or magnetic (B) field can be estimated from the angular deflection θ of protons of energy E_p passing through the field region:

$$\int E_\perp dl = 2(E_p/e)\tan\theta \quad (1)$$

$$\int B \times dl = (m_p v_p/e)\sin\theta \quad (2)$$

$$\tan\theta = M\xi/(d_{det} - d_{obj}) \quad (3)$$

where m_p is the proton mass, v_p is the proton speed, e is the fundamental unit charge, the magnification $M = 25$, and d_{det} and d_{obj} are the distances from the backlighter capsule to the detector and to the target capsule, respectively (Fig. 1). The deflection angle is determined by measuring the apparent displacement ξ of protons in the target plane via Eq. 3.

Areal density at different positions in the target capsule is studied through the downshift in proton energy relative to the incident energy of 15.0 MeV. It is proportional to the amount of matter traversed between the source and detector (*16*), quantified by ρL ($= \int \rho dl$).

Radial lineouts of the images in Fig. 3 are shown in Fig. 4. In the fluence lineout for the imploded target (Fig. 4B), the value near radius $r = 0$ μm is markedly enhanced relative to the values at large radii (by a factor of three) and at $r = 200$ μm (by a factor of six). To explain this result, we found that a radial electric field of about 1.5×10^9 V/m is necessary to "focus" 15.0-MeV protons, to the extent observed, passing near $r = 200$ μm toward the center. Scattering is insufficient to explain this result (fig. S4).

We conjecture that this coherent field is a consequence of a large, outward-directed electron pressure gradient that exists in the vicinity of the fuel-shell interface. Such a field might be expected to occur during, and shortly after, the acceleration phase of the implosion in which substantial shell mass is rapidly assembled and compressed. Such an electric field—given by $-\nabla P_e/en_e$, where P_e and n_e are the electron pressure and density—has been observed in the context of other recent laser plasma experiments (*11*). If this conjecture is correct, future measurements of the evolution of this coherent E field might effectively map capsule pressure dynamics throughout the implosion. Such information

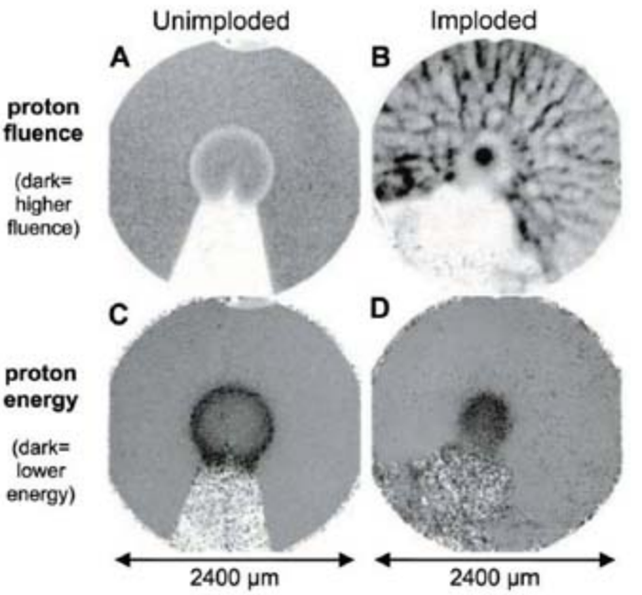

Fig. 3. Images of a 430-μm-radius spherical plastic capsule with attached Au cone, before and during implosion. (**A** and **C**) The unimploded capsule used in OMEGA shot 46531. (**B** and **D**) A capsule at 1.56 ns after the onset of the laser drive (OMEGA shot 46529). The dark areas correspond to regions of higher proton fluence [in (A) and (B)] and regions of lower proton energy [in (C) and (D)]. The energy image values in the region shadowed by the cone are mostly noise because very few protons were detected in that region. See lineouts in Figs. 4 and 5 for image values.

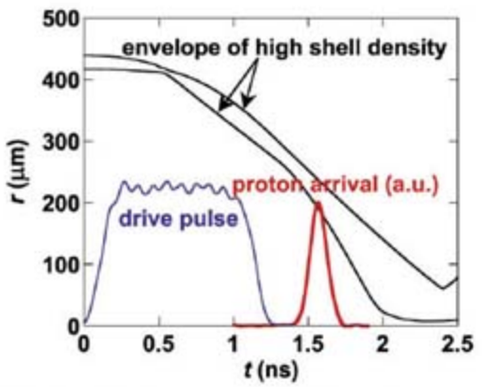

Fig. 2. Cone-in-shell capsule drive pulse (blue line), simulated (*17*) shell trajectory (black lines), and experimental backlighter proton arrival time t (red line). Simulations predict that the shell has compressed from its original radius by about a factor of two, and the ρR has doubled to 5 mg/cm^2 when the backlighter protons arrive at 1.56 ns (OMEGA shot 46529). a.u., arbitrary units.

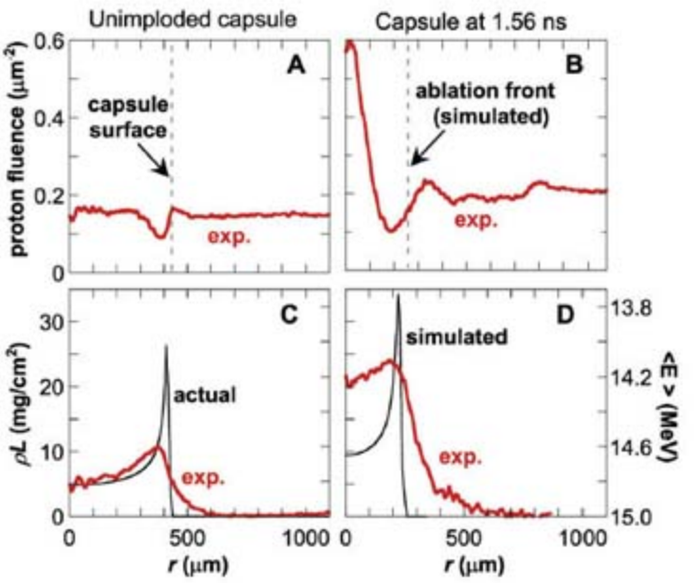

Fig. 4. Experimental (exp.) radial lineouts (red lines) of proton fluence and ρL from Fig. 3. All lineouts are averaged over the azimuth, excluding the region of the cone shadow. (**A** and **C**) Unimploded capsule of OMEGA shot 46531. (**B** and **D**) Capsule of OMEGA shot 46529, 1.56 ns after start of laser drive. The fluence lineout (A) shows the effects of angular scattering through the limb of the capsule shell. In (B), angular scattering effects alone are insufficient to explain the peak at $r = 0$. A radial electric field of ~10^9 V/m is necessary to focus the protons to the extent observed. In (C) and (D), radial lineouts of the mean energy images in Fig. 3 were converted to ρL. Also displayed are the actual ρL (C) and simulated ρL (D), assuming no angular scattering (black line). ρR is given by $\rho L/2$ at $r = 0$.

would be invaluable in assessing implosion performance.

Lineouts of the mean energy images of Fig. 3, C and D, can be used to infer the mean path areal density ρL, shown in Fig. 4, C and D. The ρL lineout of the unimploded target (Fig. 4C) gives an initial radial areal density (ρR) of 2.5 mg/cm^2, which is very close to the actual initial ρR of 2.4 mg/cm^2. Scattering of protons smears out measured ρL values near the limb of the shell at r = 410 μm. Both measurement and simulation (*17*) indicate a factor of two reduction in capsule radius at 1.56 ns. However, the ρL lineout of the imploded capsule at 1.56 ns (Fig. 4D) implies that the capsule ρR has increased to 10 mg/cm^2, which is twice the 5 mg/cm^2 predicted by numerical simulation. This high apparent experimental ρR is due in part to scattering and in part to E-field focusing of the lower-energy protons passing through the limb of the capsule shell.

Returning to the filamentary fields, we note how the outer edge of the coherent field merges, at a boundary just outside the imploding capsule, into the striated fields. As illustrated in Fig. 5C and fig. S3, the striated fields originate inside the critical surface, which is extremely close to the capsule surface. Azimuthal lineouts of the proton fluence image of Fig. 3B at radii 430 and 860 μm show the amplitude and scale of proton fluence variations (Fig. 5) due to striations. Peak-to-valley fluence modulations of a factor of four are seen at both radii. The typical angular oscillation period is 20° and 10° for the inner and outer radii, respectively, corresponding to the same spatial distance between striations of 150 μm. This distance implies a deflection angle of 0.45°, which gives a path-integrated magnetic field $\int B \times dl$ of 4000 T·μm. Assuming an integration path length equal to the typical width of striations (75 μm) results in a magnetic field strength of ~60 T. If the fluence variations are instead due to E fields, the field strength required is ~3×10^9 V/m, although quasi-neutrality of the coronal plasma with no laser energy source makes this interpretation unlikely.

The occurrence of such strong inhomogeneities inside the critical surface ~0.5 ns after the laser drive ends suggests that substantially larger fields are likely present just before laser shutoff (*18*, *19*). This situation would be reflected in a Hall parameter ($\omega\tau$) of order 1 or larger, the inverse square of which reduces the classical electron heat transport (*18*, *19*). This situation would result in the inhomogeneous inhibition of thermal transport over the capsule surface, altering even the zeroth-order hydrodynamics (*19*, *20*). Whether the source of these inhomogeneities is Rayleigh-Taylor (RT) (*21*), electrothermal (*20*), collisional Weibel (*14*, *18*), or another instability, they could provide seeds for RT growth, which, if too substantial, could degrade capsule compression and quench ignition during final stagnation phase (*4*, *18*, *19*). These issues are being actively investigated.

It seems plausible that either the electrothermal or RT instability could be the relevant source. Ongoing planar experiments, in which RT was purposely seeded, measured B fields of order 100 T with the use of the monoenergetic particle methods described here (see SOM text). Furthermore, estimates [based on (*19*)] of the RT-generated B field under similar conditions give fields of the same magnitude (see SOM text). Radiography of driven solid plastic capsules, which undergo no acceleration to drive RT growth, could be used to determine whether RT is a contributing mechanism.

Finally, the vast spatial extent of these striated fields likely reflects their outward convection resulting from the plasma flow, because the fields are tied to the outflowing plasma resulting from high plasma electrical conductivity. We conjecture that these radiographic images thus provide snapshots of filamentary structures originally produced inside the critical surface at various times during the implosion.

Two distinctly different, simultaneously occurring electromagnetic field structures, with important implications for implosion dynamics, have been characterized in imploding ICF capsules. First, a complex filamentary field topology permeates the entire 2400-μm field of view with striations corresponding to 60-T magnetic fields. This field, through the inhomogeneous inhibition of heat flux in the vicinity of the ablation surface, could generate seeds for RT growth, thereby affecting the overall implosion dynamics (*4*, *6*, *19*, *20*). Second, a coherent, radial electric field of magnitude 10^9 V/m exists in the immediate vicinity of the capsule, dramatically focusing protons toward the center (*22*). This hitherto-unobserved field is conjectured to originate from the gradient of electron pressure. If verified, a window for analyzing the evolution of the internal pressure dynamics is opened; this would be of immense value for critically assessing the entire implosion process.

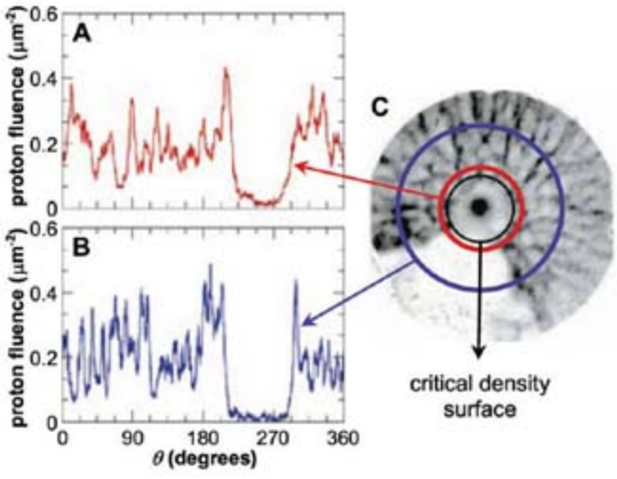

Fig. 5. Circular lineouts of proton fluence obtained from OMEGA shot 46529 at radii of 430 μm (**A**) and 860 μm (**B**). The filamentary structures represent a 2D projection of a 3D field structure that originates inside the critical density surface (**C**).

References and Notes

1. National Research Council, *Frontiers in High Energy Density Physics* (National Academies Press, Washington, DC, 2003).
2. R. P. Drake, *High-Energy-Density Physics* (Springer, New York, 2006).
3. J. Nuckolls, L. Wood, A. Thiessen, G. Zimmerman, *Nature* **239**, 139 (1972).
4. S. Atzeni, J. Meyer-ter-Vehn, *The Physics of Inertial Fusion* (Oxford Univ. Press, New York, 2004).
5. B. A. Remington, R. P. Drake, D. D. Ryutov, *Rev. Mod. Phys.* **78**, 755 (2006).
6. W. L. Kruer, *The Physics of Laser Plasma Interactions* (Westview, Boulder, CO, 2003).
7. C. K. Li *et al.*, *Rev. Sci. Instrum.* **77**, 10E725 (2006).
8. Materials and methods are available as supporting material on *Science* Online.
9. M. Tabak *et al.*, *Phys. Plasmas* **1**, 1626 (1994).
10. R. Kodama *et al.*, *Nature* **418**, 933 (2002).
11. C. K. Li *et al.*, *Phys. Rev. Lett.* **97**, 135003 (2006).
12. C. K. Li *et al.*, *Phys. Rev. Lett.* **99**, 055001 (2007).
13. A. J. Mackinnon *et al.*, *Phys. Rev. Lett.* **97**, 045001 (2006).
14. T. Mochizuki *et al.*, *Jpn. J. Appl. Phys.* **19**, L645 (1980).
15. O. Willi, P. T. Rumsby, *Opt. Commun.* **37**, 45 (1981).
16. C. K. Li, R. D. Petrasso, *Phys. Rev. Lett.* **70**, 3059 (1993).
17. Numerical simulations of full-sphere capsules, equivalent to the target capsule with no cone, were performed with the one-dimensional (1D) hydrodynamic code LILAC (*23*). The use of 1D spherical geometry to simulate the areal density of cone-in-shell capsules was previously used and found reasonable (*24*).
18. M. G. Haines, *Can. J. Phys.* **64**, 912 (1986).
19. A. Nishiguchi, *Jpn. J. Appl. Phys.* **41**, 326 (2002).
20. M. G. Haines, *Phys. Rev. Lett.* **47**, 917 (1981).
21. K. Mima, T. Tajima, J. N. Leboeuf, *Phys. Rev. Lett.* **41**, 1715 (1978).
22. The filamentary and focusing fields are present irrespective of whether the capsule is of the hot-spot or FI variety.
23. J. Delettrez *et al.*, *Phys. Rev. A* **36**, 3926 (1987).
24. C. Stoeckl *et al.*, *Plasma Phys. Controlled Fusion* **47**, B859 (2005).

25. We thank the OMEGA engineers and operations crew who supported these experiments and General Atomics for providing high-quality backlighter and target capsules. This work was supported by the Fusion Science Center (FSC) at the University of Rochester (grant no. DE-FG03-03NA00058), the National Laser Users Facility (DE-FG52-07NA28059), and the Office of Defense Programs (DE-FG52-06NA26203), all through the U.S. Department of Energy. J.R.R. also acknowledges the FSC for his postdoctoral appointment.

Supporting Online Material

www.sciencemag.org/cgi/content/full/319/5867/1223/DC1
Materials and Methods
SOM Text
Figs. S1 to S4
References and Notes

6 November 2007; accepted 25 January 2008
10.1126/science.1152640

Long-Range Order in Electronic Transport Through Disordered Metal Films

S. Aigner,[1,2] L. Della Pietra,[1] Y. Japha,[3] O. Entin-Wohlman,[3] T. David,[3] R. Salem,[3] R. Folman,[3] J. Schmiedmayer[1,2]*

Ultracold atom magnetic field microscopy enables the probing of current flow patterns in planar structures with unprecedented sensitivity. In polycrystalline metal (gold) films, we observed long-range correlations forming organized patterns oriented at ±45° relative to the mean current flow, even at room temperature and at length scales larger than the diffusion length or the grain size by several orders of magnitude. The preference to form patterns at these angles is a direct consequence of universal scattering properties at defects. The observed amplitude of the current direction fluctuations scales inversely to that expected from the relative thickness variations, the grain size, and the defect concentration, all determined independently by standard methods. Ultracold atom magnetometry thus enables new insight into the interplay between disorder and transport.

Thin metal films are the classic environment for studying the effect of geometric constraints (*1*, *2*) and crystal defects (*3*, *4*) on the transport of electrons. In a perfectly straight long wire that is free from structural defects, a direct current strictly follows the wire direction and creates a magnetic field in the plane perpendicular to the wire. An obstacle may locally change the direction of the current and consequently locally rotate the magnetic field close to the wire by an angle β in a plane parallel to the plane of the thin-film wire.

Ultracold atom magnetometry (*5*, *6*) on atom chips (*7*–*9*) allows for the sensitive probing of this angle β (and its spatial variation) with microrad (micrometer) resolution. Relative to scanning probes having micrometer-scale spatial resolution and 10^{-5} T sensitivity, or superconducting quantum interference devices (SQUIDs) having 10^{-13} T sensitivity but a resolution of tens of micrometers, ultracold atom magnetometry has both high sensitivity (10^{-10} T) and high resolution (several micrometers) (*6*). In addition, ultracold atoms enable high resolution over a large length scale (millimeters) in a single shot (*10*). This enables the simultaneous observation of microscopic and macroscopic phenomena, as described below.

Using cold atoms just above the transition to Bose-Einstein condensation (BEC), we applied ultracold atom magnetometry to study the current deflection in three different precision-fabricated polycrystalline gold wires with a rectangular cross section of 200 μm and different thicknesses and crystalline grain sizes (Table 1) (*11*). Choosing the wire length along x, its width along y, and its thickness along z, Fig. 1 shows the maps of the angular variations $\beta(x, y, z_0) = \delta B_x(x, y, z_0)/B_y$ of the magnetic field created by a current of 180 mA flowing along the wire, measured at $z_0 = 3.5$ μm above its center (far from the edges).

Even though scattering by lattice vibrations (phonons) quickly diffuses the electronic motion at ambient temperature, long-range correlations (tens of micrometers) in the current flow patterns can be seen. This is surprising, as the effects of static defects are usually observed only on a length scale of several nanometers (*12*, *13*). We observed clear patterns of elongated regions of maximal current flow deviations β inclined by about ±45° to the mean current flow direction. This angular preference was present in all the measurements, independent of wire thickness or grain size. This preference can be quantified by the normalized angular power spectra $p(\theta) = \int dk k|\beta(k, \theta)|^2$ of the magnetic field patterns, where $\mathbf{k}$ is the wave vector of the Fourier transform of the measured $\beta(x, y)$ (Fig. 1).

We observed considerable differences in the magnitude and spectral composition of the magnetic field variations above wires with different thicknesses. Table 1 summarizes the main observations and wire properties. The magnitude of β scales contrary to the surface corrugations when compared to the thickness; the thinner films (H = 280 nm) have the largest relative thickness variations but show the smallest current directional variations. Moreover, the thin wire with the large grains (grain size 150 to 170 nm) shows the smallest variations (β_{rms} = 39 μrad), much too small to be explained by the measured top surface roughness $\delta z_+^{rms}/H = 1.7 \times 10^{-3}$ of the gold film.

The observed magnetic field variations caused by the current direction variations are orders of magnitude smaller than those reported in studies of "fragmentation" of cold atom clouds on atom chips [for a review see (*9*)]. These previously reported fragmentation measurements can be fully explained by corrugations in the wire edges (*14*, *15*). In the present study, the effects caused by the wire edge roughness are strongly suppressed by the much-improved fabrication (*11*, *16*) and the flat, wide wire geometry (where the ratio between the distance to the wire surface and the distance to the wire edge is very high) (*17*).

To analyze the underlying mechanism for the current direction deviations, we consider a thin film (conductivity σ_0) in the x-y plane with a regular current $J_0\hat{x} = \sigma_0 \mathbf{E}^{(0)}$, where the electric field $\mathbf{E}^{(0)}$ is in the $\hat{x}$ direction. We consider the effect of small fluctuations in the conductivity $\delta\sigma(\mathbf{x})$ on the current flow (*10*). The current flow around a circular defect (Fig. 2, A and B) generates a dipole field with a transverse component $E_y^{(1)} \propto \sin 2\theta$ (*10*), causing the current field to be repelled from the defect (for $\delta\sigma < 0$) or attracted to the defect (for $\delta\sigma > 0$), and a 45° pattern in the transverse current flow forms.

A second illustration is a conductivity step ($\delta\sigma$) inclined by an angle θ to the current flow direction (Fig. 2C). The resulting current density fluctuation is

$$\delta\mathbf{J} = J_0 \frac{\delta\sigma}{\sigma_0} (\sin^2\theta\hat{x} - \cos\theta \sin\theta\hat{y}) \qquad (1)$$

Table 1. Properties of the wires under investigation [see text and (*10*) for definitions]. All measurements were done on the chip used for the cold atom experiment except for the low-temperature resistivity, which was measured on a duplicate chip made with an identical (simultaneous) fabrication process (*10*).

Wire	A	B	C
Thickness H (μm)	2.08	0.28	0.28
Grain size (nm)	60 to 80	30 to 50	150 to 170
Resistivity at 296 K (μohm·cm)	2.73	3.1	2.77
Resistivity at 4.2 K (μohm·cm)	0.094	0.316	0.351
Atom temperature (nK)	286 ± 15	173 ± 2	92 ± 7
Measurement height (μm)	3.5 ± 0.4	3.4 ± 0.3	3.7 ± 0.4
δz_+^{rms} (atomic force microscope) (nm)	9.4	3.5	3.1
δz_+^{rms} (white-light interferometer) (nm)	1.31	0.42	0.48
$\delta z_+^{rms}/H$ (white-light interferometer) ($\times 10^{-3}$)	0.629	1.500	1.714
β_{rms} (mrad)	0.168	0.0715	0.0388
β_{pp} (mrad)	0.4	0.2	0.1
λ_β (μm)	77	46	48

[1]Physikalisches Institut, Universität Heidelberg, Philosophenweg 12, 69120 Heidelberg, Germany. [2]Atominstitut der Österreichischen Universitäten, Technische Universität Wien, Stadionalle 2, 1020 Vienna, Austria. [3]Department of Physics, Ben-Gurion University of the Negev, P.O. Box 653, Be'er-Sheva 84105, Israel.

*To whom correspondence should be addressed. E-mail: schmiedmayer@atomchip.org

(*10*). The transverse current component J_y is again proportional to sin 2θ, which is maximal for conductivity steps inclined by θ = ±45°.

In a metal film, we expect to find a random pattern of conductivity fluctuations δσ(**x**). It can be constructed from a random spatial distribution of the above basic elements: microscopic circular defects or macroscopic conductivity steps of different angles. The relation between the microscopic and macroscopic phenomena for each of these models is described in (*10*).

For a general quantitative analysis, we expand an arbitrary distribution δσ(**x**) in a Fourier series of plane waves of the form $\delta\sigma(\mathbf{x}) = \delta\sigma_{\mathbf{k}} \sin(\mathbf{k}\cdot\mathbf{x} + \phi)$, where $\mathbf{k} = (k_x, k_y) = k(\cos\theta_{\mathbf{k}}, \sin\theta_{\mathbf{k}})$ and φ is an arbitrary phase. Each plane wave contributes to the current fluctuation angle $\alpha = \delta J_y/J_0$ according to Eq. 1, giving $\alpha(\mathbf{k}) \approx -\sin 2\theta_{\mathbf{k}}\,(\delta\sigma_{\mathbf{k}}/2\sigma_0)$ and resulting in the observed 45° pattern.

The resulting magnetic field angle fluctuations at height z above the wire is directly related to the current fluctuations by

$$\beta(\mathbf{k}, z) \approx \exp(-kz)\alpha(\mathbf{k}) \approx -\frac{1}{2}\exp(-kz)\frac{\delta\sigma_{\mathbf{k}}}{\sigma_0}\sin 2\theta_{\mathbf{k}} \qquad (2)$$

which exhibits the same angular dependence. The exponential term exp(−kz) represents a resolution limit, such that the effects of current changes on a length scale smaller than $2\pi z$ are suppressed in the spectrum of the magnetic field fluctuations. Starting from random conductivity fluctuations with a nonwhite spatial frequency distribution, the angular dependence sin 2θ will emerge, giving rise to the observed ±45° preference. We have simulated such random models, and the observable β forms two-dimensional (2D) maps similar to those in Fig. 1 (*10*). The variations δσ(**x**) in the conductivity σ in a thin metal film are caused by contributions from two physical origins: (i) bulk conductivity variations in the metal, and (ii) variations in the boundaries, namely variations in the thickness H of the film δH(**x**) leading to a change in the conductivity per unit area $\delta\sigma = \sigma_0\delta H/H$.

To investigate whether the observed current flow deviations are related to corrugations in the top surface of the wire, we measured the surface topography of the wires with a white-light interferometer. No angular preference inherent in the structure of the wires was found. Consequently, the angular pattern in the magnetic field variations presented in Fig. 1 must be a pure property of the scattering mechanism of the current flow by the wire defects, as outlined above. Moreover, when we calculated the 2D magnetic field at 3.5 μm above the surface, using the white-light interferometry measurements and the assumption $\delta H(\mathbf{x}) = \delta z_+(\mathbf{x})$, we could not find a reasonable fit between the latter and the magnetic mapping done by the atoms (Fig. 1). A detailed analysis of the top surface corrugations δz_+ (Fig. 3) shows that they are significantly larger for the thick film than for the two thin films, especially at short length scales.

To quantify our findings, we compared the power spectra of the measured magnetic field variations to those calculated from several models on the basis of the measured top surface variations, an assumed bottom surface roughness, and possible inhomogeneities in the bulk conductivity (Fig. 4). For the two thin wires B and C, the measured power spectra of the magnetic field variations are lower (by two orders of magnitude for large wavelengths) than predictions based on a model with a flat bottom surface ($\delta H = \delta z_+$). If we assume that the top surface exactly follows the bottom surface ($\delta z_+ = \delta z_-$), a lower bound on the influence of the surface on magnetic field fluctuations can be obtained, as this configuration produces vertical currents whose contribution to the longitudinal magnetic field, to which our experiment is sensitive, is very small. The measured data are in between these two cases.

A fair fit of the measured spectrum for the thin wires is obtained if we assume that the top surface partially follows the large-wavelength fluctuations of the bottom surface, whereas independent fluctuations of the top surface exist in the shorter scale. For such a model (*10*), we assume $\delta z_-(k) \approx \delta z_+(k)\exp[-(k/k_0)^2]$. Note that the resulting average thickness variations are

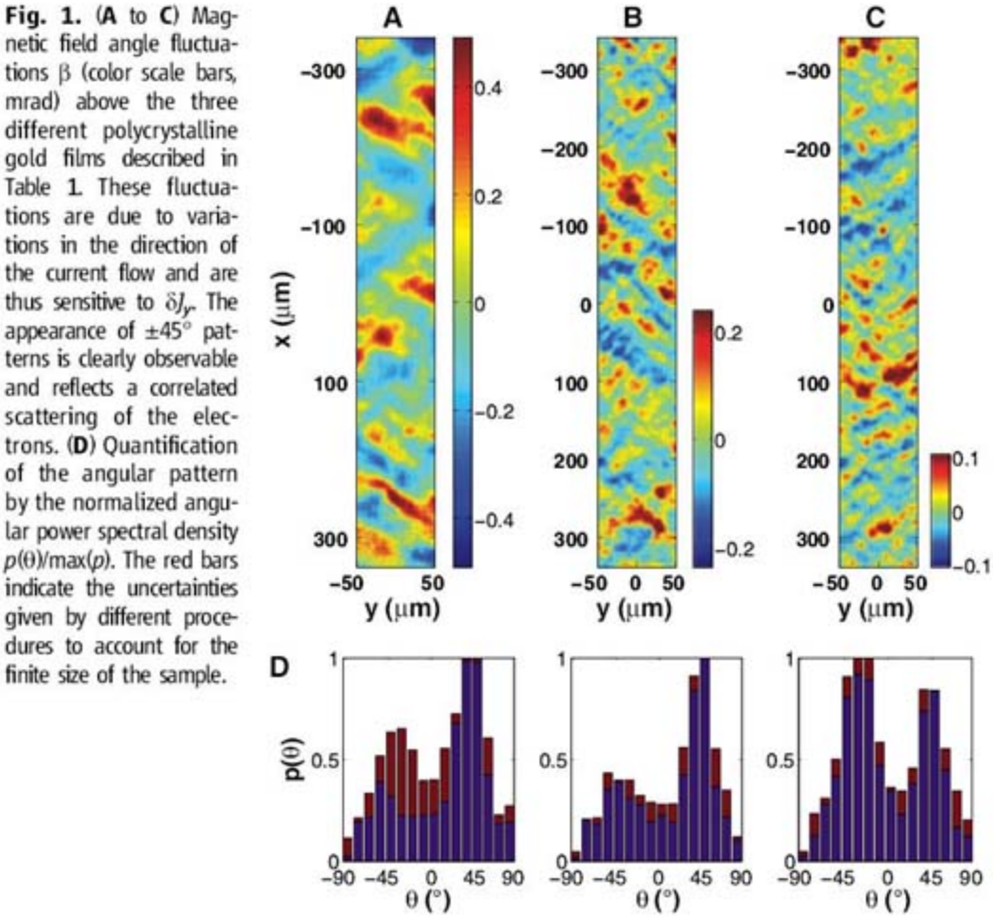

Fig. 1. (**A** to **C**) Magnetic field angle fluctuations β (color scale bars, mrad) above the three different polycrystalline gold films described in Table 1. These fluctuations are due to variations in the direction of the current flow and are thus sensitive to δJ_y. The appearance of ±45° patterns is clearly observable and reflects a correlated scattering of the electrons. (**D**) Quantification of the angular pattern by the normalized angular power spectral density $p(\theta)/\max(p)$. The red bars indicate the uncertainties given by different procedures to account for the finite size of the sample.

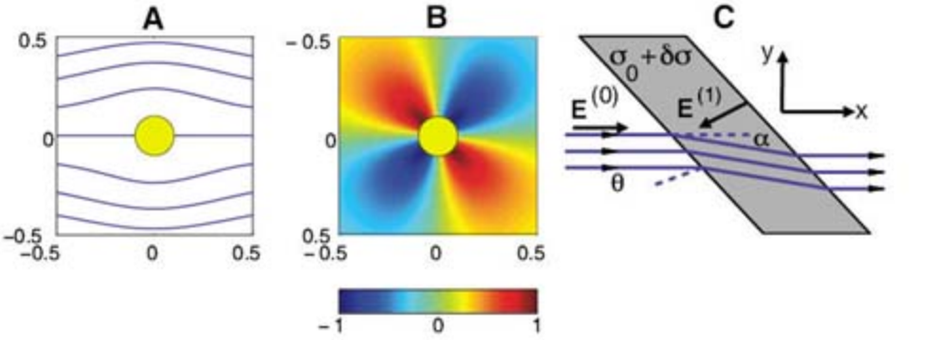

Fig. 2. (**A**) Current scattering by circularly symmetric (disk) local conductivity variations δσ < 0. (**B**) The transverse ($\hat{y}$) component of the current is proportional to sin 2θ. (**C**) Direction change of a current flow due to a conductivity step defect inclined by an angle θ relative to the current flow direction $\hat{x}$. The conductivity is σ_0 everywhere except in the shaded area, where it is $\sigma_0 + \delta\sigma$ (δσ > 0 in this example). Again, the electron scattering amplitude is proportional to sin 2θ. For details see (*10*).

extremely small: $\delta H^{rms} < 1$ Å (with $\delta H = \delta z_+^{rms} - \delta z_-^{rms}$). This value of δH^{rms} refers to length scales longer than 1 μm, whereas atomic force microscope measurements showed much larger surface variations on the scale of the grains (Table 1).

The situation is different for the thick wire A (H = 2 μm). Models assuming a flat bottom surface ($\delta H = \delta z_+$) underestimate the measured magnetic field variations, as do models assuming a corrugated bottom surface δz_- with a spectrum similar to that of wire B and no correlations with the top surface. The difference between the surface models and the measured data of wire A can be attributed to fluctuations in the bulk conductivity. A model taking the maximal contribution of surface roughness (uncorrelated top and bottom surfaces) into account gives the minimal required contribution of the bulk conductivity fluctuations (*10*). If we apply the same minimal bulk conductivity fluctuations as obtained from wire A to the two thin wires B and C, they overestimate the measured magnetic field fluctuations substantially for both wires and give a different spectral shape. This indicates that the bulk conductivity of the thinner wires should be more homogeneous than that of the thick wire.

A more homogeneous bulk conductivity in the thin wires, however, appears to be contradictory to the fact that the low-temperature resistivity is smaller for the thick wire than for the thin wires (Table 1). Nonetheless, we note that this resistivity is mainly determined by the small-scale properties of the wire (on the order of the grain size or less) and by surface scattering, whereas the magnetic field variations probe the conductivity inhomogeneities at a larger scale and provide complementary information that would not be available by standard methods.

Our analysis furthermore suggests (*10*) that the differences in the length scale λ_β of the variation in β, as seen in Fig. 1 and quantified in Table 1, may originate from the fact that conductivity variations in the thin wires (a result of thickness variations) are suppressed at long length scales because of top and bottom surface correlations. In contrast, conductivity variations in the thick wire originate at all scales from a combination of thickness variations due to uncorrelated top and bottom surfaces and a dominant contribution of bulk conductivity inhomogeneity.

Our study constitutes a direct application of ultracold atoms as a probe for solid-state science. The exceptional sensitivity of the ultracold atom magnetic field microscope (*5*, *6*) allowed us to observe long-range patterns of the current flow in a disordered metal film. The preference of features with angles around ±45° in the measured angular spectrum of the current flow fluctuations is due to the universal scattering properties at defects. A detailed quantitative analysis reveals that the observed current directional fluctuations at different wires exhibit diverse and unexpected properties due to different physical origins. Our results clearly demonstrate the power of the ultracold atom magnetic field microscope to study details of the current flow in conductors, as well as its ability to reveal previously inaccessible information. This technique may be expected to stimulate new studies of the interplay between disorder and coherent transport in a variety of systems ranging from high-T_c superconductors (*18*) to 2D electron gases (*19*) and nanowires (*20*).

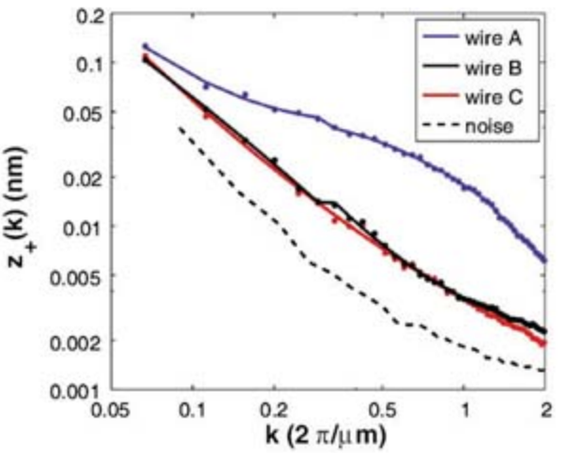

Fig. 3. Radial spectrum of the top surface corrugations $|\delta z_+(k)| = [(2\pi)^{-1}\int d\theta |\delta z_+(k, \theta)|^2]^{1/2}$ for the three wires measured with a white-light interferometer. Note the considerable difference between wire A and wires B and C. Measurement noise level was calculated by averaging over many partly overlapping images (*10*).

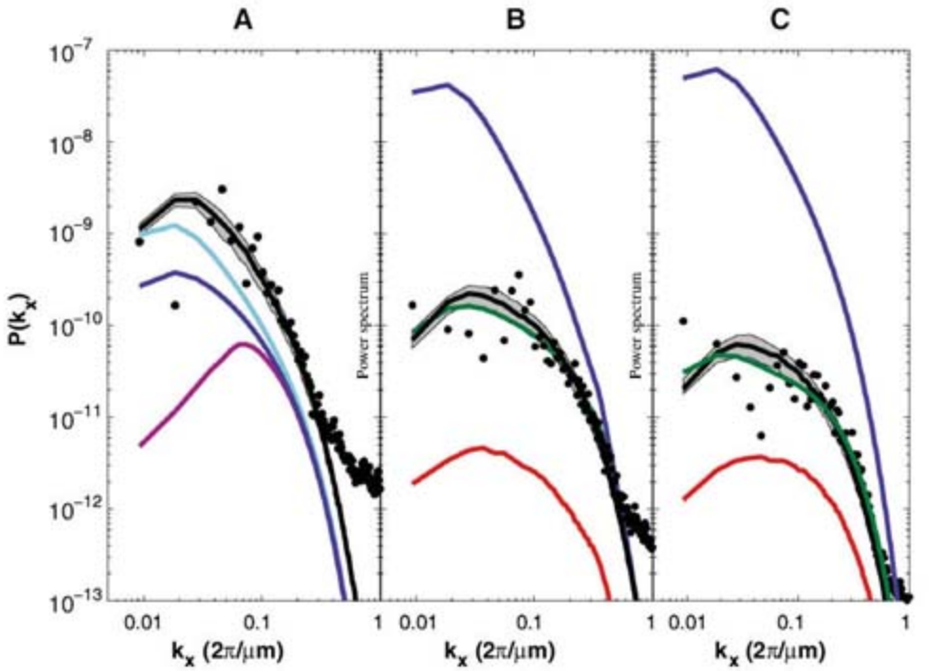

Fig. 4. Comparison of surface and bulk model calculations (lines) with the measured power spectrum $P(k_x) = \sum_{k_y} |\beta(k_x, k_y)|^2$ of the magnetic field angle β along the x direction above the three wires (points). Blue: Top surface δz_+ as in Fig. 3 with flat bottom surface $\delta z_- = 0$. Red: Top surface follows bottom surface $\delta z_+ = \delta z_-$ (i.e., no thickness variations). Green: Partially correlated top and bottom surfaces for wires B and C. For the thick wire A, we assume $\delta z_-(k)$ as in wire B, which is correlated (purple) or uncorrelated (light blue) with the top surface. The latter gives the closest estimate for the experimental data but gives a β_{rms} value that is only about half of the measured value. Black: A fit to a model assuming bulk conductivity fluctuations. The shaded area represents a 1-SD range obtained by varying the relative phases of different spectral components $\delta\sigma(k_x, k_y)$. See (*10*).

References and Notes

1. E. H. Sondheimer, *Adv. Phys.* **1**, 1 (1952).
2. R. G. Chambers, *Proc. R. Soc. London Ser. A* **202**, 378 (1950).
3. A. F. Mayadas, M. Shatzkes, *Phys. Rev. B* **1**, 1382 (1970).
4. R. Landauer, *IBM J. Res. Dev.* **1**, 223 (1957).
5. S. Wildermuth *et al.*, *Nature* **435**, 440 (2005).
6. S. Wildermuth *et al.*, *Appl. Phys. Lett.* **88**, 264103 (2006).
7. R. Folman, P. Krüger, J. Schmiedmayer, J. Denschlag, C. Henkel, *Adv. At. Mol. Opt. Phys.* **48**, 263 (2002).
8. J. Reichel, *Appl. Phys. B* **74**, 469 (2002).
9. J. Fortagh, J. C. Zimmermann, *Rev. Mod. Phys.* **79**, 235 (2007).
10. See supporting material on *Science* Online.
11. The chip was fabricated at the Weiss Family Laboratory for Nanoscale Systems, Ben-Gurion University, Israel (www.bgu.ac.il/nanofabrication).
12. W. Steinhögl, G. Schindler, G. Steinlesberger, M. Engelhardt, *Phys. Rev. B* **66**, 075414 (2002).
13. M. A. Schneider, M. Wenderoth, A. J. Heinrich, M. A. Rosentreter, R. G. Ulbrich, *Appl. Phys. Lett.* **69**, 1327 (1996).
14. D.-W. Wang, M. D. Lukin, E. Demler, *Phys. Rev. Lett.* **92**, 076802 (2004).
15. T. Schumm *et al.*, *Eur. Phys. J. D* **32**, 171 (2005).
16. S. Groth *et al.*, *Appl. Phys. Lett.* **85**, 2980 (2004).
17. P. Krüger *et al.*, *Phys. Rev. A* **76**, 063621 (2007).

18. D. A. Bonn, *Nat. Phys.* **2**, 159 (2006).
19. S. Ilani, A. Yacoby, D. Mahalu, H. Shtrikman, *Science* **292**, 1354 (2001).
20. J. Feist *et al.*, *Phys. Rev. Lett.* **97**, 116804 (2006).
21. We thank the team of the Ben-Gurion University Weiss Family Laboratory for Nanoscale Systems for the fabrication of the chip, and J. Jopp of the Ben-Gurion University Ilse Katz Center for Nanoscale Science for assisting with surface measurements. R.F. thanks Y. Imry and A. Klug for their continued support. Supported by the Fonds zur Förderung der Wissenschaftlichen Forschung, Deutsche Forschungsgemeinschaft, German Federal Ministry of Education and Research (Deutsch-Israelische Projektkooperation), European Community "Atomchip" Research Training Network, American-Israeli Binational Science Foundation, and Israeli Science Foundation.

Supporting Online Material
www.sciencemag.org/cgi/content/full/319/5867/1226/DC1
Materials and Methods
Figs. S1 to S3
References

1 November 2007; accepted 7 January 2008
10.1126/science.1152458

Chemically Derived, Ultrasmooth Graphene Nanoribbon Semiconductors

Xiaolin Li,* Xinran Wang,* Li Zhang, Sangwon Lee, Hongjie Dai†

We developed a chemical route to produce graphene nanoribbons (GNR) with width below 10 nanometers, as well as single ribbons with varying widths along their lengths or containing lattice-defined graphene junctions for potential molecular electronics. The GNRs were solution-phase–derived, stably suspended in solvents with noncovalent polymer functionalization, and exhibited ultrasmooth edges with possibly well-defined zigzag or armchair-edge structures. Electrical transport experiments showed that, unlike single-walled carbon nanotubes, all of the sub–10-nanometer GNRs produced were semiconductors and afforded graphene field effect transistors with on-off ratios of about 10^7 at room temperature.

Graphene (single-layer graphite) has emerged as a material with interesting low-dimensional physics and potential applications in electronics (*1*–*6*). Graphene nanoribbons (GNRs), if made into quasi-one-dimensional structures with narrow widths (<~10 nm) and atomically smooth edges, are predicted to exhibit band gaps useful for room-temperature transistor operations with excellent switching speed and high carrier mobility (potentially even ballistic transport) (*7*–*13*). Recent theoretical work predicted that quantum confinement and edge effects make narrow GNRs (width w < ~10 nm) into semiconductors, which differs from single-walled carbon nanotubes (SWNTs) that contain ~1/3 metallic species.

Lithographic patterning of graphene sheets has fabricated GNRs down to widths of ~20 nm thus far (*12*, *13*), but there are difficulties in obtaining smooth edges (for example, with roughness < ~5 nm) and reaching true nanometer-scale ribbon width. Chemical approaches (*14*–*17*) and self-assembly processes may produce graphene structures with desired shape and dimensions for fundamental and practical applications.

We report that, by using a widely available and abundant graphite material, we can develop simple chemical methods to produce GNRs. We exfoliated commercial expandable graphite (Grafguard 160-50N, Graftech Incorporated, Cleveland, OH) by brief (60 s) heating to 1000°C in forming gas (3% hydrogen in argon). The resulting exfoliated graphite was dispersed in a 1,2-dichloroethane (DCE) solution of poly(m-phenylenevinylene-co-2,5-dioctoxy-p-phenylenevinylene) (PmPV) by sonication for 30 min to form a homogeneous suspension. Centrifugation then removed large pieces of materials from the supernatant (Fig. 1A and fig. S1) (*18*).

We used atomic force microscopy (AFM) to characterize the materials deposited on substrates from the supernatant and observed numerous GNRs with various widths ranging from w ~ 50 nm down to sub-10 nm (Fig. 1, B to F). Topographic heights of the GNRs (average length ~ 1 μm) were mostly between 1 and 1.8 nm, which correspond to a single layer (e.g., Fig. 1B, left image) or a few layers (mostly ≤3 layers). Smooth edges were observed for the GNRs, with edge roughness well below ribbon width even for $w \leq 10$ nm. Accurate measurements of GNR width were difficult because of the finite AFM tip radius (~10 to 20 nm), especially for ultranarrow ribbons. To circumvent the problem, we used the same tips to measure the apparent widths of Hipco (Carbon Nanotechnologies Incorporated, Houston, TX)

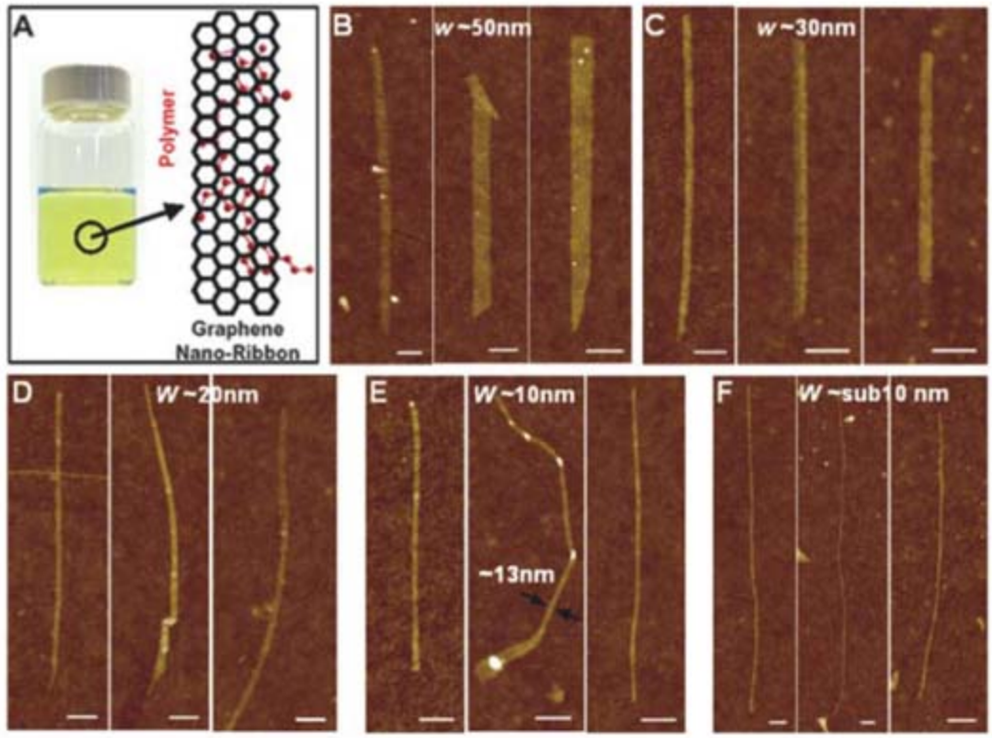

Fig. 1. Chemically derived graphene nanoribbons down to sub-10-nm width. (**A**) (Left) Photograph of a polymer PmPV/DCE solution with GNRs stably suspended in the solution. (Right) Schematic drawing of a graphene nanoribbon with two units of a PmPV polymer chain adsorbed on top of the graphene via π stacking. (**B** to **F**) AFM images of selected GNRs with widths in the 50-nm, 30-nm, 20-nm, 10 nm and sub-10-nm regions, respectively. A substrate (300-nm-thick SiO_2/p^{++}Si) was soaked in a GNR suspension for 20 min for deposition, rinsed, blow-dried, and calcined at 400°C to remove PmPV before AFM. Some of the GNRs narrow down to a sharp point near the ends. In (B), left ribbon height ~ 1.0 nm, one layer; middle ribbon height ~ 1.5 nm, two layers; right ribbon height ~ 1.5 nm, two layers. In (C), the three GNRs are two to three layers thick. In (D), ribbons are one (right image) to three layers. Two GNRs crossing in the left image are observed. In (E), ribbons are two- to three-layered. In the middle image, a single ribbon exhibits varying width along its length with mechanical bends (bright regions) between segments. In (F), the heights of the ultranarrow ribbons are ~1.5, 1.4, and 1.5 nm, respectively. All scale bars indicate 100 nm.

Department of Chemistry and Laboratory for Advanced Materials, Stanford University, Stanford, CA 94305, USA.

*These authors contributed equally to this work.
†To whom correspondence should be addressed. E-mail: hdai@stanford.edu

SWNTs in a diameter-separated sample and deduced tip size (*18*). All GNR widths reported in this work have their basis in AFM measurements after correcting for the tip-size effect.

Transmission electron microscopy (TEM, fig. S5) (*18*), electron diffraction (fig. S5) (*18*), and Raman spectroscopy (fig. S6) (*18*) (graphene G-band) were used to characterize the GNRs. Because of their topographical resemblance to SWNTs, we carried out extensive control experiments to ensure that the sub-10-nm GNRs in our samples were not SWNTs present from contamination or other causes. For example, we performed surface-enhanced Raman measurements on many GNR samples deposited on Au substrates and never observed any radial breathing modes intrinsic to SWNTs (fig. S6) (*18*). Further, all of our $w < 10$ nm GNRs were semiconductors (see below), unlike SWNTs, which form as mixtures in which one-third of nanotubes are metallic.

The formation of our GNRs constitutes several key steps. First, ~350-μm-scale graphite flakes were made into expandable graphite by chemical intercalation of oxidizing sulfuric acid and nitric acid, with oxidation of carbon atoms likely occurring at the edge, step, and defect sites of graphite (*19*, *20*). Second, rapid heating of the expandable graphite to 1000°C caused violent formation of volatile gaseous species from the intercalant and exfoliates graphite into a loose stack of few-layered graphene sheets. This thermal exfoliation step is critical and responsible for the formation of one- to few-layer graphene and was evidenced by a visible, dramatic volume expansion of graphite by ~100 to 200 times after exfoliation (fig. S1) (*18*). The 1000°C treatment can also reverse oxidation and functionalization of graphite by thermally desorbing covalently attached species and repair defects (*21*).

Solution-phase sonication and functionalization by PmPV of few-layered graphene sheets formed by 1000°C exfoliation led to stably suspending graphene in DCE. The PmPV conjugated polymers (Fig. 1A), known to adsorb onto SWNT sidewalls via π stacking, noncovalently functionalized the exfoliated graphene to afford a homogeneous black suspension during sonication (fig. S1) (*18*, *22*, *23*). We were not able to form homogeneous suspension by the same process without using PmPV. We suggest that sonication is responsible for chemomechanical breaking of the stably suspended graphene sheets into smaller pieces, including nanoribbons. Sonochemistry and ultrahot gas bubbles involved in sonication cause graphene to break into various structures, with an appreciable yield of GNRs. The supernatant after centrifugation contains micrometer-sized graphene sheets and GNRs (albeit at lower yield than sheets) in various sizes, shapes, and morphologies.

Besides regularly shaped ribbons, we observed graphene structures that were shaped irregularly, such as wedges (Fig. 2), GNRs with bends and kinks (Fig. 2, A, B, and E), and ribbons coming off larger pieces of graphene with varying widths along the ribbon length [Fig. 1E, middle image, and fig. S5, TEM data (*18*)]. These results suggest that GNRs could be formed by breaking off narrow pieces of graphene from larger sheets during sonication. However, we found that continuous sonication does not lead to higher yield of GNRs and that the degree of sonication needs to be controlled for optimal yield of GNRs. Imaging with AFM indicated that almost no sub-10-nm ribbons were obtained if sonication were excessive (for hours) because of continued cutting and breaking of ribbons into small particle-like structures.

The observed graphene nanoribbons narrowing down to diminishing width and to a point (Fig. 2, C and D) indicate that GNRs reaching true nanometer dimensions with potentially atomic-scale smoothness can form. GNRs comprised of segments of varying widths (Fig. 1E, middle image, and 2B) could be used for graphene molecular electronics with varying band gaps along the ribbon. Interestingly, GNR junctions with sharp kinks at 120° angle were observed (Fig. 2B), apparently through the joining of two GNRs with edges along well-defined atomic lattice of graphene (such as zigzag edges). Single-layered GNRs displayed remarkably mechanical flexibility and resilience, with mechanical bending and folding without obvious breakage (Fig. 2E).

Next, we fabricated field-effect transistor (FET)–like devices with our GNRs (w ~ sub-10 nm to ~55 nm). The devices had palladium (Pd) as source/drain (S/D) metal contacts (channel length L ~ 200 nm), a p^{++}-Si backgate, and 300-nm SiO_2 as gate dielectrics (*18*). We observed that the room-temperature on-off current switching (I_{on}/I_{off}) induced by the gate voltage increased exponentially as the GNR width decreased, with I_{on}/I_{off} ~1, ~5, ~100, and $>10^5$ for w ~ 50 nm [fig. S7 (*18*)], w ~ 20 nm [fig. S7 (*18*)], w ~ 10 nm (Fig. 3A), and w ~ sub-10-nm (Fig. 3C) GNRs, respectively. This trend was consistent with lithographically fabricated GNRs with $w > 20$ nm (*12*). Importantly, all of the w = sub-10-nm GNRs characterized in our experiments (more than 30, with no exceptions) exhibited $I_{on}/I_{off} > 10^5$ (Fig. 4A) even under a S/D bias V_{ds} up to ~1 V. This suggests that the GNRs are semiconducting and have substantial band gaps. This result is in stark contrast to SWNTs (with circumference ~ sub-10 nm, or diameter < ~3 nm) that contain 1/3 metallic species. Thus, our chemically derived GNRs afford graphene transistors with orders of magnitude on/off switching at room temperature.

We could estimate the band gaps (E_g) of our GNRs by $I_{on}/I_{off} \propto \exp(E_g/k_BT)$ (where k_B is the Boltzmann's constant and T is temperature) in our p-type uni-polar GNR FETs because the off current of the device was thermally activated through a body-Schottky barrier (SB) to the conduction band on the order of ~E_g [the SB to holes in our GNR FETs was small, as is the case for Pd-contacted SWNT FETs, because of the high work function of Pd (*24*)]. The band gaps extracted this way were fit into an empirical form of $E_g(\text{eV}) = \frac{0.8}{W(\text{nm})}$ (Fig. 4B), which was con-

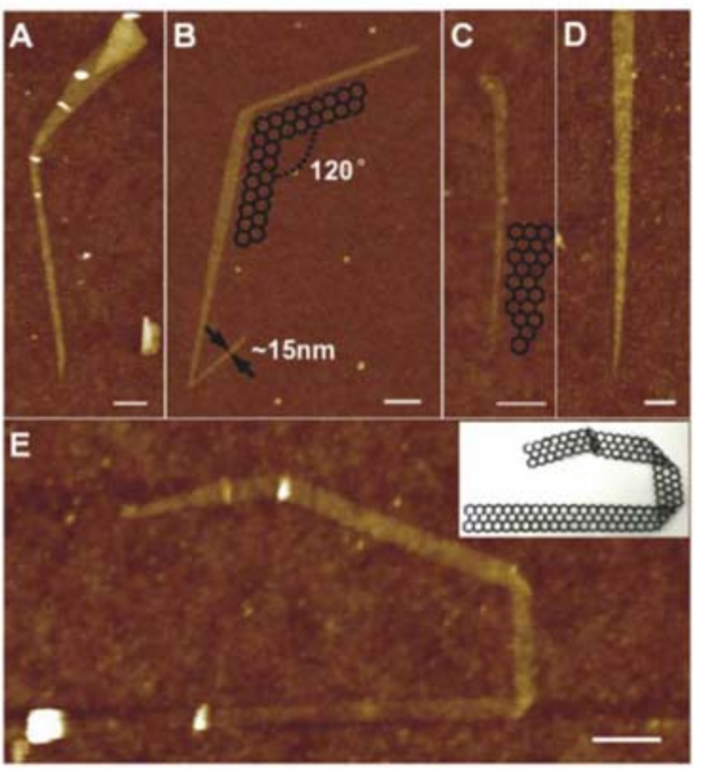

Fig. 2. Graphene nanoribbons with interesting morphologies and graphene-junctions. (**A** and **B**) AFM images of GNRs with junctions formed by different graphene structures at the two sides of the junctions. In (A), a w ~ 25 nm ribbon (two layers) forming a junction with a wedgelike graphene. In (B), a single-layer (height ~ 1.0 nm) graphene structure with three graphene segments of different widths forming two junctions. The well-defined 120° angle of the top junction suggests that the graphene segments near the kink likely have zigzag edges, as shown in the schematic drawing of the inset. (**C** and **D**) AFM images of knifelike graphene ribbons with width changing narrowing down from tens of nanometers to ultra sharp points. In (C), the ribbon is monolayer graphene with height ~ 1.0 nm. Inset of (C) A schematic drawing to illustrate the sharp tip. In (D), the ribbon is three-layer graphene with height ~ 1.9 nm. (**E**) AFM image of a GNR with several bends and folds involving mechanical deformations. It is a monolayer graphene ribbon with height ~ 1.1 nm. Inset of (E) A schematic drawing of the ribbon. All scale bars are 100 nm.

sistent with the exponential increase in I_{on}/I_{off} of our GNR FETs as ribbon width decreased. Possible errors in our E_g versus w analysis include uncertainties in w based on AFM and in the assumption of negligible SB for holes in ultranarrow (e.g., $w < \sim 3$ nm) GNR FETs.

First-principles calculations have suggested that GNRs open up band gaps through quantum confinement and edge effects and that $E_g \sim 1/w^{\alpha}$, where α is near unity (*7*, *8*). In armchair-edged GNRs, band gaps arise from quantum confinement and increased hopping integral of the π orbitals of the edge atoms caused by slight changes in atomic bonding lengths. In zigzag-edged GNRs, band gaps result from a staggered sublattice potential from magnetic ordering (*7*). The all-semiconductor nature found for our sub-10-nm GNRs is consistent with the band gap opening in GNRs with various edge structures suggested theoretically (*7*, *8*). Band gap values extracted from our experimental data fall in between the limits of theoretical calculations (*7*) for zigzag- and armchair-edged GNRs with various widths (Fig. 4B). More quantitative comparisons of our extracted band gaps with theory are difficult at the present time because the precise edge structures of the GNRs in our FETs are unknown and are likely to vary between ribbons in various devices with either zigzag, armchair, or mixed edges.

Our $w \sim$ sub-10-nm GNR devices deliver up to ~200 μA/μm on-current at $V_{ds} = 0.5$ V for $L \sim 200$ to 300 nm ribbon channel length, which is lower than the projected performance (~1000 μA/μm) for ballistic GNR transistors with similar widths (*10*, *25*). It may be possible that by further optimizing contact and reducing channel length to the $L \sim 20$ nm region (*25*), higher on-current near-ballistic graphene FETs could be obtained. Assessment of carrier mobility requires more accurate gate capacitances (*26*, *27*) than are currently available. Analysis based on electrostatic simulations of gate capacitances led to an estimated hole mobility in the $w \leq 10$ nm ribbons of ~100 to 200 cm^2/V s. This high mobility suggests that the GNRs are of high quality, nearly pristine, and free of excessive covalent functionalization, which is consistent with spectroscopic data [fig. S2 (*18*)]. More precise mobility analysis will require accurate data on gate capacitances, GNR width and edge structures (*28*), and ensuring ohmic contacts to the ribbons. At the present time, the experimentally observed all-semiconducting nature of narrow GNRs appears to be a key advantage over SWNTs as candidates for future nanoelectronics.

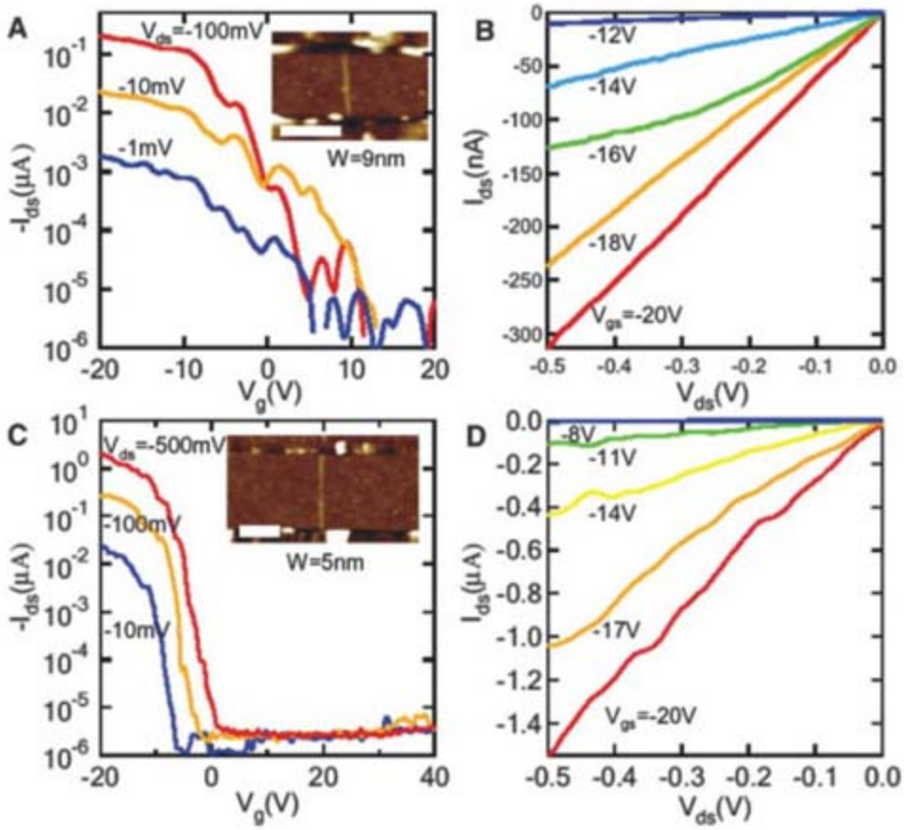

Fig. 3. Room-temperature graphene nanoribbon FETs with high on-off ratios. (**A**) Transfer characteristics (current versus gate voltage I_{ds}-V_{gs}) for a $w \approx 9$ nm (thickness ~ 1.5 nm, ~two layers) and channel length $L \sim 130$ nm GNR with Pd contacts and Si backgate. (Inset) AFM image of this device. Scale bar is 100 nm. (**B**) Current-voltage (I_{ds}-V_{ds}) curves recorded under various V_{gs} for the device in (A). (**C**) Transfer characteristics for a $w \approx 5$ nm (thickness ~ 1.5 nm, ~two layers) and channel length $L \sim 210$ nm GNR with Pd contacts. (Inset) The AFM image of this device. Scale bar is 100 nm. (**D**) I_{ds}-V_{ds} characteristics recorded under various V_{gs} for the device in (C).

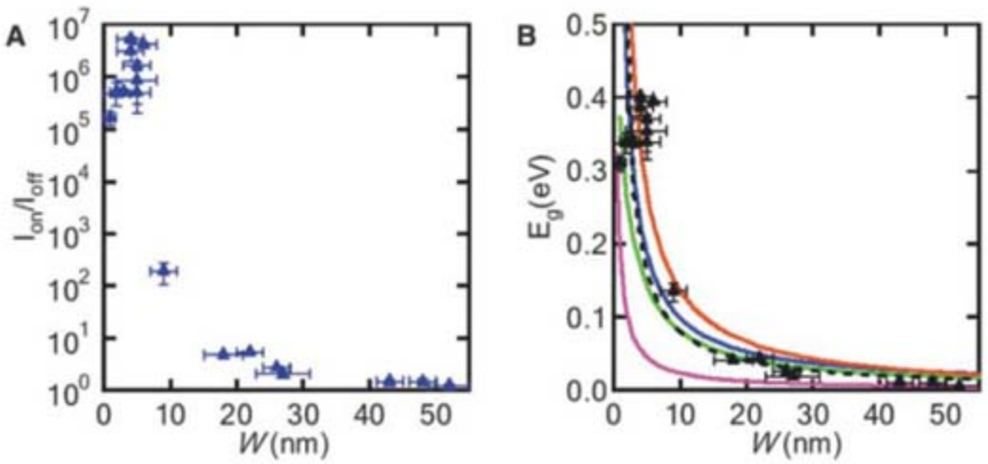

Fig. 4. Electrical properties of graphene nanoribbon FETs. (**A**) I_{on}/I_{off} ratios (under $V_{ds} = 0.5$ V) for GNRs of various ribbon widths measured in this work. Error bars for the *x* axis have their bases in uncertainties in ribbon width based from AFM measurements. Error bars for the *y* axis have their bases in the fluctuations in off state current (as shown in Fig. 3). (**B**) E_g extracted from experimental data (symbols) for various GNRs versus ribbon width. The black dashed line is a fit of our experimental data into an empirical form of E_g(eV) = 0.8/[*w*(nm)]. The purple, blue, and orange solid lines are first-principle calculations [Eqs. 1, 2, and 3 in (*18*)] for three types of armchair-edged GNRs respectively, and the green solid line is calculations for zigzag-edged GNRs [Eq. 4 of (*18*)], all based on (*7*).

References and Notes

1. A. K. Geim, K. S. Novoselov, *Nat. Mater.* **6**, 183 (2007).
2. K. S. Novoselov *et al.*, *Science* **306**, 666 (2004).
3. K. S. Novoselov *et al.*, *Nature* **438**, 197 (2005).
4. Y. B. Zhang, Y. W. Tan, H. L. Stormer, P. Kim, *Nature* **438**, 201 (2005).
5. C. Berger *et al.*, *Science* **312**, 1191 (2006); published online 12 April 2006 (10.1126/science.1125925).
6. C. Berger *et al.*, *J. Phys. Chem. B* **108**, 19912 (2004).
7. Y.-W. Son, M. L. Cohen, S. G. Louie, *Phys. Rev. Lett.* **97**, 216803 (2006).
8. V. Barone, O. Hod, G. E. Scuseria, *Nano Lett.* **6**, 2748 (2006).
9. D. A. Areshkin, D. Gunlycke, C. T. White, *Nano Lett.* **7**, 204 (2007).
10. G. C. Liang, N. Neophytou, D. E. Nikonov, M. S. Lundstrom, *IEEE Trans. Electron. Dev.* **54**, 677 (2007).
11. K. Nakada, M. Fujita, G. Dresslhaus, M. S. Dresselhaus, *Phys. Rev. B* **54**, 17954 (1996).
12. M. Y. Han, B. Ozyilmaz, Y. B. Zhang, P. Kim, *Phys. Rev. Lett.* **98**, 206805 (2007).
13. Z. Chen, Y. M. Lin, M. J. Rooks, P. Avouris, http://arxiv.org/abs/cond-mat/0701599 (2007).
14. S. Stankovich, R. D. Piner, S. T. Nguyen, R. S. Ruoff, *Carbon* **44**, 3342 (2006).
15. H. C. Schniepp *et al.*, *J. Phys. Chem. B* **110**, 8535 (2006).
16. A. P. Yu, P. Ramesh, M. E. Itkis, E. Bekyarova, R. C. Haddon, *J. Phys. Chem. C* **111**, 7565 (2007).

17. E. Rollings *et al.*, *J. Phys. Chem. Solids* **67**, 2172 (2006).
18. Materials and methods are available on *Science* Online.
19. H. Boehm, R. Setton, E. Stumpp, *Pure Appl. Chem.* **66**, 1893 (1994).
20. R. A. Greinke *et al.*, U.S. Patent 6,416,815.
21. A. D. Lueking, L. Pan, D. L. Narayanan, C. E. B. Clifford, *J. Phys. Chem. B* **109**, 12710 (2005).
22. A. Star *et al.*, *Angew. Chem. Int. Ed.* **40**, 1721 (2001).
23. X. L. Li *et al.*, *J. Am. Chem. Soc.* **129**, 4890 (2007).
24. A. Javey, J. Guo, Q. Wang, M. Lundstrom, H. Dai, *Nature* **424**, 654 (2003).
25. Y. Ouyang, Y. Yoon, J. Guo, *IEEE Trans. Electron. Dev.* **54**, 2223 (2007).
26. S. Ilani, L. A. K. Donev, M. Kindermann, P. L. McEuen, *Nat. Phys.* **2**, 687 (2006).
27. R. Tu, L. Zhang, Y. Nishi, H. Dai, *Nano Lett.* **7**, 1561 (2007).
28. Y. Yoon, J. Guo, *Appl. Phys. Lett.* **91**, 073103 (2007).
29. We thank Graftech for providing the samples. This work was supported by Microelectronics Advanced Research Corporation Materials, Structures, and Devices Focus Center (MARCO MSD) and Intel.

Supporting Online Material
www.sciencemag.org/cgi/content/full/1150878/DC1
Materials and Methods
Figs. S1 to S7
References

24 September 2007; accepted 10 January 2008
Published online 24 January 2008;
10.1126/science.1150878
Include this information when citing this paper.

Deeply Inverted Electron-Hole Recombination in a Luminescent Antibody-Stilbene Complex

Erik W. Debler,[1,2]* Gunnar F. Kaufmann,[2,3,4] Michael M. Meijler,[2,3]† Andreas Heine,[1]‡ Jenny M. Mee,[2,3] Goran Pljevaljčić,[1] Angel J. Di Bilio,[5] Peter G. Schultz,[2,3] David P. Millar,[1] Kim D. Janda,[2,3,4,6] Ian A. Wilson,[1,2] Harry B. Gray,[5]§ Richard A. Lerner[1,2,3]§

The blue-emissive antibody EP2-19G2 that has been elicited against *trans*-stilbene has unprecedented ability to produce bright luminescence and has been used as a biosensor in various applications. We show that the prolonged luminescence is not stilbene fluorescence. Instead, the emissive species is a charge-transfer excited complex of an anionic stilbene and a cationic, parallel π-stacked tryptophan. Upon charge recombination, this complex generates exceptionally bright blue light. Complex formation is enabled by a deeply penetrating ligand-binding pocket, which in turn results from a noncanonical interface between the two variable domains of the antibody.

An excited-state complex (exciplex) formed by the interaction of an electronically excited molecule with a ground-state partner features charge transfer to a various extent and typically exhibits structureless emission that is red-shifted from the emissive features of its individual components (*1*, *2*). Among the rare examples of exciplex-like behavior in proteins (*3*) is the conjugate of monoclonal antibody EP2-19G2 with the *trans*-stilbene hapten **1** (Scheme 1), which emits intense blue light upon ultraviolet (UV) excitation (movie S1) (*4*).

In striking contrast to this highly luminescent complex, electronically excited *trans*-stilbene is only weakly fluorescent in solution, owing to efficient nonradiative decay via cis-trans isomerization (*5*). Unlike other antibody-stilbene complexes (*4*, *6*), the radiative lifetime of EP2-19G2-**1** is increased by more than two orders of magnitude with respect to free **1**, which substantially exceeds those of stilbene exciplexes formed with small organic molecules (*7*). From extensive examination of the structures and photophysical properties of several antibody-**1** conjugates, we have concluded that the bright blue-emissive species is a tryptophan:stilbene charge-transfer excited complex that undergoes deeply inverted electron-hole recombination in a rigid protein matrix.

Guided by the crystal structure of EP2-19G2-**1** (*4*), we identified seven antibody residues in van der Waals' contact with the stilbene aromatic system. These seven residues were then conservatively mutated and the corresponding proteins were expressed as single-chain variable antibody fragments (scFv) (*8*, *9*). Spectroscopic measurements indicated that mutation of Trp^{H103} to Phe ($Trp^{H103}Phe$) and Tyr^{L34} to Phe ($Tyr^{L34}Phe$) markedly reduced antibody-**1** emissions when compared to scFv wild-type (wt)-**1** [Fig. 1B and fig. S1 (*9*)]. As observed in the crystal structure of the EP2-19G2-**1** complex, the indole ring of Trp^{H103} is π-stacked parallel to the deeply buried phenyl ring of the stilbene ligand at an inter-

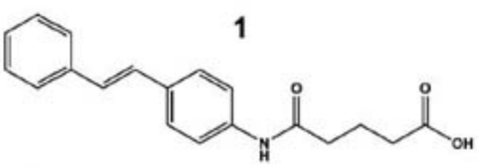

Scheme 1.

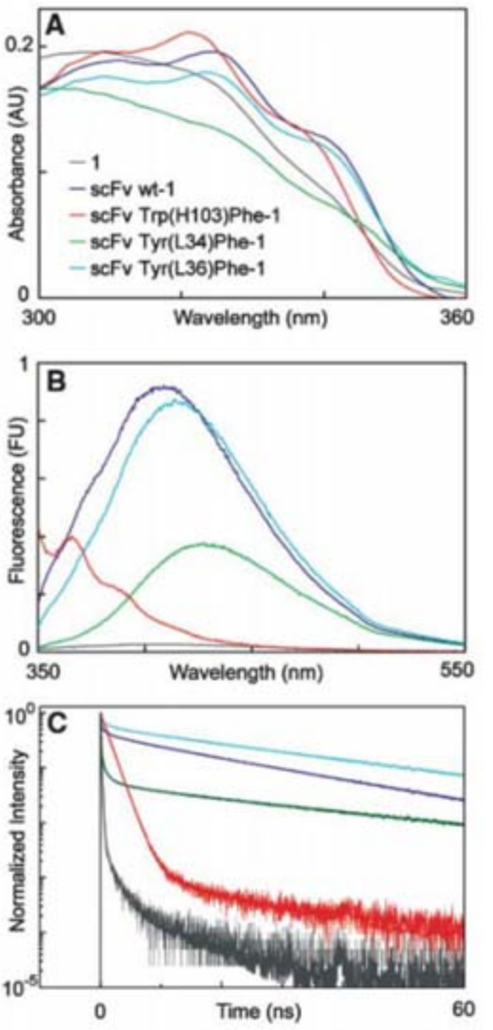

Fig. 1. (**A**) Steady-state absorption spectra of **1** (10 μM) and antibody-**1** complexes (10 μM) in PBS containing 3% DMF at room temperature. (**B**) Steady-state emission spectra of **1** (20 nM) and antibody-**1** complexes (20 nM) in PBS containing 3% DMF at room temperature. Antibody was used in large excess to ensure that the dye was completely bound by protein. (**C**) Time-resolved emission decay profiles of antibody-**1** complexes (3 μM) obtained with picosecond excitation at 303 nm. Decays were measured by time-correlated single-photon counting. Decays were recorded in 4096 channels with a time increment of 22 ps/channel and were normalized relative to the number of counts recorded in the peak channel.

[1]Department of Molecular Biology, The Scripps Research Institute, La Jolla, CA 92037, USA. [2]The Skaggs Institute for Chemical Biology, The Scripps Research Institute, La Jolla, CA 92037, USA. [3]Department of Chemistry, The Scripps Research Institute, La Jolla, CA 92037, USA. [4]Department of Immunology, The Scripps Research Institute, La Jolla, CA 92037, USA. [5]Beckman Institute, California Institute of Technology, Pasadena, CA 91125, USA. [6]Worm Institute of Research and Medicine, The Scripps Research Institute, La Jolla, CA 92037, USA.

*Present address: Laboratory of Cell Biology, The Rockefeller University, New York, NY 10065, USA.
†Present address: Department of Chemistry, Ben-Gurion University of the Negev, Israel.
‡Present address: Institute of Pharmaceutical Chemistry, Philipps-University Marburg, 35032 Marburg, Germany.
§To whom correspondence should be addressed. E-mail: rlerner@scripps.edu (R.A.L.); hbgray@caltech.edu (H.B.G.)

planar distance of 3.5 Å, whereas the Tyr^{L34} phenoxyl group is roughly perpendicular to the stilbene molecule, pointing toward its central double bond. Thus, we focused on these two residues, with the wild-type and Tyr^{L36}Phe mutant scFv fragments acting as controls. To exclude the possibility that the much weaker emission is the result of vastly diminished binding, we confirmed that mutant scFv constructs still bind tightly to hapten **1** (Table 1) (*9*).

The absorption spectra of Trp^{H103}Phe-**1** and Tyr^{L36}Phe-**1** closely resemble that of wt-**1**, featuring well-resolved, vibronic features (Fig. 1A). By contrast, the corresponding absorption system of Tyr^{L34}Phe-**1** is less structured and similar to that of free **1** in solution. The highly structured absorption system suggests that stilbene is in a constrained environment within the binding pockets of the Trp^{H103}Phe and Tyr^{L36}Phe mutants, whereas it appears to be less restricted in the Tyr^{L34}Phe protein, consistent with its decreased affinity and fluorescence anisotropy (Table 1).

The Tyr^{L34}Phe-**1** complex exhibits less intense, red-shifted emission compared with that of wt-**1** (Fig. 1B). By contrast, the emission spectrum of Trp^{H103}Phe-**1** differs markedly from that of wt-**1**, with a large blue-shift (λ_{max} at 366 nm) and even lower intensity (0.12 quantum yield) than observed for the Tyr^{L34}Phe-**1** (0.23), with a vibronically structured shoulder on the low-energy side. For comparison, both wt-**1** and Tyr^{L36}Phe-**1** emit much more intensely, with quantum yields of 0.57 and 0.55, respectively (Table 1). Notably, the scFv wt-**1** emission quantum yield is lower than that of Fab (fragment antigen binding) wt-**1** (0.71) and is most likely attributable to a less rigid binding pocket in the single-chain construct, an interpretation that also is consistent with its lower affinity for the hapten (Table 1).

Our steady-state emission measurements show clearly that the Trp^{H103} mutation greatly enhances nonradiative decay of electronically excited EP2-19G2-**1**. By using picosecond, time-resolved emission spectroscopy, we found that the long component (>20 ns) of the multi-exponential luminescence decay is essentially abolished (amplitude <0.1%) in Trp^{H103}Phe-**1** (Fig. 1C and table S1); this component, which is a major feature in the radiative decay of both wt-**1** (17%) and Tyr^{L36}Phe-**1** (27%), is also reduced substantially in Tyr^{L34}Phe-**1** (2%) (Table 1). Because of the presence of a long decay time, greatly exceeding the radiative lifetime of **1** itself, we suggest that a Trp:stilbene charge-transfer excited complex is responsible for the slow emissive decay component.

Trp^{H103} is a highly conserved framework residue of the immunoglobulin fold and, owing to its deep burial within the variable domain, rarely interacts with antigens. However, the Trp^{H103} indole closely associates with the "distal" phenyl ring of **1** in the EP2-19G2-**1** complex. If this Trp:stilbene constellation were, indeed, unique to the blue-luminescent antibody EP2-19G2-**1**, we would expect a different ligand interaction with Trp^{H103} in purple- and blue-purple–fluorescent antibodies obtained from the same immunizations with hapten **1** (*4*).

To test this hypothesis, we determined the crystal structure of the purple-fluorescent complex of Fab EP2-25C10 with **1** to 2.5 Å resolution (table S2). EP2-25C10-**1** has an emission maximum at 380 nm with a quantum yield of 0.27 and an average lifetime of 4.9 ns (*4*). The high quantum yield with respect to free stilbene most likely means that excited-state cis-trans isomerization is disfavored in the complex because the crystal structure shows that the stilbene molecule is bound in a cavity of high shape complementarity (Fig. 2A).

Table 1. Spectral data and affinities of antibody-**1** complexes and hapten **1**. All measurements were made in phosphate-buffered saline (PBS) [10 mM sodium phosphate, 150 mM NaCl (pH 7.4)] and 3% dimethyl formamide (DMF) cosolvent, at 20°C (*9*). Quinine bisulfate in 0.5 M H_2SO_4 was used as a quantum yield reference with $\Phi_f = 0.546$ (*29*). The anisotropy r is defined as $r = (I_{||} - I_{\perp})/(I_{||} + 2I_{\perp})$, where $I_{||}$ and $I_{\perp}$ are the emission intensities measured parallel and perpendicular to the vertical excitation polarization plane. The total emission intensity after pulsed excitation was fit by the multi-exponential function $I(t) = S\Sigma_i\ \alpha_i \exp(-t/\tau_i)$, convoluted with the instrument response function, where S, α_i, and τ_i are the overall scaling factor, decay amplitude, and decay time of component i (*9*). The long component 1 of the emission decay (>20 ns) is essentially abolished (amplitude α_1 of less than 0.1%) in the Trp^{H103}Phe mutant, and the relatively high anisotropy of free **1** reflects the limited depolarization that can occur during the very short lifetime of the excited state. λ_{abs} and λ_{em}, wavelength of absorption and emission maxima, respectively; K_d, dissociation constant; NA, not applicable.

Complex	λ_{abs} (nm)	λ_{em} (nm)	Φ_f	r	α_1	τ_1 (ns)	K_d (μM)
scFv wt-**1**	324	409	0.57	0.20	0.173	22.7	1.7
scFv Tyr^{L34}Phe-**1**	303	429	0.23	0.14	0.0219	34.5	3.9
scFv Tyr^{L36}Phe-**1**	323	416	0.55	0.19	0.247	30.3	2.0
scFv Trp^{H103}Phe-**1**	328	366	0.12	0.21	0.0009	15.6	2.0
Fab wt-**1**	325	409	0.71	0.23	0.330	22.8	0.3
1	307	385	0.02	0.31	1	0.0502	NA

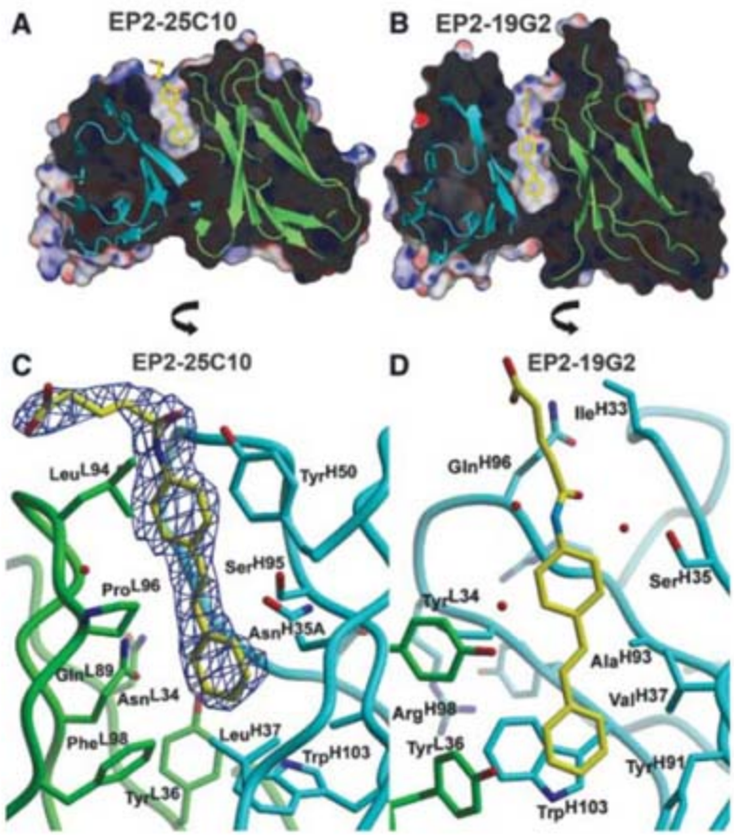

Fig. 2. Electrostatic and shape complementarity of the hapten **1** in (**A**) the EP2-25C10 and (**B**) the EP2-19G2 antibody-combining site. Slices through the center of the binding sites are shown. The heavy and light chains are colored in blue and green, respectively. The electrostatic potential was calculated in APBS (*30*) and mapped onto the surface with the color code ranging from −30 kT/e (bright red) to +30 kT/e (dark blue). Both binding pockets are highly apolar, but strongly differ in their depth and penetration of the variable antibody domain. (**C**) Crystal structure of purple-fluorescent antibody EP2-25C10 in complex with **1** (yellow). The $2F_o - F_c$ electron density map around hapten **1** is contoured at 1.5σ. (**D**) Crystal structure of the blue-emissive antibody EP2-19G2 in complex with **1** (yellow) (*4*). Trp^{H103} undergoes parallel π-stacking with **1** and forms a charge-transfer complex in the excited state. In contrast, stilbene **1** in EP2-25C10 does not engage in any π-stacking interactions with tryptophan.

The binding pocket of purple-fluorescent EP2-25C10 (Fig. 2A) is as highly hydrophobic as that of blue-luminescent EP2-19G2 (Fig. 2B), suggesting that polarity effects do not account for the 30-nm blue shift in its emission maximum. However, the overall position of the stilbene ligand within the variable part of the antibody is appreciably different in these two antibodies; in EP2-25C10, the stilbene is translated by 6 Å toward the protein surface and does not penetrate the antibody-combining site as deeply as in the EP2-19G2 complex (Fig. 2, A and B).

Consequently, the deep-seated Trp^{H103} interacts minimally with stilbene in the purple-fluorescent antibody, consistent with the relatively high emission energy. Furthermore, no EP2-25C10 tryptophan residue is involved in face-to-face or face-to-edge π-stacking interactions with stilbene (Fig. 2C). The crystal structure of the green-fluorescent antibody 11G10 in complex with a donor-acceptor–substituted stilbene reveals a binding mode similar to that in EP2-25C10 (*6*), providing strong evidence that the parallel π-stacking interaction of **1** with Trp^{H103} is attributable to the unusually deep burial of stilbene in the EP2-19G2 binding cavity.

Further structural analysis revealed that the side-chain conformation of Trp^{H103} is unusual in EP2-19G2, whereas Trp^{H103} of EP2-25C10 corresponds to the canonical rotamer that is prevalent in most antibody structures at this position (Fig. 3B). However, superimposition of the variable domains of EP2-19G2, based on the conserved framework regions, with more than 20 other antibodies, including EP2-25C10 and 11G10, yielded large root-mean-square deviations (greater than 2.0 Å) (Fig. 3A) and revealed a relatively rare disposition of heavy- and light-chain variable (V_H and V_L) domains with respect to each other in this antibody (Fig. 3C). In contrast, the individual EP2-19G2 V_H and V_L domains superimpose well onto their counterparts in other antibodies.

The geometry of the V_H/V_L interface in antibodies is generally highly conserved through invariance of ~15 side chains (*10*, *11*). Examination of the V_H/V_L interface of EP2-19G2 uncovered several notable deviations from the canonical interface and revealed factors that may synergistically contribute to the unusual relative configuration of V_H and V_L. Large deviations in the backbone conformations of the complementarity determining regions (CDRs) H3 and L3 are introduced by Pro^{H101} and Pro^{L96}, respectively (Fig. 3C). Pro^{L96} leads to a considerable displacement of conserved framework residue Trp^{H47} which, in turn, propagates this perturbation to neighboring residues and strands in V_H (Fig. 3C). The base of V_H and V_L also undergoes substantial rearrangements that include Ser^{L43} and Gln^{H105}. The latter residue now points toward V_L, unlike that in all other superimposed antibody structures. Bulky side chains at the base of CDR L1 and at the beginning of the subsequent framework region (e.g., Tyr^{L34} and Tyr^{L36}) also rearrange considerably. Thus, substantial variations at the conserved V_H/V_L interface provide a structural framework for the unusual mode of ligand recognition in EP2-19G2 that is responsible for the Trp:stilbene photophysics in the antibody-**1** complex.

Why, then, is the luminescence of EP2-19G2-**1** so intense? Consider steps 1 to 3 in the following scheme (see also Fig. 4), where TrpH represents the Trp^{H103} indole side chain carrying the N-H ring proton and *hν* is the photon energy:

1. $[\mathbf{1}/\mathrm{TrpH}] + h\nu \rightarrow [\mathbf{1}^*/\mathrm{TrpH}]$
2. $[\mathbf{1}^*/\mathrm{TrpH}] \rightarrow [\mathbf{1}^{\bullet-}/\mathrm{TrpH}^{\bullet+}]^*$
3. $[\mathbf{1}^{\bullet-}/\mathrm{TrpH}^{\bullet+}]^* \rightarrow [\mathbf{1}/\mathrm{TrpH}] + h\nu'$

In the first step, **1** absorbs a photon upon ultraviolet (UV) illumination. Because the singlet excited state of stilbene is a strong electron acceptor (*12*–*14*), an electron is transferred very rapidly from Trp^{H103} to **1*** to form a charge-transfer excited complex (step 2). Conversion of singlet-excited stilbene to the charge-transfer state does not occur at low temperatures, as only stilbene fluorescence is seen below 240 K (*4*). Owing to their close parallel interaction, the two aromatic rings in this charge-transfer state are tightly bound, which greatly disfavors nonradiative decay, because coupling of this deep and narrow excited well to the ground-state potential energy surface would be very weak (Fig. 4). As a result, radiationless deactivation would be expected to be much slower than radiative decay, hence giving rise to the exceptionally bright blue emission (step 3). Because the driving force for charge recombination is much greater than a reasonable estimate of the reorganization energy, and its rate is orders of magnitude lower than predicted for coupling-limited electron tunneling over a short distance in a folded polypeptide, we conclude that the intense luminescence is attributable to deeply inverted electron transfer (*15*, *16*).

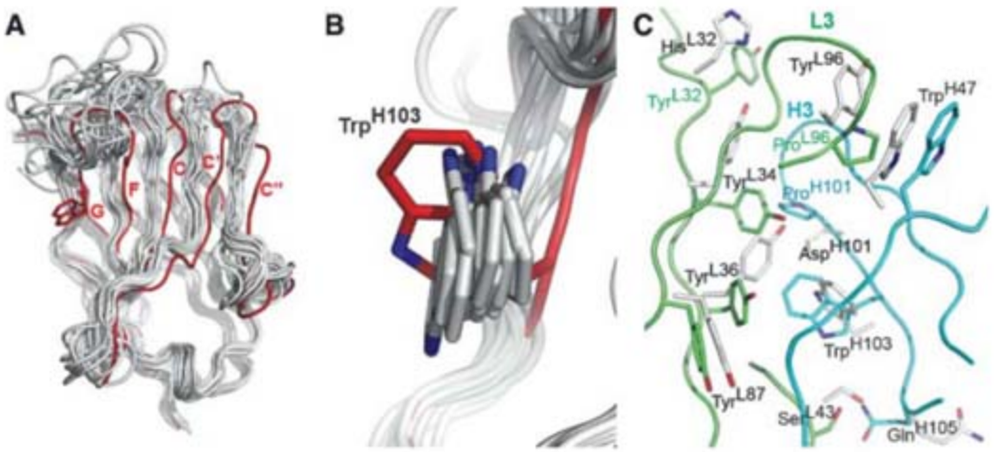

Fig. 3. (**A**) Superimposition of the EP2-19G2 variable chains (V_H + V_L domains) (red) onto other 20 catalytic antibodies (gray) based on framework regions. Only the V_H domains are shown. Trp^{H103} of EP2-19G2 is represented as a red stick. The β strands of one β sheet are labeled according to convention and clearly deviate from the corresponding strands in other antibodies. (**B**) The highly conserved Trp^{H103} features an unusual rotamer in antibody EP2-19G2 with respect to the indole side chains in the other antibodies. (**C**) Key residues at the V_H/V_L interface of EP2-19G2 (blue and green) and of a representative canonical antibody (in this case, Diels-Alder catalytic antibody 13G5, PDB ID code 1A3L, gray). Considerable structural displacements and reorientations occur over the entire interface. For clarity, some regions of EP2-19G2, as well as the backbone of 13G5, were omitted and not all conserved contacts, such as the bidentate hydrogen bond between Gln^{H39} and Gln^{L38}, are displayed. The CDRs H3 and L3 are labeled.

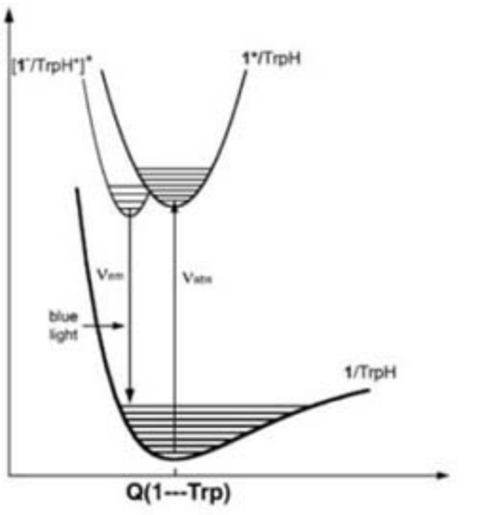

Fig. 4. Ground- and excited-state potential surfaces for EP2-19G2-**1**. After UV excitation of **1** (step 1), the stilbene excited singlet oxidizes Trp^{H103} to produce the charge-transfer complex (step 2); the interplanar distance *Q* between the cation radical Trp^{H103} and the stilbene anion **1** is shorter than in the ground state, owing to strong electrostatic binding in the hydrophobic protein cavity. In step 3, the excited charge-transfer complex returns to the ground state via electron-hole recombination that generates bright blue light in the rigid site. Radiative decay in the purple-fluorescent antibody EP2-25C10 occurs from the stilbene singlet excited state.

In view of this light-generating mechanism, the "blue-fluorescent antibody" EP2-19G2 should really be called a "blue-emissive" or "blue-luminescent" antibody.

Because roughly 3 eV of photon energy is stored in the charge-transfer excited state, it is predicted to be both a powerful reductant and oxidant. We examined the redox activity of the charge-transfer state in experiments in which irradiation of EP2-19G2-**1** was followed by flash-freezing, yielding a weak electron paramagnetic resonance signal that is attributable to a neutral tyrosyl radical having a small dihedral angle [fig. S2 (*9*)] (*17*). We suggest that a relatively small population of charge-transfer states decays by electron transfer from a tyrosine to the tryptophan radical cation, a proposal that is supported by our finding that the addition of an electron acceptor, namely $[Co(NH_3)_5Cl]^{2+}$, greatly enhances the radical signal (*17*). It is likely that the stilbene anion radical in the charge-transfer state would be oxidized rapidly by Co(III), leaving the Trp cation radical without its electron-transfer partner. The flash-quench–generated [**1**/TrpH$^{\bullet+}$] cation would then have time to oxidize any nearby protein residue, and our experiments show that tyrosine is the main electron donor.

Charge separation and recombination between a chromophore and tryptophan or tyrosine have been investigated previously in other systems (*18*–*21*). Very efficient fluorescence quenching is observed in most cases. Notably, the loss of fluorescence is due to very rapid charge recombination following femtosecond electron transfer between riboflavin and a parallel, π-stacked tryptophan after electronic excitation of the riboflavin-binding protein (*18*). Similarly, the strong fluorescence of fluorescein is quenched upon binding to antibody 4-4-20 via electron transfer from a parallel, π-stacked tyrosine in the antibody-combining site (*19*, *20*); further, the fluorescence of an anticalin-fluorescein complex is efficiently quenched by rapid electron transfer from either a coplanar tryptophan or tyrosine to singlet excited fluorescein (*21*). We conclude that the very bright blue luminescence of EP2-19G2-**1** is attributable to electron-hole recombination of the Trp:stilbene charge-transfer excited state held in the rigid EP2-19G2 matrix that disfavors nonradiative decay.

Protein luminescence (*22*) only rarely (if ever) occurs by electron-hole recombination in a charge-transfer excited state embedded in a polypeptide matrix. The distinctive photophysical properties of the antibody-stilbene complex have already been exploited in chiral sensing for high-throughput screening for the evaluation of catalysts in asymmetric synthesis (*23*, *24*), sensing mercury (*25*), DNA hybridization assays (*26*, *27*), and for analysis of accessible cysteine residues on viral surfaces (*28*). The programmed generation of antibodies against other chromophores may yield novel protein-ligand systems with similar charge recombination-induced luminescence phenomena and further biosensor applications.

References and Notes

1. J. B. Birks, *Photophysics of Aromatic Molecules* (Wiley, New York, 1970), pp. 420–421.
2. N. J. Turro, *Modern Molecular Photochemistry* (University Science Books, Mill Valley, CA, 1991), pp. 137–146.
3. A. Murza *et al.*, *Biochemistry* **39**, 10557 (2000).
4. A. Simeonov *et al.*, *Science* **290**, 307 (2000).
5. J. Saltiel, J. L. Charlton, in *Rearrangements in Ground and Excited States*, P. de Mayo, Ed. (Academic Press, New York, 1980), vol. 42, pp. 25–89.
6. F. Tian *et al.*, *Angew. Chem. Int. Ed.* **45**, 7763 (2006).
7. F. D. Lewis, *Acc. Chem. Res.* **12**, 152 (1979).
8. Heavy-chain mutants: Ser(H35)Ala, Val(H37)Leu, Tyr(H91)Phe, Trp(H103)Phe; light-chain mutants: Tyr(L34)Phe, Tyr(L36)Phe, Phe(L98)Tyr, Tyr(L34)Phe/Phe(L98)Tyr.
9. Details for the preparation of the scFv mutants and for the biophysical characterization are available as supporting material on *Science* Online.
10. C. Chothia, J. Novotny, R. Bruccoleri, M. Karplus, *J. Mol. Biol.* **186**, 651 (1985).
11. J. Novotny, E. Haber, *Proc. Natl. Acad. Sci. U.S.A.* **82**, 4592 (1985).
12. The glutaric amide group of **1** minimally perturbs the electronic structure of *trans*-stilbene (*4*). Thus, we estimate the reduction potential of **1** to be −1.9 V versus the normal hydrogen electrode (NHE) (*13*), and that of **1*** to be about +1.4 V versus NHE. The Trp cation radical reduction potential is estimated to be +1.1 V versus NHE (*14*).
13. R. S. Ruoff, K. M. Kadish, P. Boulas, E. C. M. Chen, *J. Phys. Chem.* **99**, 8843 (1995).
14. C. Tommos, J. J. Skalicky, D. L. Pilloud, A. J. Wand, P. L. Dutton, *Biochemistry* **38**, 9495 (1999).
15. H. B. Gray, J. R. Winkler, *Annu. Rev. Biochem.* **65**, 537 (1996).
16. H. B. Gray, J. R. Winkler, *Q. Rev. Biophys.* **36**, 341 (2003).
17. A. J. Di Bilio *et al.*, *J. Am. Chem. Soc.* **123**, 3181 (2001).
18. D. Zhong, A. H. Zewail, *Proc. Natl. Acad. Sci. U.S.A.* **98**, 11867 (2001).
19. M. Whitlow, A. J. Howard, J. F. Wood, E. W. Voss Jr., K. D. Hardman, *Protein Eng.* **8**, 749 (1995).
20. L. K. Denzin, G. A. Gulliver, E. W. Voss Jr., *Mol. Immunol.* **30**, 1331 (1993).
21. M. Götz, S. Hess, G. Beste, A. Skerra, M. E. Michel-Beyerle, *Biochemistry* **41**, 4156 (2002).
22. N. C. Shaner, P. A. Steinbach, R. Y. Tsien, *Nat. Methods* **2**, 905 (2005).
23. M. Matsushita *et al.*, *Angew. Chem. Int. Ed.* **42**, 5984 (2003).
24. H. Matsushita *et al.*, *Mol. Biosyst.* **1**, 303 (2005).
25. M. Matsushita, M. M. Meijler, P. Wirsching, R. A. Lerner, K. D. Janda, *Org. Lett.* **7**, 4943 (2005).
26. D. W. Chen *et al.*, *J. Org. Chem.* **66**, 1725 (2001).
27. G. F. Kaufmann *et al.*, *Angew. Chem. Int. Ed.* **44**, 2144 (2005).
28. Q. Wang, K. S. Raja, K. D. Janda, T. W. Lin, M. G. Finn, *Bioconjug. Chem.* **14**, 38 (2003).
29. G. A. Crosby, J. N. Demas, *J. Phys. Chem.* **75**, 991 (1971).
30. N. A. Baker, D. Sept, S. Joseph, M. J. Holst, J. A. McCammon, *Proc. Natl. Acad. Sci. U.S.A.* **98**, 10037 (2001).

31. We thank S. Ferguson for assistance in Fab preparation and the staff at Advanced Light Source beamline 5.0.1 for their support. We gratefully acknowledge A. Deniz for providing access to his fluorimeter, and S. Mukhopadhyay for assistance with anisotropy measurements as well as helpful discussions. We thank J. Saltiel as well as the reviewers for critically reading the manuscript and providing helpful comments. Coordinates and structure factors for the EP2-25C10-**1** complex have been deposited at the Protein Data Bank (PDB) with accession number 2NZR. Supported by NIH grants GM38273 (I.A.W.), GM56528 (P.G.S.), and DK19038 (H.B.G.) and a Skaggs predoctoral fellowship and Jairo H. Arévalo fellowship from The Scripps Research Institute graduate program (E.W.D.). This is publication 18959-MB from The Scripps Research Institute.

Supporting Online Material

www.sciencemag.org/cgi/content/full/319/5867/1232/DC1
Materials and Methods
Figs. S1 to S3
Tables S1 and S2
References
Movie S1

27 November 2007; accepted 18 January 2008
10.1126/science.1153445

Land Clearing and the Biofuel Carbon Debt

Joseph Fargione,[1] Jason Hill,[2,3] David Tilman,[2]* Stephen Polasky,[2,3] Peter Hawthorne[2]

Increasing energy use, climate change, and carbon dioxide (CO_2) emissions from fossil fuels make switching to low-carbon fuels a high priority. Biofuels are a potential low-carbon energy source, but whether biofuels offer carbon savings depends on how they are produced. Converting rainforests, peatlands, savannas, or grasslands to produce food crop–based biofuels in Brazil, Southeast Asia, and the United States creates a "biofuel carbon debt" by releasing 17 to 420 times more CO_2 than the annual greenhouse gas (GHG) reductions that these biofuels would provide by displacing fossil fuels. In contrast, biofuels made from waste biomass or from biomass grown on degraded and abandoned agricultural lands planted with perennials incur little or no carbon debt and can offer immediate and sustained GHG advantages.

Demand for alternatives to petroleum is increasing the production of biofuels from food crops such as corn, sugarcane, soybeans, and palms. As a result, land in undisturbed ecosystems, especially in the Americas and Southeast Asia, is being converted to biofuel production as well as to crop production when existing agricultural land is diverted to biofuel production. Such land clearing may be further accelerated by lignocellulosic biofuels,

which will add to the agricultural land base needed for biofuels, unless those biofuels are produced from crops grown on abandoned agricultural lands or from waste biomass.

Soils and plant biomass are the two largest biologically active stores of terrestrial carbon, together containing ~2.7 times more carbon than the atmosphere (*1*). Converting native habitats to cropland releases CO_2 as a result of burning or microbial decomposition of organic carbon stored in plant biomass and soils. After a rapid release from fire used to clear land or from the decomposition of leaves and fine roots, there is a prolonged period of GHG release as coarse roots and branches decay and as wood products decay or burn (*2*–*4*).

We call the amount of CO_2 released during the first 50 years of this process the "carbon debt" of land conversion. Over time, biofuels from converted land can repay this carbon debt if their production and combustion have net GHG emissions that are less than the life-cycle emissions of the fossil fuels they displace. Until the carbon debt is repaid, biofuels from converted lands have greater GHG impacts than those of the fossil fuels they displace. For crops with nonbiofuel coproducts (e.g., palm kernel oil and meal, soybean meal, or distillers' dry grains), we partition the carbon debt into a "biofuel carbon debt" and a "coproduct carbon debt" based on the market values of the biofuel and its coproducts (*5*).

We calculate how large biofuel carbon debts are, and how many years are required to repay them, for six different cases of native habitat conversion: Brazilian Amazon to soybean biodiesel, Brazilian Cerrado to soybean biodiesel, Brazilian Cerrado to sugarcane ethanol, Indonesian or Malaysian lowland tropical rainforest to palm biodiesel, Indonesian or Malaysian peatland tropical rainforest to palm biodiesel, and U.S. central grassland to corn ethanol (*5*) (table S1). These cases illustrate current impacts of biofuels on habitat conversion. Indonesia and Malaysia account for 86% of global palm oil production (*6*). Accelerating demand for palm oil is contributing to the 1.5% annual rate of deforestation of tropical rainforests in these nations (*7*). An estimated 27% of concessions for new palm oil plantations are on peatland tropical rainforests, totaling 2.8×10^6 ha in Indonesia (*7*). Brazilian Cerrado is being converted to sugarcane and soybeans, and the Brazilian Amazon is being converted to soybeans (*8*–*10*). Grassland in the United States, primarily rangeland or former cropland currently retired in conservation programs, is being converted to corn production. Rising prices for corn, wheat, and soybeans could cause a substantial portion of the 1.5×10^7 ha of land currently in the U.S. Conservation Reserve Program to be converted to cropland (*11*).

We estimated carbon debts by calculating the amount of CO_2 released from ecosystem biomass and soils. Our analyses account for the amount of plant carbon released as CO_2 through decomposition and combustion, the amount converted to charcoal (charcoal is not part of the carbon debt because it is recalcitrant to decomposition), and the amount incorporated into

[1]The Nature Conservancy, 1101 West River Parkway, Suite 200, Minneapolis, MN 55415, USA. [2]Department of Ecology, Evolution, and Behavior, University of Minnesota, St. Paul, MN 55108, USA. [3]Department of Applied Economics, University of Minnesota, St. Paul, MN 55108, USA.

*To whom correspondence should be addressed. E-mail: tilman@umn.edu

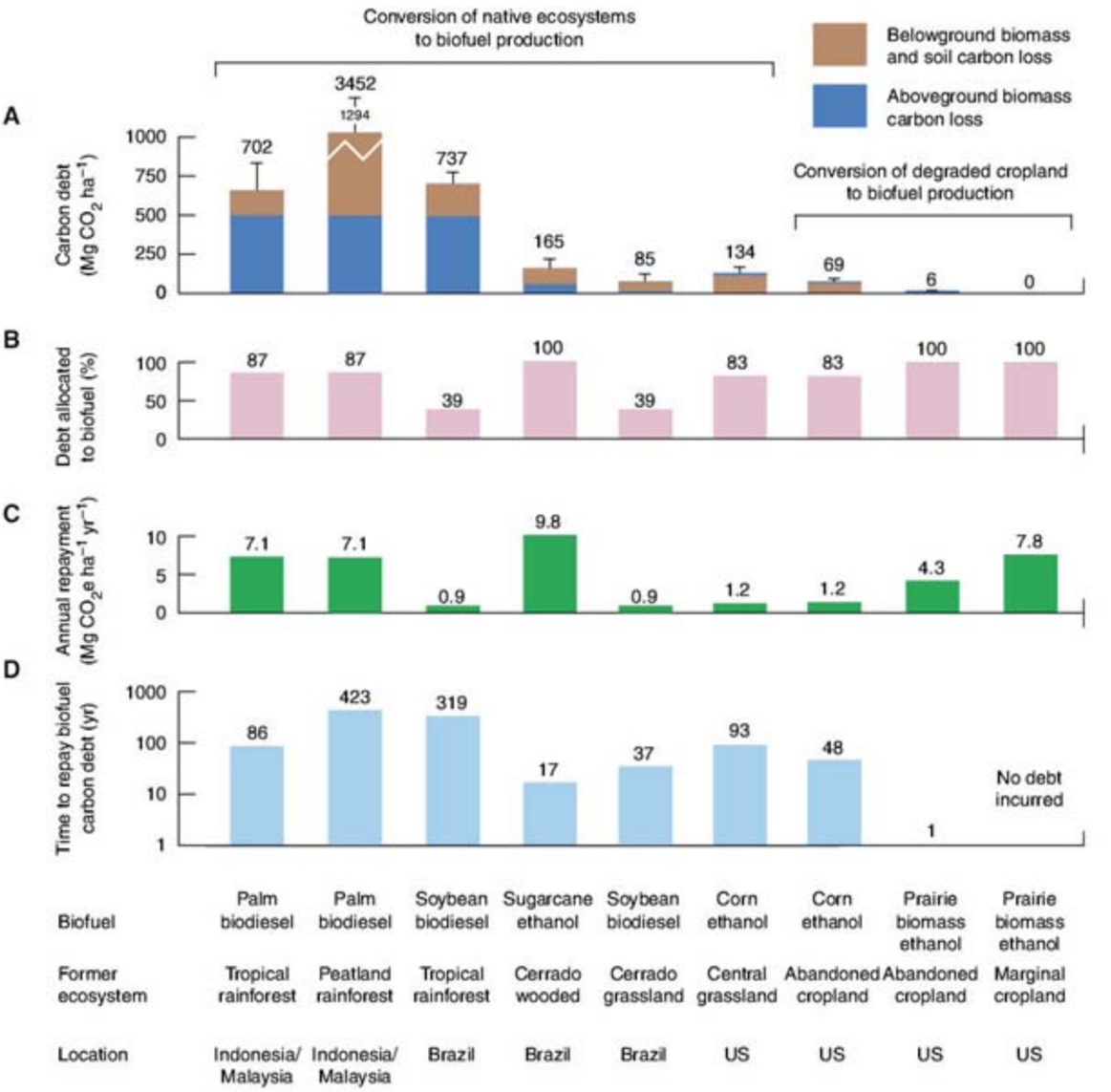

Fig. 1. Carbon debt, biofuel carbon debt allocation, annual carbon repayment rate, and years to repay biofuel carbon debt for nine scenarios of biofuel production. Means and SDs are from Monte Carlo analyses of literature-based estimates of carbon pools and fluxes (*5*). (**A**) Carbon debt, including CO_2 emissions from soils and aboveground and belowground biomass resulting from habitat conversion. (**B**) Proportion of total carbon debt allocated to biofuel production. (**C**) Annual life-cycle GHG reduction from biofuels, including displaced fossil fuels and soil carbon storage. (**D**) Number of years after conversion to biofuel production required for cumulative biofuel GHG reductions, relative to the fossil fuels they displace, to repay the biofuel carbon debt.

merchantable timber and other long-lived forestry products, which have a half-life of about 30 years (*3*, *12*). Changes in carbon stores caused by land conversion and biofuel production, mainly from accelerated decomposition, were based on evaluation and synthesis of published studies in the relevant ecosystems (*5*). Our estimate of the carbon debt is conservative because timber products continue to decay after 50 years, but this time frame captures most of the carbon debt in systems with mineral soils.

Our results show that converting native ecosystems to biofuel production results in large carbon debts (Fig. 1A). We attribute 13, 61, and 17% of this carbon debt to coproducts for palm, soybeans, and corn, respectively (Fig. 1B) (*5*). The carbon debts attributed to biofuels (quantities of Fig. 1A multiplied by the proportions of Fig. 1B) would not be repaid by the annual carbon repayments from biofuel production (Fig. 1C and table S2) for decades or centuries (Fig. 1D). Converting lowland tropical rainforest in Indonesia and Malaysia to palm biodiesel would result in a biofuel carbon debt of ~610 Mg of CO_2 ha^{-1} that would take ~86 years to repay (Fig. 1D). Until then, producing and using palm biodiesel from this land would cause greater GHG release than would refining and using an energy-equivalent amount of petroleum diesel. Converting tropical peatland rainforest to palm production incurs a similar biofuel carbon debt from vegetation, but the required drainage of peatland causes an additional sustained emission of ~55 Mg of CO_2 ha^{-1} yr^{-1} from oxidative peat decomposition (*5*) (87% attributed to biofuel; 13% to palm kernel oil and meal). After 50 years, the resulting biofuel carbon debt of ~3000 Mg of CO_2 ha^{-1} would require ~420 years to repay. However, peatland of average depth (3 m) could release peat-derived CO_2 for about 120 years (*7*, *13*). Total net carbon released would be ~6000 Mg of CO_2 ha^{-1} over this longer time horizon, which would take over 840 years to repay. Soybean biodiesel produced on converted Amazonian rainforest with a biofuel carbon debt of >280 Mg of CO_2 ha^{-1} would require ~320 years to repay as compared with GHG emissions from petroleum diesel. The biofuel carbon debt from biofuels produced on converted Cerrado is repaid in the least amount of time of the scenarios that we examined. Sugarcane ethanol produced on Cerrado sensu stricto (including Cerrado aberto, Cerrado densu, and Cerradão), which is the wetter and more productive end of this woodland-savanna biome, would take ~17 years to repay the biofuel carbon debt. Soybean biodiesel from the drier, less productive grass-dominated end of the Cerrado biome (Campo limpo and Campo sujo) would take ~37 years. Ethanol from corn produced on newly converted U.S. central grasslands results in a biofuel carbon debt repayment time of ~93 years.

Our analyses suggest that biofuels, if produced on converted land, could, for long periods of time, be much greater net emitters of greenhouse gases than the fossil fuels that they typically displace. All but two—sugarcane ethanol and soybean biodiesel on Cerrado—would generate greater GHG emissions for at least half a century, with several forms of biofuel production from land conversion doing so for centuries. At least for current or developing biofuel technologies, any strategy to reduce GHG emissions that causes land conversion from native ecosystems to cropland is likely to be counterproductive.

We also evaluated the possibility that U.S. cropland that has been retired from annual crop production and planted with perennial grasses may have a short payback time when converted to corn ethanol production, because these systems have already lost a substantial portion of their carbon stores. However, after abandonment from cropping, perennial systems gradually recover their carbon stores. For U.S. central grassland on cropland that has been enrolled in the U.S. Conservation Reserve Program for 15 years, we found that converting it to corn ethanol production creates a biofuel carbon debt that would take ~48 years to repay (Fig. 1D).

If biofuels are to help mitigate global climate change, our results suggest that they need to be produced with little reduction of the storehouses of organic carbon in the soils and vegetation of natural and managed ecosystems. Degraded and abandoned agricultural lands could be used to grow native perennials for biofuel production (*14*, *15*), which could spare the destruction of native ecosystems and reduce GHG emissions (Fig. 1). Diverse mixtures of native grassland perennials growing on degraded soils, particularly mixtures containing both warm-season grasses and legumes, have yield advantages over monocultures (*14*, *16*–*18*), provide GHG advantages from high rates of carbon storage in degraded soils (*14*, *19*), and offer wildlife benefits (*20*). Monocultures of perennial grasses and woody species also can offer GHG advantages over food-based crops, especially if they are sufficiently productive on degraded soils (*21*), as can slash and thinnings from sustainable forestry, animal and municipal wastes, and crop residue (*22*).

Additional factors may influence biofuel impacts on GHG emissions. First, biofuel production can displace crops or pasture from current agricultural lands, indirectly causing GHG release via conversion of native habitat to cropland elsewhere (*23*). Second, improvements in biofuel production could reduce payback times (*24*, *25*). Third, if land cleared for biofuel production had been accruing carbon (we assumed lands were at steady state), the debt would be increased by the loss of this future storage. Fourth, greater biofuel production might decrease overall energy prices, which could increase energy consumption and GHG release (*26*, *27*).

Biofuel production that causes land clearing and GHG release may be favored by landowners who receive payments for biofuels but not for carbon management. Our results suggest that, in order to incorporate the costs of carbon emissions accurately, policy approaches to GHG emission reductions must be extended to include the net GHG emission or sequestration from land-use change. Indeed, the recently enacted U.S. Energy Independence and Security Act of 2007 specifies reductions in life-cycle GHG emissions, including land-use change, relative to a fossil fuel baseline. Moreover, it is important that international policy negotiations to extend the Kyoto Protocol beyond 2012 address emissions from land-use change due to increased demand for biofuels (*28*, *29*).

Our results demonstrate that the net effect of biofuel production via clearing of carbon-rich habitats is to increase CO_2 emissions for decades or centuries relative to the emissions caused by fossil fuel use. Conversely, biofuels from perennials grown on degraded cropland and from waste biomass would minimize habitat destruction, competition with food production, and carbon debts, all of which are associated with direct and indirect land clearing for biofuel production.

References and Notes

1. W. H. Schlesinger, *Biogeochemistry: An Analysis of Global Change* (Academic Press, San Diego, CA, ed. 2, 1997).
2. T. O. West *et al.*, *Environ. Manage.* **33**, 507 (2004).
3. J. K. Winjum, S. Brown, B. Schlamadinger, *For. Sci.* **44**, 272 (1998).
4. W. L. Silver, R. K. Miya, *Oecologia* **129**, 407 (2001).
5. Materials and methods are available as supporting material on *Science* Online.
6. Y. Basiron, *Eur. J. Lipid Sci. Technol.* **109**, 289 (2007).
7. A. Hooijer, M. Silvius, H. Wösten, S. Page, "Peat-CO_2: Assessment of CO_2 emissions from drained peatlands in SE Asia" (Tech. Report No. Q3943, Delft Hydraulics, Delft, Netherlands, 2006).
8. C. E. P. Cerri *et al.*, *Agric. Ecosyst. Environ.* **122**, 58 (2007).
9. P. M. Fearnside, *Environ. Conserv.* **28**, 23 (2001).
10. C. A. Klink, R. B. Machado, *Conserv. Biol.* **19**, 707 (2005).
11. S. Secchi, B. A. Babcock, "Impact of high crop prices on environmental quality: A case of Iowa and the Conservation Reserve Program" (Report No. 07-WP-447, Center for Agricultural and Rural Development, Iowa State University, Ames, IA, 2007).
12. Intergovernmental Panel on Climate Change (IPCC), *2006 IPCC Guidelines for National Greenhouse Gas Inventories: Prepared by the National Greenhouse Gas Inventories Programme*, H. S. Eggleston, L. Buendia, K. Miwa, T. Ngara, K. Tanabe, Eds. (Institute for Global Environmental Strategies, Hayama, Japan, 2006).
13. S. E. Page *et al.*, *Nature* **420**, 61 (2002).
14. D. Tilman, J. Hill, C. Lehman, *Science* **314**, 1598 (2006).
15. C. B. Field, J. E. Campbell, D. B. Lobell, *Trends Ecol. Evol.* **23**, 65 (2008).
16. G. A. Jung, J. L. Griffin, R. E. Kocher, J. A. Shaffer, C. F. Gross, *Agron. J.* **77**, 846 (1985).
17. J. R. George, K. M. Blanchet, R. M. Gettle, D. R. Buxton, K. J. Moore, *Agron. J.* **87**, 1147 (1995).
18. D. U. Hooper *et al.*, *Ecol. Monogr.* **75**, 3 (2005).
19. M. D. Robles, I. C. Burke, *Ecol. Appl.* **7**, 345 (1997).

20. D. W. Sample, thesis, University of Wisconsin (1989).
21. D. J. Parrish, J. H. Fike, *Crit. Rev. Plant Sci.* **24**, 423 (2005).
22. R. L. Graham, R. Nelson, J. Sheehan, R. D. Perlack, L. L. Wright, *Agron. J.* **99**, 1 (2007).
23. T. Searchinger *et al.*, *Science* **319**, 1238 (2008).
24. R. Hammerschlag, *Environ. Sci. Technol.* **40**, 1744 (2006).
25. B. D. Solomon, J. R. Barnes, K. E. Halvorsen, *Biomass Bioenergy* **31**, 416 (2007).
26. D. J. Graham, S. Glaister, *J. Transport Econ. Policy* **36**, 1 (2002).
27. T. Sterner, *Energy Policy* **35**, 3194 (2007).
28. Y. Malhi *et al.*, *Science* **319**, 169 (2008).
29. R. E. Gullison *et al.*, *Science* **316**, 985 (2007).
30. Supported by the University of Minnesota's Initiative for Renewable Energy and the Environment, NSF grant no. DEB0620652, Princeton Environmental Institute, and the Bush Foundation. We thank T. Searchinger for valuable comments and insights and J. Herkert for providing references.

Supporting Online Material
www.sciencemag.org/cgi/content/full/1152747/DC1
Materials and Methods
Tables S1 and S2
References

8 November 2007; accepted 24 January 2008
Published online 7 February 2008;
10.1126/science.1152747
Include this information when citing this paper.

Use of U.S. Croplands for Biofuels Increases Greenhouse Gases Through Emissions from Land-Use Change

Timothy Searchinger,[1]* Ralph Heimlich,[2] R. A. Houghton,[3] Fengxia Dong,[4] Amani Elobeid,[4] Jacinto Fabiosa,[4] Simla Tokgoz,[4] Dermot Hayes,[4] Tun-Hsiang Yu[4]

Most prior studies have found that substituting biofuels for gasoline will reduce greenhouse gases because biofuels sequester carbon through the growth of the feedstock. These analyses have failed to count the carbon emissions that occur as farmers worldwide respond to higher prices and convert forest and grassland to new cropland to replace the grain (or cropland) diverted to biofuels. By using a worldwide agricultural model to estimate emissions from land-use change, we found that corn-based ethanol, instead of producing a 20% savings, nearly doubles greenhouse emissions over 30 years and increases greenhouse gases for 167 years. Biofuels from switchgrass, if grown on U.S. corn lands, increase emissions by 50%. This result raises concerns about large biofuel mandates and highlights the value of using waste products.

Most life-cycle studies have found that replacing gasoline with ethanol modestly reduces greenhouse gases (GHGs) if made from corn and substantially if made from cellulose or sugarcane (*1*–*7*). These studies compare emissions from the separate steps of growing or mining the feedstocks (such as corn or crude oil), refining them into fuel, and burning the fuel in the vehicle. In these stages alone (Table 1), corn and cellulosic ethanol emissions exceed or match those from fossil fuels and therefore produce no greenhouse benefits. But because growing biofuel feedstocks removes carbon dioxide from the atmosphere, biofuels can in theory reduce GHGs relative to fossil fuels. Studies assign biofuels a credit for this sequestration effect, which we call the feedstock carbon uptake credit. It is typically large enough that overall GHG emissions from biofuels are lower than those from fossil fuels, which do not receive such a credit because they take their carbon from the ground.

[1]Woodrow Wilson School, Princeton University, Princeton, NJ 08544, USA. German Marshall Fund of the United States, Washington, DC 20009, USA. Georgetown Environmental Law and Policy Institute, Washington, DC 20001, USA. [2]Agricultural Conservation Economics, Laurel, MD 20723, USA. [3]Woods Hole Research Center, Falmouth, MA 02540–1644, USA. [4]Center for Agricultural and Rural Development, Iowa State University, Ames, IA 50011, USA.

*To whom correspondence should be addressed. E-mail: tsearchi@princeton.edu

For most biofuels, growing the feedstock requires land, so the credit represents the carbon benefit of devoting land to biofuels. Unfortunately, by excluding emissions from land-use change, most previous accountings were one-sided because they counted the carbon benefits of using land for biofuels but not the carbon costs, the carbon storage and sequestration sacrificed by diverting land from its existing uses. Without biofuels, the extent of cropland reflects the demand for food and fiber. To produce biofuels, farmers can directly plow up more forest or grassland, which releases to the atmosphere much of the carbon previously stored in plants and soils through decomposition or fire. The loss of maturing forests and grasslands also foregoes ongoing carbon sequestration as plants grow each year, and this foregone sequestration is the equivalent of additional emissions. Alternatively, farmers can divert existing crops or croplands into biofuels, which causes similar emissions indirectly. The diversion triggers higher crop prices, and farmers around the world respond by clearing more forest and grassland to replace crops for feed and food. Studies have confirmed that higher soybean prices accelerate clearing of Brazilian rainforest (*8*). Projected corn ethanol in 2016 would use 43% of the U.S. corn land harvested for grain in 2004 (*1*), overwhelmingly for livestock (*9*), requiring big land-use changes to replace that grain.

Because existing land uses already provide carbon benefits in storage and sequestration (or, in the case of cropland, carbohydrates, proteins, and fats), dedicating land to biofuels can potentially reduce GHGs only if doing so increases the carbon benefit of land. Proper accountings must reflect the net impact on the carbon benefit of land, not merely count the gross benefit of using land for biofuels. Technically, to generate greenhouse benefits, the carbon generated on land to displace fossil fuels (the carbon uptake credit) must exceed the carbon storage and sequestration given up directly or indirectly by changing land uses (the emissions from land-use change) (Table 1).

Many prior studies have acknowledged but failed to count emissions from land-use change because they are difficult to quantify (*1*). One prior quantification lacked formal agricultural modeling and other features of our analysis (*1*, *10*). To estimate land-use changes, we used a worldwide model to project increases in cropland in all major temperate and sugar crops by country or region (as well as changes in dairy and livestock production) in response to a possible increase in U.S. corn ethanol of 56 billion liters above projected levels for 2016 (*11*, *12*). The model's historical supply and demand elasticities were updated to reflect the higher price regime of the past 3 years and to capture expected long-run equilibrium behavior (*1*). The analysis identifies key factors that determine the change in cropland.

1) New crops do not have to replace all corn diverted to ethanol because the ethanol by-product, dry distillers' grains, replaces roughly one-third of the animal feed otherwise diverted.

2) As fuel demand for corn increases and soybean and wheat lands switch to corn, prices increase by 40%, 20%, and 17% for corn, soybeans, and wheat, respectively. These increases modestly depress demand for meat and other grain products beside ethanol, so a small percentage of diverted grain is never replaced.

3) As more American croplands support ethanol, U.S. agricultural exports decline sharply (compared to what they would otherwise be at the time) (corn by 62%, wheat by 31%, soybeans by 28%, pork by 18%, and chicken by 12%).

4) When other countries replace U.S. exports, farmers must generally cultivate more land per ton of crop because of lower yields.

Farmers would also try to boost yields through improved irrigation, drainage, and fertilizer (which have their own environmental effects), but reduced crop rotations and greater reliance on marginal lands would depress yields. Our analysis assumes that present growth trends in yields continue but

that positive and negative effects on yields from biofuels balance out.

We calculated that an ethanol increase of 56 billion liters, diverting corn from 12.8 million ha of U.S. cropland, would in turn bring 10.8 million ha of additional land into cultivation. Locations would include 2.8 million ha in Brazil, 2.3 million ha in China and India, and 2.2 million ha in the United States.

Greenhouse emissions will depend on the type of lands converted. We assigned the new cropland in each region to different types of forest, savannah, or grassland on the basis of the proportion of each ecosystem converted to cultivation in the 1990s and assumed that conversion emits 25% of the carbon in soils (*13*, *14*) and all carbon in plants, which must be cleared for cultivation. For mature forests in carbon equilibrium, we only calculated emissions from the initial conversion. For growing forests, we attributed emissions to biofuels equal to the carbon those lost forests would no longer sequester over 30 years (adjusted for disturbances like fire). Our estimates of the carbon content of ecosystems compare roughly to figures cited by the Intergovernmental Panel on Climate Change (IPCC) (*15*). Our analysis does not reflect the full opportunity costs of using lands for biofuels, which include the additional carbon lands could store if managed optimally (e.g., through reforestation), but only the carbon lands would otherwise store in their existing use. Our method yielded an average GHG emission of 351 metric tons per converted hectare (CO_2 equivalent).

We allocated the total emissions for all converted land into emissions per MJ of fuel and factored them into the GREET model (Table 1). GREET provides a commonly used lifecycle analysis of GHG emissions from the different stages of biofuel and gasoline production (*3*–*5*), and its default assumptions calculate that replacing gasoline with corn ethanol reduces GHGs by 20% in the 2015 scenario excluding land-use change (*5*, *16*). As land generates more ethanol over years, the reduced emissions from its use will eventually offset the carbon debt from land-use change, which mostly occurs quickly and is limited in our analysis to emissions within 30 years. We calculated that GHG savings from corn ethanol would equalize and therefore "pay back" carbon emissions from land-use change in 167 years, meaning GHGs increase until the end of that period. Over a 30-year period, counting land-use change, GHG emissions from corn ethanol nearly double those from gasoline for each km driven (Table 1). [We chose 30 years because reductions of greenhouse gases in that period will be both difficult to achieve and important to avoid irreversible adverse effects from climate change (*17*) and because ethanol is typically viewed as a bridge to more transformative energy technologies.]

As part of our sensitivity analysis, we found that, even if corn ethanol caused no emissions except those from land-use change, overall GHGs would still increase over a 30-year period (*1*). We also hypothesized a scenario in which (i) increased ethanol and higher prices spur enough yield increases beyond current trends to supply 20% of the replacement grain; (ii) emissions per ha of converted land are only half of our estimates, and (iii) improved technology allows corn ethanol to reduce GHGs compared with gasoline by 40% excluding land-use change. In that scenario, the payback period would last 34 years, which means emissions modestly increase over a 30-year period (*1*).

By the workings of our model, the emissions from land-use change per unit of ethanol would be similar regardless of the ethanol increase analyzed. For example, a smaller ethanol increase of 30.6 billion liters had only modestly different results, with emissions from land-use change per MJ of ethanol 10% lower (*1*). Far larger biofuel increases could change the magnitude of results in unclear ways that would require modification to the model.

Although these estimates face several uncertainties, the general finding flows from three reliable projections. First, farmers will replace most of the grain diverted from food and feed by ethanol because the demand for overall food and feed, as opposed to any particular grain, is inelastic (*18*). Second, increases in cropland will provide most replacement grain because they are cost-effective and fast, the yield effects of biofuel demands are both positive and negative, and the world has many convertible acres: up to 170 million ha in Brazil alone (*19*, *20*) and perhaps 2.8 billion ha worldwide (*21*). Most significantly, the potential emissions per hectare of land conversion greatly exceed the annual greenhouse reductions per ha of biofuels. According to GREET and at 2015 yields, a ha of corn for ethanol reduces GHGs by 1.8 metric tons ha^{-1} $year^{-1}$ (CO_2 equivalent), but each ha of forest converted has up-front emissions of 604 to 1146 metric tons (varying by type and maturity), and each hectare of grassland or savannah from 75 to 305 metric tons (*1*). If new cropland replaces any substantial fraction of diverted cropland, the payback period for these up-front emissions will be long (even without counting foregone annual

Table 1. Comparison of corn ethanol and gasoline greenhouse gasses with and without land-use change by stage of production and use (grams of GHGs CO_2 equivalents per MJ of energy in fuel) (*28*). Figures in total column may not sum perfectly because of rounding in each row. Land-use change was amortized over 30 years. Dash entries indicate "not included."

				Net land-use effects			
Source of fuel	Making feedstock	Refining fuel	Vehicle operation (burning fuel)	Feedstock carbon uptake from atmosphere (GREET)	Land-use change	Total GHGs	% Change in net GHGs versus gasoline
Gasoline	+4	+15	+72	0	–	+92	–
Corn ethanol (GREET)	+24	+40	+71	−62	–	+74 +135 without feedstock credit	−20% +47% without feedstock credit
Corn ethanol plus land use change	+24	+40	+71	−62	+104	+177	+93%
Biomass ethanol (GREET)	+10	+9	+71	−62	–	+27	−70%
Biomass ethanol plus land use change	+10	+9	+71	−62	+111	+138	+50%

sequestration). This result makes intuitive sense because potential biofuel benefits originate in the annual carbon uptake from growing a feedstock, but growing that feedstock will typically require up-front release of carbon previously sequestered on land over decades.

This analysis has implications for other biofuels. Cellulosic ethanol could use wastes that do not trigger land-use change. But if American corn fields of average yield were converted to switchgrass for ethanol, replacing that corn would still trigger emissions from land-use change that would take 52 years to pay back and increase emissions over 30 years by 50% (*1*).

Ethanol from Brazilian sugarcane, based on estimated GHG reductions of 86% excluding land-use changes (*6*), could pay back the up-front carbon emissions in 4 years if sugarcane only converts tropical grazing land. However, if displaced ranchers convert rainforest to grazing land, the payback period could rise to 45 years (*1*). The extraordinary productivity of Brazilian sugarcane merits special future analysis.

Even if excess croplands in the United States or Europe became available because of dramatic yield improvements beyond existing trends (*22*) or the release of agricultural reserve lands (*7*), biofuels would still not avoid emissions from land-use change. Truly excess croplands would revert either to forest or grassland and sequester carbon. Use of those lands instead for biofuels sacrifices this carbon benefit, which could exceed the carbon saved by using the same land for biofuels (*24*). In addition, even as cropland declined in Europe in recent years, changing technology and economics led cropland to expand into forest and grassland in Latin America (*24*). Higher prices triggered by biofuels will accelerate forest and grassland conversion there even if surplus croplands exist elsewhere. Most problematically, even with large increases in yields, cropland must probably consume hundreds of millions more ha of grassland and forest to feed a rising world population and meat consumption (*21*, *25*), and biofuels will only add to the demand for land.

This study highlights the value of biofuels from waste products (*26*) because they can avoid land-use change and its emissions. To avoid land-use change altogether, biofuels must use carbon that would reenter the atmosphere without doing useful work that needs to be replaced, for example, municipal waste, crop waste, and fall grass harvests from reserve lands. Algae grown in the desert or feedstocks produced on lands that generate little carbon today (*27*) might also keep land-use change emissions low, but the ability to produce biofuel feedstocks abundantly on unproductive lands remains questionable.

Because emissions from land-use change are likely to occur indirectly, proposed environmental criteria that focus only on direct land-use change (*7*) would have little effect. Barring biofuels produced directly on forest or grassland would encourage biofuel processors to rely on existing croplands, but farmers would replace crops by plowing up new lands. An effective system would have to guarantee that biofuels use a feedstock, such as a waste product, or carbon-poor lands that will not trigger large emissions from land-use change.

Counteracting increases in biofuels with controls or disincentives against land conversion would not only face great practical challenges but also have harsh social consequences. In our analysis, a diversion of 12.8 million ha, otherwise generating 10% of the world's feed grain by weight, would reduce world consumption of meat 0.9% by weight and dairy products 0.6% (fluid milk equivalents) (*1*). This effect, of which around half reflects poorer diets in developing countries, depresses emissions and has a GHG "benefit" but probably not a desirable one. Effective controls on land conversion would constrain the major source of new supply to meet increased biofuel demands, resulting in less additional cropland and higher prices as markets seek equilibrium. In that event, more greenhouse benefits would stem in reality from reduced food consumption.

Use of good cropland to expand biofuels will probably exacerbate global warming in a manner similar to directly converting forest and grasslands (*29*). As a corollary, when farmers use today's good cropland to produce food, they help to avert GHGs from land-use change.

References and Notes

1. Materials and methods are available at *Science* Online.
2. A. E. Farrell *et al.*, *Science* **311**, 506 (2006).
3. M. Wang, C. Saricks, D. Santini, "Effects of fuel ethanol use on fuel-cycle energy and greenhouse gas emissions" (Center for Transportation Research, Energy Systems Division, Argonne National Laboratory, Argonne, IL, 1999).
4. M. Wang, paper presented at the 15th International Symposium on Alcohol Fuels, San Diego, CA, 26 to 28 September 2005.
5. Argonne National Laboratory, "Greenhouse gases, regulated emissions, and energy use in transportation (GREET) computer model" (2007), www.transportation.anl.gov/software/GREET/publications.html.
6. I. Macedo, M. R. Lima, V. Leal, J. E. Azevedo Ramos da Silva, "Assessment of greenhouse gas emissions in the production and use of fuel ethanol in Brazil," (Government of the State of São Paulo, São Paulo, Brazil, 2004).
7. Commission of the European Communities, "Biofuels progress report: Report on the progress made in the use of biofuels and other renewable fuels in the member states of the European Union" [COM(2006) 845 final, Brussels, 2006].
8. D. C. Morton *et al.*, *Proc. Natl. Acad. Sci. U.S.A.* **103**, 14637 (2006).
9. Iowa Corn Growers Association, "Uses for corn fact sheet," www.iowacorn.org/cornuse/cornuse_3.html.
10. M. Delucchi, "A multi-country analysis of lifecycle emissions from transportation fuels and motor vehicles" (UCD-ITS-RR-05-10, University of California at Davis, Davis, CA, 2005).
11. S. Tokgoz *et al.*, "Emerging biofuels outlook of effects on U.S. grain, oilseed and livestock markets" (Staff Report 0-7-SR 101, Center for Agricultural and Rural Development, Iowa State University, Ames, IA, 2007).
12. S. Tokgoz *et al*, "Data files for revised 2015/16 baseline and scenario without E-85 constraint" (Center for Agricultural and Rural Development, Iowa State University, Ames, IA, 2007)
13. L. B. Guo, R. M. Gifford, *Glob. Change Biol.* **8**, 345 (2002).
14. D. Murty, M. U. F. Kirschbaum, R. E. McMurtie, H. McGilvray, *Glob. Change Biol.* **8**, 105 (2002).
15. IPCC, "Climate change 2001: The scientific basis, contribution of working group 1 to the third assessment report of the Intergovernmental Panel on Climate Change" (Cambridge Univ. Press, Cambridge, 2001)
16. Unlike nearly all other studies, GREET incorporates an estimate of emissions from agricultural conversion in its "making feedstock" calculations for corn ethanol at an extremely modest 0.82 g MJ^{-1} for reasons discussed in (*1*). We deleted that emission from the making feedstock estimate in Table 1 to substitute our own estimate in the column marked land use change. Table 1 retains a GREET-calculated credit for biomass in "making feedstock" to reflect the increased carbon sequestration in soils from growing switchgrass instead of annual crops.
17. IPCC, "Fourth Assessment Report: Climate Change 2007: Synthesis Report Summary for Policymakers," www.ipcc.ch/pdf/assessment-report/ar4/syr/ar4_syr_spm.pdf.
18. The elasticity for the aggregate demand for grains is lower than the demand elasticities for individual grains. Demand for individual grains reflects the ability of consumers to substitute other grains when prices rise, whereas the aggregate demand for grains declines only to the extent that consumers reduce their demand for total food and feed. The amount of replacement cropland depends primarily on reduced demand for all grains.
19. R. D. Schnepf, E. Dohlman, C. Bolling, "Agriculture in Brazil and Argentina: Developments and prospects for major field crops" (WRS-01-03, Economic Research Service, U.S. Department of Agriculture, Washington, DC, 2001).
20. M. J. Shean, "Brazil: Future agricultural expansion potential underrated" (Foreign Agricultural Service, U.S. Department of Agriculture, Washington, DC, 2003)
21. J. Bruinsma, Ed., *World Agriculture: Toward 2015/30, an FAO Perspective* [Food and Agricultural Organization, United Nations (UN), Rome, 2003].
22. M. Johanns, Transcript of remarks at Advancing Renewable Energy Conference, U.S. Department of Agriculture, St. Louis, MO, 11 October 2007.
23. R. Righelato, D. V. Spracklen, *Science* **317**, 902 (2007).
24. H. Steinfeld *et al.*, *Livestock's Long Shadow: Environmental Issues and Options* (Food and Agricultural Organization, UN, Rome, 2006)
25. D. Tilman *et al.*, *Science* **292**, 281 (2001).
26. R. D. Perlack *et al.*, "Biomass as a feedstock for a bioenergy and bioproducts industry: The technical feasibility of a billion-ton annual supply" (Tech. Rep. ORNL/TM 2006/66, Oak Ridge National Laboratory, Oak Ridge, TN, 2005)
27. D. Tilman, J. Hill, C. Lehman, *Science* **314**, 1598 (2006).
28. Table 1 is calculated with GREET 1.7(4) using default assumptions for the 2015 scenario and as described in (*16*). Gasoline is a combination of conventional and reformulated gasoline. Ethanol rows are based on E-85 and adjusted to isolate effects of ethanol by proportionately removing emissions of gasoline. Land-use change emissions are amortized over 30 years and for biomass assume use of U.S. corn fields of average yield to produce switchgrass at 18 metric tons ha^{-1} (*26*) with no feed by-product. Emissions from burning ethanol are slightly higher than feedstock uptake credit because some carbon is emitted as more potent GHGs than CO_2. By GREET estimates, 3.04 MJ provides power for 1 km.
29. J. Fargione, J. Hill, D. Tilman, S. Polasky, P. Hawthorne, *Science* **319**, 1235 (2008).

30. We appreciate the valuable suggestions by T. Male and M. Delucchi. This material is based in part upon work supported by NASA under grant number NNX06AF15G issued through the Terrestrial Ecology Program and by the William and Flora Hewlett Foundation.

Supporting Online Material

www.sciencemag.org/cgi/content/full/1151861/DC1
SOM Text
Tables S1 to S3
Appendices A to F
References

17 October 2007; accepted 28 January 2008
Published online 7 February 2008;
10.1126/science.1151861
Include this information when citing this paper.

Local Positive Feedback Regulation Determines Cell Shape in Root Hair Cells

Seiji Takeda,[1] Catherine Gapper,[1] Hidetaka Kaya,[2,3] Elizabeth Bell,[1] Kazuyuki Kuchitsu,[2,3] Liam Dolan[1]*

The specification and maintenance of growth sites are tightly regulated during cell morphogenesis in all organisms. ROOT HAIR DEFECTIVE 2 reduced nicotinamide adenine dinucleotide phosphate (RHD2 NADPH) oxidase–derived reactive oxygen species (ROS) stimulate a Ca^{2+} influx into the cytoplasm that is required for root hair growth in *Arabidopsis thaliana*. We found that Ca^{2+}, in turn, activated the RHD2 NADPH oxidase to produce ROS at the growing point in the root hair. Together, these components could establish a means of positive feedback regulation that maintains an active growth site in expanding root hair cells. Because the location and stability of growth sites predict the ultimate form of a plant cell, our findings demonstrate how a positive feedback mechanism involving RHD2, ROS, and Ca^{2+} can determine cell shape.

Cells develop polarized shapes by generating and maintaining localized sites of growth. Although many proteins and physiological processes that are required for tip growth have been identified, the manner by which they interact in the stable maintenance of local growth sites is unknown in plants. Important among these processes in growing root hair cells of *A. thaliana* is the elevation of the concentration of cytoplasmic Ca^{2+} and the localized production of ROS by the RHD2 NADPH oxidase (*1*–*4*). We hypothesized that RHD2 protein would be located at the sites of growth and ROS accumulation and therefore determined the distribution of RHD2 protein using transgenic plants expressing RHD2 fused with green fluorescent protein (GFP) under the control of the *RHD2* promoter and terminator. The GFP:RHD2 (N-terminal fusion) complemented the Rhd2$^-$ phenotype (fig. S1). RHD2 was present in all epidermal cells of the elongation zone but became restricted to the trichoblasts (specialized cells that form root hairs) in the zone just before hair outgrowth occurred (fig. S2), where it accumulated at future sites of hair outgrowth (Fig. 1, A and B). RHD2 remained at the site of growth during hair elongation and disappeared when growth stopped (Fig. 1, C to F). These data suggest that the localization of RHD2 restricts ROS production to the growth points of the cell.

Given that RHD2 carries six putative transmembrane domains (*5*–*7*), we predicted that RHD2 would be located in the plasma membrane. Indeed, RHD2 colocalized with the plasma membrane when separated from the cell wall after plasmolysis (Fig. 1, G and H). This localization depended on vesicle trafficking because treatment with brefeldin A (BFA) resulted in the colocalization of RHD2 and the endocytic vesicle marker FM4-64 in small aggregates within cells (Fig. 1, I to N) (*8*). Thus, the decrease in root hair length observed upon BFA treatment is due at least in part to RHD2 delocalization (*9*), and endocytotic turnover is likely to be an important process maintaining RHD2 in the plasma membrane.

ROS accumulate ectopically in *supercentipede1* (*scn1*) mutant trichoblasts, suggesting that the Rho guanosine triphosphate dissociation inhibitor (RhoGDI)—SCN1—restricts ROS production to a single site (*2*). Because these foci of ectopic ROS production result from RHD2 activity, we predicted that SCN1 controls the spatial accumulation of RHD2. We found that RHD2 accumulated in several distinct foci in the *scn1* mutant as compared with the wild type, where it accumulated at a single location (Fig. 1, O and P). Thus, SCN1 RhoGDI restricts the accumulation of RHD2 to a single site within the trichoblast.

Because a target of SCN1 RhoGDI regulation [ROP2 guanosine triphosphatase (GTPase), which is located to the hair tip (*2*, *10*)] regulates actin microfilament dynamics in root hair cells (*11*), we predicted that microfilaments would spatially control the distribution of RHD2 within the cell. RHD2 accumulated in cytoplasmic clumps in the *deformed root hairs 1* (*der1*) mutant, which lacks the ACTIN2 protein (*12*) (Fig. 1, Q and R). Furthermore, RHD2 accumulated in clumps in the cytoplasm upon treatment of wild type with the microfilament-disrupting drug cytochalasin D (cytD) (Fig. 1, S and T) at the concentration that did not change the polar localization of ROP GTPase in the trichoblast (*13*). To test whether microtubules were also required, RHD2 localization was determined in the *ectopic root hair 3* (*erh3*) mutant in which microtubules are disorganized

[1]Department of Cell and Developmental Biology, John Innes Centre, Norwich NR4 7UH, UK. [2]Genome and Drug Research Center, Tokyo University of Science, 2641 Yamazaki, Noda, Chiba 278-8510, Japan. [3]Department of Applied Biological Science, Tokyo University of Science, 2641 Yamazaki, Noda, Chiba 278-8510, Japan.

*To whom correspondence should be addressed. E-mail: liam.dolan@bbsrc.ac.uk

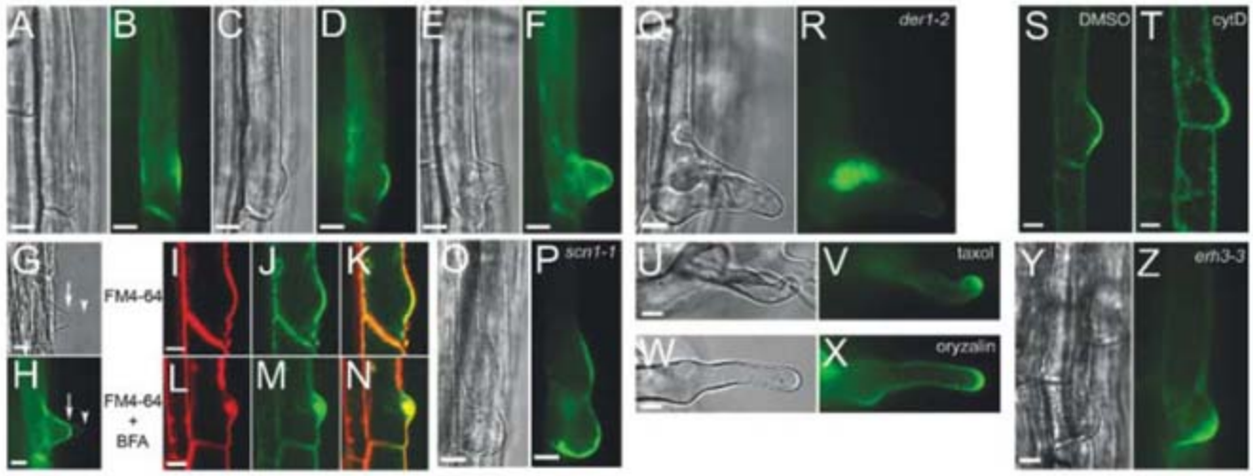

Fig. 1. RHD2 is located at the growing tip of root hair cells. GFP:RHD2 accumulation in initiating hairs (**A** and **B**) and growing hairs (**C** to **F**). (**G** and **H**) GFP:RHD2 is located at the plasma membrane (arrows), which is pulled back from cell wall (arrowheads) in a root treated with 450 mM mannitol to cause plasmolysis. (**I** and **L**) FM4-64 labeling (red). (**J** and **M**) GFP:RHD2 (green). (**K** and **N**) merged channels (yellow). Before BFA treatment, [(I) to (K)]; after treatment of 25 μM BFA for 30 min, [(L) to (N)]. (**O** and **P**) GFP:RHD2 in the ectopic hair bulges of *scn1-1* mutant. (**Q** and **R**) GFP:RHD2 accumulated in cytosolic clumps of *der1-2* root hairs. (**S** and **T**) GFP:RHD2 localization was not affected by dimethyl sulfoxide (DMSO) control (S), whereas treatment of 10 μM cytD for 2 hours caused GFP:RHD2 to locate to clumps inside the cell (T). (**U** to **X**) GFP:RHD2 is localized at the tip of deformed hairs after treatment with 5 μM taxol [(U) and (V)] or 5 μM oryzalin [(W) and (X)]. (**Y** and **Z**) GFP:RHD2 located at the growth sites in *erh3-3* trichoblast. (A), (C), (E), (G), (O), (Q), (U), (W), and (Y), bright-field images; (B), (D), (F), (H), (P), (R), (V), (X), and (Z), GFP images from charge-coupled device camera; (I) to (N), (S), and (T), fluorescent images from confocal microscopy. Scale bars, 10 μm.

and in wild type treated with the microtubule-disrupting drugs oryzalin or taxol (*14*, *15*). RHD2 was located at the growing tips in all cases (Fig. 1, U to Z), indicating that microfilaments but not microtubules are required for the localization of RHD2 to the growing tip.

Given that RHD2 carries two conserved EF-hand motifs near its N terminus where Ca^{2+} binds (Fig. 2A) (*5*, *7*) and that ROS produced by RHD2 activate hyperpolarization-activated Ca^{2+} channels, causing Ca^{2+} influx into cells (*1*), we hypothesized that Ca^{2+} could activate RHD2, forming a positive feedback network. To test this hypothesis, we determined the role of Ca^{2+} in regulating ROS production by the RHD2 in human embryonic kidney (HEK) 293T cells in which NADPH oxidase activity is abolished (*16*, *17*). HEK293T cells were transfected with a full-length RHD2 cDNA fused with FLAG tag that allowed us to confirm the production of RHD2 protein by immune blotting (Fig. 2B). To determine whether Ca^{2+} stimulates RHD2 NADPH oxidase activity, we treated the transfected HEK293T cells with ionomycin, an ionophore that causes Ca^{2+} influx into cells, thereby raising the concentrations of cytoplasmic Ca^{2+} (*18*). Ionomycin treatment transiently activated RHD2 ROS production as compared with that in the empty vector transfection control (Fig. 2C), indicating that Ca^{2+} stimulated RHD2 NADPH oxidase activity. Ionomycin-induced ROS production in the *RHD2*-transfected cells was inhibited by treatment with diphenylene iodonium (DPI), a general inhibitor of flavin-containing oxidases, in a dose-dependent manner without changing RHD2 protein levels (fig. S3A). Thus, the elevation in cytoplasmic Ca^{2+} concentrations stimulates ROS production in the transfected cells through the activation of RHD2.

To investigate whether Ca^{2+}-dependent activation is mediated by EF-hand motifs in the RHD2 protein, we changed the last glutamic acid residue of the Ca^{2+}-binding loop in the first hand motif to an alanine [Glu^{250}→Ala^{250} (E250A) (*19*)] (Fig. 2A). This glutamic acid is conserved among EF-hand motifs and is required for Ca^{2+} binding (*20*). Ionomycin-induced ROS production in cells transfected with RHD2 harboring the E250A substitution was 50 to 60% lower than that in cells transfected with wild-type (WT) RHD2 (Fig. 2C), despite the levels of RHD2 protein in each transfected cell type being the same (Fig. 2B). Similarly, other substitutions in conserved amino acid residues within the EF-hand motifs (D239A or G244E in the first hand; D283A or G288E in the second hand; Fig. 2A) decreased ROS production as compared with WT controls, without affecting the protein levels (fig. S3B). Thus, Ca^{2+} binding to the EF-hand motifs is required for the activation of ROS production by RHD2.

Because Ca^{2+} may control microfilament dynamics (*3*, *21*), we determined whether Ca^{2+} binding through the EF hand regulated the subcellular localization of RHD2. The subcellular localization of GFP:$RHD2_{E250A}$ was identical to that of the WT GFP:RHD2 protein (Fig. 2D), indicating that although Ca^{2+} activates RHD2 NADPH oxidase activity through the EF hand, it does not regulate the distribution of RHD2 protein within the cell.

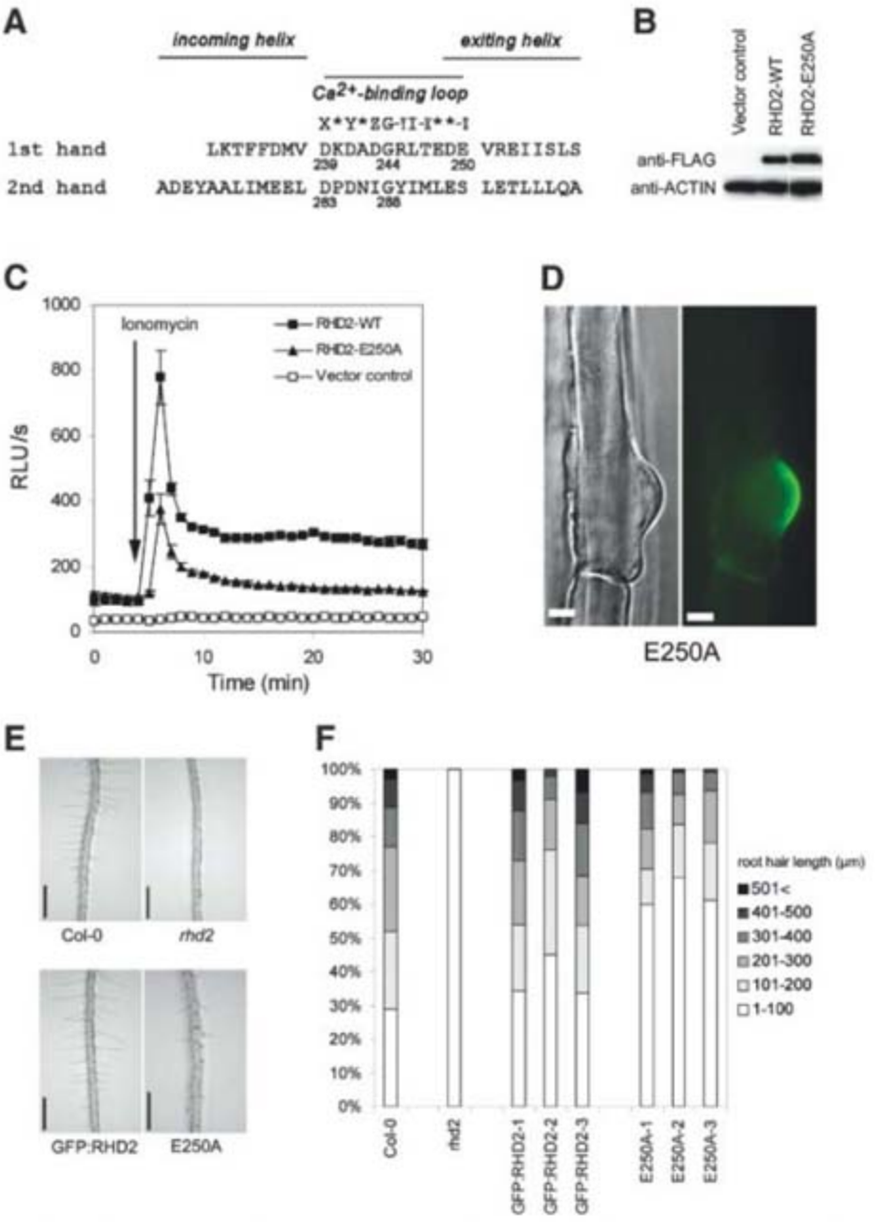

Fig. 2. Ca^{2+} activates RHD2. (**A**) The Ca^{2+}-binding amino acid residues (X, Y, Z, –X, –Y, and –Z) in RHD2 EF-hand motifs. Asterisks indicate nonconserved amino acids. (**B**) Protein levels in HEK293T cells shown by immune blotting with actin as a loading control. (**C**) Ionomycin treatment induced ROS production. Arrow indicates the time point when ionomycin was added. RLU, relative luminescence units. Error bars indicate SE. (**D**) Subcellular localization of GFP:RHD2 carrying the E250A substitution in a trichoblast. Scale bars, 10 μm. (**E**) Rescue of *rhd2* root hair defects by GFP:RHD2 fusion genes. Scale bars, 500 μm. (**F**) Elongating hairs located within 2.5 mm from initiation were measured in different backgrounds and represented by percentage of hair length.

GFP:RHD2 construct developed WT root hairs (Fig. 2, E and F). This suggests that Ca^{2+} binding to the RHD2 EF-hand motif is required for ROS production and root hair tip growth.

We identified possible sites of phosphorylation on RHD2 by comparing the amino acid sequence of RHD2 with other members of the family (Fig. 3A) (*22*) and predicted that RHD2 would be regulated by phosphorylation. To test whether these residues were phosphorylated directly, we performed in vitro kinase assays using a recombinant peptide corresponding to amino acids 316 to 351 of RHD2 ($RHD2_{316-351}$). $RHD2_{316-351}$ was directly phosphorylated in a Ca^{2+}-dependent manner (Fig. 3B). The peptide in which both serine

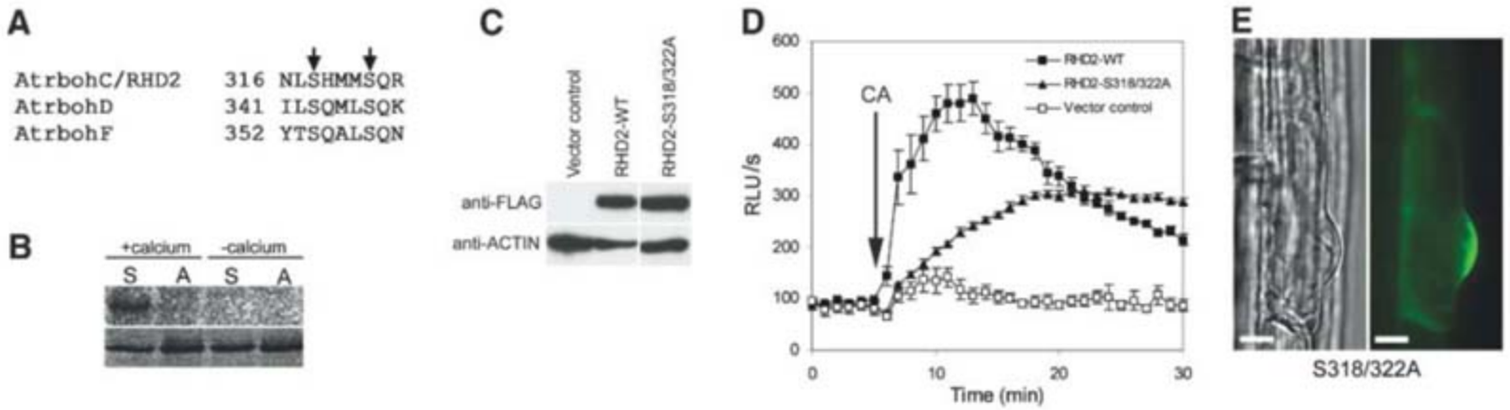

Fig. 3. Ca^{2+}-dependent phosphorylation activates RHD2. (**A**) Alignment of region containing putative phosphorylation residues of RHD2, AtrbohD, and AtrbohF. Arrows highlight conserved phosphorylation serine residues. (**B**) In vitro kinase assays of $RHD2_{316–351}$. "S" indicates WT protein, and "A" indicates protein in which 318 and 322 serine residues are converted to alanines. (**C**) Protein levels in HEK293T cells confirmed by immune blotting. (**D**) CA enhanced ROS production in WT RHD2 and RHD2-S318/322A. Arrow indicates the time point when CA was added. Error bars indicate SE. (**E**) Subcellular localization of GFP:RHD2 with S318/322A substitution. Scale bars, 10 μm.

Fig. 4. Synergistic activation of RHD2 by Ca^{2+} and Ca^{2+}-dependent phosphorylation. Arrows indicate the time points when CA or ionomycin was added. Error bars indicate SE.

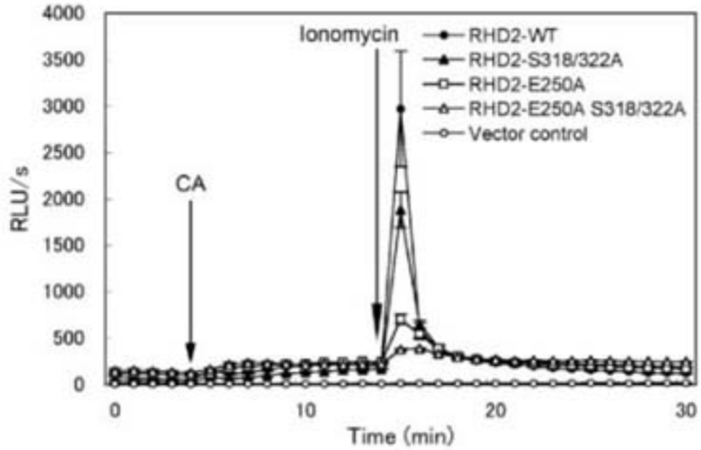

residues were changed to alanine ($RHD2_{316–351}$-S318/322A) was not phosphorylated (Fig. 3B). To determine whether the phosphorylation of RHD2 enhanced NADPH oxidase activity, we determined the effect of calyculin A (CA)—a phosphatase inhibitor that causes proteins to remain phosphorylated (*23*)—on ROS production by RHD2. We expressed a full-length RHD2 cDNA (RHD2-WT) in HEK293T cells (Fig. 3C). ROS production of RHD2-WT was activated upon addition of CA (Fig. 3D), indicating that phosphorylation stimulates ROS production by RHD2. CA-induced ROS production was suppressed by DPI in a dose-dependent manner (fig. S3C), indicating that the ROS production results from the stimulation of the NADPH oxidase activity of RHD2.

To test whether this CA-stimulated ROS production is mediated by conserved serine residues, we determined the levels of ROS produced by full-length RHD2 cDNA carrying the S318/322A substitution (RHD2-S318/322A). The mutant proteins produced less ROS than WT proteins in response to CA treatment, without changing the protein levels (Fig. 3, C and D). Furthermore, these substitutions did not change the subcellular localization of RHD2 (Fig. 3E). Taken together, these data indicate that Ca^{2+}-dependent phosphorylation is required for the activation of RHD2.

We investigated if Ca^{2+} binding to the EF hand and Ca^{2+}-dependent phosphorylation act together to control ROS production by RHD2. When cells were pretreated with CA, the transient ROS production in response to ionomycin treatment was increased as compared with that in cells treated only with CA or ionomycin (Fig. 4). This suggests that RHD2-catalyzed ROS production is synergistically activated by cytosolic Ca^{2+} and Ca^{2+}-dependent phosphorylation. The amino acid substitutions in the EF-hand motifs or phosphorylation sites caused a greater than 50% reduction in ROS production as compared with that in RHD2-WT (Fig. 4 and fig. S3D), and versions of the RHD2 protein carrying amino acid substitutions in both the phosphorylation sites and EF hand produced even less ROS (Fig. 4). Thus, these different domains of the RHD2 NADPH oxidase serve as targets for Ca^{2+}-mediated activation.

Our data provide evidence for a two-part mechanism that determines the shape of root hair cells (fig. S4). A prerequisite is the apical localization of RHD2 protein at the hair cell tip. Once located at the tip, a positive feedback loop involving RHD2 is initiated. ROS derived from the RHD2 NADPH oxidase may activate hyperpolarization-activated Ca^{2+} channels that transport Ca^{2+} into the cells that in turn activates RHD2 NADPH oxidase activity through its EF hand and a Ca^{2+}-dependent protein kinase activity. Such a system of positive feedback, in concert with an independent mechanism for locating RHD2 protein to the tip of the cell, provides a robust mechanism that explains how cells such as root hairs maintain polarity during morphogenesis.

References and Notes

1. J. Foreman *et al.*, *Nature* **422**, 442 (2003).
2. R. J. Carol *et al.*, *Nature* **438**, 1013 (2005).
3. P. K. Hepler, L. Vidali, A. Y. Cheung, *Annu. Rev. Cell Dev. Biol.* **17**, 159 (2001).
4. C. L. Wymer, T. N. Bibikova, S. Gilroy, *Plant J.* **12**, 427 (1997).
5. K. Bedard, B. Lardy, K. H. Krause, *Biochimie* **89**, 1107 (2007).
6. T. Keller *et al.*, *Plant Cell* **10**, 255 (1998).
7. M. A. Torres *et al.*, *Plant J.* **14**, 365 (1998).
8. A. Nebenfuhr, C. Ritzenthaler, D. G. Robinson, *Plant Physiol.* **130**, 1102 (2002).
9. S. H. Lee, H. T. Cho, *Plant Cell* **18**, 1604 (2006).
10. J. Xu, B. Scheres, *Plant Cell* **17**, 525 (2005).
11. M. A. Jones *et al.*, *Plant Cell* **14**, 763 (2002).
12. C. Ringli, N. Baumberger, A. Diet, B. Frey, B. Keller, *Plant Physiol.* **129**, 1464 (2002).
13. A. J. Molendijk *et al.*, *EMBO J.* **20**, 2779 (2001).
14. T. N. Bibikova, E. B. Blancaflor, S. Gilroy, *Plant J.* **17**, 657 (1999).
15. M. Webb, S. Jouannic, J. Foreman, P. Linstead, L. Dolan, *Development* **129**, 123 (2002).
16. B. Bánfi *et al.*, *J. Biol. Chem.* **276**, 37594 (2001).
17. Y. Ogasawara *et al.*, *J. Biol. Chem.*, published online 23 January 2008; 10.1074/jbc.M708106200, in press.
18. C.-M. Liu, T. E. Hermann, *J. Biol. Chem.* **253**, 5892 (1978).
19. Single-letter abbreviations for the amino acid residues are as follows: A, Ala; C, Cys; D, Asp; E, Glu; F, Phe; G, Gly; H, His; I, Ile; K, Lys; L, Leu; M, Met; N, Asn; P, Pro; Q, Gln; R, Arg; S, Ser; T, Thr; V, Val; W, Trp; and Y, Tyr.
20. Z. Grabarek, *J. Mol. Biol.* **359**, 509 (2006).
21. J. Samaj, J. Müller, M. Beck, N. Böhm, D. Menzel, *Trends Plant Sci.* **11**, 594 (2006).
22. T. S. Nühse *et al.*, *Plant J.* **51**, 931 (2007).
23. H. Ishihara *et al.*, *Biochem. Biophys. Res. Commun.* **159**, 871 (1989).

24. We thank R. Horn, M. Pernas-Ochoa, and K. Yi for comments; S. Peck for advice and guidance; and J. Xu, B. Scheres, T. Nakagawa, and M. Tomlinson for materials. This work is supported by a Marie Curie International Incoming Fellowship (0A272J05C) to S.T.; by a John Innes

Foundation scholarship to C.G.; by a Grant-in-Aid for Young Scientists (B) (19770035) from the Ministry of Education, Culture, Sports, Science and Technology (MEXT) of Japan to H.K.; by Grants-in-Aid for Scientific Research (B) (19370023) from MEXT of Japan to K.K.; and by a Grant-in-Aid to the John Innes Centre and a Biotechnology and Biological Sciences Research Council grant (BBS/B/04498) to L.D.

Supporting Online Material
www.sciencemag.org/cgi/content/full/319/5867/1241/DC1
Materials and Methods
Figs. S1 to S4
Tables S1 and S2
References

2 November 2007; accepted 22 January 2008
10.1126/science.1152505

Ceramide Triggers Budding of Exosome Vesicles into Multivesicular Endosomes

Katarina Trajkovic,[1,2*] Chieh Hsu,[1,2*] Salvatore Chiantia,[5] Lawrence Rajendran,[6] Dirk Wenzel,[3] Felix Wieland,[4] Petra Schwille,[5] Britta Brügger,[4] Mikael Simons[1,2,7†]

Intraluminal vesicles of multivesicular endosomes are either sorted for cargo degradation into lysosomes or secreted as exosomes into the extracellular milieu. The mechanisms underlying the sorting of membrane into the different populations of intraluminal vesicles are unknown. Here, we find that cargo is segregated into distinct subdomains on the endosomal membrane and that the transfer of exosome-associated domains into the lumen of the endosome did not depend on the function of the ESCRT (endosomal sorting complex required for transport) machinery, but required the sphingolipid ceramide. Purified exosomes were enriched in ceramide, and the release of exosomes was reduced after the inhibition of neutral sphingomyelinases. These results establish a pathway in intraendosomal membrane transport and exosome formation.

After endocytosis, proteins and lipids that are destined for lysosomal degradation are first incorporated into intraluminal vesicles (ILVs) of multivesicular endosomes (MVEs) and delivered to lysosomes for digestion (*1*, *2*). Alternatively, MVEs can directly fuse with the plasma membrane, which leads to release of the ILVs to the extracellular environment as exosomes, where they function in a multitude of intercellular signaling processes (*3*–*5*). How proteins and lipids are sorted to these subsets of ILVs directed either for lysosomal degradation or for secretion as exosomes is unknown.

To address this issue, we studied the membrane trafficking of the proteolipid protein (PLP) in Oli-neu cells, a mouse oligodendroglial cell line that contains a large number of MVEs (*6*). To analyze whether PLP was released in association with exosomes, we subjected the cell culture medium of transiently transfected Oli-neu cells to sequential centrifugation steps with increasing centrifugal forces to obtain, finally, a 100,000*g* pellet, which mainly contained small membrane vesicles with a diameter of about 50 to 100 nm (Fig. 1B), similar to previously described exosomes (*3*–*5*). Relatively large amounts of PLP were found in the 100,000*g* pellet (Fig. 1A), and immunoelectron microscopy analysis revealed the presence of PLP on the vesicles (Fig. 1B). In contrast, PLP containing the cytotoxic, missense mutation [Val replaces Ala at position 242 (A242V); msd-PLP] that leads to misfolding of the protein and to retention in the endoplasmic reticulum (ER) was not detected in the 100,000*g* pellet (Fig. 1A); this finding excluded cell lysis as a major contributing factor. In addition, ER, Golgi, and early endosomal proteins and several exogenously expressed membrane proteins were not detected in the 100,000*g* pellet, which did contain the two exosomal proteins, Alix and flotillin (fig. S1) (*7*, *8*). In a continuous sucrose density gradient, the majority of PLP was enriched in the same fraction as the exosomal protein Alix (Fig. 1C). To explore whether PLP requires transport through the endosomal system to be released with exosomes, we cotransfected PLP with the early-endosomal guanosine triphosphatase–deficient Rab5 (Rab5^{Q79L}, in which Leu replaces Gln at position 79) to impair intraendosomal trafficking (*9*). Electron microscopy analysis of these endosomes revealed that they were filled with ILVs (fig. S2). A large fraction of PLP was

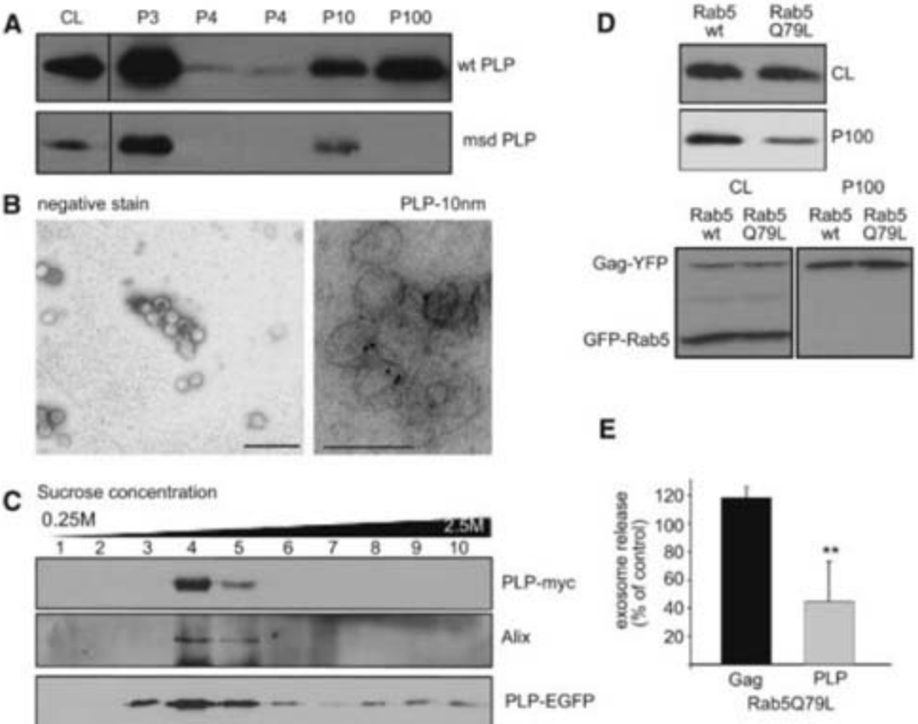

Fig. 1. Identification and characterization of exosomes. (**A**) Oli-neu cells were transiently transfected with Myc-tagged, wild-type (wtPLP) or mutant (msd-PLP) PLP; the medium was collected and submitted to sequential centrifugation steps as indicated. The resulting pellets of each centrifugation step were analyzed by Western blotting for PLP. (**B**) Cells were transiently transfected with PLP-Myc; 100,000*g* pellets were prepared and negatively stained with 1% uranyl acetate and immunolabeled with antibodies against PLP (right). Scale bar, 200 nm. (**C**) A 0.25 to 2.5 M sucrose gradient was loaded on top of the 100,000*g* pellet, and the resulting fractions were analyzed for PLP from transiently (PLP-Myc) or stably transfected (PLP-EGFP) cells and for the exosomal protein Alix. (**D** and **E**) Cells were cotransfected with either GFP-Rab5^{Q79L} or wild-type GFP-Rab5 (wt) and PLP-Myc or Gag-YFP; the amount of PLP and Gag in the cell lysates and 100,000*g* pellets was determined and quantified. Results are expressed as the mean ± SD of five experiments (**$P < 0.01$; one-sample *t* test against 100%).

[1]Centre for Biochemistry and Molecular Cell Biology, University of Göttingen, 37073 Göttingen, Germany. [2]Max-Planck-Institute for Experimental Medicine, 37075 Göttingen, Germany. [3]Max-Planck-Institute for Biophysical Chemistry, 37077 Göttingen, Germany. [4]Heidelberg University Biochemistry Center, 69120 Heidelberg, Germany. [5]BioTec, TU Dresden, 01307 Dresden, Germany. [6]Max-Planck-Institute of Cell Biology and Genetics, 01307 Dresden, Germany. [7]Department of Neurology, University of Göttingen, 37073 Göttingen, Germany.

*These authors contributed equally to this work.
†To whom correspondence should be addressed. E-mail: msimons@gwdg.de

entrapped in these enlarged endosomes, and the release of PLP with exosomes was significantly reduced (Fig. 1, D and E). The release from the plasma membrane of Moloney murine leukemia virus Gag fused to yellow fluorescent protein (Gag-YFP) with virus-like particles was not affected by $Rab5^{Q79L}$, which demonstrated the specificity of the effect (Fig. 1, D and E).

Thus, PLP-containing exosomes are derived from the endosomal system. How then is exosomal cargo segregated from nonexosomal cargo in endosomes? To study the possible segregation of cargo within distinct endosomal microdomains, we transfected cells with $Rab5^{Q79L}$ to enlarge early endosomes and to facilitate domain inspection by confocal immunofluorescence analysis (*10*). Clathrin-coated microdomains on early endosomes contain the ubiquitin-binding protein Hrs, which sorts ubiquitinated proteins into these domains to mediate degradative protein sorting (*11*). To analyze whether PLP localized to these microdomains, we analyzed the localization of PLP in $Rab5^{Q79L}$ enlarged endosomes. Little PLP colocalized with either Hrs or epidermal growth factor receptor (EGFR) (Fig. 2), whereas Hrs colocalized to a large extent with EGFR (fig. S3). The PLP-enriched domains colocalized with flotillin, a membrane scaffolding protein of lipid-raft microdomains, and with glycosylphosphatidylinositol fused to cyan fluorescent protein (GPI-CFP), which suggested that segregation of PLP from EGFR involves raft-based microdomains (Fig. 2).

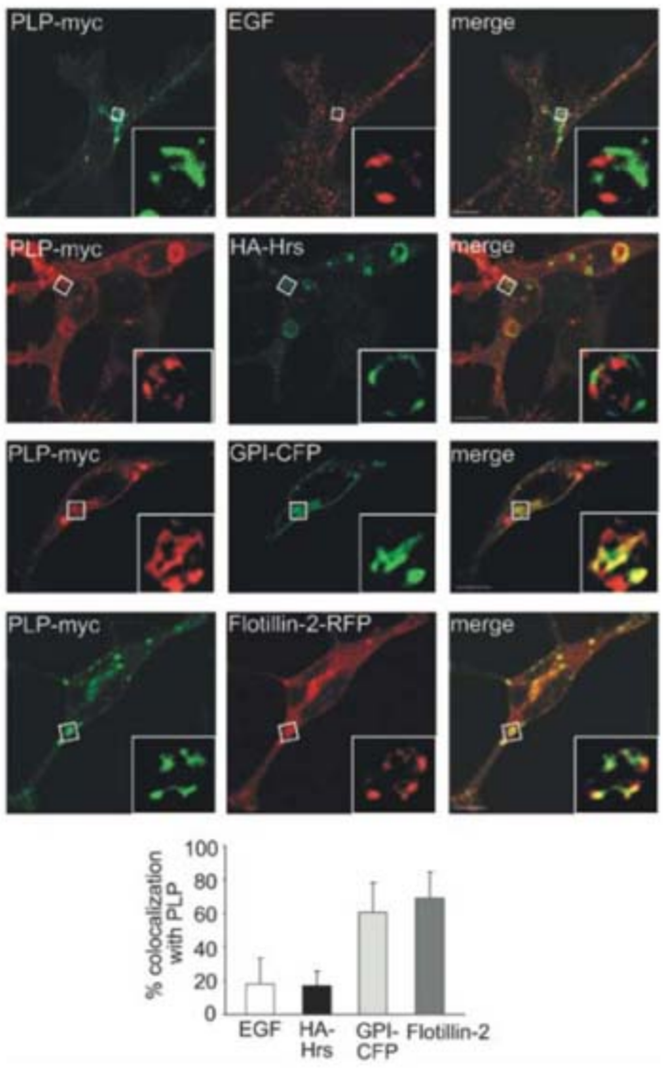

Fig. 2. Endosomal subdomain structure. Oli-neu cells were cotransfected with $Rab5^{Q79L}$ and PLP-Myc, EGFR, hemagglutinin (HA) epitope–tagged Hrs (HA-Hrs), GPI-CFP, or flotillin-2 fused with red fluorescent protein (flotillin-2–RFP) as indicated. Cells transfected with EGFR were incubated for 15 min with rhodamine-labeled EGF. Cells were then processed and analyzed for immunofluorescence microscopy. The white box indicates the (inset) region reimaged in higher resolution and contrast to resolve the subdomain structure. Quantification of colocalization of the different proteins on endosome membranes is shown (n = ~25 endosomes). Scale bar, 10 μm.

We next addressed whether EGFR or PLP uses distinct pathways of inward budding into endosomes. Sorting of EGFR into ILVs requires the sequential action of different components of the ESCRT (endosomal sorting complex required for transport) machinery (*12*, *13*). To interfere with the function of the ESCRT machinery, we used either RNA interference (RNAi) or dominant-negative mutants against Hrs, Tsg101, Alix, or Vps4. Depletion of either Hrs or Tsg101 significantly reduced the intraluminal transport of EGF into enlarged endosomes, whereas Alix depletion only had a minor effect (fig. S4). The reduction of EGF in the endosomal lumen correlated with a defect in EGF degradation (fig. S5) (*13*). We also analyzed the effect of the Tsg101 depletion (knockdown) on intraendosomal transport of vesicular stomatitis virus G (VSV-G) to investigate ligand-independent transport. Depletion of Tsg101 reduced the amount of VSV-G within the lumen of the endosomes (fig. S6).

In contrast, knockdown of Hrs, Tsg101, or Alix had no influence on the inward budding of PLP (fig. S4). In addition, the functional inhibition of the ESCRT machinery did not change the colocalization of PLP with Lamp-1 (fig. S7). Thus, the pathway for intraendosomal transport of PLP may be ESCRT-independent. Furthermore, neither knockdown of Tsg101 and Alix nor expression of a dominant-negative Vps4 impaired the secretion of PLP with exosomes (fig. S8). Likewise, the release of CD63 (with enhanced GFP fusion, EGFP-CD63) was not affected by coexpression with dominant-negative Vps4 (fig. S9). Secretion of Gag-YFP with virus-like particles was strongly reduced by the expression of dominant-negative Vps4 (fig. S7) (*14*). In addition, overexpression of Tsg101, which inhibits HIV-1 budding (*15*), did not affect exosome release of PLP (fig. S10). Thus, PLP is transferred

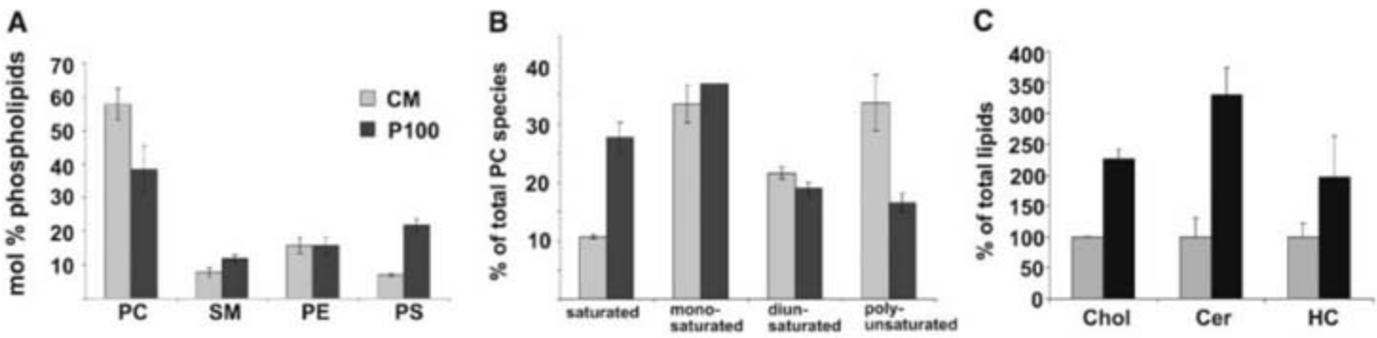

Fig. 3. Lipid analysis of exosomes. Analysis of (**A**) phospholipid classes, (**B**) PC composition, and (**C**) ratios of individual lipid classes from total cellular membranes (CM) and the exosome fractions (P100). The data are from three independent experiments; values are means ± SD. Chol, cholesterol; HC, hexosylceramide; Cer, ceramide; PE, phosphatidylethanolamine; and PS, phosphatidylserine.

into the lumen of endosomes and released with exosomes in an ESCRT-independent fashion.

To get insight into the ESCRT-independent budding machinery, we used nano-electrospray ionization tandem mass spectrometry to examine the molecular composition of exosomes. The lipid composition was remarkably similar to that of lipid rafts (*16*, *17*). Exosomes not only were enriched in cholesterol but also contained higher amounts of sphingolipids [sphingomyelin (SM) and hexosylceramide] and lower amounts of phosphatidylcholine (PC) than total cellular membrane (Fig. 3A). In addition, quantitative analysis of lipid molecular species revealed an increase in saturated PC, at the expense of polyunsaturated species in exosomes (Fig. 3B and fig. S11). Most important, we found a marked enrichment of ceramide in exosomes (Fig. 3C). Ceramide is formed after the hydrolytic removal of the phosphocholine moiety of SM by sphingomyelinases (SMases) (*18*). Exogenous SMase treatment or application of C_6-ceramide can induce the formation of vesicles (*19*–*21*). To analyze the role of ceramide in exosome biogenesis and release, we treated Oli-neu cells with the neutral sphingomyelinase (nSMase) inhibitor, GW4869. Exosome release was markedly reduced after treatment with GW4869 (Fig. 4, A and B, and fig. S9). The effect was also observed after treatment with the two structurally unrelated nSMase inhibitors, spiroepoxide and glutathione (Fig. 4, A and B). Furthermore, depletion of neutral sphingomyelinase 2 (nSMase2) with RNAi reduced the release of PLP but not Gag with exosomes. Next, we studied the effect of nSMase inhibition in intraendosomal transport of PLP. After treatment with GW4869, a significant reduction of the amount of PLP within the endosomal lumen was observed (Fig. 4B). This was not due to an unspecific derangement of the endosomal system, because the amount of intraendosomal VSV-G remained unchanged (Fig. 4, C and D) and because the degradation of EGF was not impaired (fig. S12). Furthermore, a reduction of PLP within the endosomal lumen was also observed after depletion of nSMase2 using RNAi (Fig. 4, C and D).

To further explore the role of ceramide in the formation of intravesicular membrane, we performed experiments using giant unilamellar vesicles (GUVs). We used a mixture of dioleoylphosphatidylcholine (DOPC), SM, and cholesterol to generate vesicles with two different lipid phases. 1,1′-Dioctadecyl-3,3,3′,3′-tetramethylindodicarbocyanine perchlorate (DiD-C18) and cholesterol with dipyrromethene boron difluoride (Bodipy-cholesterol) were used to mark the liquid-disordered and liquid-ordered (raftlike) lipid phases, respectively. We added SMase exogenously to these GUVs to analyze whether intravesicular membranes were formed from one of these lipid phases. Shortly after the addition of the SMase, small vesicles started to bud from the liquid-ordered lipid phase and to accumulate in the lumen of the GUVs (Fig. 4E). The intravesicular membrane was predominantly labeled by Bodipy-cholesterol and contained only small amounts of DiD-C18 (Fig. 4E).

Together, these data provide evidence for an alternative pathway for sorting cargo into MVEs, which is independent of the ESCRT machinery but seems to depend on raft-based microdomains for the lateral segregation of cargo within the endosomal membrane. These microdomains may contain high concentrations of sphingolipids from which ceramides are formed. Ceramide can induce the coalescence of small microdomains into larger domains, which promotes domain-induced budding (*22*). In addition, the cone-shaped structure of ceramide might induce

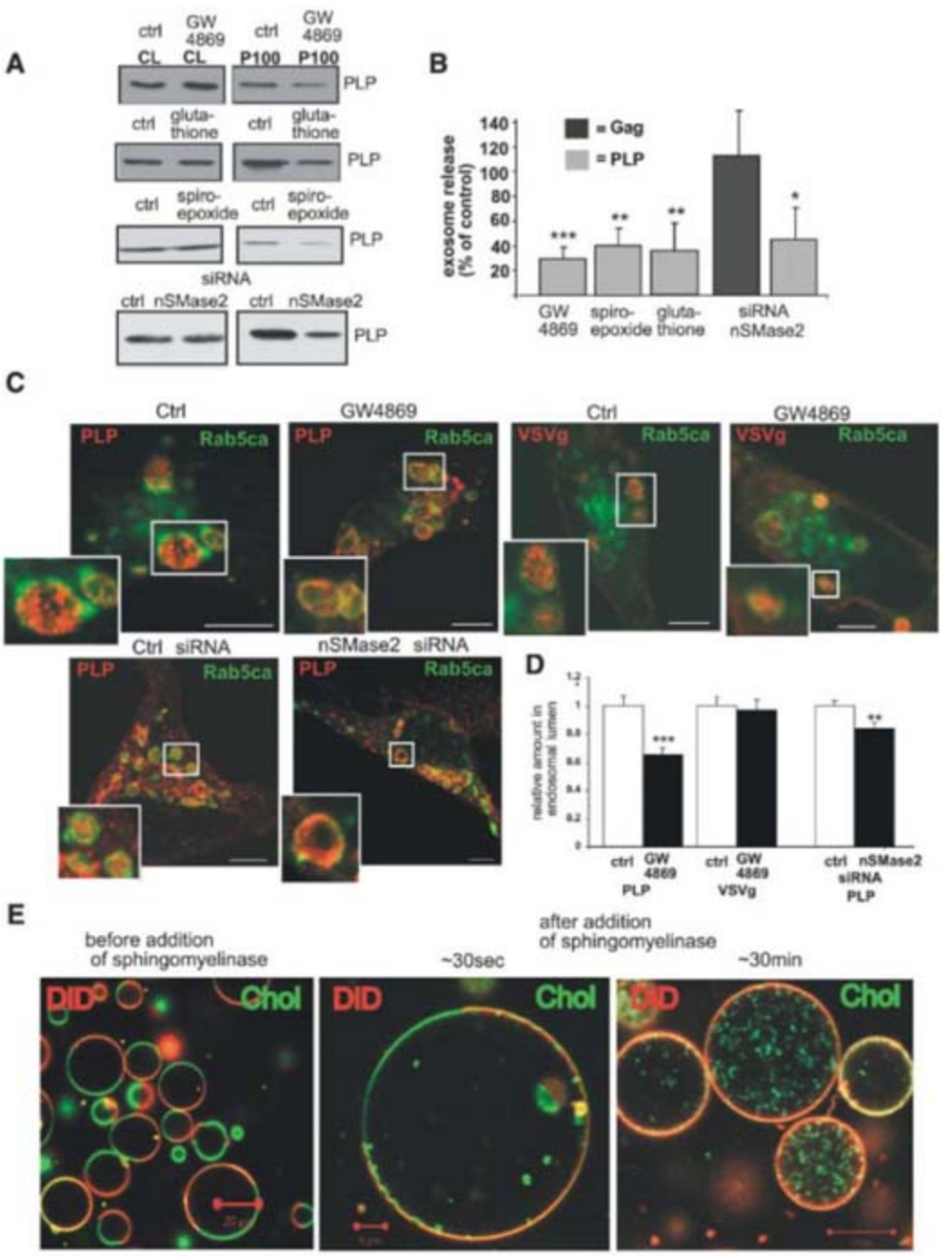

Fig. 4. Ceramide in the formation of intravesicular membrane and exosome release. (**A**) Oli-neu cells stably expressing PLP-EGFP were treated with 5 μM GW4869, 5 μM spiroepoxide, or 5 mM glutathione or with the respective vehicle. nSMase2 small interfering RNA (siRNA) was delivered by nucleofection into the cells. The amount of PLP-EGFP and Gag-YFP was determined in the cell lysates (CL) and in the exosome fractions (P100). (**B**) Results are expressed as means ± SD of three to six experiments (*$P < 0.05$; **$P < 0.01$; ***$P < 0.001$; one-sample *t* test against 100%). (**C**) Cells were treated as indicated and cotransfected with GFP-Rab5^{Q79L} and PLP-Myc or VSV-G and then processed and analyzed by immunofluorescence microscopy. (**D**) The amount of PLP or VSV-G in the endosomal lumen was quantified (fluorescence intensity in the lumen versus the limiting membrane; normalized to 1 for the controls). Values represent means ± SE ($n > 40$ endosomes; **$P < 0.01$, ***$P < 0.001$; *t* test). Scale bar, 5 μm. (**E**) GUVs were prepared with a mixture of DOPC, SM, and cholesterol. DiD-C18 (red) and Bodipy-cholesterol (green) were used to mark the two lipid phases. GUVs were incubated with SMase from *Staphylococcus aureus*. Confocal pictures are shown before and at two different time points after the addition of SMase, as indicated.

spontaneous negative curvature by creating an area difference between the membrane leaflets. Another cone-shaped lipid, lysobisphosphatidic acid, induces the formation of internal vesicles in liposomes (*23*). This lipid, which is absent from exosomes (*16*), may regulate biogenesis and dynamics of ILVs along the degradative pathway (*24*). Ceramide, in contrast, seems to be used for the generation of another population of ILVs that are not destined for transport to the lysosomes but are secreted as one class of exosomes.

References and Notes

1. R. C. Piper, D. J. Katzmann, *Annu. Rev. Cell Dev. Biol.* **23**, 519 (2007).
2. J. Gruenberg, H. Stenmark, *Nat. Rev. Mol. Cell Biol.* **5**, 317 (2004).
3. C. Thery, L. Zitvogel, S. Amigorena, *Nat. Rev. Immunol.* **2**, 569 (2002).
4. W. Stoorvogel, M. J. Kleijmeer, H. J. Geuze, G. Raposo, *Traffic* **3**, 321 (2002).
5. G. van Niel, I. Porto-Carreiro, S. Simoes, G. Raposo, *J. Biochem.* **140**, 13 (2006).
6. K. Trajkovic *et al.*, *J. Cell Biol.* **172**, 937 (2006).
7. A. de Gassart, C. Geminard, B. Fevrier, G. Raposo, M. Vidal, *Blood* **102**, 4336 (2003).
8. B. Fevrier *et al.*, *Proc. Natl. Acad. Sci. U.S.A.* **101**, 9683 (2004).
9. H. Stenmark *et al.*, *EMBO J.* **13**, 1287 (1994).
10. C. Raiborg *et al.*, *Nat. Cell Biol.* **4**, 394 (2002).
11. C. Raiborg, J. Wesche, L. Malerod, H. Stenmark, *J. Cell Sci.* **119**, 2414 (2006).
12. J. H. Hurley, S. D. Emr, *Annu. Rev. Biophys. Biomol. Struct.* **35**, 277 (2006).
13. R. L. Williams, S. Urbe, *Nat. Rev. Mol. Cell Biol.* **8**, 355 (2007).
14. J. E. Garrus *et al.*, *Cell* **107**, 55 (2001).
15. R. Goila-Gaur, D. G. Demirov, J. M. Orenstein, A. Ono, E. O. Freed, *J. Virol.* **77**, 6507 (2003).
16. R. Wubbolts *et al.*, *J. Biol. Chem.* **278**, 10963 (2003).
17. B. Brügger *et al.*, *Proc. Natl. Acad. Sci. U.S.A.* **103**, 2641 (2006).
18. C. J. Clarke *et al.*, *Biochemistry* **45**, 11247 (2006).
19. J. M. Holopainen, M. I. Angelova, P. K. Kinnunen, *Biophys. J.* **78**, 830 (2000).
20. X. Zha *et al.*, *J. Cell Biol.* **140**, 39 (1998).
21. R. Li, E. J. Blanchette-Mackie, S. Ladisch, *J. Biol. Chem.* **274**, 21121 (1999).
22. E. Gulbins, R. Kolesnick, *Oncogene* **22**, 7070 (2003).
23. H. Matsuo *et al.*, *Science* **303**, 531 (2004).
24. F. G. van der Goot, J. Gruenberg, *Trends Cell Biol.* **16**, 514 (2006).

25. We are grateful to R. Bittman, D. Caplan, M. Zerial, D. Arndt-Jovin, U. Coskun, P. Keller, D. Cutler, P. Burfeind, and H. Stenmark for providing reagents and R. White for help with RNAi experiments. The work was supported by the Deutsche Forschungsgemeinschaft (SFB 523, GRK521).

Supporting Online Material

www.sciencemag.org/cgi/content/full/319/5867/1244/DC1
Materials and Methods
SOM Text
Figs. S1 to S12
References

19 November 2007; accepted 8 January 2008
10.1126/science.1153124

Membrane Proteins of the Endoplasmic Reticulum Induce High-Curvature Tubules

Junjie Hu,[1] Yoko Shibata,[1] Christiane Voss,[2] Tom Shemesh,[3] Zongli Li,[4] Margaret Coughlin,[5] Michael M. Kozlov,[3] Tom A. Rapoport,[1*] William A. Prinz[2*]

The tubular structure of the endoplasmic reticulum (ER) appears to be generated by integral membrane proteins, the reticulons and a protein family consisting of DP1 in mammals and Yop1p in yeast. Here, individual members of these families were found to be sufficient to generate membrane tubules. When we purified yeast Yop1p and incorporated it into proteoliposomes, narrow tubules (~15 to 17 nanometers in diameter) were generated. Tubule formation occurred with different lipids; required essentially only the central portion of the protein, including its two long hydrophobic segments; and was prevented by mutations that affected tubule formation in vivo. Tubules were also formed by reconstituted purified yeast Rtn1p. Tubules made in vitro were narrower than normal ER tubules, due to a higher concentration of tubule-inducing proteins. The shape and oligomerization of the "morphogenic" proteins could explain the formation of the tubular ER.

How the characteristic shape of an organelle is generated and maintained is largely unknown. The endoplasmic reticulum (ER), for example, consists of continuous membrane sheets and tubules (*1*, *2*), but it is unclear how these domains are made and kept morphologically distinct. The tubules are interconnected in a polygonal network and have diameters ranging from ~30 nm in *Saccharomyces cerevisiae* (*3*) to ~50 nm in mammals (*4*). The most plausible models for shaping ER tubules are based on mechanisms that generate or stabilize the high membrane curvature seen in cross sections. A curvature-stabilizing role has been suggested for a class of integral membrane proteins, the reticulons and a protein family that includes DP1 in mammals and Yop1p in yeast (*5*). These proteins are found in most, if not all, eukaryotic cells. They form homo- and heterooligomers and localize exclusively to ER tubules. Their overexpression generates long, unbranched tubules, and their deletion in yeast leads to the loss of tubular ER. The reticulon and Yop1p (DP1) families are not related in sequence, but they each contain a conserved domain of ~200 amino acids that includes two hydrophobic segments, which seem to form a hairpin in the membrane. It remains unclear whether the reticulons or Yop1p (DP1) are sufficient for tubule formation and how they might deform the membrane.

[1]Howard Hughes Medical Institute and Department of Cell Biology, Harvard Medical School, 240 Longwood Avenue, Boston, MA 02115, USA. [2]Laboratory of Cell Biochemistry and Biology, National Institute of Diabetes and Digestive and Kidney Disorders (NIDDK), National Institutes of Health, Bethesda, MD 20892, USA. [3]Department of Physiology and Pharmacology, Sackler Faculty of Medicine, Tel Aviv University, Ramat Aviv, 69978 Tel Aviv, Israel. [4]Department of Cell Biology, Harvard Medical School, 240 Longwood Avenue, Boston, MA 02115, USA. [5]Department of Systems Biology, Harvard Medical School, 240 Longwood Avenue, Boston, MA 02115, USA.

*To whom correspondence should be addressed. E-mail: tom_rapoport@hms.harvard.edu (T.A.R.); wprinz@helix.nih.gov (W.A.P.)

We first tested whether the reticulon and Yop1p (DP1) proteins would each generate membrane tubules when reconstituted with lipids into proteoliposomes. Yop1p was purified from *S. cerevisiae* with a cleavable N-terminal histidine (His) tag in the detergent lauryldimethylamine-*N*-oxide (LDAO) (Fig. 1A) (*6*). After cleavage of the His tag, *Escherichia coli* polar lipids were added, and the detergent was removed with Biobeads to generate proteoliposomes. At early time points during the reconstitution reaction, small vesicles and short tubules were seen by negative-stain electron microscopy (EM), both with a diameter of ~17 nm (Fig. 1B). Over the course of a day, the vesicles disappeared and the tubules grew in length, reaching several hundred nanometers, but their diameter remained the same (Fig. 1C). The tubules occasionally had branch points (Fig. 1C), which indicated that the lipid bilayers could branch or fuse during reconstitution. No tubules were seen when the lipids were omitted (Fig. 1D). In the absence of protein, round liposomes with heterogeneous size were generated (Fig. 1E). Yop1p formed tubules of identical diameter when reconstituted with other lipids (fig. S1), which suggested that the protein was primarily responsible for the shape of the proteoliposomes.

Next, we tested whether yeast reticulon Rtn1p could also induce tubules in vitro. Tubules were indeed seen in negative-stain EM when purified Rtn1p (Fig. 1F) was mixed with *E. coli* polar lipids and the detergent was removed by dialysis (Fig. 1G). The diameter of these tubules was about the same as with Yop1p, but bulges were frequently observed. When the detergent was removed by Biobeads, Rtn1p tubules were not generated, whereas, with Yop1p, both Biobeads and dialysis resulted in tubule formation. Because Rtn1p was less efficient than Yop1p in forming tubules, most of the subsequent experiments were performed with Yop1p.

Increasing the lipid concentration or decreasing the protein concentration in the reconstitution reaction resulted in fewer Yop1p tubules and an increased number of large vesicles (table

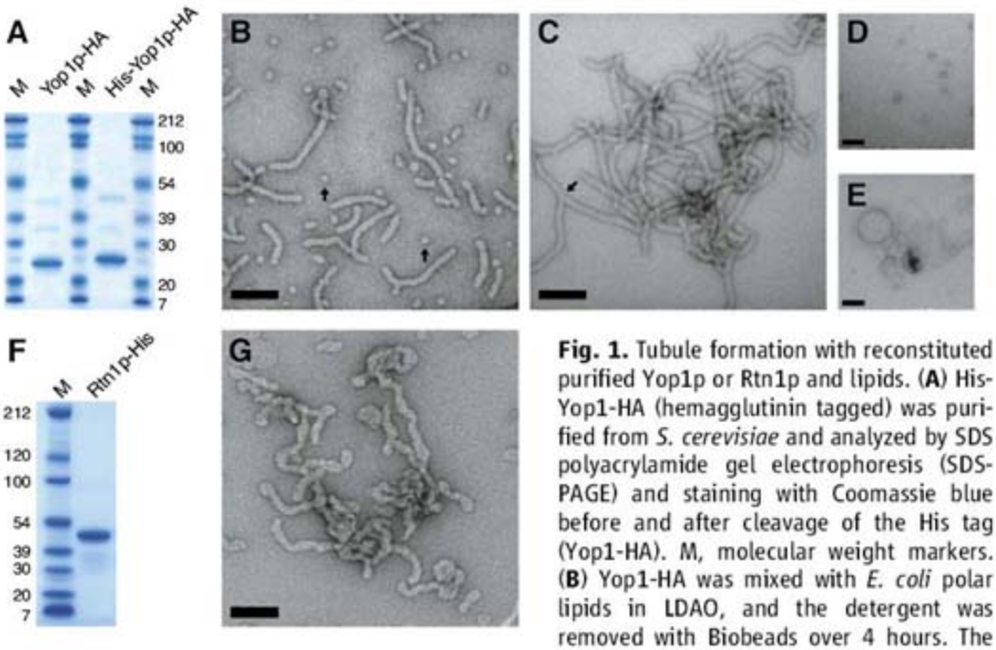

Fig. 1. Tubule formation with reconstituted purified Yop1p or Rtn1p and lipids. (**A**) His-Yop1-HA (hemagglutinin tagged) was purified from *S. cerevisiae* and analyzed by SDS polyacrylamide gel electrophoresis (SDS-PAGE) and staining with Coomassie blue before and after cleavage of the His tag (Yop1-HA). M, molecular weight markers. (**B**) Yop1-HA was mixed with *E. coli* polar lipids in LDAO, and the detergent was removed with Biobeads over 4 hours. The proteoliposomes were analyzed by negative-stain EM. Arrows indicate small vesicles. (**C**) As in (B), but after one day. The arrow indicates a branch point. (**D**) As in (B), but with protein only. (**E**) As in (B), but with lipid only. (**F**) Rtn1-His was purified from *S. cerevisiae* and analyzed by SDS-PAGE and Coomassie staining. (**G**) Rtn1-His was reconstituted with *E. coli* polar lipids in Fos-choline-12. The detergent was removed by dialysis for 1 week. Scale bars, 100 nm.

S1). The segregation of excess lipid from the tubules suggests that Yop1p self-associates during detergent removal and cannot easily be diluted in the plane of the membrane. Both Rtn1p and Yop1p indeed have the propensity to form oligomers. Up to five molecules could be cross-linked using a bifunctional cross-linker (fig. S2, A and B). Ladders of Yop1p oligomers were formed both with tubules generated in vitro and with native membranes (fig. S2A). Also, Yop1p solubilized from yeast membranes by digitonin migrated in sucrose gradients as oligomers containing about eight molecules (fig. S2C). The oligomers dissociated in LDAO but were resistant to high salt, which suggested that they are formed mainly through hydrophobic interactions.

Reconstituted Yop1p tubules sedimented rapidly in sucrose-gradient centrifugation experiments; the peak fractions contained almost all the Yop1p protein added to the reconstitution (fig. S3). In contrast, as expected, pure lipids or Yop1p in detergent stayed close to the top of the gradient. The gradient-purified tubules contain a lipid-to-protein molar ratio of ~10:1 (*6*). Although the protein molecules must be densely packed in the tubules, they did not show a regular arrangement in negative-stain EM.

Fig. 2. Correlation between tubule formation in vitro and in vivo. (**A**) Yop1-HA, His-Yop1-HA, or Yop1_ΔC1 were reconstituted as in Fig. 1B. Scale bars, 100 nm. (**B**) His-tagged Rtn1p wild type or M91 mutant [mutations: H7Y, K48I, T127I, I137P, and N277Y (*26*)] were reconstituted as in Fig. 1G. Scale bars, 100 nm. (**C**) The ER was visualized in yeast cells lacking Rtn1p, Rtn2p, and Yop1p by expressing a green fluorescent protein (GFP) fusion to Sec63p. The cells also contained either an empty vector, or centromere (CEN) plasmids expressing Yop1-HA, His-Yop1-HA, Yop1_ΔC1, Rtn1-His, or M91-His under the endogenous promoters. The microscope was focused at either the center or periphery of the cells. Scale bars, 1 μm.

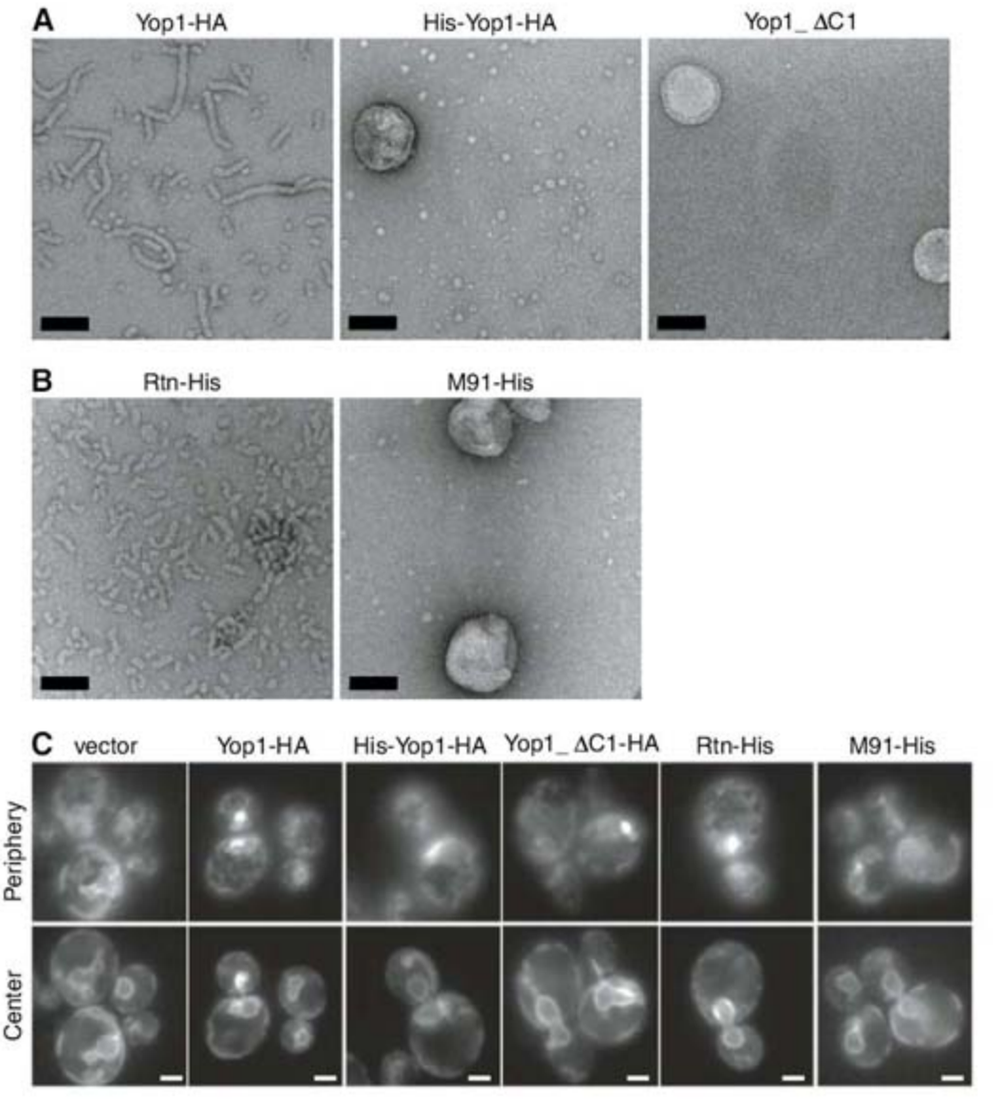

To determine the tubule-forming domain of Yop1p, the tubules were treated with increasing concentrations of trypsin. Both termini of reconstituted Yop1p were readily cleaved (fig. S4), which was consistent with their proposed localization in the cytosol. A stable fragment protected by the lipid bilayer corresponded to amino acids 24 to 165. When purified as a recombinant protein from yeast, this fragment (Yop1_ΔC2) was even more efficient in tubule formation than the full-length protein (fig. S5). However, a Yop1p fragment lacking an additional 28 residues at the C terminus (Yop1_ΔC1) was inactive (Fig. 2A). Thus, the tubule-inducing domain of Yop1p comprises the two hydrophobic segments and the intervening domain, as well as a few flanking residues.

Purified His-tagged Yop1p did not induce tubules in vitro (Fig. 2A), even though it was able to form small vesicles similar to those formed by the nontagged protein (compare Fig.1B and fig. S6C) when the detergent was diluted. We thus tested whether His-Yop1p and Yop1_ΔC1, both defective in tubule formation in vitro (Fig. 2A), were also nonfunctional in vivo. Indeed, although Yop1p without a His tag restored the tubular ER in *S. cerevisiae* cells lacking Yop1p, Rtn1p, and Rtn2p, neither His-Yop1p nor Yop1_ΔC1 was active (Fig. 2C). In addition, the His tag prevented the formation of long tubules seen with overexpression of Yop1p in wild-type cells (fig. S6A). His-Yop1p still formed ladders in cross-linking experiments and migrated at higher molecular weight in sucrose-gradient centrifugation (fig. S2C), which indicated that oligomerization alone is insufficient for tubule formation. We also identified an Rtn1p mutant (M91) that carried multiple amino acid changes and was unable to complement the triple knockout mutant in vivo (Fig. 2C); the purified His-tagged M91 protein did not form tubules in vitro, but wild-type Rtn1-His did (Fig. 2B). Thus, there is a good correlation between tubule formation in vitro and in vivo.

The narrow diameter of the tubules generated by reconstituted Yop1p was confirmed by cryo-EM analysis (Fig. 3A). The diameter was ~15 nm, somewhat smaller than the width of the flattened tubules seen by negative-stain EM (~17 nm). In vitreous ice, the outer edge of the tubules appeared much darker than their interior, verifying that the observed structures consist of a bilayer enclosing a lumen. A tubule diameter of ~15 nm was also determined in thin-section EM (Fig. 3B). Given that each lipid bilayer has a thickness of about 3 to 4 nm (*7*), the tubules have an extreme curvature, perhaps the highest achievable.

We reasoned that the in vitro tubules are narrower than those normally found in cells because they have a higher concentration of tubule-inducing protein in the lipid bilayer (by a factor of ~20). Indeed, whereas endogenous Rtn4 co-localized with the luminal protein calreticulin in mammalian cells, overexpressed Rtn4a, DP1, Rtn3c, or Yop1p squeezed calreticulin out of the tubules (Fig. 3C and fig. S7). The overexpression of reticulon in yeast or plant cells also displaced luminal proteins from the tubular ER [Fig. 3D and (*8*)]. The diameter of ER tubules in COS cells overexpressing Rtn4a was determined to be ~20 nm (Fig. 3E), significantly smaller than that of normal ER tubules (~50 nm) [(*4*) and fig. S7].

Thus, individual members of the reticulon and Yop1p (DP1) families are sufficient to induce membrane tubules. Rtn1p and Yop1p are integral membrane proteins, whereas previously identified tubule-forming proteins, such as those containing a BAR domain (*9*–*12*), are soluble. The reticulons and Yop1p (DP1) could shape the phospholipid bilayer by two mechanisms. First, the two hydrophobic hairpin segments could cause local spontaneous curvature by forming a wedge in the lipid bilayer. Second, oligomerization of these proteins could generate arcs whose shape may deform the bilayer into tubules. These mechanisms might cooperate with one another.

To illustrate the effect of arc-like protein oligomers on membrane tubule formation, we have developed a simple model. It assumes that the membrane shape is determined by the opposing effects of the protein arcs to bend the lipid bilayer and the bilayer resisting such bending (*6*). If the arcs are ordered into rings encircling a tubule, which corresponds to a maximal localization of the constraints imposed by them on the

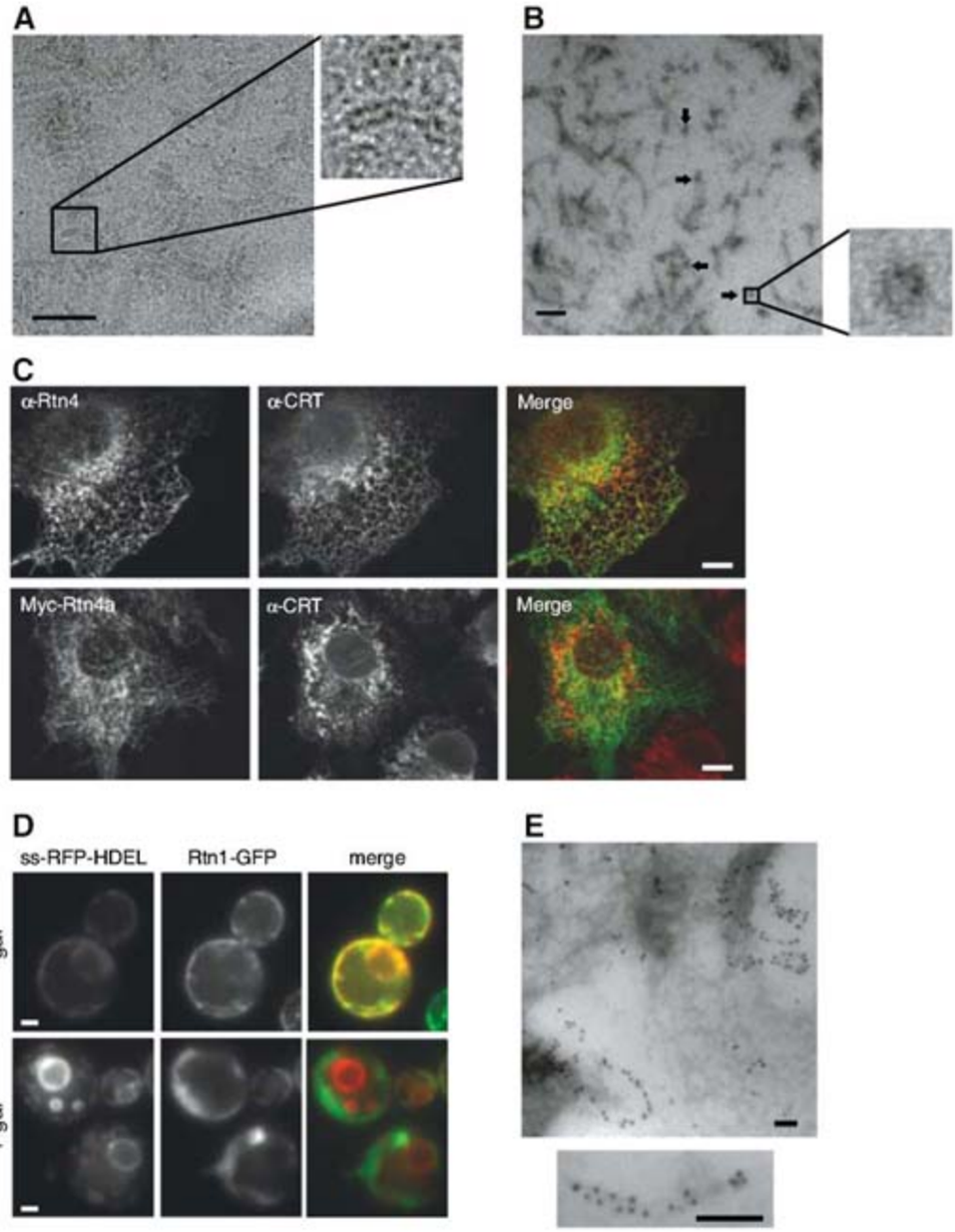

Fig. 3. Determining the diameter of tubules. (**A**) Yop1p tubules generated in vitro were analyzed by cryo-EM. Scale bar, 200 nm. (**B**) Yop1p tubules were analyzed by thin-section EM. Arrows indicate cross sections. Scale bar, 100 nm. (**C**) Nontransfected COS cells (top row) or COS cells overexpressing Myc-Rtn4a were immunostained for endogenous Rtn4 or the Myc tag (green), co-immunostained for endogenous calreticulin (red), and analyzed by confocal fluorescence microscopy. The right panels show merged images. Scale bars, 10 μm. (**D**) Yeast cells expressing a fusion of a signal sequence with the red fluorescent protein and HDEL (*26*) (ss-RFP-HDEL) and Rtn1-GFP were imaged with or without overexpression of Rtn1-HA (±gal). Scale bars, 1 μm. (**E**) Ultrathin frozen sections of COS cells expressing Rtn4a-GFP were labeled with antibodies to GFP followed by protein A–conjugated 10-nm gold. The lower panel shows a magnified image. Scale bars, 100 nm.

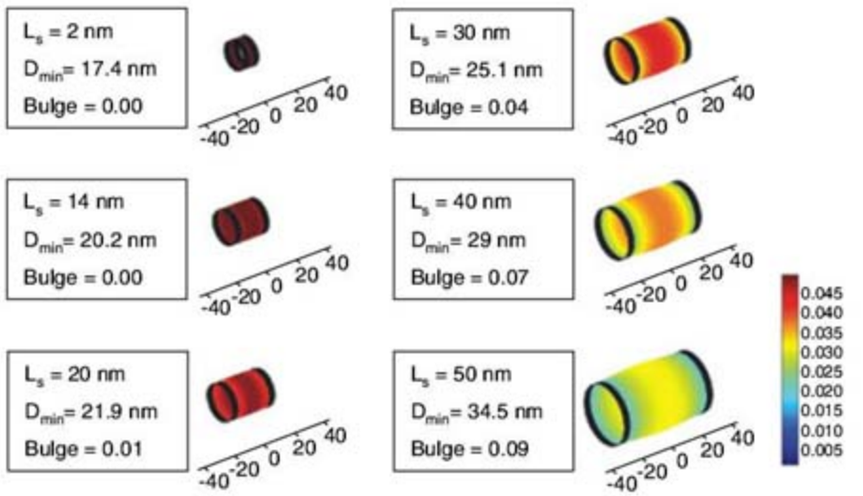

Fig. 4. Calculated shapes of membrane tubules constricted by protein rings. The barrel-shaped structures were calculated for different distances L_s between the rings. D_{min} is the minimal diameter at a ring. Bulging between rings is defined as BULGE = $(D_{max} - D_{min})/D_{min}$, with D_{max} being the maximal diameter between rings. The bending rigidity of protein and lipid were assumed to be 800 $k_BT \cdot$ nm and 20 k_BT, respectively (where k_BT = 0.6 kcal/mol is the thermal energy). The spontaneous curvature of the protein and the thickness of the protein ring were taken to be 0.13 nm^{-1} and 4 nm, respectively. The color maps represent local mean curvature of the membrane in nm^{-1}.

bilayer, a change of the distance between rings from 2 to 50 nm can explain the increase of tubule diameter from 17 nm in the in vitro experiments to ~30 nm in vivo (Fig. 4). The bulging between rings is negligible, even for relatively large distances. Almost perfect cylindrical tubules can thus be generated with the tubule-forming proteins occupying a small fraction of the total membrane surface (fig. S8). We estimate that in fact ~10% of the total tubular ER surface in *S. cerevisiae* could be occupied by the tubule-forming proteins. In reality, the arc-shaped oligomers may be distributed randomly along the tubule, and they may be disassembled actively, which would allow other ER proteins to diffuse in the plane of the membrane.

We hypothesize that the reticulons and Yop1p (DP1) use both their wedgelike shapes and their oligomerization into arcs or rings to generate the tubular ER with minimal surface coverage. Some membrane-shaping proteins, such as synaptotagmin and epsin, use only the wedging mechanism and insert hydrophobic amino acids into the outer leaflet of the bilayer (*13*, *14*), but they need to occupy a large percentage of the membrane surface to induce curvature (*13*). Other proteins, such as the F-BAR proteins and dynamins, primarily form ring- or spiral-shaped scaffolds to generate tubules (*15*–*20*). A combination of the wedging and scaffolding mechanisms, as proposed for the reticulons and Yop1p (DP1), is employed by endophilin and amphiphysin (*9*–*12*, *21*). A combination of the two mechanisms also may be used by other integral membrane proteins that shape organelles. For example, caveolin, which shapes flasklike invaginations of the plasma membrane, called caveoli, has a single hairpin membrane anchor and forms filaments or spirals on the cytoplasmic face of the organelle (*22*). The dynamin-like protein Fzo1p in yeast (Mfn in mammals) in the outer mitochondrial membrane (*23*), which is required for the maintenance of proper mitochondrial tubules, has a hairpin-shaped membrane anchor and oligomerization domains that are essential for its function (*24*, *25*). The proposed mechanisms might thus be generally used to generate organelles with high membrane curvature.

References and Notes

1. O. Baumann, B. Walz, *Int. Rev. Cytol.* **205**, 149 (2001).
2. G. K. Voeltz, W. A. Prinz, *Nat. Rev. Mol. Cell Biol.* **8**, 258 (2007).
3. S. Bernales, K. L. McDonald, P. Walter, *PLoS Biol.* **4**, e423 (2006).
4. D. W. Fawcett, *The Cell* (Saunders, Philadelphia, ed. 2, 1981).
5. G. K. Voeltz, W. A. Prinz, Y. Shibata, J. M. Rist, T. A. Rapoport, *Cell* **124**, 573 (2006).
6. Materials and methods are available as supporting material on *Science* Online.
7. K. Mitra, I. Ubarretxena-Belandia, T. Taguchi, G. Warren, D. M. Engelman, *Proc. Natl. Acad. Sci. U.S.A.* **101**, 4083 (2004).
8. N. Tolley *et al.*, *Traffic* **9**, 94 (2008).
9. K. Takei, V. I. Slepnev, V. Haucke, P. De Camilli, *Nat. Cell Biol.* **1**, 33 (1999).
10. B. J. Peter *et al.*, *Science* **303**, 495 (2004).
11. M. Masuda *et al.*, *EMBO J.* **25**, 2889 (2006).
12. J. L. Gallop *et al.*, *EMBO J.* **25**, 2898 (2006).
13. S. Martens, M. M. Kozlov, H. T. McMahon, *Science* **316**, 1205 (2007).
14. M. G. Ford *et al.*, *Nature* **419**, 361 (2002).
15. A. Frost, P. De Camilli, V. M. Unger, *Structure* **15**, 751 (2007).
16. W. M. Henne *et al.*, *Structure* **15**, 839 (2007).
17. A. Shimada *et al.*, *Cell* **129**, 761 (2007).
18. K. Takei, P. S. McPherson, S. L. Schmid, P. De Camilli, *Nature* **374**, 186 (1995).
19. J. E. Hinshaw, S. L. Schmid, *Nature* **374**, 190 (1995).
20. B. Marks *et al.*, *Nature* **410**, 231 (2001).
21. J. L. Gallop, P. J. Butler, H. T. McMahon, *Nature* **438**, 675 (2005).
22. K. G. Rothberg *et al.*, *Cell* **68**, 673 (1992).
23. G. J. Praefcke, H. T. McMahon, *Nat. Rev. Mol. Cell Biol.* **5**, 133 (2004).
24. G. J. Hermann *et al.*, *J. Cell Biol.* **143**, 359 (1998).
25. E. E. Griffin, D. C. Chan, *J. Biol. Chem.* **281**, 16599 (2006).
26. Mutations are the result of amino acid substitutions; for example, H7Y indicates that Tyr was substituted for His at position 7. Single-letter abbreviations for the amino acid residues are as follows: A, Ala; C, Cys; D, Asp; E, Glu; F, Phe; G, Gly; H, His; I, Ile; K, Lys; L, Leu; M, Met; N, Asn; P, Pro; Q, Gln; R, Arg; S, Ser; T, Thr; V, Val; W, Trp; and Y, Tyr.
27. We thank D. Moazed, B. Glick, and R. Yan for materials; T. Walz and T. Mitchison for discussions; D. Kelly and G. Skiniotis for comments; and J. F. Ménétret and M. Ericsson for help with EM experiments. C.V. and W.A.P. were supported by the NIDDK intramural program. T.A.R. is a Howard Hughes Medical Institute Investigator.

Supporting Online Material

www.sciencemag.org/cgi/content/full/319/5867/1247/DC1
Materials and Methods
Figs. S1 to S8
Table S1
References

30 November 2007; accepted 18 January 2008
10.1126/science.1153634

Leading-Edge Vortex Improves Lift in Slow-Flying Bats

F. T. Muijres,[1] L. C. Johansson,[1] R. Barfield,[1] M. Wolf,[1] G. R. Spedding,[2] A. Hedenström[1]*

Staying aloft when hovering and flying slowly is demanding. According to quasi–steady-state aerodynamic theory, slow-flying vertebrates should not be able to generate enough lift to remain aloft. Therefore, unsteady aerodynamic mechanisms to enhance lift production have been proposed. Using digital particle image velocimetry, we showed that a small nectar-feeding bat is able to increase lift by as much as 40% using attached leading-edge vortices (LEVs) during slow forward flight, resulting in a maximum lift coefficient of 4.8. The airflow passing over the LEV reattaches behind the LEV smoothly to the wing, despite the exceptionally large local angles of attack and wing camber. Our results show that the use of unsteady aerodynamic mechanisms in flapping flight is not limited to insects but is also used by larger and heavier animals.

Generating enough lift during hovering and slow forward flight is problematic according to traditional quasi–steady-state wing theory (*1*, *2*). Yet several species of small flying vertebrates are adapted to foraging using this flight mode. Insects are able to hover by using a range of possible unsteady high-lift mechanisms, including rotational circulation (*3*),

clap-and-fling (*4*, *5*), wake capture (*3*, *6*), and added mass (*7*, *8*). However, arguably the most important mechanism is a leading-edge vortex (LEV) (*5*, *9*–*12*), which may generate up to two-thirds of the total lift in insect flight (*13*, *14*). Although unsteady lift mechanisms have been studied extensively in insects or scaled models of their flapping wings (*5*, *6*, *11*–*17*), vertebrates have only been studied indirectly. Such measurements derived from kinematics or wakes suggest that some birds (*18*) and bats (*19*) require additional lift for weight support, other than quasi–steady-state lift alone (*2*). A recent study of hovering hummingbirds found traces of previously shed LEVs in their wakes (*20*), and sharp-edged model wings of gliding swifts with high sweep (60°) developed stable LEVs (*21*).

We quantitatively measured the airflow, using digital particle image velocimetry (DPIV), around the wings of three individuals of Pallas' long-tongued bat, *Glossophaga soricina* (table S1), flying freely in front of a feeder in a low-turbulence wind tunnel at a forward flight speed U_∞ = 1 m/s (*22*). At this flight speed, the average local Reynolds number of the bat wing is $Re \approx 5 \times 10^3$ (*23*) and the Strouhal number $St \approx 1.36$ (*24*).

The DPIV image plane was orientated vertically in the freestream flow direction, and measurements were made at different span-wise locations along the wing, when the wing was positioned horizontally. At this wing position, the wing does not block the DPIV image, the wingspan is at its maximum, and the wing is two-thirds into the downstroke (*22*). Cross-stream DPIV measurements were also performed closely behind the bats (a distance of ~3 mean wing chord lengths at U_∞ = 1.35 m/s). From the DPIV data, we determined the two in-plane velocity components of the airflow, resulting in a planar velocity field. Spatial gradients of this planar velocity field also yield the divergence, which is a measure of the variation in out-of-plane velocity (*25*), and the vorticity, which is a measure of the local angular velocity.

From the streamwise DPIV data, the wing profile and its motion (Fig. 1, A to D) were also determined by tracking the part of the wing profile illuminated by the laser sheet (*22*). The velocity of the wing profile was used as a no-slip boundary condition in the DPIV calculations (*22*). The average wing camber is 18 ± 3% (mean ± SD, n = 68 observations) of the wing chord (fig. S5D), and the average effective angle of attack is 51° ± 19° (n = 68 observations) (fig. S5F) (*22*). Both are high values for steady-state wing theory: A fixed wing at similar Re with such high camber and angle of attack would stall and lose lift (*26*).

The vorticity field and velocity vectors around the bat wing (Fig. 1) show that the flow separates at the leading edge, generating a patch of high negative vorticity (clockwise spin). But, remarkably, behind this patch of vorticity the airflow reattaches, resulting in attached and laminar flow at the trailing edge. The vorticity patch at the leading edge of the wing was present at all measured span-wise locations but was stronger near the wingtip (Fig. 1C) than toward the wing root (Fig. 1A). Instantaneous streamlines computed from the measured streamwise flow (Fig. 1D) form a recirculating region at the vorticity patch, which also spirals inward at the core. All these facts are consistent with the presence of an attached LEV (*10*). In the neighborhood of the LEV, the divergence of the flow in the image plane is on average positive (source flow) (25) and small compared to the vorticity magnitude (fig. S4). Both sign and magnitude differ from theoretical expectations for LEV stabilization (*10*), which could imply that no LEV stabilizing mechanism is needed (*27*).

In some of the images (mainly distally on the wing), an area of high negative vorticity is also found near the trailing edge but without recirculation (Fig. 1D). The presence of negative vorticity near the trailing edge is associated with the outer wing making a strong rotational (pitch-up) movement before the end of the downstroke (Fig. 1D). Therefore this patch of high vorticity could be a result of rotational circulation (*3*), which is an alternative aerodynamic mechanism for enhanced lift generation.

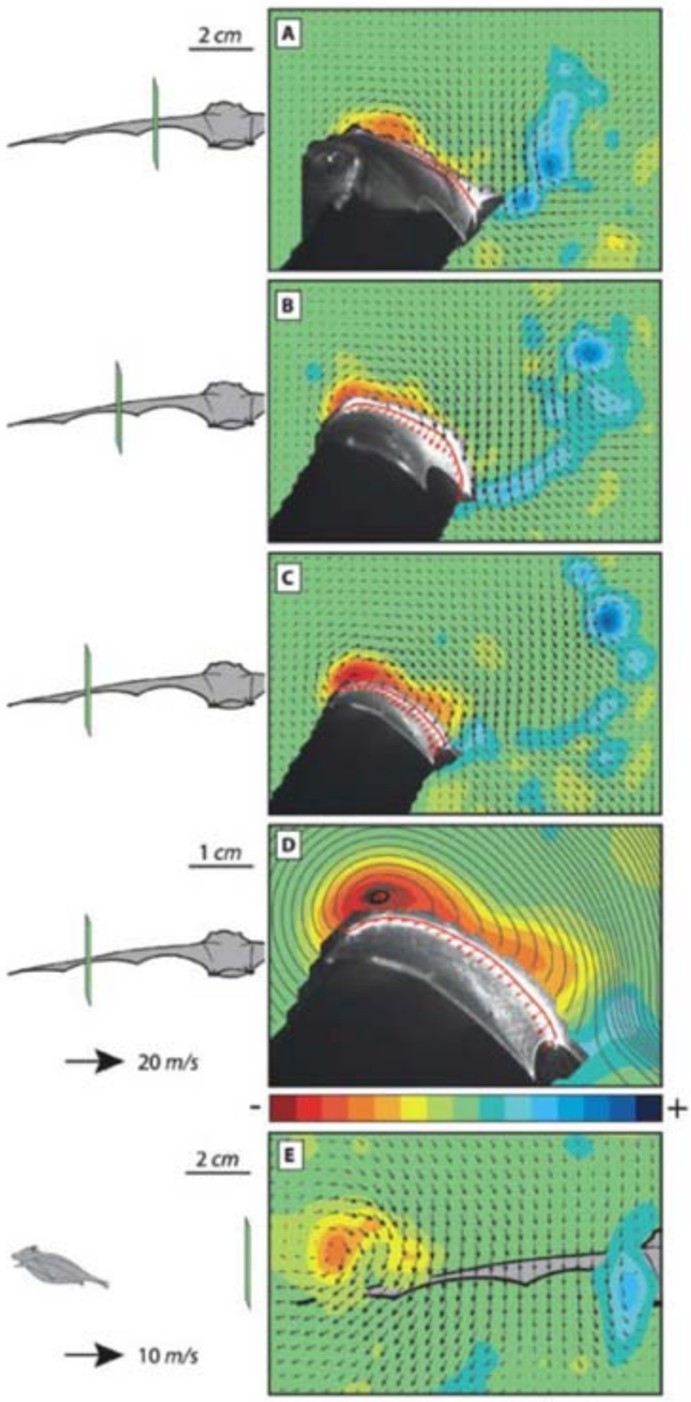

Fig. 1. Velocity and vorticity fields around a bat wing in slow forward flight (1 m/s), when the wing is positioned horizontally in the downstroke. The vectors show the disturbance caused by the wing with the uniform mean flow (of 1 m/s) removed. (**A** to **C**) show streamwise measurements at different positions along the span. The span locations are 33, 50, and 65% of the semi-wingspan for (A), (B), and (C), respectively, as indicated on the bat silhouettes to the left. The flight direction is from right to left. Instantaneous two-dimensional streamlines of part of (C) are shown in (**D**). In (A) to (D), The bat wing and its shadow in the DPIV laser sheet are visible; the local wing profile and its relative motion are shown with a red curve and arrows. (**E**) Data derived from cross-stream measurements, with the position of the bat indicated by the bat silhouette. The vorticity field is scaled according to the color bar; it ranges from −1750 to +1750 s^{-1}, for (A) to (D) and from −700 to +700 s^{-1} for (E). The velocity vectors are scaled to the reference vector at the left of the color bar for (A) to (D) and at left of (E). Space scale bars are located at left of (A) for (A) to (C), at left of (D), and at left of (E).

[1]Department of Theoretical Ecology, Lund University, SE-223 62 Lund, Sweden. [2]Department of Aerospace and Mechanical Engineering, University of Southern California, Los Angeles, CA 90089–1191, USA.

*To whom correspondence should be addressed. E-mail: anders.hedenstrom@teorekol.lu.se

To investigate the contribution of the LEV to the total lift, the circulation of the LEV was determined at different span locations (Fig. 2). The average chord length and average effective wing velocity ($\bar{c}$ = 0.042 m and $\bar{U}_{eff}$ = 4.0 m/s) were used to nondimensionalize the circulation ($\Gamma/\bar{U}_{eff}\bar{c}$) (*22*). The results show that the LEV circulation increases toward the wingtip (Fig. 2), which is consistent with LEV structures found for some insects (*1*). When assuming that a LEV enhances lift by adding its own circulation to the bound circulation of a wing (*1*), the nondimensional circulation of the LEV is related to its associated lift coefficient by $C_{LEV} \approx 2 \cdot \Gamma_{LEV}/\bar{U}_{eff}\bar{c}$ (*22*, *28*). The average nondimensional LEV circulation is about 1 (Fig. 3), which corresponds to a $C_{LEV} \approx 2$.

During the downstroke of a flapping wing, positive vorticity is generated at the trailing edge and is shed into the wake. This vorticity can be generated throughout the downstroke, and we will label it trailing-edge vorticity (TEV). According to Kelvin's theorem (*29*), the circulation of the TEV (Γ_{TEV}) is related to the bound circulation on the wing and thus to the total lift coefficient by $C_L \approx 2 \cdot \Gamma_{TEV}/\bar{U}_{eff}\bar{c}$ (*22*). The shed TEV is clearly visible in Fig. 1, A to C, as a distinct patch of positive vorticity (counterclockwise spin) to the right of the wing, called the start vortex, and a trail of positive vorticity between this start vortex and the trailing edge. Because the tip of the wing travels a larger distance during the downstroke than does the wing root, the start vortex is located further behind the wing near the wingtip (Fig. 1C) than near the wing root (Fig. 1A). This pattern of vorticity shedding is strikingly similar to that of a hawkmoth (*30*). Γ_{TEV} was determined at different span locations (Fig. 2), but no systematic variation was found. The average nondimensional Γ_{TEV} is 2.4 (Fig. 3), for an effective lift coefficient of 4.8 (*22*), which is beyond that considered to be the maximum possible for quasi–steady-state wings (*2*) at the same *Re* and aspect ratio (*26*), but is similar to results from previous studies of bats (*19*) and within the possible range of pitching and heaving plates (*31*).

As mentioned above, the nondimensional $\Gamma_{LEV} \approx 1$, which means that the LEV contributes to more than 40% of the total lift ($\Gamma_{LEV}/\Gamma_{TEV}$ = 0.42) (*22*). This value is similar to LEV contributions reported for insects [hawkmoth, up to 65% (*13*, *14*), and fruit fly ≈ 45% (*3*)] but is considerably higher than the 15% estimated from the wake of hovering hummingbirds (*20*). The TEV minus the LEV nondimensional circulation is 1.4, resulting in a non-LEV lift coefficient of 2.8 (*22*). This value is also higher than conventional quasi–steady-state wing models at similar conditions (*26*), suggesting that other unsteady lift mechanisms may also be involved, such as rotational circulation (*3*) and delayed stall (*15*), resulting in high lift due to a high angle of attack.

To obtain an image of the three-dimensional wake structure, near-wake cross-stream DPIV measurements were performed for two bats (Fig. 1E). The vorticity field and velocity vectors show the presence of a tip vortex with negative vorticity (clockwise spin) and a weaker vortex near the wing root (root vortex) with positive vorticity (counterclockwise spin). The average tip- and root-vortex circulation were nondimensionalized using the mean wing chord length ($\bar{c}$) and the average effective wing velocity ($\bar{U}_{eff}$) determined from kinematic measurements (*22*). The average tip-vortex circulation has a similar strength as Γ_{TEV}, and the average Γ_{LEV} is 65% of the root-vortex circulation (Fig. 3).

Based on the qualitative and quantitative data, we suggest a cartoon model of the vortex system around the bat wing during the downstroke (Fig. 4). At the beginning of the downstroke, a start vortex is formed at the trailing edge of the wing. During the downstroke, this vortex travels downward and backward because of self-convection, creating a trail of vorticity between the start vortex and the trailing edge of the wing. In inviscid vortex dynamics, a line vortex must terminate either as a closed loop or at a solid surface, and so the start vortex connects to two tip and two root vortices, which grow in length during the downstroke. The tip and root vortices are connected to the wing and to the LEV. The start vortices of each wing are probably connected to each other behind the body (*19*). Because the LEV circulation strength is similar to the root-vortex circulation, these are probably connected, hence the absence of a LEV across the body. The near wake of slow-flying bats did not show a separately shed LEV (*19*), suggesting that the LEV stays attached throughout the downstroke and merges with the stop vortex.

For hovering and slow-flying insects, three different types of LEV systems have been proposed

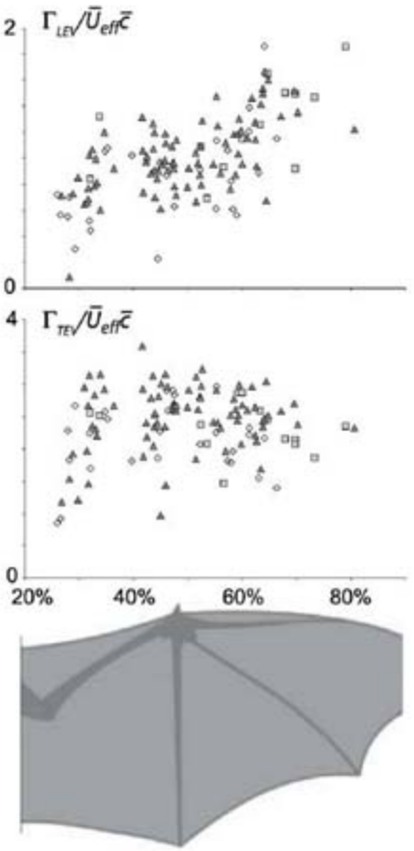

Fig. 2. Circulation Γ_{LEV} (**top**) and Γ_{TEV} (**bottom**) at different wing positions for three bats. The circulation was nondimensionalized using $\bar{c}$ and $\bar{U}_{eff}$ of the measured points (fig. S5). Dimonds represent bat 1, squares represent bat 2, and triangles represent bat 3.

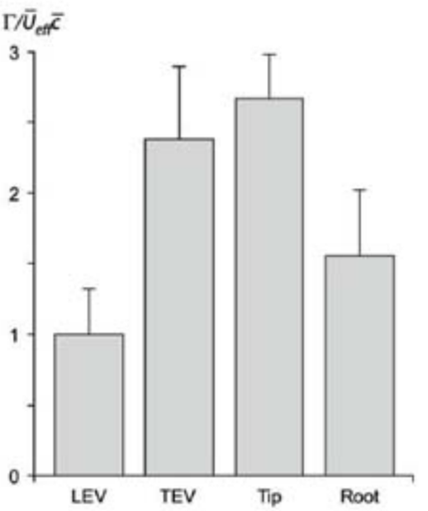

Fig. 3. Mean ± SD for circulations in different parts of the wake structure during the downstroke when the wing is horizontal, at a forward speed of 1 m/s. The circulation was nondimensionalized using $\bar{c}$ and $\bar{U}_{eff}$ (fig. S5). For the LEV and TEV, n = 119 observations; for the tip and root vortex, n = 98 observations (*22*).

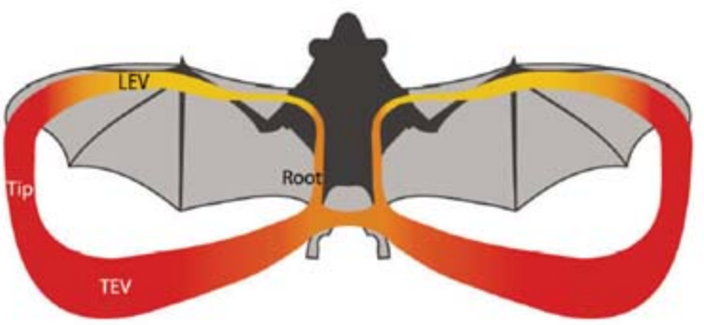

Fig. 4. Cartoon of the primary vortex structure for a bat during the downstroke when the wing is horizontal, at a forward speed of 1 m/s. The structure consists of two closed loops, one for each wing, consisting of a LEV on top of the wing, connected to a start vortex shed in the wake via a tip vortex (Tip) and a root vortex (Root). The color coding indicates the absolute value of local circulation; yellow is low circulation and red is high circulation.

(*14*): a helical-shaped LEV starting at the inner wing, increasing in size along the wingspan, and finally connecting to the tip vortex (*9*, *27*); a cylindrical-shaped LEV that expands across the thorax and is connected to the two tip vortices (*6*, *14*); and a LEV that is connected to a small root vortex and a large tip vortex (*5*). The vortex system proposed here (Fig. 4) is most similar to the latter case.

The sharp leading edge of the bat wing probably facilitates the generation of the LEV (*21*), whereas the ability to actively change the wing shape and camber (*32*) could contribute to the control and stability of the LEV.

LEVs have now been observed in active unrestricted bat flight, with a strength that is important to the overall aerodynamics. Unsteady aerodynamic mechanisms for enhanced lift are therefore not unique to insect flight, and larger animals adapted for slow and hovering flight, such as these nectar-feeding bats, can (and perhaps must) use LEVs to enhance flight performance.

References and Notes

1. F.-O. Lehmann, *Naturwissenschaften* **91**, 101 (2004).
2. Quasi–steady-state wing theory assumes that the forces on a moving wing are equivalent to the sum of the forces on a fixed wing over a sequence of attitudes that track the wing motion. This model neglects acceleration forces and unsteady aerodynamic effects.
3. M. H. Dickinson, F.-O. Lehmann, S. P. Sane, *Science* **284**, 1954 (1999).
4. T. Weis-Fogh, *J. Exp. Biol.* **59**, 169 (1973).
5. T. Maxworthy, *J. Fluid Mech.* **93**, 47 (1979).
6. R. B. Srygley, A. L. R. Thomas, *Nature* **420**, 660 (2002).
7. C. Ellington, *Philos. Trans. R. Soc. London Ser. B* **305**, 1 (1984).
8. S. Vogel, *Life in Moving Fluids* (Princeton Univ. Press, Princeton, NJ, 1994).
9. C. P. Ellington, C. van den Berg, A. P. Willmott, A. L. R. Thomas, *Nature* **384**, 626 (1996).
10. T. Maxworthy, *J. Fluid Mech.* **587**, 471 (2007).
11. M. W. Luttges, in *Frontiers in Experimental Fluid Mechanics*, M. Gad-El-Hak, Ed. (Springer, Berlin, 1989), pp. 429–456.
12. A. L. R. Thomas, G. K. Taylor, R. B. Srygley, R. L. Nudds, R. J. Bomphrey, *J. Exp. Biol.* **207**, 4299 (2004).
13. C. van den Berg, C. P. Ellington, *Philos. Trans. R. Soc. London Ser. B* **352**, 329 (1997).
14. R. J. Bomphrey, N. J. Lawson, N. J. Harding, G. K. Taylor, A. L. R. Thomas, *J. Exp. Biol.* **208**, 1079 (2005).
15. M. H. Dickinson, K. G. Gotz, *J. Exp. Biol.* **174**, 45 (1993).
16. A. Willmott, C. Ellington, *J. Exp. Biol.* **200**, 2693 (1997).
17. C. Somps, M. Luttges, *Science* **228**, 1326 (1985).
18. U. M. Norberg, in *Swimming and Flying in Nature*, vol. 2, T. Y.-T. Wu, C. J. Brokaw, C. Brennen, Eds. (Plenum, New York, 1975), pp. 869–881.
19. A. Hedenström *et al.*, *Science* **316**, 894 (2007).
20. D. R. Warrick, B. W. Tobalske, D. R. Powers, *Nature* **435**, 1094 (2005).
21. J. J. Videler, E. J. Stamhuis, G. D. E. Povel, *Science* **306**, 1960 (2004).
22. See supporting material on *Science* Online.
23. $Re = \bar{U}_{\mathrm{eff}}\bar{c}/\nu$ ($\bar{U}_{\mathrm{eff}}$ is average effective wing speed, which is the sum of the flight velocity and the wing-flapping velocity; $\bar{c}$ is the average wing chord length; and ν is the kinematic viscosity of air). *Re* is the ratio between inertial and viscous aerodynamic forces and is an index of the relative instability of the fluid around an airfoil. The bats operate at a *Re* range with rather stable aerodynamic characteristics, just below the *Re* range ($10^4 \leq Re \leq 10^5$) where the aerodynamics are notoriously hard to predict and control.
24. $St = fA/U_{\infty}$ (*f* is wingbeat frequency and *A* is the tip-to-tip vertical excursion of the wing tip). *St* is proportional to the ratio of the average wingbeat velocity to the steady forward speed and is an indication of the unsteadiness and efficiency of vortex generation.
25. For an incompressible fluid, the divergence in a planar velocity field is related to the change in out-of-plane flow velocity. When the divergence is positive, the fluid works as a fluid source in the planar velocity field, decreasing the out-of-plane velocity. When it is negative, it is a fluid sink, which increases the out-of-plane velocity.
26. E. V. Laitone, *Exp. Fluids* **23**, 405 (1997).
27. J. M. Birch, M. H. Dickinson, *Nature* **412**, 729 (2001).
28. J. M. Birch, W. B. Dickson, M. H. Dickinson, *J. Exp. Biol.* **207**, 1063 (2004).
29. J. D. Anderson, *Fundamentals of Aerodynamics* (McGraw-Hill, Singapore, 1991).
30. R. Bomphrey, N. Lawson, G. Taylor, A. Thomas, *Exp. Fluids* **40**, 546 (2006).
31. D. A. Read, F. S. Hover, M. S. Triantafyllou, *J. Fluids Struct.* **17**, 163 (2003).
32. S. M. Swartz, M. S. Groves, H. D. Kim, W. R. Walsh, *J. Zool.* **239**, 357 (1996).

33. We thank R. von Busse and Y. Winter for their support. This work was supported by grants from the Swedish Research Council, the Swedish Foundation for International Cooperation in Research and Higher Education, the Knut and Alice Wallenberg Foundation, the Crafoord Foundation, the Magnus Bergvall Foundation, and the Royal Physiographical Society.

Supporting Online Material

www.sciencemag.org/cgi/content/full/319/5867/1250/DC1
Materials and Methods
Figs. S1 to S5
Table S1
References and Notes

15 November 2007; accepted 17 January 2008
10.1126/science.1153019

Synaptic Protein Degradation Underlies Destabilization of Retrieved Fear Memory

Sue-Hyun Lee, Jun-Hyeok Choi, Nuribalhae Lee, Hye-Ryeon Lee, Jae-Ick Kim, Nam-Kyung Yu, Sun-Lim Choi, Seung-Hee Lee, Hyoung Kim, Bong-Kiun Kaang*

Reactivated memory undergoes a rebuilding process that depends on de novo protein synthesis. This suggests that retrieval is dynamic and serves to incorporate new information into preexisting memories. However, little is known about whether or not protein degradation is involved in the reorganization of retrieved memory. We found that postsynaptic proteins were degraded in the hippocampus by polyubiquitination after retrieval of contextual fear memory. Moreover, the infusion of proteasome inhibitor into the CA1 region immediately after retrieval prevented anisomycin-induced memory impairment, as well as the extinction of fear memory. This suggests that ubiquitin- and proteasome-dependent protein degradation underlies destabilization processes after fear memory retrieval. It also provides strong evidence for the existence of reorganization processes whereby preexisting memory is disrupted by protein degradation, and updated memory is reconsolidated by protein synthesis.

Memory retrieval is a process of recalling a previously stored memory. Recently, memory retrieval has attracted much attention because it has been found that inhibition of protein synthesis before or immediately after memory retrieval impairs the previously consolidated memory (*1*–*4*). Retrieval of a consolidated memory thus returns the memory storage site to a labile state, after which new protein synthesis is required for stabilizing or reconsolidating the memory (*1*–*9*). This suggests that the retrieval of the consolidated memory is a dynamic and active process in which remodeling or reorganization of the already-formed memories occurs to incorporate new information (*2*, *3*, *6*).

Although it has attracted less attention than the gene transcription and protein synthesis model for long-lasting synaptic changes and memory stabilization, protein degradation is also critical for long-term memory (*10*–*16*). A major cellular mechanism controlling protein turnover is the ubiquitin and proteasome system, in which polyubiquitinated proteins are degraded by the multisubunit proteasome complex (*11*, *17*). A subunit of the 26*S* proteasome, S5a, which selectively binds to polyubiquitinated proteins, plays a critical role in protein degradation (*18*, *19*).

If retrieval stimuli trigger new protein synthesis for the remodeling of consolidated memory, protein degradation via the ubiquitin and proteasome system might be necessary because remodeling of synapses, which encode the memory, would be mediated by removal of existing proteins and by incorporation of new proteins (*11*). However, little is known about the protein degradation mechanism during the reorganization process after memory retrieval in vivo. We therefore investigated the involvement of the ubiquitin and proteasome system and the roles of protein degradation during the destabilization and restabilization process after fear memory retrieval.

We first performed a total protein polyubiquitination assay after fear memory retrieval

National Creative Research Initiative Center for Memory, Department of Biological Sciences, College of Natural Sciences, Seoul National University, San 56-1 Silim-dong, Gwanak-gu, Seoul 151-747, Korea.

*To whom correspondence should be addressed. E-mail: kaang@snu.ac.kr

(*20*). Polyubiquitinated proteins were purified by immobilized fusion proteins of S5a (*11*) from the crude synaptosomal membranes of the hippocampi, which were isolated after contextual fear memory retrieval (Fig. 1A). The polyubiquitinated protein expression levels found in the 15-min group and the 60-min group whose hippocampi were isolated 15 min and 60 min after the beginning time point of retrieval, respectively, increased remarkably, whereas the polyubiquitination level was little changed in the absence of retrieval (No R group) compared with "naïve" mice, which received only handling (Fig. 1B). Reconsolidation is not affected by a protein synthesis inhibitor when the retrieval duration is very short (up to 1 min of reexposure) (*2*). Thus, we examined the effect of retrieval duration on protein polyubiquitination. Anisomycin treatment after a 1-min reexposure did not affect the instances of conditioned freezing behavior after 24 hours (fig. S1, A and B). The amount of polyubiquitinated protein found in the 1-min reexposure group was comparable to that in the No R group and was significantly lower than that of the 5-min reexposure group (fig. S1, C and D). These findings indicate that protein polyubiquitination is increased specifically in response to a retrieval signal that induces protein synthesis–dependent reconsolidation.

We next asked which proteins are polyubiquitinated and degraded after fear memory retrieval in the hippocampus. It has been shown that neuronal activity induces the turnover and remodeling of several postsynaptic density (PSD) proteins that are critical for long-term potentiation (*11*, *21*). To examine whether proteins in PSD may be possible targets for degradation during retrieval, we performed immunoblot analyses with antibodies against three different PSD proteins: Shank, guanylate kinase–associated protein (GKAP), and PSD-95, by using glutathione *S*-transferase (GST) in complex with S5a (GST-S5a) in a pull-down assay. Polyubiquitinated Shank and GKAP, but not PSD-95, increased remarkably 1 hour after retrieval (Fig. 2, A and B). In the mouse hippocampus, multiple Shank bands, which indicate the products of alternative splicing with diverse sizes ranging from 120 kD to 240 kD, were observed as previously described in the rat cortex (*22*) (fig. S2). It was noteworthy that the amount of 130 kD and 160 kD endogenous Shank was decreased 1 to 2 hours after retrieval in the synaptic region (Fig. 2, C to E). This decrease may reflect the ubiquitin- and proteasome-dependent degradation process, as the time course of the increase of Shank polyubiquitination almost coincided with the time course of the reduction of the amount of endogenous Shank (Fig. 2). To elucidate this point more clearly, we infused either the proteasome inhibitor clasto-lactacystin-β-lactone (βlac) or vehicle into area CA1. We found that βlac infusion blocked the decrease of the amount of Shank at 2 hours after retrieval and kept the Shank level up to the basal amount in control animals without retrieval (fig. S3). Thus, the dynamic change in the expression level of specific PSD proteins such as Shank (Fig. 2, C to E) implies the possibility that synaptic destabilizing and restabilizing states are triggered after the memory retrieval process, as previously suggested (*1*–*3*, *6*). Furthermore, the protein synthesis during the reconsolidation may be a compensatory mechanism for protein degradation induced by the retrieval.

The increase in polyubiquitinated proteins at the synapses during fear memory retrieval raises a question: What is the physiological function of protein degradation after memory retrieval? We bilaterally administered βlac or the protein synthesis blocker anisomycin into the CA1 region immediately after the 1st retrieval (Fig. 3, A and B; retrieval 1). The percentage of freezing behavior was not significantly different among groups on retrieval 1 before the drug infusion (fig. S4A). Then, we retested the fear level (freezing behavior) 24 hours after the infusion (Fig. 3B; retrieval 2). We did not observe any difference between the vehicle control and the βlac group, whereas we

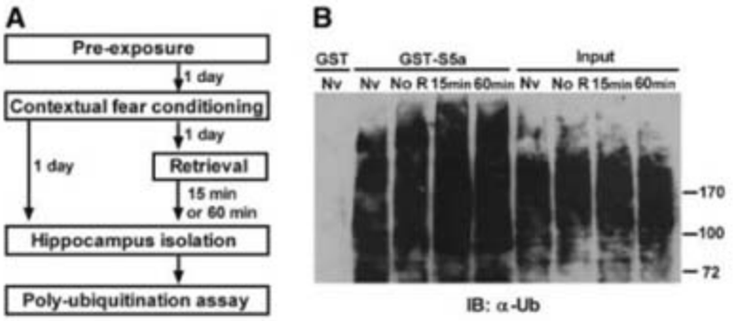

Fig. 1. Fear memory retrieval increases polyubiquitination in the hippocampal synaptosomal membrane fraction. (**A**) The schematic experimental procedure used for examining the level of polyubiquitination after retrieval. One day after contextual fear conditioning, mice were reexposed to the context to retrieve the fear memory. Then, 15 min or 60 min after retrieval, we isolated hippocampi and performed a polyubiquitination assay. (**B**) Representative data from the polyubiquitination assay show the total polyubiquitinated proteins that were pulled down by GST-S5a and detected by ubiquitin-specific antibody (α-Ub). The amount of polyubiquitination is increased 15 min and 60 min after retrieval when it is compared with the level in Nv (naïve, the mice group that received only handling) or No R (no retrieval, the mice from which hippocampi were isolated without retrieval). Polyubiquitinated proteins were not bound to GST alone. Input indicates an aliquot of total ubiquitinated proteins in each extract.

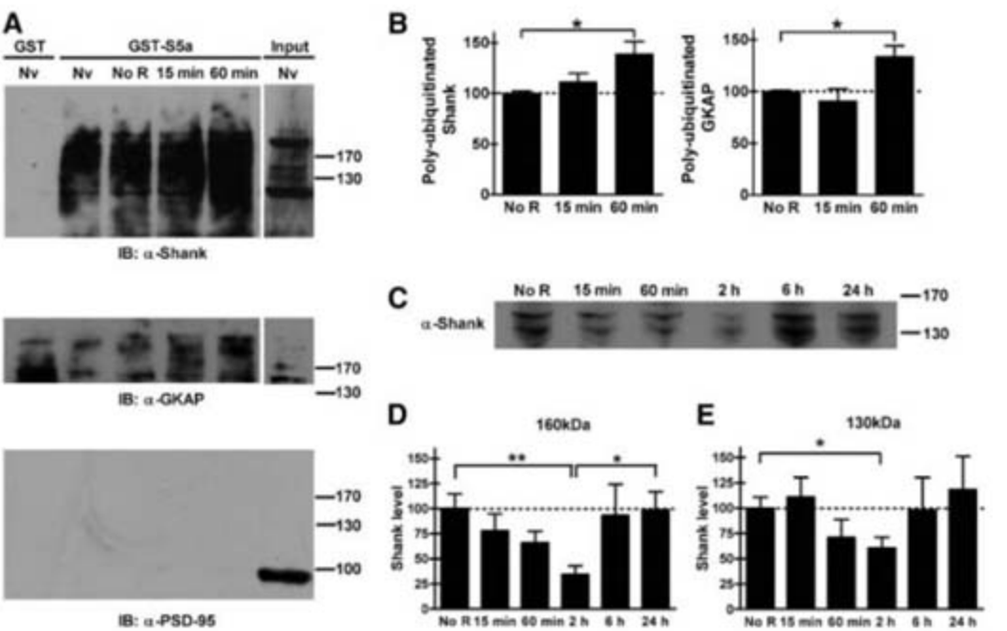

Fig. 2. Retrieval stimuli regulate the degradation of specific postsynaptic proteins. (**A** and **B**) Polyubiquitinated Shank and GKAP, but not PSD-95, are significantly increased 1 hour after retrieval. (A) Representative data show the level of Shank (top), GKAP (middle), and PSD-95 (bottom) in the isolated polyubiquitinated proteins from the hippocampal synaptosomal fraction. Polyubiquitinated proteins were isolated by the same experimental protocol as in Fig. 1. (B) Bars represent the means ± SEM of the percent change of polyubiquitinated Shank and GKAP proteins (*$P < 0.05$; unpaired *t* test; $n = 3$ for each group). (**C** to **E**) Dynamics of endogenous Shank protein after retrieval. (C) The protein expression level of Shank isoforms (160 kD, upper band; 130 kD, lower band) in the hippocampal synaptosomal membrane fraction was decreased up to 2 hours after retrieval, but it was restored to the basal level at 6 hours. (D and E) Bars represent the means ± SEM of the quantified level of Shank isoforms. Both Shank isoforms were significantly reduced at 2 hours after retrieval (*$P < 0.05$, **$P < 0.01$; unpaired *t* test; $n = 4$ for each group).

could observe fear memory impairment at retrieval 2 of the anisomycin group as reported previously (*1*, *2*) (Fig. 3, C and D). However, coinfusion of βlac with anisomycin prevented the memory impairment caused by the single infusion of anisomycin at retrieval 2 (Fig. 3, C and D). The increase in protein degradation may contribute to both the destabilization of preexisting fear memory and the restabilization of reorganized fear memory (*11*–*15*). Our data support the idea that protein degradation after memory retrieval is important for the destabilization of preexisting fear memory, rather than for the restabilization process. If the major function of protein degradation after retrieval was removal of inhibitory proteins for the memory restabilization, βlac infusion should have impaired the fear memory at retrieval 2 (*16*, *23*, *24*). However, the infusion of βlac alone did not affect the fear level. If the ubiquitin-proteasome pathway was involved in forgetting the preexisting fear memory, blocking the ubiquitin-proteasome pathway would have suppressed the anisomycin-induced impairment of fear memory retrieval by inhibiting the destruction of the preexisting fear memory (*8*). Consistent with this idea, we found that the coinfusion of βlac with anisomycin was able to prevent memory impairment caused by anisomycin after retrieval (Fig. 3, C and D). This indicates that βlac may inhibit the destruction process of the previously formed fear memory and may maintain the freezing behavior even when the reconsolidation is inhibited without new protein synthesis.

To further support this idea, we examined the effect of βlac infusion during fear memory acquisition (Fig. 4A). Because there is no preexisting fear memory at the initial phase of fear memory consolidation, the βlac infusion immediately after training may not bring about recovery from the anisomycin-induced amnesia. Consistent with this idea, we found that the infusion of βlac did not affect either anisomycin-induced memory impairment during memory acquisition or the memory acquisition itself (Fig. 4B), even though the polyubiquitinated protein level increased after fear conditioning (fig. S5). Combined with the data in Fig. 3, these results support the idea that the infusion of βlac mainly suppresses the destabilizing process of the preexisting fear memory and that protein synthesis in the hippocampus is required for the association of shock and context. The increase in polyubiquitination after conditioning may reflect the destabilization of preexisting synapses that were

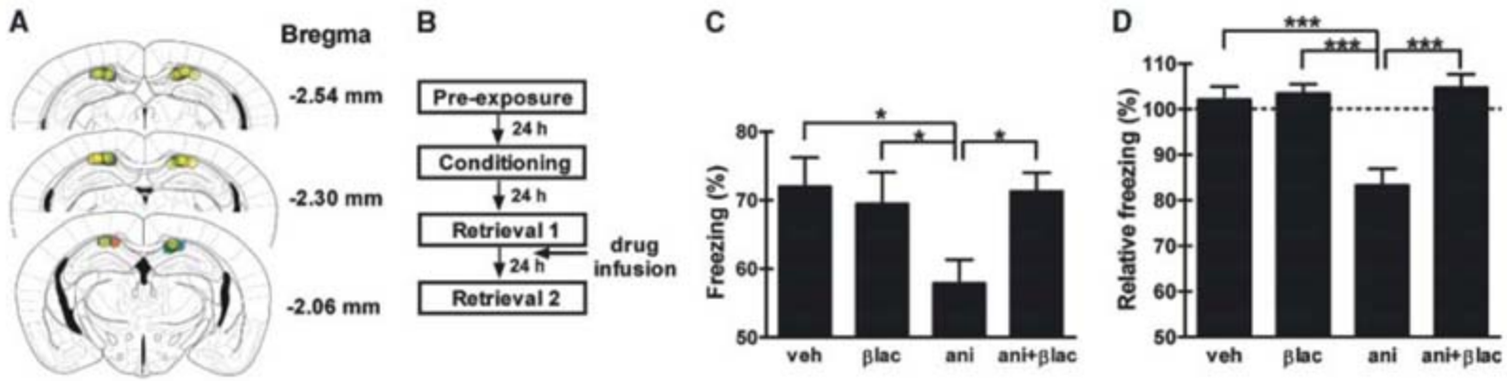

Fig. 3. Proteasome inhibitor blocks the anisomycin-induced memory impairment after retrieval. (**A**) Schematic illustration showing the cannula locations in the hippocampus at three different rostral-caudal planes. Numbers indicate the posterior direction from the bregma. Yellow circles, green squares, blue squares, and red circles indicate the infusion areas of vehicle, anisomycin, βlac, and anisomycin with βlac, respectively. (**B**) Schematic view of the experimental procedure used for evaluating the effect of βlac on the retrieval. (**C**) Bars represent the means ± SEM of the percentage of freezing behavior with respect to total number of scorings per mouse at retrieval 2. Compared with the vehicle-infused control group (veh, $n = 11$), βlac infusion (βlac, $n = 10$) alone had no effect on the fear memory retrieval, whereas the anisomycin-infused group (ani, $n = 14$) showed impaired fear memory retrieval. However, concurrent infusion of βlac with anisomycin (ani+βlac, $n = 10$) prevented the impairment of fear memory retrieval induced by anisomycin [$^*P < 0.05$; one-way analysis of variance (ANOVA) and Newman-Keuls multiple comparison test]. (**D**) Bars represent the means ± SEM of the relative freezing level of retrieval 2 [$(R_2/R_1) \times 100$ (%)]. Dotted line indicates the freezing level of retrieval 1. Significant reduction in the freezing level at the anisomycin-infused group was reversed by the coinfusion of βlac ($^{***}P < 0.001$; one-way ANOVA and Newman-Keuls multiple comparison test).

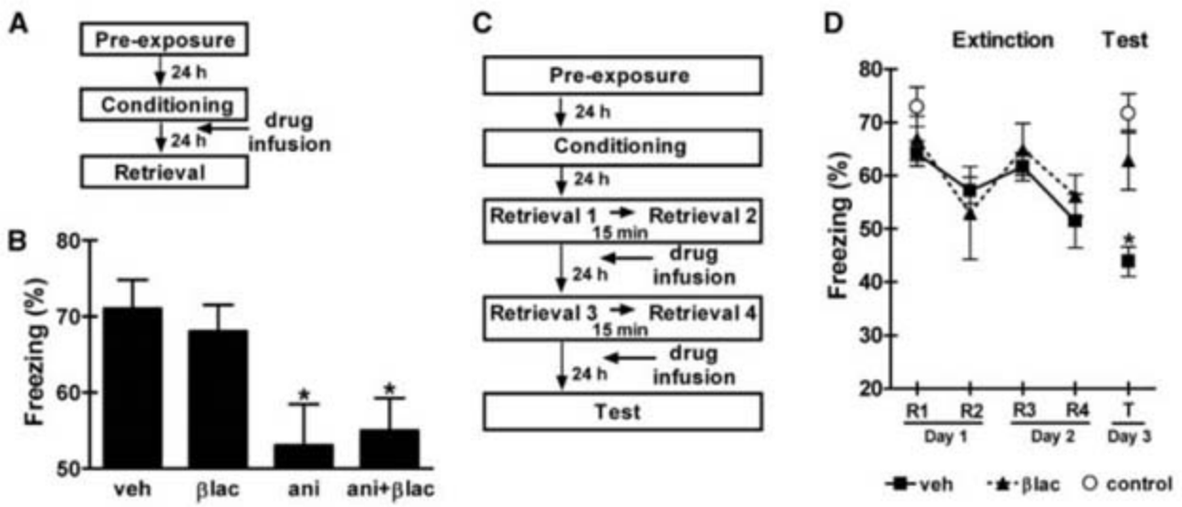

Fig. 4. Protein degradation is not required for memory consolidation, whereas it is critical for memory extinction. (**A**) Schematic view showing the protocol of behavioral experiments to examine the effect of βlac on acquiring fear memory. (**B**) Bars represent the means ± SEM of the freezing level at the retrieval day. Single infusion of βlac ($n = 12$) had no effect on the formation of fear memory compared with the vehicle-infused control group ($n = 11$), whereas the anisomycin-infused group ($n = 14$) showed significant impairment of the fear memory. Coinfusion of βlac with anisomycin ($n = 12$) also had no effect on the anisomycin-induced amnesia during memory acquisition ($^*P < 0.05$; one-way ANOVA and Newman-Keuls multiple comparison test). (**C**) Schematic view of the behavioral experiments performed to examine the effect of βlac on the fear memory extinction. (**D**) Fear memory extinction is impaired in the βlac-infused group ($n = 7$) compared with the vehicle-infused group (veh, $n = 7$). Control group ($n = 8$) indicates the vehicle-infused animals without extinction training ($^*P < 0.05$; one-way ANOVA and Newman-Keuls multiple comparison test).

related to the context or shock but did not encode the contextual fear memory.

If the retrieval induces the destabilization of the preexisting memory, it would also occur in the extinction, which is produced by repetitive retrievals in the absence of unconditioned stimuli. To test this idea, we performed the extinction training for 2 days, with two spaced retrievals per day (*25*). Either vehicle or βlac was infused immediately after the retrievals, and the freezing level was tested on the third day (Fig. 4C). It is noteworthy that βlac infusions into area CA1 suppressed the extinction of contextual fear memory (Fig. 4D and fig. S4B). The freezing behavior was significantly reduced by the extinction in the animals reexposed to the context with vehicle infusions, whereas control animals without context reexposure showed no extinction (Fig. 4D and fig. S4B). Thus, our data suggest that ubiquitin- and proteasome-dependent protein degradation is required for the memory extinction. This supports the idea that extinction is not only "inhibitory new learning" of a context–no shock association, but also involves at least some "unlearning" (or forgetting) of the preexisting context-shock association (*26*, *27*). Furthermore, extinction has been suggested to involve a memory-updating process (*27*). Combined, our results support the idea that memory retrieval makes preexisting memory labile via ubiquitin- and proteasome-dependent protein degradation in order to update or reorganize the memory with new information.

Our data also showed that infusion of βlac alone immediately after conditioning did not impair the acquisition of fear memory. This result disagrees with previous studies in some aspects (*14*, *28*). In these studies, the consolidation of inhibitory avoidance or contextual fear memory is impaired by disturbance of the ubiquitin and proteasome pathway. These discrepancies may reflect the differences in the experimental system, animal species, or brain regions involved (*29*). It is known that the circuits involved in the processing of an inhibitory avoidance task are somewhat different from the circuits of classical fear conditioning (*30*). Moreover, in contextual fear conditioning, three variables—reexposure duration, the age of the memory, and the strength of the memory—influence the memory processes activated during retrieval (*2*).

NMDA receptor activation triggers the destabilization of the consolidated fear memory (*8*). In cultured neurons, glutamatergic transmission activates the ubiquitin and proteasome system (*31*, *32*). It would be interesting to speculate that ubiquitin- and proteasome-dependent protein degradation is increased by downstream signaling of NMDA receptor activation and destabilizes the retrieved fear memory.

We have shown that ubiquitin- and proteasome-dependent degradation of preexisting postsynaptic proteins is involved in memory reorganization after retrieval. Our results support the idea that memory reorganization occurs via both degradation of preexisting synapses and synthesis of updated synapses. Preexisting memory may be rebuilt in conjunction with new information via the protein degradation and concurrent synthesis especially in the synaptic region.

References and Notes

1. K. Nader, G. E. Schafe, J. E. Le Doux, *Nature* **406**, 722 (2000).
2. A. Suzuki *et al.*, *J. Neurosci.* **24**, 4787 (2004).
3. M. H. Milekic, C. M. Alberini, *Neuron* **36**, 521 (2002).
4. P. W. Frankland *et al.*, *Learn. Mem.* **13**, 451 (2006).
5. C. M. Alberini, *Trends Neurosci.* **28**, 51 (2005).
6. R. G. Morris *et al.*, *Neuron* **50**, 479 (2006).
7. Y. Dudai, *Curr. Opin. Neurobiol.* **16**, 174 (2006).
8. C. Ben Mamou, K. Gamache, K. Nader, *Nat. Neurosci.* **9**, 1237 (2006).
9. M. Eisenberg, T. Kobilo, D. E. Berman, Y. Dudai, *Science* **301**, 1102 (2003).
10. O. Steward, E. M. Schuman, *Annu. Rev. Neurosci.* **24**, 299 (2001).
11. M. D. Ehlers, *Nat. Neurosci.* **6**, 231 (2003).
12. A. N. Hegde *et al.*, *Cell* **89**, 115 (1997).
13. A. N. Hegde, A. L. Goldberg, J. H. Schwartz, *Proc. Natl. Acad. Sci. U.S.A.* **90**, 7436 (1993).
14. M. Lopez-Salon *et al.*, *Eur. J. Neurosci.* **14**, 1820 (2001).
15. R. Fonseca, R. M. Vabulas, F. U. Hartl, T. Bonhoeffer, U. V. Nagerl, *Neuron* **52**, 239 (2006).
16. E. R. Kandel, *Science* **294**, 1030 (2001).
17. A. Ciechanover, *Nat. Rev. Mol. Cell Biol.* **6**, 79 (2005).
18. Q. Deveraux, V. Ustrell, C. Pickart, M. Rechsteiner, *J. Biol. Chem.* **269**, 7059 (1994).
19. K. Ferrell, Q. Deveraux, S. van Nocker, M. Rechsteiner, *FEBS Lett.* **381**, 143 (1996).
20. Materials and methods are available as supporting material on *Science* Online.
21. C. Luscher, R. A. Nicoll, R. C. Malenka, D. Muller, *Nat. Neurosci.* **3**, 545 (2000).
22. S. Lim *et al.*, *J. Biol. Chem.* **274**, 29510 (1999).
23. J. A. Lee *et al.*, *J. Cell Biol.* **174**, 827 (2006).
24. T. Abel, K. C. Martin, D. Bartsch, E. R. Kandel, *Science* **279**, 338 (1998).
25. K. M. Lattal, T. Abel, *J. Neurosci.* **21**, 5773 (2001).
26. K. M. Myers, M. Davis, *Neuron* **36**, 567 (2002).
27. J. Ji, S. Maren, *Hippocampus* **17**, 749 (2007).
28. Y. H. Jiang *et al.*, *Neuron* **21**, 799 (1998).
29. S. J. Martin, P. D. Grimwood, R. G. Morris, *Annu. Rev. Neurosci.* **23**, 649 (2000).
30. A. E. Wilensky, G. E. Schafe, J. E. LeDoux, *J. Neurosci.* **20**, 7059 (2000).
31. B. Bingol, E. M. Schuman, *Nature* **441**, 1144 (2006).
32. L. Guo, Y. Wang, *Neuroscience* **145**, 100 (2007).

33. We thank E. Kandel, A. Silva, P. Frankland, S. Josselyn, and Y.-S. Lee for reading the manuscript and critical discussion. We are grateful to lab members for their technical help. We also thank E. Kim for providing Shank antibody. This work was supported by the Creative Research Initiative Program of the Korean Ministry of Science and Technology (to B.-K.K.).

Supporting Online Material

www.sciencemag.org/cgi/content/full/1150541/DC1
Materials and Methods
Figs. S1 to S5
References

14 September 2007; accepted 11 January 2008
Published online 7 February 2008;
10.1126/science.1150541
Include this information when citing this paper.

Hybrid Neurons in a MicroRNA Mutant Are Putative Evolutionary Intermediates in Insect CO_2 Sensory Systems

Pelin Cayirlioglu,[1]* Ilona Grunwald Kadow,[1]*† Xiaoli Zhan,[1] Katsutomo Okamura,[2] Greg S. B. Suh,[3]‡ Dorian Gunning,[1] Eric C. Lai,[2] S. Lawrence Zipursky[1]§

Carbon dioxide (CO_2) elicits different olfactory behaviors across species. In *Drosophila*, neurons that detect CO_2 are located in the antenna, form connections in a ventral glomerulus in the antennal lobe, and mediate avoidance. By contrast, in the mosquito these neurons are in the maxillary palps (MPs), connect to medial sites, and promote attraction. We found in *Drosophila* that loss of a microRNA, *miR-279*, leads to formation of CO_2 neurons in the MPs. *miR-279* acts through down-regulation of the transcription factor Nerfin-1. The ectopic neurons are hybrid cells. They express CO_2 receptors and form connections characteristic of CO_2 neurons, while exhibiting wiring and receptor characteristics of MP olfactory receptor neurons (ORNs). We propose that this hybrid ORN reveals a cellular intermediate in the evolution of species-specific behaviors elicited by CO_2.

In insects, both the position of CO_2 neurons and the behavior elicited by CO_2 differ among species. For example, olfactory detection of CO_2 through neurons positioned in or around the mouthparts of an insect, such as maxillary palps (MPs) and labial palps, correlates with feeding-related behaviors. Indeed, in some blood-feeding insects such as mosquitoes and tsetse flies, these neurons are harbored in the MPs and are important in locating hosts via plumes of CO_2 that they emit (*1*–*3*). The hawkmoth, *Manduca sexta*, monitors nectar profitability of newly opened *Datura wrightii* flowers through CO_2 receptor neurons located in their labial palps (*4*, *5*). In these examples, CO_2 acts as an attractant. Conversely, in *Drosophila* CO_2 is a component of a stress-induced odor that triggers avoidance behavior (*6*). This repellent response is driven by antennal neurons expressing the CO_2 receptor complex Gr21a-Gr63a (*7*, *8*). How did these diverse behavioral responses to CO_2 arise during insect evolution? We propose that this diversity emerged through multiple steps, including changes in cellular position (arising from elimination of CO_2 neurons in one appendage and generation of these neurons in another) and changes in circuitry.

In the course of a genetic screen for mutants disrupting the organization of the olfactory system, we isolated a mutant (*S0962-07*) that resulted in the formation of ectopic Gr21a-expressing neurons in the MPs (Fig. 1A). Some 22 ± 1.5 (mean ± SEM) green fluorescent protein (GFP)–positive cells were observed in the mutant MP, whereas the number of antennal Gr21a olfactory receptor neurons (ORNs) was unaffected (Fig. 1B). In the wild type, Gr21a cell bodies were restricted to the antenna (Fig. 1A). The ectopic MP cells expressed both CO_2 receptors (Gr21a and Gr63a) (Fig. 1C). Consistent with this finding, mutant cells conferred CO_2 sensitivity to the MP (Fig. 1D). Staining the MP with an antibody to the pan-neuronal marker Elav revealed an increase of 21 ± 3.4 neurons in the mutant, which suggests that all ectopic neurons expressed Gr21a (fig. S1).

In wild-type MPs, each sensillum contains two ORNs. By contrast, in the mutant MP sensilla, additional neurons expressing Elav and the general receptor Or83b were observed (Fig. 1E and fig. S1). This was also apparent when a MP ORN marker (MPS-GAL4) expressed in a subset of MP ORNs was used (Fig. 1E) (*9*). This marker labels single cells within a subset of wild-type MP sensilla (Fig. 1E, arrows); however, in mutant MPs, two additional neurons were observed (Fig. 1E, arrowheads), bringing the total number of neurons within these sensilla to four. Thus, the generation of ectopic Gr21a-Gr63a neurons is due to an increase in the number of neurons within sensilla rather than transformation of MP ORNs (fig. S1).

In the wild type, each class of adult ORNs sends projections from both antennae or MPs to the antennal lobe (AL). ORNs expressing same odorant receptors (ORs) typically form synapses in the same glomerulus within the AL (fig. S2) (*10*). CO_2 neurons in the antenna target the V-glomerulus (Fig. 1F). To specifically assess the targeting of ectopic MP CO_2 neurons, we examined flies where the antennae were surgically removed (Fig. 1F). We found that ectopic CO_2 neurons targeted the V-glomerulus and other medial sites in the AL (Fig. 1F; see also below). The wiring specificity of antennal CO_2 neurons in the mutants was identical to that in the wild type (Fig. 1F). Thus, the ectopic CO_2 neurons in the MP target, at least in part, the same glomerulus innervated by the wild-type CO_2 neurons in the antennae.

We mapped *S0962-07* to a P-element insertion some 1 kb upstream of a microRNA, *miR-279* (fig. S3). MicroRNAs (miRNAs) are small noncoding RNAs of about 22 nucleotides that bind to specific sequences of the 3′-untranslated region (3′UTR) of target genes and thereby repress gene expression posttranscriptionally. In recent years, miRNAs were implied in a variety of functions in the nervous system of different organisms (*11*). To assess whether *miR-279* is responsible for the observed phenotype, we generated three small deletions that uncovered the *miR-279* genomic region (fig. S3). These deletion mutants exhibited phenotypes indistinguishable from *S0962-07* (fig. S3). The ectopic CO_2 phenotype was rescued by a 3-kb fragment of genomic DNA encoding only *miR-279* (fig. S3) (*9*). Thus, *miR-279* is the gene disrupted in *S0962-07* and must repress targets in the MP to inhibit ectopic CO_2 neuron development.

To assess whether *miR-279* is expressed in the developing MPs, we generated transgenic

[1]Department of Biological Chemistry, Howard Hughes Medical Institute, David Geffen School of Medicine, University of California, Los Angeles, CA 90095, USA. [2]Sloan-Kettering Institute, 521 Rockefeller Research Labs, 1275 York Avenue, Box 252, New York, NY 10021, USA. [3]Division of Biology 216-76, California Institute of Technology, Pasadena, CA 91125, USA.

*These authors contributed equally to this work.
†Present address: Department of Molecular Neurobiology, Max Planck Institute of Neurobiology, Am Klopferspitz 18, 82152 Martinsried, Germany.
‡Present address: Molecular Neurobiology Program, Skirball Institute, Department of Cell Biology, New York University School of Medicine, New York, NY 10016, USA.
§To whom correspondence should be addressed. E-mail: lzipursky@mednet.ucla.edu

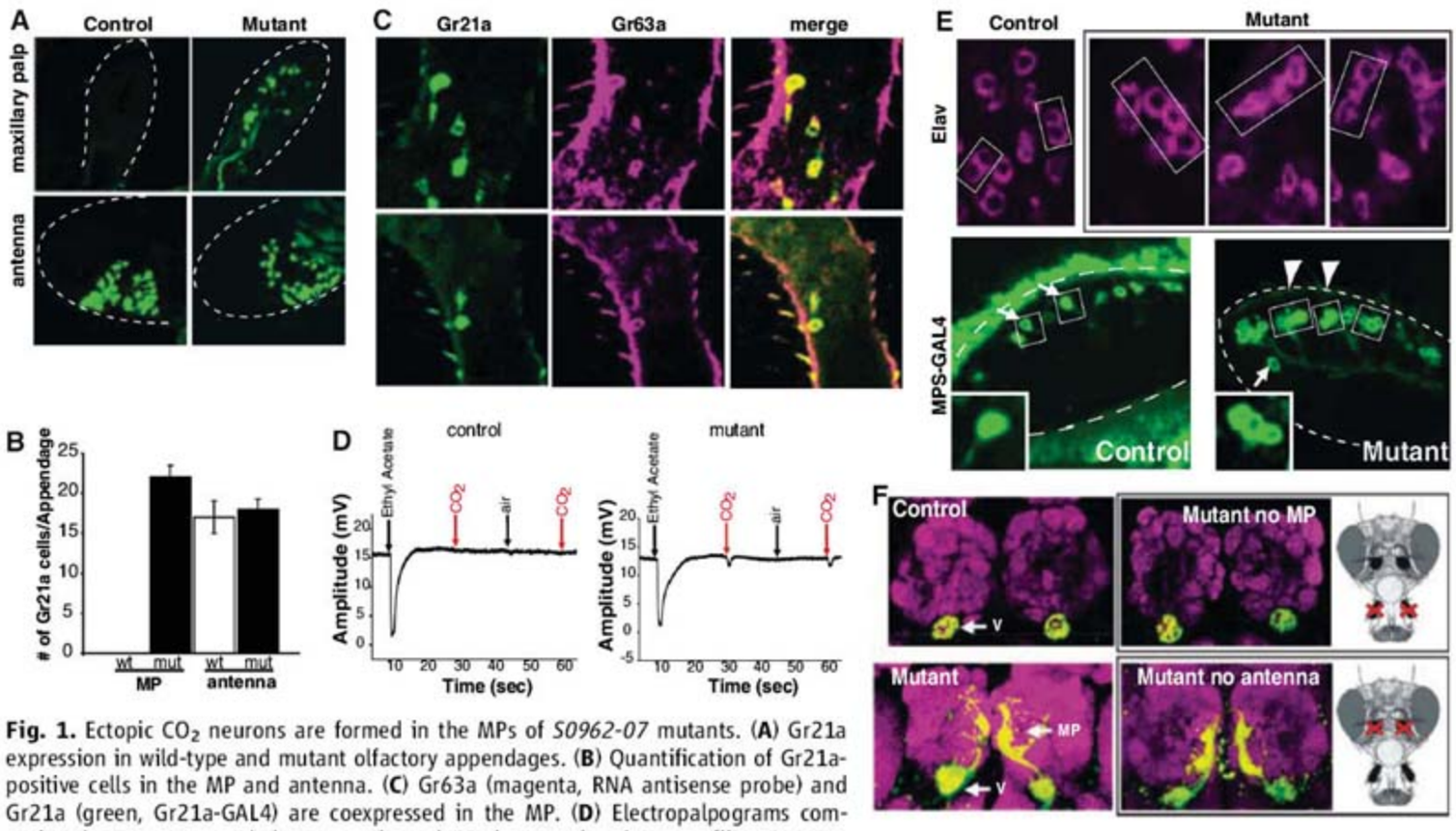

Fig. 1. Ectopic CO_2 neurons are formed in the MPs of *S0962-07* mutants. (**A**) Gr21a expression in wild-type and mutant olfactory appendages. (**B**) Quantification of Gr21a-positive cells in the MP and antenna. (**C**) Gr63a (magenta, RNA antisense probe) and Gr21a (green, Gr21a-GAL4) are coexpressed in the MP. (**D**) Electropalpograms comparing the response to ethyl acetate, air, and CO_2 in control and mutant flies. Contrary to lack of response from the control palps, 5 of 12 mutant MPs responded to CO_2 (*9*). MPs recorded: $n = 12$ (control), $n = 12$ (mutant), $P = 0.016$. (**E**) Single confocal sections of MPs labeled with antibody to Elav (magenta) at 60 to 80 hours APF or with MPS-GAL4 and UAS-mCD8GFP (green) at 80 hours APF. Two neurons (Elav) or single ORNs (MPS-GAL4) are labeled in wild-type MP sensilla (arrows). Two additional neurons are observed in a subset of mutant sensilla (arrowheads and inset). (**F**) Mutant neurons in the MP target the V and medial glomeruli. Mutant flies without MP (upper right) and without antenna (lower right). Magenta, anti-NC82. In (A) and (E), dashed lines outline MPs.

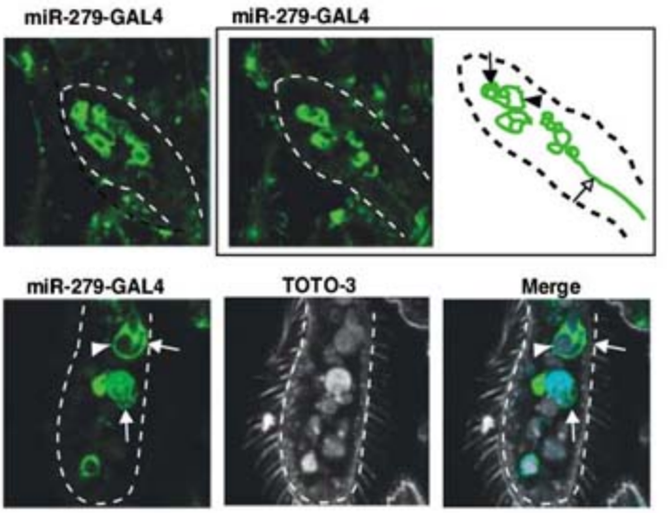

Fig. 2. *miR-279* is expressed in precursor cells in the developing MP. Expression of *miR-279* was visualized with miR-279-GAL4 and UAS-CD8GFP (green). The arrowhead and arrow in both the schematic and the image panels point to a big cell and a cluster of small cells, respectively. The open arrow in the schematic points to a nerve fiber from one of the cell clusters. Nuclear counterstain TOTO-3 is used in the bottom panels. Dashed lines outline the developing MPs.

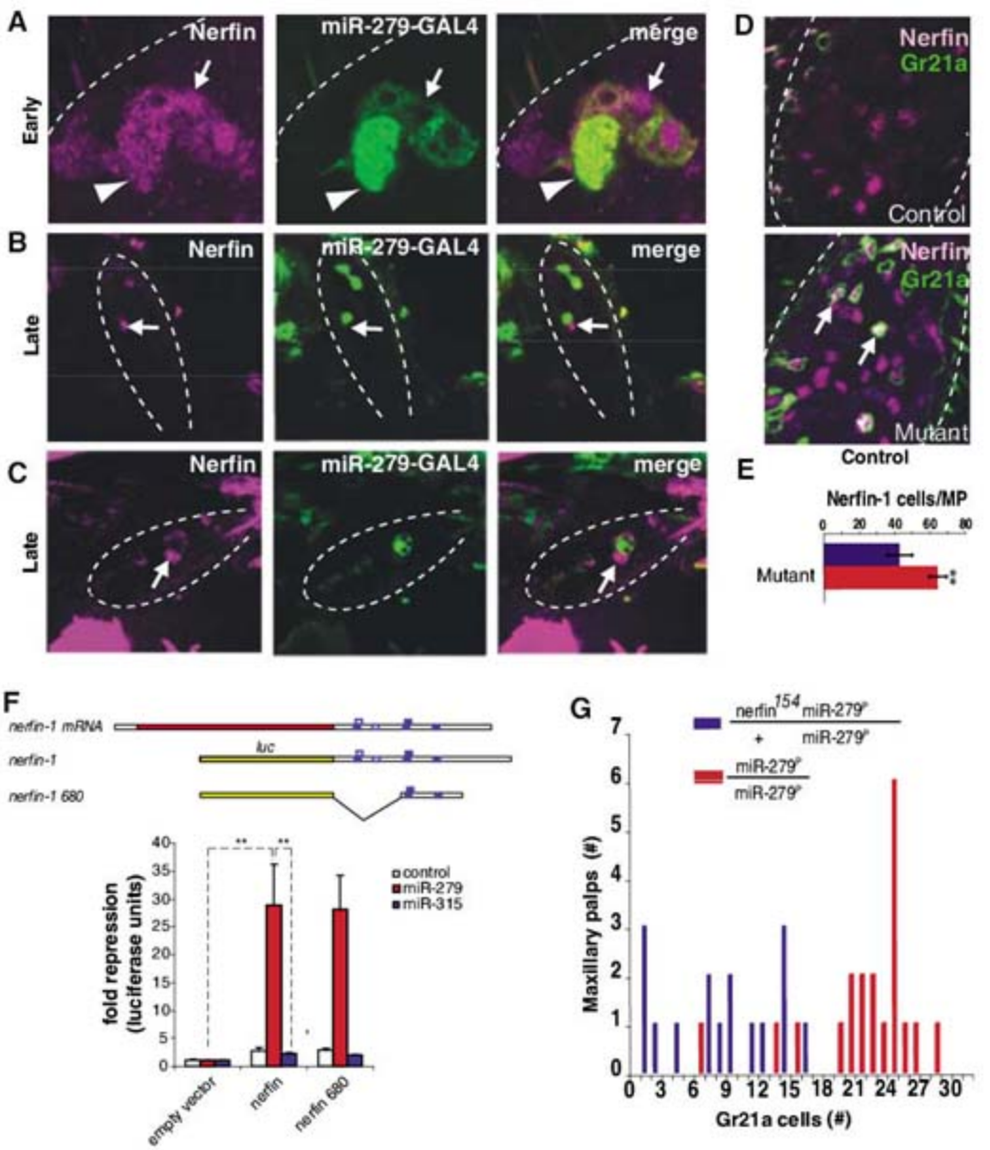

Fig. 3. Nerfin-1 is a target of *miR-279*. (**A** to **C**) Expression pattern of Nerfin-1 (magenta) and *miR-279* (green, see Fig. 2) in developing MPs at early (A) and later [(B) and (C)] stages. (**D**) Nerfin-1 (magenta) is expressed in ectopic CO_2 neurons (green) in the mutant MPs (arrows). (**E**) Quantification of Nerfin-1–positive nuclei in wild-type and mutant MPs at 60 to 80 hours APF. MPs scored: wild type, $n = 7$; mutant $n = 9$; $^{**}P < 0.001$. (**F**) *miR-279* inhibits *nerfin-1* expression in cultured *Drosophila* S2 cell lines ($^{**}P < 0.001$). (**G**) *nerfin-1* is a dominant suppressor of *miR-279* ($P < 0.001$).

flies carrying a transcriptional reporter construct (miR-279-GAL4). Expression was monitored in flies carrying this GAL4 construct and the reporter UAS-mCD8GFP (Fig. 2 and fig. S4). Around 40 to 50 hours after puparium formation (APF), large cells reminiscent of sensory organ precursors in other epithelia expressed *miR-279* (Fig. 2 and fig. S4). At later stages, miR-279–expressing cells were found in clusters with smaller cells, some of which expressed neuronal markers (fig. S4). As ORNs matured, *miR-279* expression was lost (fig. S4).

We next sought to identify the target gene(s) responsible for the *miR-279* mutant phenotype. About 205 potential target mRNAs of *miR-279* were previously predicted (*12*, *13*). One of the strongest candidates for *miR-279* regulation is Nerfin-1. The Nerfin-1 3′UTR contains multiple *miR-279* binding sites (Fig. 3F) and encodes a transcription factor expressed in neuronal precursors and transiently in nascent neurons in the embryonic central nervous system (*14*). Nerfin-1 protein appeared in *miR-279*–positive cells between 50 and 60 hours APF (Fig. 3A). Nerfin-1 and *miR-279* gradually redistributed, generating complementary expression patterns. Cells with high levels of Nerfin-1 expressed low levels of *miR-279* and vice versa (Fig. 3, B and C, and fig. S5).

To test whether Nerfin-1 is up-regulated in *miR-279* mutants, we stained mutant MPs with antibodies to Nerfin-1. We found 22 ± 4.8 additional Nerfin-1–expressing cells in *miR-279* mutant MPs relative to controls (Fig. 3E). This is similar to the number of ectopic CO_2 neurons in the MP (Fig. 1B). The vast majority of CO_2 ORNs in the MP expressed Nerfin-1 (Fig. 3D and fig. S5). Thus, the expression pattern of Nerfin-1 protein in the wild type and in mutant MPs is consistent with *nerfin-1* mRNA being a target for *miR-279* in vivo.

To determine whether *miR-279* directly binds to *nerfin-1* 3′UTR and inhibits its expression, we used a luciferase reporter assay in cultured cells. The luciferase-coding region was fused to the full-length *nerfin-1* 3′UTR, which contains four conserved 8-nucleotide oligomer target sites for *miR-279* (*15*), as well as to a subregion containing three of these sites (Fig. 3F). Luciferase activity of both *nerfin-1* sensor constructs was strongly repressed when cells were cotransfected with *miR-279* (Fig. 3F). By contrast, the activity of either *nerfin-1* sensor was unaffected by noncognate *miR-315*. Antisense oligomers directed against the *miR-279* core sequence specifically relieved *nerfin-1* reporter repression (fig. S6). Thus, we conclude that *nerfin-1* is a direct target of *miR-279*.

We next assessed whether Nerfin-1 down-regulation by *miR-279* inhibits the development of CO_2 neurons in the MPs. To do this, we reduced the level of *nerfin-1* by half genetically in a *miR-279* mutant background. This decreased the number of CO_2 neurons in the MP relative to *miR-279* mutants (Fig. 3G), providing strong in

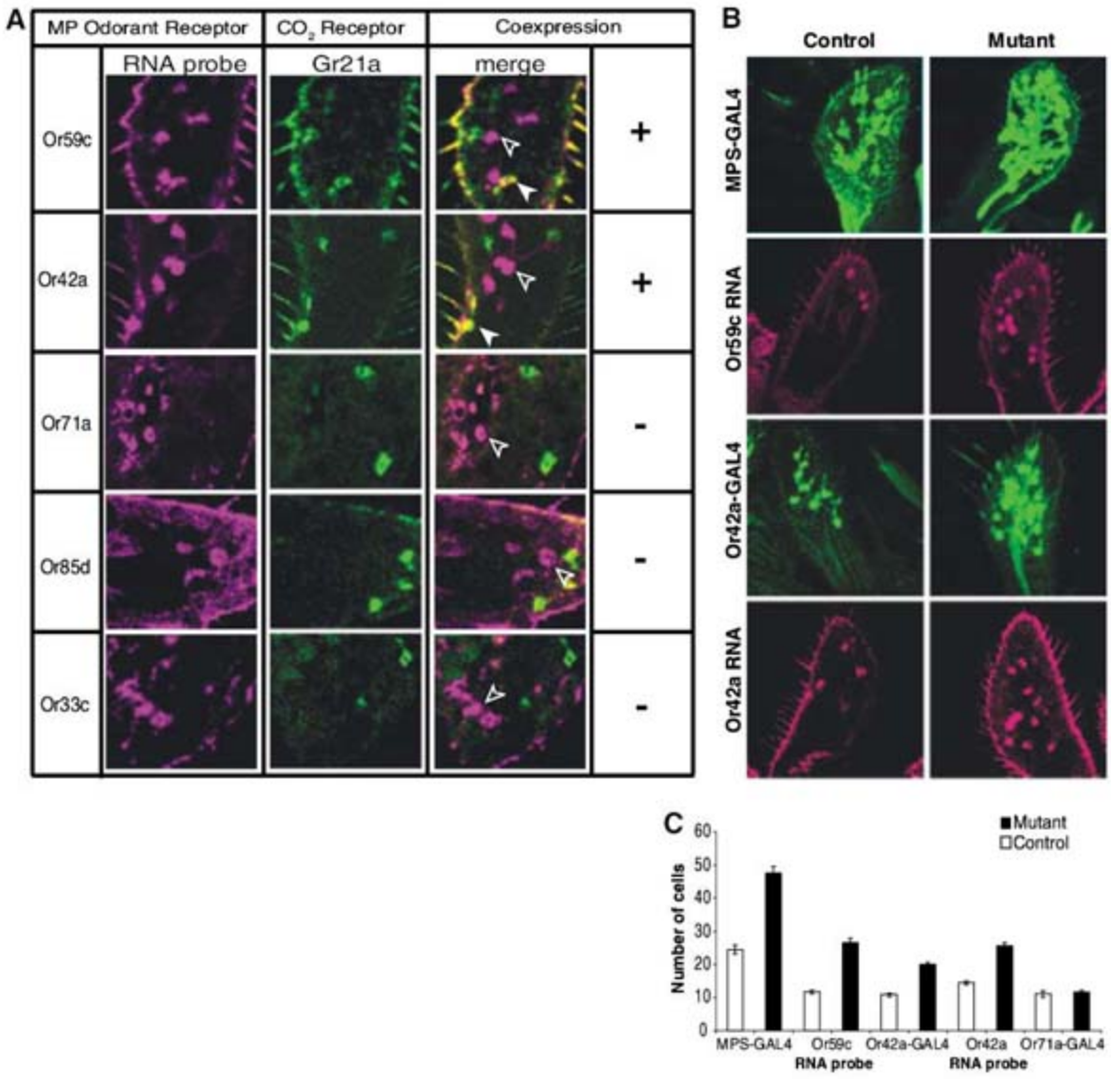

Fig. 4. Ectopic neurons exhibit mixed sensory identity. (**A**) MPs of mutant flies labeled with RNA antisense probes (magenta) and with Gr21a-GAL4 and UAS-mCD8GFP (green). Or59c and Or42a transcript (magenta) overlaps partly with Gr21a-expressing cells (green, solid arrowhead). Cells only positive for Or59c or Or42a are labeled only in magenta (open arrowhead). (**B** and **C**) MPs of mutant flies contain more Or42a- and Or59c-expressing cells. (B) Labeling of MP ORNs with GAL4 reporter constructs (Or42a-GAL4 and MPS-GAL4) or Or59c or Or42a RNA probe. (C) Quantification of the data from (B). Total increase in the number of cells in mutants using MPS-GAL4 driver corresponds to the number of ectopic CO_2 neurons (see Fig. 1B).

vivo evidence that *miR-279* is necessary to down-regulate Nerfin-1 in MPs during normal development. Nerfin-1 up-regulation alone was not sufficient to generate a miR-279–like phenotype (fig. S7). Taken together, these findings suggest that *miR-279* down-regulates Nerfin-1 and other targets to prevent CO_2 neuron development in the MPs.

When analyzing the axonal projections of the CO_2 neurons in the MPs, we observed that these neurons targeted one or more medial glomeruli in addition to the V-glomerulus, the target of antennal CO_2 neurons (Fig. 1F and fig. S2). These medial glomeruli are normally innervated by MP Or42a and Or59c ORNs. Double-labeling experiments revealed that mutant neurons also coexpressed Or42a and Or59c, but not other MP ORs (Fig. 4A). Analysis of subsets of MP ORNs also revealed that Or42a and Or59c classes each showed an approximate increase of 10 cells in the MPs, whereas others were unaffected (Fig. 4, B and C). These results indicate that the ectopic CO_2 neurons are formed as additional cells within Or42a and Or59c sensilla and are hybrid in identity. They express ORs and exhibit wiring characteristics of two classes of neurons.

It is interesting that the loss of *miR-279* generates a CO_2 neuron within a sensillum harboring four neurons in the MP (Fig. 1E and fig. S1), given that the antennal CO_2 sensilla in *Drosophila* are the only sensilla in the olfactory system to harbor four ORNs (*16*). Because *miR-279* acts within the precursor cells in the MP to prevent Nerfin-dependent formation of olfactory neurons, this observation raises the intriguing possibility that positioning of CO_2 neurons on different olfactory appendages might have evolved through changes at the level of precursor cell development. Thus, the evolutionary elimination of CO_2 neurons from MP sensilla might have required decreasing the number of cells with neuronal identities through down-regulation of Nerfin-1 by *miR-279*.

Although we hypothesize that relocation of CO_2 ORNs to different appendages was important in the evolution of differences in CO_2 sensing, additional mechanisms must have evolved to modify the neural circuitry to alter species-specific behaviors in response to CO_2. The ectopic CO_2 neurons are hybrid cells, which express additional receptors (Or59c or Or42a) and also target medial glomeruli, typically innervated by wild-type ORNs expressing these ORs. This is particularly interesting given that CO_2 neurons in mosquitoes connect to medial glomeruli, driving an attractive response (*17*–*19*). We speculate that this hybrid cell represents an evolutionary intermediate on a path leading to species-specific CO_2 behavior (*20*). Perhaps suppressing the expression of Or59c or Or42a ORs could convert this hybrid cell to one dedicated only to CO_2 reception. The nature of the behavioral output to CO_2 (i.e., attraction versus repulsion) by this cell, however, may be dictated by altering the wiring specificity to one site or the other (medial versus ventral, respectively). More generally, we propose that natural selection can work on such an evolutionary intermediate to generate different combinations of OR, wiring, and cellular positional specificities, depending on the insects' environmental needs. This may in turn lead to novel olfactory responses to different odorants, or to the same odorant in different species.

References and Notes

1. F. E. Kellogg, *J. Insect Physiol.* **16**, 99 (1970).
2. A. J. Grant, R. J. O'Connell, *Ciba Found. Symp.* **200**, 233 (1996).
3. F. Bogner, *Physiol. Entomol.* **17**, 1992 (1992).
4. C. Thom, P. G. Guerenstein, W. L. Mechaber, J. G. Hildebrand, *J. Chem. Ecol.* **30**, 1285 (2004).
5. F. Bogner, M. Boppre, K. D. Ernst, J. Boeckh, *J. Comp. Physiol. A* **158**, 741 (1986).
6. G. S. Suh *et al.*, *Nature* **431**, 854 (2004).
7. W. D. Jones, P. Cayirlioglu, I. G. Kadow, L. B. Vosshall, *Nature* **445**, 86 (2007).

8. J. Y. Kwon, A. Dahanukar, L. A. Weiss, J. R. Carlson, *Proc. Natl. Acad. Sci. U.S.A.* **104**, 3574 (2007).
9. See supporting material on *Science* Online.
10. L. B. Vosshall, *Curr. Opin. Neurobiol.* **10**, 498 (2000).
11. K. S. Kosik, A. M. Krichevsky, *Neuron* **47**, 779 (2005).
12. A. Stark, J. Brennecke, R. B. Russell, S. M. Cohen, *PLoS Biol.* **1**, e60 (2003).
13. D. Grun, Y. L. Wang, D. Langenberger, K. C. Gunsalus, N. Rajewsky, *PLoS Comput. Biol.* **1**, e13 (2005).
14. A. Kuzin, T. Brody, A. W. Moore, W. F. Odenwald, *Dev. Biol.* **277**, 347 (2005).
15. B. P. Lewis, C. B. Burge, D. P. Bartel, *Cell* **120**, 15 (2005).
16. A. Couto, M. Alenius, B. J. Dickson, *Curr. Biol.* **15**, 1535 (2005).
17. S. Anton *et al.*, *Arthropod Struct. Dev.* **32**, 319 (2003).
18. P. Distler, J. Boeckh, *J. Exp. Biol.* **200**, 1873 (1997).
19. R. Ignell, T. Dekker, M. Ghaninia, B. S. Hansson, *J. Comp. Neurol.* **493**, 207 (2005).
20. F. J. Poelwijk, D. J. Kiviet, D. M. Weinreich, S. J. Tans, *Nature* **445**, 383 (2007).
21. We thank L. Vosshall, B. Dickson, W. Odenwald, R. Klein, G. Tavosanis, J. Carlson, and D. Anderson for providing reagents and comments on experiments; W. Tom, A. Lorenze, and P. Alcala for technical assistance; A. Acker-Palmer, T. Suzuki, G. Tavosanis, R. Klein, and members of the laboratories for comments on the manuscript; A. Luke for helping with *miR-279* deletions; and Y.-T. Chou for cloning the luciferase sensors. Supported by the Jane Coffin Childs Memorial Fund and a National Research Service Award (P.C.); EMBO and the Human Frontiers Science Program (I.G.K.); the Leukemia and Lymphoma Foundation, the Burroughs Wellcome Foundation, and the V-Foundation for Cancer Research (E.C.L.); and NIH grant DC006485 (S.L.Z.). G.S.B.S. is an HHMI Associate; S.L.Z. is an HHMI Investigator.

Supporting Online Material

www.sciencemag.org/cgi/content/full/319/5867/1256/DC1
Materials and Methods
Figs. S1 to S7
References

20 August 2007; accepted 17 January 2008
10.1126/science.1149483

Transgenic Inhibition of Synaptic Transmission Reveals Role of CA3 Output in Hippocampal Learning

Toshiaki Nakashiba, Jennie Z. Young, Thomas J. McHugh, Derek L. Buhl, Susumu Tonegawa*

The hippocampus is an area of the brain involved in learning and memory. It contains parallel excitatory pathways referred to as the trisynaptic pathway (which carries information as follows: entorhinal cortex → dentate gyrus → CA3 → CA1 → entorhinal cortex) and the monosynaptic pathway (entorhinal cortex → CA1 → entorhinal cortex). We developed a generally applicable tetanus toxin–based method for transgenic mice that permits inducible and reversible inhibition of synaptic transmission and applied it to the trisynaptic pathway while preserving transmission in the monosynaptic pathway. We found that synaptic output from CA3 in the trisynaptic pathway is dispensable and the short monosynaptic pathway is sufficient for incremental spatial learning. In contrast, the full trisynaptic pathway containing CA3 is required for rapid one-trial contextual learning, for pattern completion–based memory recall, and for spatial tuning of CA1 cells.

The medial temporal lobes of the brain, including the hippocampus, are crucial for learning and memory of events and space across species (*1*–*3*). The hippocampus receives input from virtually all associative areas of the neocortex via the entorhinal cortex (EC). In the main excitatory hippocampal network (Fig. 1A), information flows from the superficial layer (layer II) of the EC to the dentate gyrus (DG) to CA3 to CA1 and finally to the deep layers of EC directly or indirectly through the subiculum. This loop is referred to as the trisynaptic pathway (TSP). The hippocampus also contains a parallel excitatory monosynaptic pathway (MSP) [EC (layer III) → CA1 → EC (layer V)] as well as other excitatory and inhibitory circuits.

The prevailing view of the contribution of these circuits to hippocampal function (*4*–*7*) is that synaptic transmission and plasticity in the feed-forward pathway from EC → DG → CA3, a part of the TSP, are primarily responsible for pattern separation, whereas those in a recurrent network within CA3 are crucial for the rapid association of diverse sets of information and pattern completion. Furthermore, CA1 may be instrumental in recognizing the novelty of an event or context (*8*, *9*).

Some of these ideas have been tested by lesioning (*10*) portions of the hippocampus or EC, although it is difficult to restrict damage to specific subregions and cell types in a quantitative and reproducible manner (*11*, *12*). These difficulties have in part been addressed by deleting the *N*-methyl-D-aspartate (NMDA) receptor gene *NR1* in specific hippocampal subregions with Cre-loxP recombination technology. These studies found that NMDA receptor–dependent synaptic plasticity in postnatal excitatory neurons of each of several hippocampal subregions is required for specific aspects of hippocampal learning and memory (*13*–*16*). In order to completely analyze hippocampal function, we developed a method to block neural transmission rather than synaptic plasticity and used it to assess the differential role of CA3 and EC outputs into area CA1 in hippocampus-dependent learning and memory.

We generated a triple transgenic mouse (Fig. 1B) by doxycycline (Dox)–inhibited circuit exocytosis knockdown (DICE-K), in which synaptic transmission is blocked by cell type–restricted and temporally controlled expression of the tetanus toxin (TeTX) light chain (*17*). TeTX is an endopeptidase specific for VAMP2 (*18*), which is essential for activity-dependent neurotransmitter release from presynaptic terminals (*19*). The rationale for this general method is described fully in the supporting online material (SOM).

We used the KA1 promoter (*14*) and α-CaMKII promoter (*20*) for the transgenic1 (Tg1) and transgenic2 (Tg2) mice, respectively, to block CA3 output in the TSP while keeping EC output in the MSP intact (Fig. 1B). Before generating the triple transgenic TeTX mouse line, we investigated several parameters of the DICE-K method by crossing the Tg1×Tg2 double transgenic mouse with a Tg3–green fluorescent protein (GFP) reporter line (CA3-GFP) (Fig. 1B). Immunohistology (Fig. 1, C to H) indicated that GFP expression was restricted to CA3 and DG in mice maintained on a Dox-free diet (Fig. 1, C to E). There was no expression of GFP in the CA1 pyramidal cell layer [stratum (s.) pyramidale] or temporoammonic (TA) pathway (s. lacunosum moleculare) but abundant expression in the Schaffer collateral (SC) pathway (s. radiatum and s. oriens) (Fig. 1E). In the Tg1×Tg2 mouse, the spatial restriction was much greater than in the Tg1 mouse (fig. S1). GFP expression was repressed in the Dox-on state (Fig. 1F), de-repressed in the Dox-on-off state (Fig. 1G), and re-repressed in the Dox-on-off-on state (Fig. 1H).

We crossed Tg1×Tg2 double transgenic mice with Tg3-TeTX mice to produce a triple transgenic mouse, CA3-TeTX. In hippocampal slices from control double transgenic mice (Tg1×Tg3-TeTX), VAMP2 immunoreactivity (IR) was observed where axonal terminals are known to exist (Fig. 1, I and M). Hippocampal VAMP2 IR patterns were indistinguishable between repressed CA3-TeTX and control mice (Fig. 1J). In hippocampal slices from CA3-TeTX mice that had been on Dox followed by 4 weeks of Dox withdrawal, there was a striking reduction of VAMP2 IR in the s. radiatum and s. oriens of CA1 and CA3 and in the inner one-third of the molecular layer (ML) of DG, but not in other strata (Fig. 1K). Similar patterns of VAMP2 IR were observed in hippocampal slices throughout the dorsoventral axis. The CA3-SC innervates CA1 in the s. radiatum and s. oriens, whereas CA3-recurrent collateral (RC) innervates CA3 in these

The Picower Institute for Learning and Memory, Howard Hughes Medical Institute, RIKEN-MIT Neuroscience Research Center, Department of Biology and Department of Brain and Cognitive Sciences, Massachusetts Institute of Technology, Cambridge, MA 02139, USA.

*To whom correspondence should be addressed. E-mail: tonegawa@mit.edu

strata. The inner one-third of ML is where mossy cells (MCs) innervate DG granule cells (*21*). Although the triple transgenic GFP mice showed moderate GFP IR in DG granule cells (Fig. 1G), there was no significant reduction of VAMP2 IR in the s. lucidum of CA3-TeTX mice where mossy fibers (MFs) from DG granule cells innervate CA3 (Fig. 1K). These results indicate that in the hippocampus of de-repressed CA3-TeTX mice, synaptic transmission should be impaired at SC-CA1 synapses, at the CA3-RC synapses, and possibly at MC-DG granule cell synapses, but not at MF-CA3 synapses. There was no indication of VAMP2 IR reduction in the s. lacunosum moleculare where the TA axons synapse onto CA1 neurons, suggesting that TA synaptic transmission remained intact (Fig. 1K). In CA3-TeTX mice that underwent 3 weeks of Dox withdrawal followed by 7 weeks of Dox readministration, the VAMP2 IR distribution was similar to that in repressed CA3-TeTX mice (Fig. 1J), indicating that TeTX-mediated blockade of synaptic transmission is reversible (Fig. 1L).

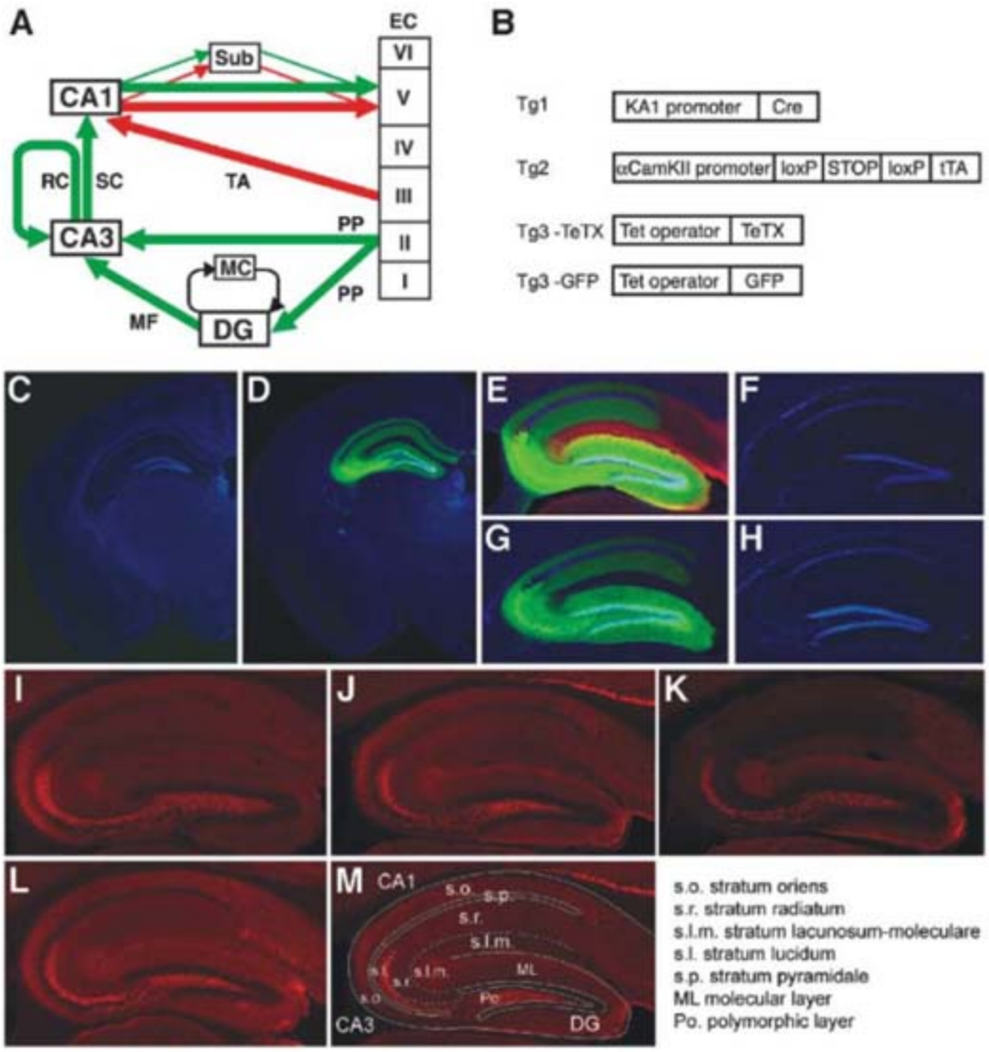

Fig. 1. Excitatory hippocampal-EC pathways and the DICE-K method applied to the TSP. (**A**) Excitatory pathways in the hippocampal formation and EC. Green and red arrows designate the TSP and MSP, respectively. Sub, subiculum; MC, mossy cells; PP, perforant pathway. (**B**) Tg1, a Cre transgenic line under control of the transcriptional regulator from the *kainate receptor 1* (*KA-1*) gene. Tg2, a tTA transgenic line under control of the αCaMKII promoter and Cre-loxP recombination. Tg3-TeTX and Tg3-GFP are TeTX and GFP transgenic lines, respectively, under control of the tetracycline (Tet) operator. (**C** and **D**) Double immunofluorescence staining of coronal sections from a Tg1×Tg3-GFP control mouse (C) and chronically de-repressed CA3-GFP mouse (D) with antibodies specific for GFP (green) and for a cell nuclei marker, DAPI (blue). (**E**) Triple immunofluorescence staining of a hippocampal sagittal section from a chronically de-repressed CA3-GFP mouse with antibodies specific for GFP (green), DAPI (blue), and netrin-G1 (red, a marker for TA and lateral perforant axons) (*34*). The outer one-third of DG dendrites stain yellow because they are positive for both netrin-G1 (red) and GFP (green). (**F** to **H**) DAPI and GFP double staining of a hippocampal section from a chronically repressed CA3-GFP mouse (F), followed by 2 weeks of Dox withdrawal (G), followed by 2 weeks of Dox readministration (H). (**I** to **L**) Immunofluorescence staining with VAMP2 antibodies of a hippocampal section from control mice that have been on Dox diet (I). VAMP2 staining of a section from a CA3-TeTX littermate raised on a Dox diet (J) and after 4 weeks of Dox withdrawal (K) is shown. (L) A CA3-TeTX mouse having undergone 3 weeks of Dox withdrawal followed by 7 weeks of Dox readministration. (**M**) Locations of various hippocampal strata.

We characterized the input-output relationship of SC and TA inputs to a common population of postsynaptic CA1 neurons using extracellular field recordings. We found no significant genotype-specific effect on SC or TA inputs in repressed mice kept chronically on Dox (Fig. 2A). CA3-TeTX mice raised on Dox and shifted to Dox-off for 1, 2, 3, 4, or 6 weeks showed a sharp dropoff in synaptic transmission at SC inputs between 2 and 3 weeks after Dox withdrawal (fig. S2). At 4 weeks after Dox withdrawal, synaptic transmission was impaired at SC inputs but remained intact at TA inputs (Fig. 2B). Residual synaptic transmission at SC inputs in these mice failed to elicit population spikes in the field excitatory postsynaptic potential (fEPSP) at any stimulation intensity (Fig. 2, B and C insets, and table S2) or in response to high-frequency stimulation. Synaptic transmission at SC inputs was restored by a readministration of Dox for 6 weeks (Fig. 2C), confirming the reversibility of the DICE-K method. Based on these results, we used 4 weeks of Dox withdrawal (de-repressed mice) in most behavioral and in vivo electrophysiological studies. De-repressed CA3-TeTX mice exhibited no detectable abnormalities in the hippocampal cytoarchitecture (fig. S3) (*22*) or in locomotor activity, anxiety, motor coordination, or pain sensitivity (figs. S4 and S5).

We subjected de-repressed CA3-TeTX mice to the Morris water maze (MWM) task (*16*). The latency curves of these and control mice were indistinguishable (Fig. 3A) (see SOM for statistics of this and following experiments). Memory recall was tested by probe trials on days 6 and 11. On day 6, there was only a slight preference for the target quadrant (Fig. 3B) and the target platform location (Fig. 3, C and D) in both CA3-TeTX and control animals, and there was no difference between the two genotypes. On day 11, the preference was robust in both genotypes for both criteria (Fig. 3, B to D), but again there was no robust difference between genotypes.

To test a possible role of CA3 output in rapidly forming representation of a novel context in the hippocampus, we subjected CA3-TeTX mice to a contextual fear conditioning (CFC) task using a novel context. De-repressed CA3-TeTX mice exhibited less freezing than control littermates (Fig. 3, E and F). The context specificity of conditioning was comparable between genotypes (fig. S6A), as was the level of tone fear conditioning (fig. S6B). The freezing deficit observed while the mice were in the Dox-on-off state (fig. S7, C and D) was absent when the same mice were reconditioned in another chamber and tested after 6 weeks of Dox re-administration (Fig. 3, G and H), demonstrating the reversibility of the DICE-K method at the behavioral level. When the de-repressed CA3-TeTX mice were habituated to the chamber before receiving a foot shock, they still tended to freeze less than the control littermates,

but the difference between the two genotypes was not significant (Fig. 3, I and J).

Our earlier study implicated NMDA receptor–dependent synaptic plasticity in CA3 pyramidal cells in pattern completion–based recall (*14*). To examine whether CA3 output in the TSP is crucial for this form of recall, we subjected CA3-TeTX mice to the pre-exposure mediated contextual fear conditioning (PECFC) paradigm (*23*, *24*). De-repressed CA3-TeTX mice exhibited less freezing than control littermates, unlike repressed CA3-TeTX mice (fig. S8). To test whether de-repressed mice are defective in the recall phase, we habituated CA3-TeTX mice to the chamber under Dox-on conditions to ensure the formation of a contextual representation and then switched them to Dox-off conditions. Four weeks later, the animals were returned to the chamber for a 10-s exposure followed by a foot shock. CA3-TeTX mice displayed a deficit in freezing when tested on the following day (Fig. 3K), indicating that CA3 output in the TSP is crucial for pattern completion–based recall.

To investigate a possible role of CA3 output in the TSP in the detection and encoding of novel space, we recorded CA1 ensemble activity using multi-tetrode recordings (*25*) as freely moving mice completed 10 laps on a novel linear track (day 1). During this first experience, we observed a significant increase in the average firing rate of CA1 pyramidal cells in de-repressed CA3-TeTX mice, which accompanied a significant decrease in spatial tuning of these cells and spatial information (Fig. 4, A to E, and table S1). There were no differences in peak firing rate, bursting properties of these cells, or spike width (table S1). No differences were found in average firing rates of inhibitory interneurons recorded from CA3-TeTX and control littermates (table S1), suggesting that coding deficits are not due to a loss of feed-forward inhibition from CA3. The mice were then returned to the same linear track 24 (day 2) and 48 (day 3) hours after the initial exposure. Place fields remained larger and spatial information was less in CA3-TeTX mice than in controls (Fig. 4, A to E), indicating that CA3 output is crucial for spatial tuning not only on a novel but also a familiar track. Earlier work with CA3-lesioned rats reported a much milder impairment, if any, in a familiar environment (*12*). We found a decrease in place field size and average firing rate along with an increase in spatial information between days 1 and 2 in CA3-TeTX mice, whereas no difference was found between days in control mice (Fig. 4, A to E).

The spatial restriction and temporal control over the expression of the transgenic TeTX gene of the DICE-K method permit a greater degree of specificity in silencing neural pathways than is possible with traditional lesion or pharmacological methods. Several new genetic methods allow the inactivation or activation of specific neurons by manipulation of ligand- or light-activated cell-surface receptors or channels to permit rapid inactivation or activation of cells on the subsecond-to-minute time scale. Hence, these are useful for studying relatively fast processes such as perception and short-term memory (*26*–*30*). In contrast, the kinetics of the DICE-K system are too slow for studying fast cognitive processes. Instead, this method can dissect the contribution of specific synaptic inputs to processes occurring over times from hours to weeks, such as intermediate- to long-term explicit memories and skill and habit learning. Because Dox can cross the blood-brain barrier, the DICE-K method can be used without complications from direct continuous injections of impermeable ligands into the brain or invasive deep brain light delivery.

Our data show that CA3 output in the TSP is dispensable for both acquisition and recall of incremental spatial learning and memory recall in the MWM task. The nearly identical latency curves and probe trial behaviors of CA3-TeTX and control mice, along with the lack of thigmotactic behavior, indicate that CA3-TeTX mice indeed used an allocentric spatial strategy to locate the platform (Fig. 3D). Thus, it is likely

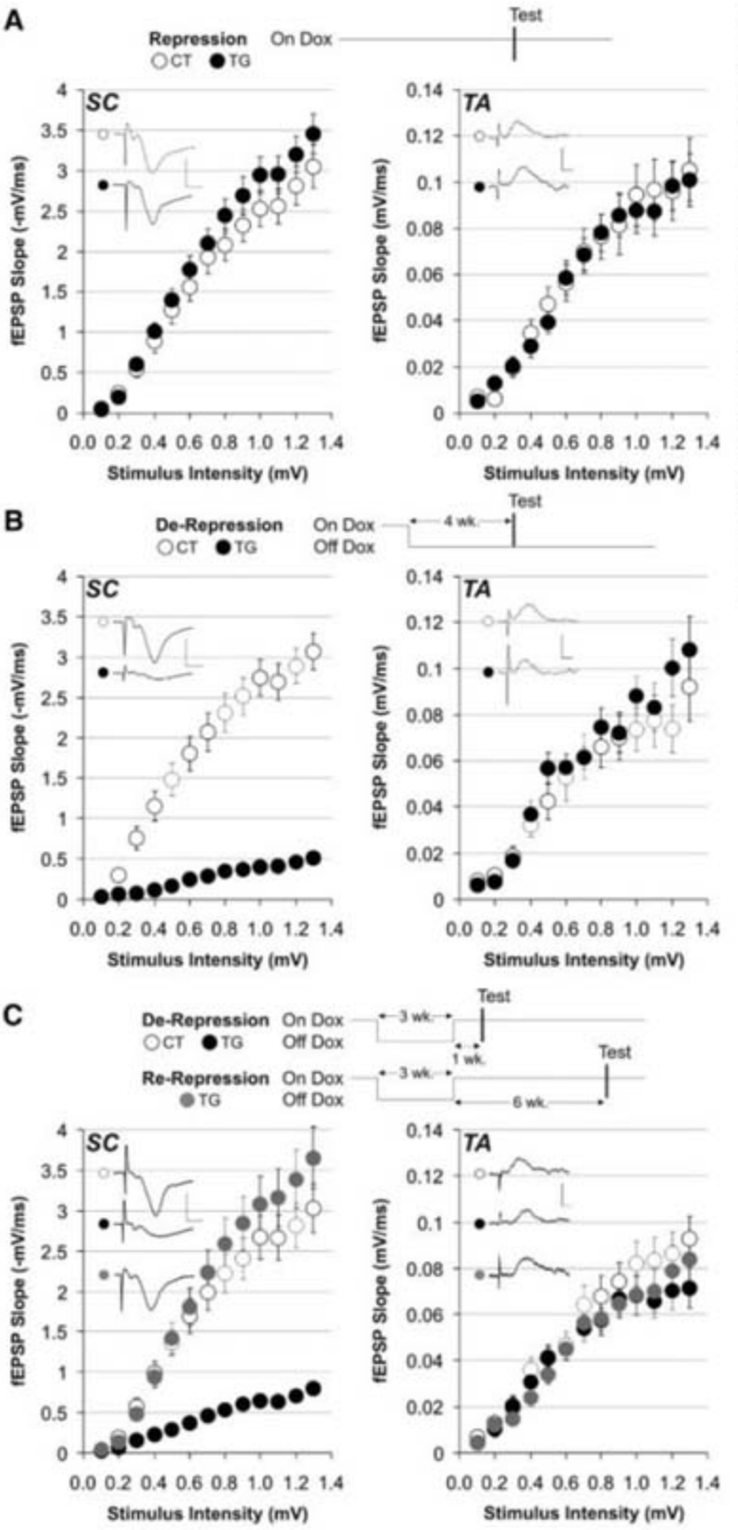

Fig. 2. Input-output relationships of SC and TA inputs to CA1 in CA3-TeTX (TG) mice and control littermates (CT). (**A**) Repressed (Dox-on) mice. (**B**) De-repressed (Dox on-off) mice after 4 weeks of Dox withdrawal. (**C**) De-repressed (Dox-on-off: 3 + 1 week) and re-repressed (Dox-on-off-on: 3 + 6 weeks) mice. Sample traces are representative of recorded mean maximal fEPSP slopes. Note the absence of population spikes in TG traces of (B) and (C). SC scale bar, 4 mV/2 ms; TA scale bar, 0.4 mV/4 ms. All statistics are given in the SOM.

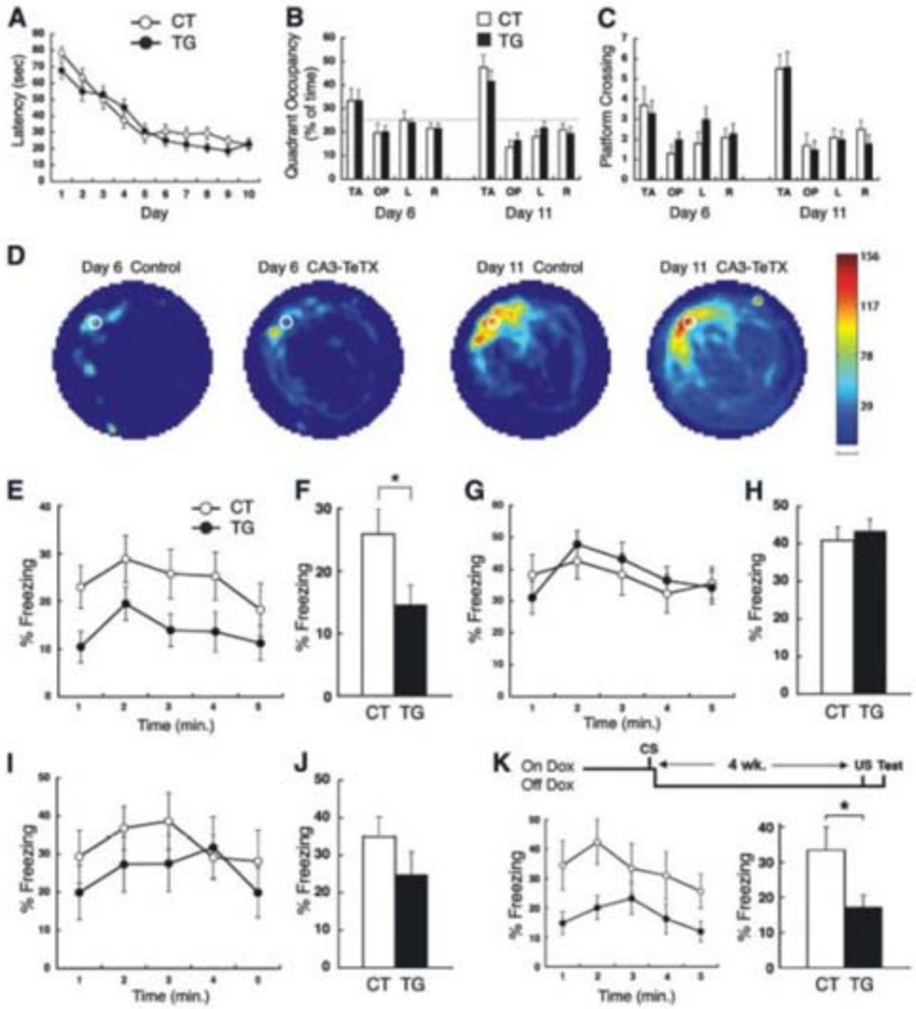

Fig. 3. MWM and CFC. (**A** to **D**) Performance in MWM of CA3-TeTX (TG) and double transgenic (Tg1×Tg3-TeTX) control littermates (CT) having undergone 4 weeks of Dox withdrawal. (A) Averaged latencies. (B) Probe trials by relative quadrant occupancy time. (C) Numbers of platform crossings. Quadrant designations: TA, target; OP, opposite; L/R, left/right to target. (D) Heat maps of average search time during probe trials. (**E** and **F**) CFC in a novel context of de-repressed mice (4 weeks off Dox). (E) Kinetics of averaged freezing. (F) Freezing averaged over the 3-min test session. (**G** and **H**) CFC in a novel context of re-repressed mice (3 weeks off Dox followed by 6 weeks of Dox re-administration). (G) Kinetics of freezing. (H) Freezing averaged over the first 3-min test session. (**I** and **J**) CFC in de-repressed mice (4 weeks off Dox) after 3-day familiarization (10 min/day) with the conditioning chamber. (I) Kinetics of freezing. (J) Freezing averaged over the first 3-min session. (**K**) PECFC of mice having undergone Dox diet schedules indicated on top. Kinetics of averaged freezing (left) and reezing averaged over the 5-min test session (right) are shown. CS, pre-exposure; US, foot shock. All statistics are given in the SOM.

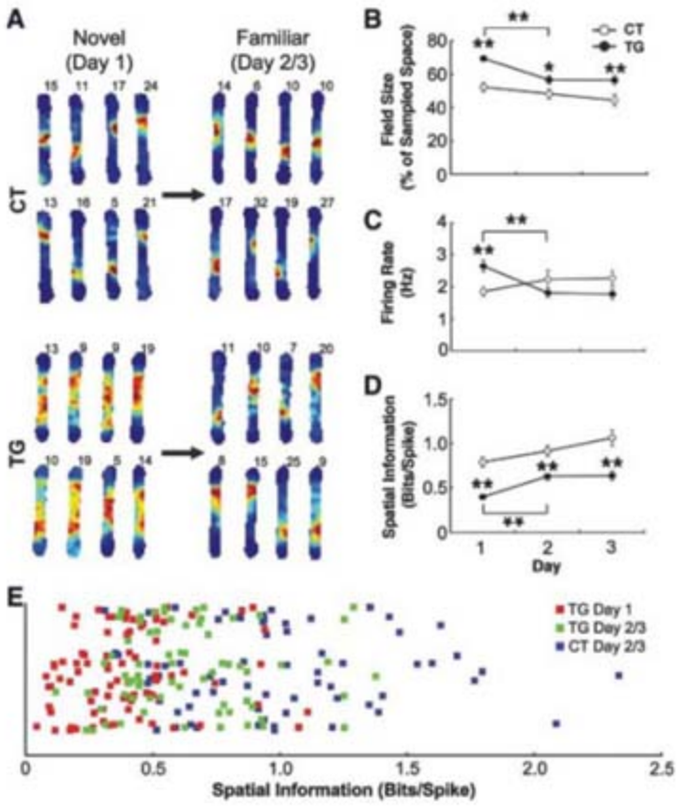

Fig. 4. CA1 place cells. (**A**) Representative examples of CA1 firing-rate maps in novel (day 1) and familiar (day 3) environments from CA3-TeTX (TG) mice and their double transgenic control littermates (CT) having undergone 4 weeks of Dox withdrawal, as mice completed 10 laps on a linear track. Colors are scaled to peak firing rates (in hertz) indicated at the top right of each map (blue, minimum; red, maximum). (**B**) Size of CA1 place fields, determined by the percentage of space where cells fire on the track for each day. (**C**) Average firing rate of all place cells plotted for each day. (**D**) Average spatial information (see SOM) for each day. (**E**) Spatial information for individual cells in novel (day 1) and familiar (day 3) environments. All statistics are given in the SOM. In (B) to (D), stars above solid circles indicate highly significant (**) or significant (*) differences between TG and CT. Double stars at the brackets indicate highly significant differences between TG day 1 and TG day 2.

that direct EC input to CA1 in the MSP can support these mnemonic processes. Our data contradict those of earlier studies conducted with rats with chemical or physical lesions, in which the integrity of CA3 or CA3 output was crucial for acquisition and/or recall in the MWM task (*11*, *12*). Although this contradiction may be due to species or protocol differences, it is more likely a result of the greater specificity of our DICE-K method. Tuned spatial and navigational information is present in the superficial layers of EC, which may provide CA1 the necessary information for spatial learning (*31*, *32*). Additionally, although CA1 neurons are poorly connected by recurrent collaterals, the MSP does form a closed loop EC III → CA1 → ECV → EC III (*21*) that may associate diverse spatial information, albeit less rapidly and less efficiently than the direct and robust recurrent network of CA3. Further, plasticity at MSP synapses of CA3-TeTX mice may mediate experience-dependent improvement in the MWM.

Our data also show that CA3 output is crucial for rapid one-trial learning in a novel context. It is thought that for CFC to occur, a representation of various contextual features must first be formed in the hippocampus and then must be conveyed to the amygdala via CA1 and/or the subiculum to be associated with the footshock representation (*33*). Evidently, the MSP cannot

provide these functions. The CFC deficit is reduced when animals are habituated to the context before the foot shock is delivered. Thus, with sufficient experience, the MSP seem to be able to fulfill a representation-forming and -conveying function.

Our in vivo recordings also illustrate a dichotomy between the ability of the TSP and MSP to support learning in novel and familiar space. The greatly reduced spatial tuning of CA1 pyramidal cells in CA3-TeTX mice on a novel track suggests that information contained in CA3 output is critical for rapid formation of a high-quality spatial representation and is consistent with the CFC deficit in a novel context. Further, the unexpectedly higher firing rates in CA3-TeTX mice under novel conditions suggests that in addition to providing spatial information, CA3 output may also help maintain appropriate levels of network excitability during novelty. On the other hand, the reduced deficit of spatial tuning during visits to the same track on days 2 and 3 indicates that the MSP alone can improve CA1 spatial tuning by experience, which is consistent with the reduced CFC deficit in a familiar context (Fig. 3, I and J) and the normal MWM performance (Fig. 3, A to D).

Thus, application of the DICE-K method to CA3 pyramidal cells demonstrates that the MSP (which bypasses CA3) can support slow incremental learning in familiar environments but that the CA3 output of the TSP is needed for rapid acquisition of memories in novel environments and for pattern completion–based recall.

References and Notes

1. W. B. Scoville, B. Milner, *J. Neuropsychiatry Clin. Neurosci.* **12**, 103 (1957).
2. L. R. Squire, C. E. Stark, R. E. Clark, *Annu. Rev. Neurosci.* **27**, 279 (2004).
3. L. E. Jarrard, *Behav. Neural Biol.* **60**, 9 (1993).
4. D. Marr, *Philos.Trans. R. Soc. London Ser. B* **262**, 23 (1971).
5. B. L. McNaughton, R. G. M. Morris, *Trends Neurosci.* **10**, 408 (1987).
6. R. C. O'Reilly, J. L. McClelland, *Hippocampus* **4**, 661 (1994).
7. J. L. McClelland, N. H. Goddard, *Hippocampus* **6**, 654 (1996).
8. J. E. Lisman, N. A. Otmakhova, *Hippocampus* **11**, 551 (2001).
9. D. Kumaran, E. A. Maguire, *Hippocampus* **17**, 735 (2007).
10. E. T. Rolls, R. P. Kesner, *Prog. Neurobiol.* **79**, 1 (2006).
11. B. Roozendaal *et al.*, *Nat. Neurosci.* **4**, 1169 (2001).
12. V. H. Brun *et al.*, *Science* **296**, 2243 (2002).
13. J. Z. Tsien, P. T. Huerta, S. Tonegawa, *Cell* **87**, 1327 (1996).
14. K. Nakazawa *et al.*, *Science* **297**, 211 (2002).
15. K. Nakazawa *et al.*, *Neuron* **38**, 305 (2003).
16. T. J. McHugh *et al.*, *Science* **317**, 94 (2007).
17. M. Yamamoto *et al.*, *J. Neurosci.* **23**, 6759 (2003).
18. G. Schiavo *et al.*, *Nature* **359**, 832 (1992).
19. S. Schoch *et al.*, *Science* **294**, 1117 (2001).
20. M. Mayford *et al.*, *Science* **274**, 1678 (1996).
21. M. P. Witter, D. G. Amaral, in *The Rat Nervous System*, G. Paxinos, Ed. (Academic Press, New York, 2004), pp. 635–710.
22. K. J. Harms, A. M. Craig, *J. Comp. Neurol.* **490**, 72 (2005).
23. M. S. Fanselow, *Anim. Learn. Behav.* **18**, 264 (1990).
24. J. W. Rudy, R. C. O'Reilly, *Behav. Neurosci.* **113**, 867 (1999).
25. M. A. Wilson, B. L. McNaughton, *Science* **261**, 1055 (1993).
26. E. M. Tan *et al.*, *Neuron* **51**, 157 (2006).
27. W. Lerchner *et al.*, *Neuron* **54**, 35 (2007).
28. F. Zhang *et al.*, *Nature* **446**, 633 (2007).
29. X. Han, E. S. Boyden, *PLoS One* **2**, e299 (2007).
30. A. Y. Karpova, D. G. Tervo, N. W. Gray, K. Svoboda, *Neuron* **48**, 727 (2005).
31. T. Hafting, M. Fyhn, S. Molden, M. B. Moser, E. I. Moser, *Nature* **436**, 801 (2005).
32. F. Sargolini *et al.*, *Science* **312**, 758 (2006).
33. S. Maren, *Annu. Rev. Neurosci.* **24**, 897 (2001).
34. S. Nishimura-Akiyoshi, K. Niimi, T. Nakashiba, S. Itohara, *Proc. Natl. Acad. Sci. U.S.A.* **104**, 14801 (2007).

35. We thank F. Bushard, C. Carr, X. Zhou, J. Derwin, A. Ogawa, C. Lovett, and M. Ragion for technical assistance; N. Arzoumanian for her help in manuscript preparation; and A. Govindarajan, S. Itohara, M. Remondes, M. Wilson, and members of the Tonegawa lab for advice and discussion. Supported by NIH grants R01-MH078821 and P50-MH58880 to S.T.

Supporting Online Material

www.sciencemag.org/cgi/content/full/1151120/DC1
Materials and Methods
SOM Text
Figs. S1 to S8
Tables S1 and S2
References

28 September 2007; accepted 11 January 2008
Published online 24 January 2008;
10.1126/science.1151120
Include this information when citing this paper.

BOLD Responses Reflecting Dopaminergic Signals in the Human Ventral Tegmental Area

Kimberlee D'Ardenne,[1,2*] Samuel M. McClure,[2,3] Leigh E. Nystrom,[2,3] Jonathan D. Cohen[2,3,4]

Current theories hypothesize that dopamine neuronal firing encodes reward prediction errors. Although studies in nonhuman species provide direct support for this theory, functional magnetic resonance imaging (fMRI) studies in humans have focused on brain areas targeted by dopamine neurons [ventral striatum (VStr)] rather than on brainstem dopaminergic nuclei [ventral tegmental area (VTA) and substantia nigra]. We used fMRI tailored to directly image the brainstem. When primary rewards were used in an experiment, the VTA blood oxygen level–dependent (BOLD) response reflected a positive reward prediction error, whereas the VStr encoded positive and negative reward prediction errors. When monetary gains and losses were used, VTA BOLD responses reflected positive reward prediction errors modulated by the probability of winning. We detected no significant VTA BOLD response to nonrewarding events.

Functional magnetic resonance imaging (fMRI) has become a prominent method for imaging brain activity in humans. Commonly used fMRI protocols acquire functional data with a spatial resolution on the order of several millimeters. These protocols are adequate for measuring blood oxygen level–dependent (BOLD) responses from relatively large neural structures such as the cortex and basal ganglia. However, they are not suitable for imaging brainstem structures that are of long-standing interest to neuroscientists. In particular, the brainstem nuclei of the dopamine, norepinephrine, and serotonin systems have long been known to play a critical role in the regulation of brain function, and disturbances of these systems have been implicated in most major psychiatric disorders. Recent theoretical advances have begun to identify specific functions for these brainstem systems. In particular, the reward prediction error theory of dopamine function (*1*, *2*) proposes a role for this neuromodulator in reinforcement learning. This theory makes specific predictions that have been tested in direct neuronal recordings from brainstem dopaminergic nuclei in nonhuman species. However, imaging studies in humans have been restricted to measurements from projection areas of the dopamine system [such as the ventral striatum (VStr) and medial prefrontal cortex] that are larger and therefore more easily imaged with fMRI. Here, we report the use of a combination of recently developed neuroimaging techniques that address the difficulties inherent to brainstem imaging in order to directly image the VTA.

There are several methodological challenges to imaging brainstem nuclei. First among them is the small size of the nuclei. The VTA is ~60 mm^3 in volume (*3*), or roughly the size of 2 voxels at the resolution common in fMRI studies (*4*–*18*). To address this issue, we acquired high-resolution echo planar images that have been shown to be sufficient to discern individual subcortical nuclei

[1]Department of Chemistry, Princeton University, Princeton, NJ 08544, USA. [2]Center for the Study of Brain, Mind, and Behavior, Princeton University, Princeton, NJ 08544, USA. [3]Department of Psychology, Princeton University, Princeton, NJ 08544, USA. [4]Department of Psychiatry, University of Pittsburgh, Pittsburgh, PA 15260, USA.

*To whom correspondence should be addressed. E-mail: dardenne@princeton.edu

and reduce partial volume effects [e.g. (*19*, *20*)]. Second, brainstem structures are near large pulsatile blood vessels that create physiological movement artifacts and consequent magnetic field inhomogeneities. We therefore acquired functional data synchronized with the participants' cardiac cycles so that these effects were minimized (*21*). Third, image contrasts commonly used for anatomical localization (such as T1-weighted images) are poorly suited to brainstem studies because they do not provide contrast between different brainstem nuclei. For the midbrain, several alternate pulse sequences have been shown to produce desired contrast (*22*, *23*). We used proton-density weighted images to visualize the substantia nigra (SN) and then used the SN as a landmark to locate the VTA (*22*) (Fig. 1). Finally, it has been shown that the brainstem does not reliably align to standard brain templates used for spatial normalization in the group analysis of data. We used a new normalization algorithm that significantly improves registration of the brainstem across participants (*24*).

We used these methods in two experiments modeled on previous nonhuman primate studies (*25*, *26*) and motivated directly by the reward prediction error theory of dopamine function (*1*, *2*). According to this theory, the firing rate of dopamine neurons directly encodes the difference between expected and received reward. This assumes that inputs to dopaminergic midbrain structures relay both the reward experienced at a given time and the reward expected at that time (*27*). Dopamine neurons are thought to calculate the difference between these two inputs to produce a reward prediction error signal (*1*, *2*). Because the BOLD response is thought to correlate most strongly with synaptic current (*28*, *29*), and therefore is likely to reflect afferent input, the BOLD response in midbrain dopaminergic structures could reflect several quantities: (i) current reward, (ii) expected reward, or (iii) a sum of the inputs equal to the reward prediction error (*30*). We hypothesized that BOLD responses measured in midbrain dopaminergic structures would reflect a reward prediction error. We positioned our slices to incorporate the VTA and as much of the SN (*2*, *31*, *32*) and VStr (*33*–*37*) as possible (*38*).

In our first experiment, we used a classical conditioning procedure known to elicit responses to unpredictable rewards and cues predicting rewards in the nonhuman primate dopamine system (*2*). Thirsty human participants were trained to expect a liquid reward at a fixed interval after the display of a visual cue (*35*, *39*, *40*). After training, delivery of the liquid reward was delayed in a subset of trials. This design allowed for investigation of signals related to both positive and negative reward prediction errors. Previous studies indicate that the omission of reward at the expected time generates a negative reward prediction error (*1*, *25*). Subsequently, when reward is delivered at the untrained, delayed, time, its delivery produces a positive reward prediction error (*1*, *2*, *25*). We estimated a general linear model (GLM) to look for deviations in the BOLD response at times when positive and negative reward prediction errors were expected (*41*).

The BOLD response in VTA was significantly related to positive ($P < 0.05$, two-sample t test corrected for multiple comparisons) but not negative reward prediction error signals (Fig. 2). The BOLD response in the VStr was significantly related to negative reward prediction error signals ($P < 0.05$, two-sample t test corrected for multiple comparisons) and also showed a nonsignificant trend toward a relation with positive reward prediction error signals (Fig. 3) (*38*). Post hoc analyses of the mean event-related time courses in the VStr indicated that BOLD responses were significantly enhanced by positive reward prediction errors (fig. S4).

If the BOLD response to positive reward prediction errors in the striatum resulted at least in part from activity in the VTA, then the responses in the two structures should correlate with one another. To test this prediction, we correlated the BOLD response in these two regions after the delivery of delayed, unexpected rewards. VTA and VStr BOLD responses were positively

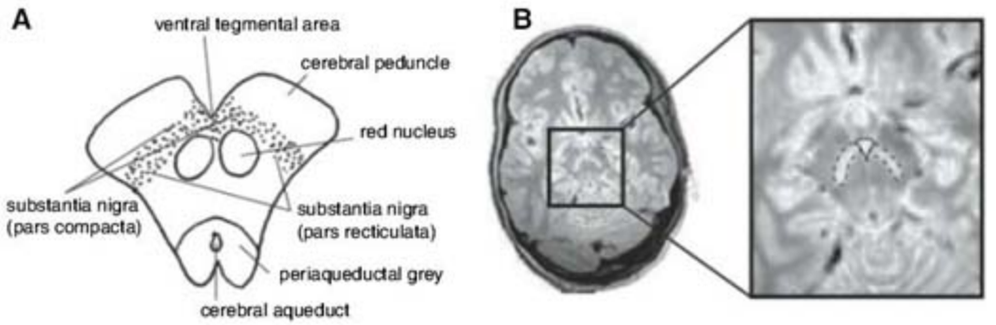

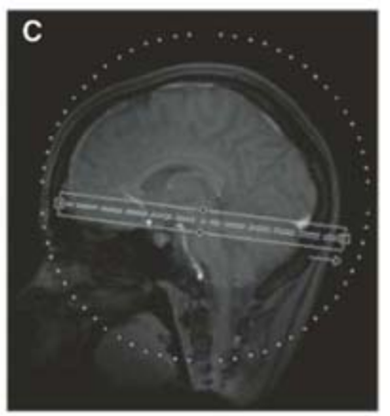

Fig. 1. Localization of midbrain dopamine nuclei with MRI. (**A**) The SN are located in the lateral portions of the midbrain, between the red nucleus and the cerebral peduncle. The VTA flanks the midline, medial to the SN (*3*, *50*). (**B**) Midbrain dopamine nuclei are clearly visible on proton-density weighted images; the midbrain is outlined in the box and expanded in the rightmost image. An axial slice is shown. The SN are the hyperintense areas adjacent to the hypointense red nucleus and cerebral peduncle (*22*). The SN are outlined with a dashed line and the VTA with a solid line in the expanded view. (**C**) Slice placement for one participant. The midbrain was identified in the central sagittal slice of the T1-weighted structural image. An oblique slab comprising axial/coronal slices (each slice 1.9 mm thick) was centered on the VTA and tilted to include as much of the SN and VStr as possible (*38*). The number of slices used was determined by the participant's heart rate. (See supporting online material for details of image acquisition.)

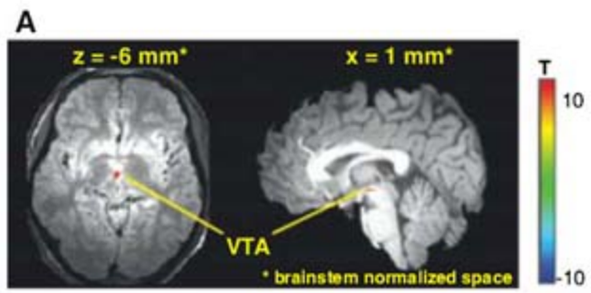

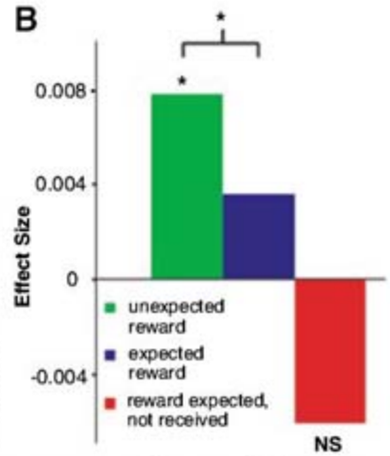

Fig. 2. The VTA BOLD response encoded positive reward prediction errors from delivery of primary rewards. (**A**) A random effects GLM analysis showed that VTA BOLD responses encoded positive reward prediction error signals ($n = 18$; $P < 0.05$, two-sample t test corrected for multiple comparisons). The cluster volume is 39 mm^3. Statistical maps are displayed on "brainstem-normalized" images (*24*): a proton-density weighted image in the axial view (left) and a T1-weighted image in the sagittal view (right). Coordinates shown are in brainstem-normalized space. (**B**) Plot of contrast estimates. Bars are average of regression coefficients (beta-weights from the GLM) for all voxels shown in (A). The VTA BOLD response to an unexpected reward was significantly larger than the BOLD response to an expected reward (*$P < 0.05$, two-sample t test corrected for multiple comparisons). The VTA BOLD response to a negative reward prediction error was not significant (NS; $P = 0.2671$, two-sample t test).

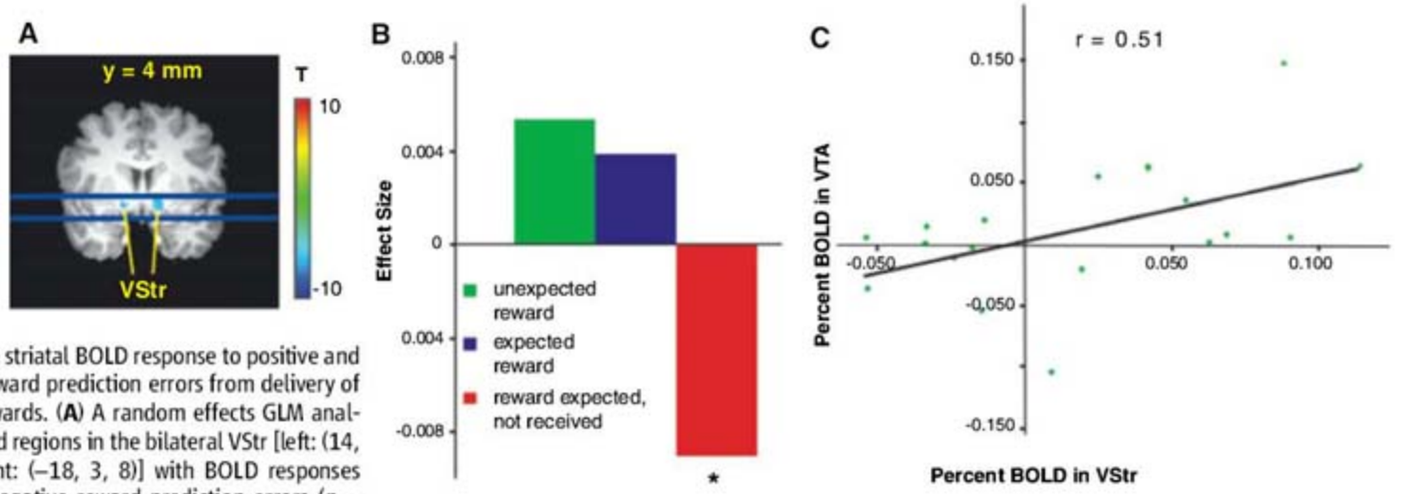

Fig. 3. The striatal BOLD response to positive and negative reward prediction errors from delivery of primary rewards. (**A**) A random effects GLM analysis revealed regions in the bilateral VStr [left: (14, 2, −7); right: (−18, 3, 8)] with BOLD responses reflecting negative reward prediction errors (n = 18; $P < 0.05$, two-sample t test corrected for multiple comparisons). Statistical maps are displayed on a T1-weighted image in Talairach space. The region of the VStr that we recorded from is delineated with blue lines (*38*). (**B**) Plot of contrast estimates. Bars are average of regression coefficients (beta-weights from the GLM) for all voxels shown in (A). VStr BOLD response reflects a negative reward prediction error (reward expected but not received; *$P < 0.05$, two-sample t test corrected for multiple comparisons). To determine if the VStr region shown in (A) also responded to positive reward prediction errors, we examined the contrast estimates for unexpected and expected reward receipt. The VStr region in (A) showed a trend toward a stronger BOLD response to unexpected than expected rewards. (**C**) Correlation analysis between BOLD responses to a positive reward prediction error measured from VStr and the VTA.

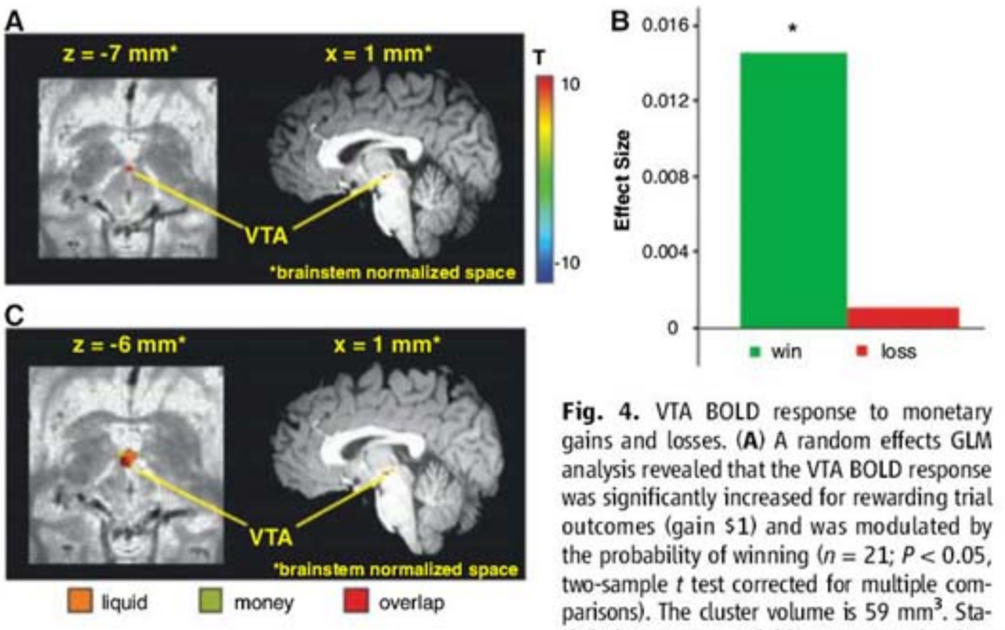

Fig. 4. VTA BOLD response to monetary gains and losses. (**A**) A random effects GLM analysis revealed that the VTA BOLD response was significantly increased for rewarding trial outcomes (gain $1) and was modulated by the probability of winning (n = 21; $P < 0.05$, two-sample t test corrected for multiple comparisons). The cluster volume is 59 mm^3. Statistical maps are overlaid on a proton density–weighted image (left) and T1-weighted image (right) in brainstem-normalized space (*24*). (**B**) Plot of contrast estimates for trial outcome. VTA BOLD responses reflected a positive reward prediction error (*$P < 0.05$, two-sample t test corrected for multiple comparisons). Because no brainstem regions were found to respond to negative reward prediction error signals (trial outcome when participant lost $1), the same voxels shown in (A) were used to generate this contrast estimate. (**C**) The VTA regions identified in both experiments overlap.

correlated (r = 0.51; Fig. 3C), suggesting a functional connection between the two areas (*42*).

We conducted a second experiment to verify that the BOLD response in the VTA encoded positive but not negative reward prediction errors. The experiment was also designed to assess the generality of these signals, by testing whether secondary (monetary) rewards were effective in producing BOLD responses in the VTA. Finally, we tested whether BOLD responses to reward prediction errors scale with reward probability, as predicted by theory. Participants were shown a number and indicated by button-press their guess as to whether a second number would be greater or less than the first number. Both numbers were randomly selected from the range of 0 to 10 and were never equal. Thus, the probability of guessing correctly was greatest when the first number was toward the extremes of the range. The outcome of the trial was displayed after a variable delay; participants won $1 for correct guesses and lost $1 for incorrect guesses. According to reinforcement learning models, the positive reward prediction error signal should decrease with increasing probability of winning (*1*, *43*). Conversely, negative reward prediction error signals (resulting from losses) should increase in magnitude with the probability of winning (*1*, *43*).

We estimated a model that included separate regressors for outcomes in which the participant won and lost. For outcomes in which the participant won, we found that BOLD responses in the VTA significantly scaled with the probability of winning ($P < 0.05$, two-sample t test corrected for multiple comparisons; Fig. 4). This replicated the finding from the first experiment that the VTA BOLD response reflects a positive reward prediction error. Though the two experiments used different reward modalities, the VTA regions we identified in both experiments overlapped (Fig. 4C).

We found no midbrain regions showing BOLD responses that correlated with negative reward prediction errors. In the first experiment, negative reward prediction errors resulted from the omission of an expected reward, whereas in the second experiment they were elicited by the loss of money. Although theory predicts that the dopamine system should report a negative reward prediction error (*1*, *2*), the underlying physiology of such a response remains unclear. Dopamine neurons have been shown, as predicted, to exhibit phasic decreases in firing for negative reward prediction errors (*2*). However, such reductions in dopamine firing rate are subtle (*32*) and their significance remains controversial (*44*). Furthermore, negative reward prediction errors resulting from aversive events (such as losses, as opposed to the omission of a reward) may produce no response at all in dopamine neurons (*45*, *46*).

Negative reward prediction errors might also have been expected to elicit an increase in activity within the VTA, among a subpop-

ulation of neurons that are known to respond to aversive stimuli ("tertiary cells") (*46*, *47*). However, tertiary cells constitute less than 30% of the neurons in the VTA (*47*). Therefore, while it is possible that tertiary cells did respond to monetary losses in our second experiment, it is likely that the corresponding positive BOLD response was too small to be resolved with the imaging protocols used. The absence of such BOLD responses suggests that the ones we did observe were sensitive selectively to dopamine-related signals.

We have shown that BOLD responses can be measured in the brainstem at a spatial resolution sufficient for investigating individual nuclei. Our findings are consistent with the reward prediction error theory of dopamine function in the human brain. Not only does this work add precision and accuracy to the study of dopamine function in humans, it also opens the door to the careful study of the role of dopamine in cognition at large (for example, its hypothesized role in updating working memory representations in prefrontal cortex) (*48*). It should now be possible to carry out similar investigations of other brainstem nuclei, such as norepinephrine and serotonin, that have been related to human cognition in recent theoretical work (*49*, *44*).

References and Notes

1. P. R. Montague, P. Dayan, T. J. Sejnowski, *J. Neurosci.* **16**, 1936 (1996).
2. W. Schultz, P. Dayan, P. R. Montague, *Science* **275**, 1593 (1997).
3. G. Paxinos, X. Huang, *Atlas of the Human Brainstem* (Academic Press, San Diego, CA, 1995).
4. Several recent studies (*5*–*18*) report findings from the SN and VTA with spatial resolution not better than 21 mm^3, which is inadequate for imaging from the VTA and only gives a small number of measurements in the SN.
5. B. Seymour *et al.*, *Nature* **429**, 664 (2004).
6. B. H. Schott *et al.*, *Learn. Mem.* **11**, 383 (2004).
7. B. C. Wittmann *et al.*, *Neuron* **45**, 459 (2005).
8. P. Dunckley *et al.*, *J. Neurosci.* **25**, 7333 (2005).
9. V. Menon, D. J. Levitin, *Neuroimage* **28**, 175 (2005).
10. J. P. O'Doherty, T. W. Buchanan, B. Seymour, R. J. Dolan, *Neuron* **49**, 157 (2006).
11. B. H. Schott *et al.*, *J. Neurosci.* **26**, 1407 (2006).
12. J. C. Dreher, P. Kohn, K. F. Berman, *Cereb. Cortex* **16**, 561 (2006).
13. N. Bunzeck, E. Duzel, *Neuron* **51**, 369 (2006).
14. M. Fairhurst, K. Wiech, P. Dunckley, I. Tracey, *Pain* **128**, 101 (2007).
15. P. N. Tobler, P. C. Fletcher, E. T. Bullmore, W. Schultz, *Neuron* **54**, 167 (2007).
16. B. H. Schott *et al.*, *Brain* **130**, 2412 (2007).
17. B. C. Wittmann, N. Bunzeck, R. J. Dolan, E. Duzel, *Neuroimage* **38**, 194 (2007).
18. N. Bunzeck *et al.*, *Cereb. Cortex* **17**, 2940 (2007).
19. K. A. Schneider, M. C. Richter, S. Kastner, *J. Neurosci.* **24**, 8975 (2004).
20. K. A. Schneider, S. Kastner, *J. Neurophysiol.* **94**, 2491 (2005).
21. A. R. Guimaraes *et al.*, *Hum. Brain Mapp.* **6**, 33 (1998).
22. H. Oikawa, M. Sasaki, Y. Tamakawa, S. Ehara, K. Tohyama, *AJNR Am. J. Neuroradiol.* **23**, 1747 (2002).
23. T. Eckert *et al.*, *Neuroimage* **21**, 229 (2004).
24. V. Napadow, R. Dhond, D. Kennedy, K. K. Hui, N. Makris, *Neuroimage* **32**, 1113 (2006).
25. J. R. Hollerman, W. Schultz, *Nat. Neurosci.* **1**, 304 (1998).
26. C. D. Fiorillo, P. N. Tobler, W. Schultz, *Science* **299**, 1898 (2003).
27. The reward prediction error term depends on time through a value function, $V(t)$, that gives the reward expected into the infinite future. It is the time derivative of $V(t)$, $dV(t)/dt$, that gives the reward expected at time t and is hypothesized to be communicated to midbrain dopamine nuclei (*1*).
28. N. K. Logothetis, J. Pauls, M. Augath, T. Trinath, A. Oeltermann, *Nature* **412**, 150 (2001).
29. A. Viswanathan, R. D. Freeman, *Nat. Neurosci.* **10**, 1308 (2007).
30. The reward prediction error signal could also be generated by recurrent collaterals in the VTA.
31. H. M. Bayer, P. W. Glimcher, *Neuron* **47**, 129 (2005).
32. H. M. Bayer, B. Lau, P. W. Glimcher, *J. Neurophysiol.* **98**, 1428 (2007).
33. G. Pagnoni, C. F. Zink, P. R. Montague, G. S. Berns, *Nat. Neurosci.* **5**, 97 (2002).
34. B. Knutson, A. Westdorp, E. Kaiser, D. Hommer, *Neuroimage* **12**, 20 (2000).
35. S. M. McClure, G. S. Berns, P. R. Montague, *Neuron* **38**, 339 (2003).
36. J. P. O'Doherty, P. Dayan, K. Friston, H. Critchley, R. J. Dolan, *Neuron* **38**, 329 (2003).
37. J. O'Doherty *et al.*, *Science* **304**, 452 (2004).
38. The VTA and SN include a variety of neuron types, not just dopaminergic neurons, and the BOLD response measured from these nuclei presumably reflects the composite activity of these neurons. Nevertheless, as discussed further on, our findings suggest that the BOLD responses we observed reflected a dominant, if not exclusive, influence of dopamine neuron activity. In addition, the methods we used were not optimized for detecting responses in the SN or VStr. Because of the cardiac gated functional data acquisition, image acquisition time was necessarily less than the time between heartbeats, which limited the number of slices we were able to acquire (see supporting online material for details). Slices were placed so as to optimize our coverage of the VTA. The VTA is small and thus, even with the number of slices we were limited to by the participant's heart rate, we were able to record from the entire region. However, we were only able to record from portions of the striatum (Fig. 3A) and SN. Given this limited coverage of the striatum and SN, our measurements from these structures are likely to have been underpowered.
39. A recent study reports an equal BOLD-fMRI response in the VStr to delivery of juice and water (*40*). Consequently, we included both juice and water trials in our study to keep participants as interested as possible. Juice and water trials were randomized across all scanning runs, and results are collapsed across both trial types.
40. S. M. McClure, K. M. Ericson, D. I. Laibson, G. Loewenstein, J. D. Cohen, *J. Neurosci.* **27**, 5796 (2007).
41. In addition to regressors for reward prediction errors, we also included regressors for the display of the visual cue and for dV/dt. No brain regions showed a significant response to the display of the cue during and after training [compare to (*37*)]; however, the visual cortex was not imaged in this experiment due to slice positioning (Fig. 1C). Additionally, no brain regions showed a significant response to dV/dt.
42. Mean event-related BOLD responses were calculated for the receipt of expected and unexpected rewards (see supporting online material for details on impulse response function generation and for plots of time course data). The areas under the response curves were calculated from time $t = 3$ s to 7 s after reward receipt and correlated across subjects in the VTA and VStr. This segment of the response curves was selected because it corresponds to the time points of the peak in the BOLD response.
43. In temporal difference reinforcement learning, the reward prediction error is given by $\delta(t) = r(t) + E\{r(t+1)|S_{t+1}\} - E\{r(t)|S_t\}$. $\delta(t)$ is the reward prediction error, $r(t)$ is the reward value at time t, and $E\{r(t)|S_t\}$ is the expected value of reward given the history of stimuli up to time t, which is termed S_t (*1*, *2*). When the stimulus is shown, the BOLD response should be proportional to $\delta(t) = E\{r(t+1)|S_{t+1}\}$ because we assume that the expected value is constant or zero between events. We represented the BOLD response to the display of the first number as not varying in magnitude because the probability of winning is unknown until participants press a button indicating their decision. It is important to note that when reward, $r(t)$, is less than 1 (i.e., when the participant loses \$1), predictions for adverse outcomes can be made. Rewriting the prediction error equation in terms of reward value and probability of reward gives $\delta(t) = r(t) + 1 \times p(r(t)|S_t) - 1 \times (1 - p(r(t)|S_t)) = r(t) - 2\,p(r(t)|S_t) + 1$. For wins, $\delta(t) = 2(1 - p(r(t)|S_t))$ and decreases linearly with the probability of winning. For losses, $\delta(t) = 2p(r(t)|S_t)$ and increases linearly with the probability of winning.
44. N. D. Daw, S. Kakade, P. Dayan, *Neural Netw.* **15**, 603 (2002).
45. J. Mirenowicz, W. Schultz, *Nature* **379**, 449 (1996).
46. M. A. Ungless, P. J. Magill, J. P. Bolam, *Science* **303**, 2040 (2004).
47. D. L. Cameron, M. W. Wessendorf, J. T. Williams, *Neuroscience* **77**, 155 (1997).
48. T. S. Braver, J. D. Cohen, in *Control of Cognitive Processes: Attention and Performance XVIII*, S. Monsell, J. Driver, Eds. (MIT Press, Cambridge, MA, 2000) pp. 713–737.
49. G. Aston-Jones, J. D. Cohen, *Annu. Rev. Neurosci.* **28**, 403 (2005).
50. H. M. Duvernoy, *The Human Brain Stem and Cerebellum: Surface, Structure, Vascularization, Three Dimensional Sectional Anatomy, and MRI* (Springer, New York, 1995).

51. We thank V. Napadow for access to the brainstem normalization algorithm ahead of its publication and for guidance with data acquisition. We thank C. L. Buck, K. Lowenberg, and E. Barkley-Levenson for help with participant recruitment and scanning. We also thank R. Tengi for helping manage the large amount of disk space necessary to accomplish data analysis. This work was supported by NIH grants P50 MH062196 (J.D.C.), T32 MH065214 (J.D.C.), and F32 MH072141 (S.M.M.).

Supporting Online Material

www.sciencemag.org/cgi/content/full/319/5867/1264/DC1
Materials and Methods
Figs. S1 to S5
References

17 September 2007; accepted 11 January 2008
10.1126/science.1150605

New Products

Integral Water Purification System

The Milli-Q Integral water purification system uses tap water to supply constant-quality Type II (pure) and Type I (ultrapure) water from a single water production unit. The system produces pure and/or ultrapure water for needs ranging from 60 to 300 liters per day. The flow rate is adjustable from drop-by-drop to 2 liters per minute. The dispensers can be adapted with a choice of final polishers to remove specific contaminants, including pyrogens, nucleases, bacteria, particulates, and organics. The dispensers accommodate a complete range of laboratory glassware and provide automatic and manual dispensing options.

Millipore
For information 800-548-7853
www.millipore.com

Oncomine Software

Oncomine Research Premium Edition software is designed for laboratories engaged in advanced cancer genomics research. It includes custom gene filters, integration with Ingenuity Pathway Analysis software, and full support for Oncomine Concepts Map, including the ability to upload custom and proprietary concepts in a secure environment. The premium edition is an extension of Oncomine Research Edition; the more basic edition is available under a free license for academic and nonprofit users.

Compendia Bioscience
For information 734-330-2259
www.compendiabio.com

Stem-Cell Tested Products

Millipore has launched a new initiative to validate many of its filter products for use on stem cells. The Stericup with Express Plus membrane is the first product available under this initiative. After filtering media through a Stericup with Express Plus membrane with a 0.22 m pore size, stem cells are passed five times and tested for pluripotency with no negative effect. Stericup filter cups combine a filter unit with a receiver flask and cap for processing and storage. Stericups are supplied sterile and ready to use, and offer fast flow with high throughput and low protein binding to ensure that key growth factors and proteins are not absorbed. When used with Express Plus membranes and media, Stericups offer an optimized and cost-effective system for stem cell culture that eliminates concern over whether filtering complete media will remove valuable factors or add deleterious components to the growth media.

Millipore
For information 800-548-7853
www.millipore.com

Fruit Fluorescent Proteins

Clontech is distributing vectors encoding several fruit fluorescent proteins. mCherry is available in four different vector formats to not-for-profit entities and academic labs. All four mCherry vectors, plus source vectors for five additional fruit fluorescent proteins, are available to for-profit entities through Clontech's licensing program. The fruit fluorescent proteins have a wide emission range and perform successfully in many fusion applications. These proteins can all be detected with Clontech Living Colors DsRed monoclonal and polyclonal antibodies.

Clontech
For information 650-919-7382
www.clontech.com

Dispenser

The Pipetboy Acu Pipettor is a lightweight, single-channel dispenser for safe, accurate, and reproducible filling and dispensing of plastic and glass pipettes, 1–100 ml. The unit is ergonomically designed, with aspirating and dispensing speed continuously adjustable using the thumbwheel dial. Touch-sensitive buttons enable precise one-handed operation, which is important when manipulating liquids in a confined laminar flow hood.

Integra Biosciences
For information +41 81 286 9530
www.integra-biosciences.com

Inverted Microscope for Live Cell Imaging

The Leica DMI3000 B inverted microscope is designed for live cell research applications. A new, integrated incident light fluorescence axis produces brilliant images for all fluorescence techniques. The instrument also offers integrated modulation and phase contrast methods that do not require the use of special objectives. It is suitable for all manual fluorescence techniques. It features a five-position fluorescence turret for the fluorescence filter cubes. A Fluorescence Intensity Manager regulates the illumination as well as the aperture and field diaphragm and their centering. The fluorescence cubes feature light traps for background light reduction to produce a perfectly black background. The DMI3000 B also offers a variety of illumination options for transmitted light applications. It offers five different condensers with different working distances (1, 23, 28, 40, and 70 mm). The special S40 condenser, with a working distance of 40 mm for micromanipulation, is suitable for integrated phase contrast and integrated modulation contrast. Leica has improved its integrated modulation contrast to increase the depth of field, which increases the spatial visibility of thicker specimens.

Leica
For information 800-248-0123
www.leica-microsystems.com

Electronically submit your new product description or product literature information! Go to **www.sciencemag.org/products/newproducts.dtl** for more information.

Newly offered instrumentation, apparatus, and laboratory materials of interest to researchers in all disciplines in academic, industrial, and governmental organizations are featured in this space. Emphasis is given to purpose, chief characteristics, and availabilty of products and materials. Endorsement by *Science* or AAAS of any products or materials mentioned is not implied. Additional information may be obtained from the manufacturer or supplier.